

Ministry of Education and Science of the Russian Federation  
Saint Petersburg National Research University of Information  
Technologies, Mechanics, and Optics

***NANOSYSTEMS:***  
***PHYSICS, CHEMISTRY, MATHEMATICS***

**2019, volume 10(3)**

**Наносистемы: физика, химия, математика**

**2019, том 10, № 3**



# NANOSYSTEMS:

PHYSICS, CHEMISTRY, MATHEMATICS

## ADVISORY BOARD MEMBERS

**Chairman:** V.N. Vasiliev (*St. Petersburg, Russia*),  
V.M. Buznik (*Moscow, Russia*); V.M. Ievlev (*Voronezh, Russia*), P.S. Kop'ev (*St. Petersburg, Russia*), N.F. Morozov (*St. Petersburg, Russia*), V.N. Parmon (*Novosibirsk, Russia*),  
A.I. Rusanov (*St. Petersburg, Russia*),

## EDITORIAL BOARD

**Editor-in-Chief:** I.Yu. Popov (*St. Petersburg, Russia*)

### Section Co-Editors:

Physics – V.M. Uzdin (*St. Petersburg, Russia*),  
Chemistry, material science – V.V. Gusarov (*St. Petersburg, Russia*),  
Mathematics – I.Yu. Popov (*St. Petersburg, Russia*).

### Editorial Board Members:

V.M. Adamyan (*Odessa, Ukraine*); O.V. Al'myashaeva (*St. Petersburg, Russia*);  
A.P. Alodjants (*Vladimir, Russia*); S. Bechta (*Stockholm, Sweden*); J. Behrndt (*Graz, Austria*);  
M.B. Belonenko (*Volgograd, Russia*); A. Chatterjee (*Hyderabad, India*); S.A. Chivilikhin  
(*St. Petersburg, Russia*); A.V. Chizhov (*Dubna, Russia*); A.N. Enyashin (*Ekaterinburg, Russia*),  
P.P. Fedorov (*Moscow, Russia*); E.A. Gudilin (*Moscow, Russia*); V.K. Ivanov  
(*Moscow, Russia*), H. Jónsson (*Reykjavik, Iceland*); A.A. Kiselev (*Durham, USA*);  
Yu.S. Kivshar (*Canberra, Australia*); S.A. Kozlov (*St. Petersburg, Russia*); P.A. Kurasov  
(*Stockholm, Sweden*); A.V. Lukashin (*Moscow, Russia*); I.V. Melikhov (*Moscow, Russia*);  
G.P. Miroshnichenko (*St. Petersburg, Russia*); I.Ya. Mittova (*Voronezh, Russia*);  
V.V. Pankov (*Minsk, Belarus*); K. Pankrashkin (*Orsay, France*); A.V. Ragulya (*Kiev, Ukraine*);  
V. Rajendran (*Tamil Nadu, India*); A.A. Rempel (*Ekaterinburg, Russia*);  
V.Ya. Rudyak (*Novosibirsk, Russia*); D Shoikhet (*Karmiel, Israel*); P Stovicek (*Prague, Czech Republic*);  
V.M. Talanov (*Novocherkassk, Russia*); A.Ya. Vul' (*St. Petersburg, Russia*); A.V. Yakimansky (*St. Petersburg, Russia*), V.A. Zagrebnov (*Marseille, France*).

### Editors:

I.V. Blinova; A.I. Popov; A.I. Trifanov; E.S. Trifanova (*St. Petersburg, Russia*),  
R. Simoneaux (*Philadelphia, Pennsylvania, USA*).

**Address:** University ITMO, Kronverkskiy pr., 49, St. Petersburg 197101, Russia.

**Phone:** +7(812)232-67-65, **Journal site:** <http://nanojournal.ifmo.ru/>,

**E-mail:** [popov1955@gmail.com](mailto:popov1955@gmail.com)

## AIM AND SCOPE

The scope of the journal includes all areas of nano-sciences. Papers devoted to basic problems of physics, chemistry, material science and mathematics inspired by nanosystems investigations are welcomed. Both theoretical and experimental works concerning the properties and behavior of nanosystems, problems of its creation and application, mathematical methods of nanosystem studies are considered.

The journal publishes scientific reviews (up to 30 journal pages), research papers (up to 15 pages) and letters (up to 5 pages). All manuscripts are peer-reviewed. Authors are informed about the referee opinion and the Editorial decision.

# CONTENT

## PHYSICS

- J. Kori, Pratibha  
**Effect of periodic permeability of lung airways on the flow dynamics of viscous fluid** 235
- Munavar Hussain M., B.H. Doreswamy, N.C. Shobha,  
V.N. Vijayakumar, K. Fakruddin  
**Orientational order parameter of liquid crystalline nanocomposites by Newton's rings and image analysis methods** 243
- Rozina Patel, Pratibha Sawadh  
**Tunable multiferroic properties of cerium doped bismuth ferrite** 255
- O.N. Sergaeva, I.A. Volkov, R.S. Savelev  
**Resonant dielectric waveguide-based nanostructure for efficient interaction with color centers in nanodiamonds** 266
- O.P. Swami, V. Kumar, B. Suthar, A.K. Nagar  
**A theoretical study of the propagation of light soliton produced by semiconductor quantum dots through optical fibers** 273

## CHEMISTRY AND MATERIAL SCIENCE

- E.A. Chernova, I.V. Roslyakov, S.G. Dorofeev, A.V. Lukashin  
**Composite membranes based on geometrically constrained PIM-1 for dehumidification of gas mixtures** 282
- E.Yu. Krysanov, T.B. Demidova, O.S. Ivanova, K.G. Ordzhonikidze,  
A.B. Shcherbakov, V.K. Ivanov  
**Synergetic action of ceria nanoparticles and doxorubicin on the early development of two fish species, *Danio rerio* and *Puntius tetrazona*** 289
- I.S. Kuryndin, I.Yu. Dmitriev, V.K. Lavrentyev,  
N.N. Saprykina, G.K. Elyashevich  
**Nano- and micro-scales structure and properties of the liquid-permeable piezoactive polyvinylidene fluoride films** 303
- K.D. Martinson, S.S. Kozyritskaya, I.B. Panteleev, V.I. Popkov  
**Low coercivity microwave ceramics based on LiZnMn ferrite synthesized via glycine-nitrate combustion** 313

A.A. Ostroushko, I.D. Gagarin, I.G. Danilova, I.F. Gette <b>The use of nanocluster polyoxometalates in the bioactive substance delivery systems</b>	<b>318</b>
M.V. Someswararao, R.S. Dubey <b>Experimental studies of barium titanate nanofibers prepared by electrospinning</b>	<b>350</b>
Venkatesh Yepuri, R.S. Dubey, Brijesh Kumar <b>Morphological and optical properties of dielectric multilayer structures prepared with distinct precursor concentrations</b>	<b>355</b>
A.Yu. Zavialova, A.N. Bugrov, R.Yu. Smyslov, D.A. Kirilenko, T.V. Khamova, G.P. Kopitsa, C. Licitra, D. Rouchon <b>Structure and photoluminescent properties of TiO<sub>2</sub>:Eu<sup>3+</sup> nanoparticles synthesized under hydro and solvothermal conditions from different precursors</b>	<b>361</b>
V.P. Zhukov, M.G. Kostenko, A.A. Rempel, I.R. Shein <b>Influence of carbon or nitrogen dopants on the electronic structure, optical properties and photocatalytic activity of partially reduced titanium dioxide</b>	<b>374</b>
<b>Information for authors</b>	<b>383</b>

## Effect of periodic permeability of lung airways on the flow dynamics of viscous fluid

J. Kori\*, Pratibha

Department of Mathematics, Indian Institute of Technology Roorkee, Roorkee-247667, Uttarakhand, India

\*jyotikorii@gmail.com

DOI 10.17586/2220-8054-2019-10-3-235-242

In this study, we aimed to find the effect of periodic permeability on the flow dynamics of an incompressible, Newtonian, viscous and pulsatile flow of air flowing through airway generations 5–10. To solve this problem, we used a generalized Navier Stokes equation by including the Darcy law of a porous media with periodic permeability for the flow of air and Newton equation of motion for the flow of nanoparticles. The finite difference explicit numerical scheme has been carried out to solve the governing nonlinear equations and then computational work is done on MATLAB R2016 by user defined code. After performing numerical computation we found by varying mean permeability of porous media velocity of air and particle increased gradually with axial and radial distance respectively.

**Keywords:** lung generation, deposition, periodic permeability, pulsatile flow, nanoparticle.

*Received:* 22 May 2019

*Revised:* 6 June 2019

### 1. Introduction

Every day billions of particles are inhaled with the ambient air [1, 2]. Concerning the effect of inhaled particulate matter on different regions of human lung, a number of studies are done. Tian et al. [3] stated that nanoparticles of range 5.52–98.2 nm pose risks for occupational workers and are the cause of various respiratory, cardiovascular, and neurological disorders. A study based on CT scanner images carried out by Debo et al. [4] to find the effect of micron particles (1–10  $\mu\text{m}$ ) and nanoparticles (1–100 nm) in the nasal cavity up to the upper six-generation of the lung has observed that the deposition efficiency of micron particles there is much higher than nanoparticles in the nasal region. A theoretical study by Sturm [5] states that due to very small size, nanoparticles are aggregates with highly irregular shape (chain-like, loose, compact) and that these particles are taken after inhalation up into the respiratory tract by the mechanism of Brownian diffusion, sedimentation [6] and are then stored in the epithelial cells for a longer time span, which causes the formation of cancerous cells. Recently, Saini et al. [7] studied the deposition of nanoparticles of diameter 100 nm and found that these particles travel deeper into the lung and ultimately deposit in the alveolar ducts of the human lung.

According to Haber et al. [8] the deposition of particles also depends on media porosity due to the large number of alveoli inside the human lung. Many researchers [9, 10] defined it as a sponge or porous medium. Cheng [11] and Vafai et al. [12] used the porous media approach for convective mass transfer in the airway and its surrounding wall tissue. Also, Kuwahara et al. [13] obtained mass transfer resistance between the inlet of the trachea and the blood in the capillaries using the porous media approach. Saini et al. [14] treated the alveolar region as a biofilter and found removal efficiency of lung for nanoparticles by using generalized Navier-Stokes equations. Recently DeGroot and Straatman [9] worked on expansion and contraction of alveolar duct and assumed lung is a porous medium by using theory of volume-averaging technique for unit cell of an alveolar duct to predict permeability of human lung.

Based on our literature review we found that there are a few studies which considered the lung as a porous medium. Those studies which took this point of view, however, assumed either that the permeability depends on the porosity or that it is constant. Thus, we aimed to study the effect of periodic permeability on the two dimensional pulsatile flow of viscous air flowing through airway generations 5–10 due to periodic breathing. The governing nonlinear equations are described in detail and then solved numerically by using finite difference methods. The computational work was carried out using MATLAB 2016 through a user defined code.

### 2. Mathematical modeling

#### 2.1. Physical configuration

To understand the flow regime within airway generations 5–10, an extended horizontal circular cylindrical tube (representing an airway tube) of the circular cross section is considered whose radius is 'b' and is placed perpendicularly to the incoming flow [15]. A schematic diagram is shown in Fig. 1, where, 'z' is the axial direction of flow and 'r' is the radial direction of flow.

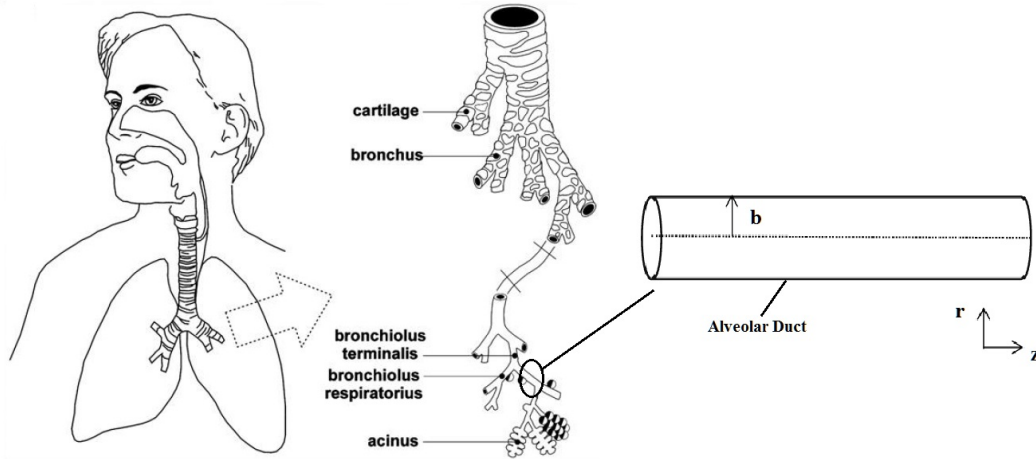


FIG. 1. Cross sectional view of airway duct (circular cylindrical tube) of a tracheobronchial tree [16], where 'r' is the radial direction and 'z' is the axial direction of viscous air flow

## 2.2. Governing equations for viscous air flowing through airway tube

We assumed that an incompressible, laminar, unsteady, axi-symmetric, Newtonian and fully-developed fluid is flowing along the axis of the circular tube with time dependent sinusoidal pressure gradient. The tissue of the airway tube is approximated as a homogeneous porous medium, which is viewed as a continuum, and saturated with an incompressible fluid. A mathematical model proposed by Saini et al. [7] is taken under consideration by using Darcy law of porous media together with the periodic permeability of the medium in order to find their effect on the flow of fluid<sup>1</sup>. The corresponding two dimensional conservation equations of mass, momentum together with particle motion in the cylindrical polar coordinates system ( $r, z$ ) for symmetrical flow ( $\theta = \text{constant}$ ) which satisfy our assumptions are given below:

First, there is the equation of continuity, given by:

$$\frac{\partial u_r}{\partial r} + \frac{u_r}{r} + \frac{\partial u_z}{\partial z} = 0. \quad (1)$$

$$\frac{\partial v_r}{\partial r} + \frac{v_r}{r} + \frac{\partial v_z}{\partial z} = 0. \quad (2)$$

Secondly there is the equation of radial momentum, given by:

$$\frac{\partial u_r}{\partial t} + \frac{u_r}{\epsilon} \frac{\partial u_r}{\partial r} + \frac{u_z}{\epsilon} \frac{\partial u_r}{\partial z} = -\frac{\epsilon}{\rho_a} \frac{\partial p}{\partial r} + \nu \left( \frac{\partial^2 u_r}{\partial r^2} + \frac{1}{r} \frac{\partial u_r}{\partial r} + \frac{\partial^2 u_r}{\partial z^2} \right) + k_f \frac{\rho_p}{\rho_a} (v_r - u_r) - \frac{\epsilon \nu}{K} u_r. \quad (3)$$

Finally we have the equation of axial momentum, given by:

$$\frac{\partial u_z}{\partial t} + \frac{u_r}{\epsilon} \frac{\partial u_z}{\partial r} + \frac{u_z}{\epsilon} \frac{\partial u_z}{\partial z} = -\frac{\epsilon}{\rho_a} \frac{\partial p}{\partial z} + \nu \left( \frac{\partial^2 u_z}{\partial r^2} + \frac{1}{r} \frac{\partial u_z}{\partial r} + \frac{\partial^2 u_z}{\partial z^2} \right) + k_f \frac{\rho_p}{\rho_a} (v_z - u_z) - \frac{\epsilon \nu}{K} u_z. \quad (4)$$

where,  $\epsilon$  is the porosity of lung and  $K$  is the permeability of porous medium. We also have the equations for the particle motion. In the radial direction, we have:

$$\frac{\partial v_r}{\partial t} + v_z \frac{\partial v_r}{\partial z} + v_r \frac{\partial v_r}{\partial r} = \frac{k_f (u_r - v_r)}{m}. \quad (5)$$

In the axial direction, we have:

$$\frac{\partial v_z}{\partial t} + v_z \frac{\partial v_z}{\partial z} + v_r \frac{\partial v_z}{\partial r} = \frac{k_f (u_z - v_z)}{m}. \quad (6)$$

$$k_f = 3\pi\mu d.$$

<sup>1</sup>Henry Darcy was a French engineer who gave a mathematical relationship between permeability and velocity of media, which is known as Darcy law of porous media [17]

### 2.3. Assumption

There is no radial flow along the axis of the airway duct and the axial velocity gradient of the streaming air may be implicit to be equal to zero:

$$u_r = 0, v_r = 0, \frac{\partial u_z}{\partial r} = 0, \frac{\partial v_z}{\partial r} = 0. \quad (7)$$

### 2.4. Initial and boundary condition

- At rest  $t \leq 0$ , no flow takes place therefore,

$$u_r = v_r = u_r = v_r = 0, \quad (8)$$

The boundary conditions for  $t > 0$  are given as follows,

- Due to periciliary liquid layer, no-slip condition is forced at the inner surface of the wall:

$$u_r = 0, u_z = 0, v_r = 0, v_z = 0. \quad (9)$$

## 3. Methodology

### 3.1. Transformation of the governing equations

In order to solve the equations numerically we have to make the above equations dimensionless by using following quantities:

$$R^* = \frac{r}{b}, Z^* = \frac{z}{b}, P^* = \frac{P}{\rho_a U_0^2}, \tau^* = \frac{t U_0}{b}, U_r^* = \frac{u_r}{U_0}, U_z^* = \frac{u_z}{U_0}, V_r^* = \frac{v_r}{U_0}, V_z^* = \frac{v_z}{U_0},$$

$$Da = \frac{K}{b^2}, Pl = \frac{\rho_p}{\rho_a}, S_m = \frac{rk}{U_0}, Re = \frac{r U_0}{\nu}.$$

Finally, we obtain the following equations:

$$\frac{\partial U_r}{\partial R} + \frac{U_r}{R} + \frac{\partial U_z}{\partial Z} = 0. \quad (10)$$

$$\frac{\partial V_r}{\partial R} + \frac{V_r}{R} + \frac{\partial V_z}{\partial Z} = 0. \quad (11)$$

$$\frac{\partial U_z}{\partial \tau} + \frac{U_r}{\epsilon} \frac{\partial U_z}{\partial R} + \frac{U_z}{\epsilon} \frac{\partial U_z}{\partial Z} = -\epsilon \frac{\partial P}{\partial Z} + \frac{1}{Re} \left( \frac{\partial^2 U_z}{\partial R^2} + \frac{1}{R} \frac{\partial U_z}{\partial R} + \frac{\partial^2 U_z}{\partial Z^2} \right) + S_m Pl (V_z - U_z) - \frac{\epsilon}{Da Re} U_z. \quad (12)$$

$$\frac{\partial V_z}{\partial \tau} + V_r \frac{\partial V_z}{\partial R} + V_z \frac{\partial V_z}{\partial Z} = \frac{S_m (U_z - V_z)}{m}. \quad (13)$$

In equation 12, due to rhythmic breathing, expansion and contraction and the right heart pressure we assumed a non-dimensional time dependent sinusoidal pressure gradient inside airway duct as follows,

$$\frac{\partial P}{\partial Z} = -a_0 \sin \omega t, \quad \omega = 2\pi f \quad (14)$$

where  $f$  is the frequency of breathing. Also, in this equation, we assumed permeability,  $K$ , of media is periodic [18] due to an oscillation of velocity about a nonzero constant mean. So,  $K$  can be defined in non-dimensional form as

$$K = \frac{K_0}{1 - a_0 \cos(\pi Z)}, \quad (15)$$

where,  $K_0$  is the mean permeability of porous medium and  $a_0$  is the amplitude of oscillation.

Also, transformed initial and boundary conditions together with assumptions respectively are as follows:

$$U_r = 0, U_z = 0, V_r = 0, V_z = 0. \quad (16)$$

$$U_r = 0, V_r = 0, U_z = 0, V_z = 0. \quad (17)$$

$$U_r = 0, \frac{\partial U_z}{\partial R} = 0, V_r = 0, \frac{\partial V_z}{\partial R} = 0 \quad (18)$$

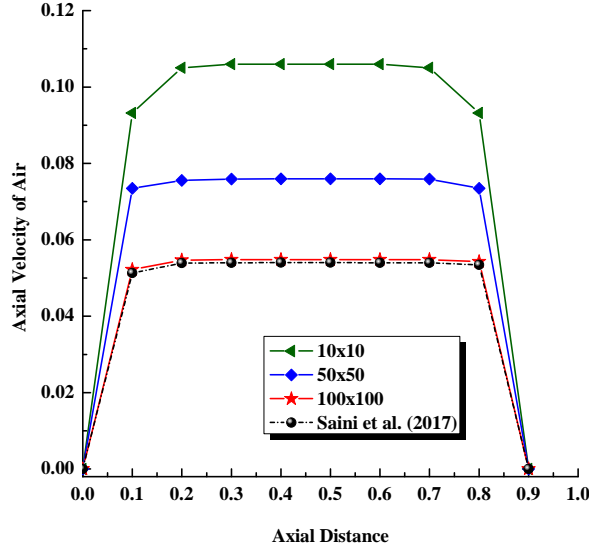


FIG. 2. A comparative result between published [7] and present work for axial velocity profile of air at  $\tau = 0.9$ ,  $R = 0$ ,  $Z = [0, 1]$ ,  $Re = 10$ ,  $d = 100 \text{ nm}$  and  $a = 125 \text{ }\mu\text{m}$

#### 4. Numerical scheme

Analytical approaches are suitable for linear problems, but the governing equations of the present issue are non-linear. Consequently it is difficult to find the solution of these nonlinear equations subject to the initial and boundary conditions by an analytical approach. For this reason, we have adopted a numerical procedure to find solutions of the problem. Although there are various numerical techniques, for example, the finite difference method (FDM) [7,19–21], the finite element method (FEM) [10, 22] or the finite volume method (FVM) [23] have been used to solve such non-linear problem. Among those methods, FDM is a basic and less tedious technique for regular geometry. Our problem is related to the flow in a circular cylinder, with a regular geometry. Thus, to solve the present problem we also applied finite difference numerical scheme. The discretization of the axial velocity  $U(R, Z, \tau)$  is written as  $U_z(R_i, Z_j, \tau)$  or  $((U_z)_{i,j})^k$  and computational grid that has been used is of the following form:

$$\begin{aligned}
 R_i &= i.\Delta R; & i &= 0, 1, 2, \dots M, R_M = 1.0, \\
 Z_j &= j.\Delta Z; & j &= 0, 1, 2, \dots N, \\
 \tau_k &= k.\Delta \tau; & k &= 0, 1, 2, \dots O.
 \end{aligned}
 \tag{19}$$

Where  $i, j$  and  $k$  are the space and time indices, and  $\Delta R = 0.01$ ,  $\Delta Z = 0.01$  and  $\Delta \tau = 10^{-5}$  are increments in radial, axial and time respectively. We used central difference approximations, for all the spatial derivatives, as follows,

$$\frac{\partial U_z}{\partial Z} = \frac{(U_z)_{i,j+1}^n - (U_z)_{i,j-1}^n}{2\Delta Z}.
 \tag{20}$$

For the second order central difference approximation for the time and space derivatives we have used:

$$\frac{\partial^2 U_z}{\partial Z^2} = \frac{(U_z)_{i,j+1}^n - 2(U_z)_{i,j}^n + (U_z)_{i,j-1}^n}{(\Delta Z)^2}.
 \tag{21}$$

and for first order time derivative at point  $(R_i, Z_j, \tau_k)$  we applied forward difference approximation as follows:

$$\frac{\partial (U_z)}{\partial \tau} = \frac{(U_z)_{i,j}^{n+1} - (U_z)_{i,j}^n}{2\Delta \tau}.
 \tag{22}$$

After applying the above mentioned discretization techniques, we have obtained velocity profiles at the  $(j + 1)^{th}$  time level in terms of the velocity at  $j^{th}$  time level for Equations (11)-(18) respectively.

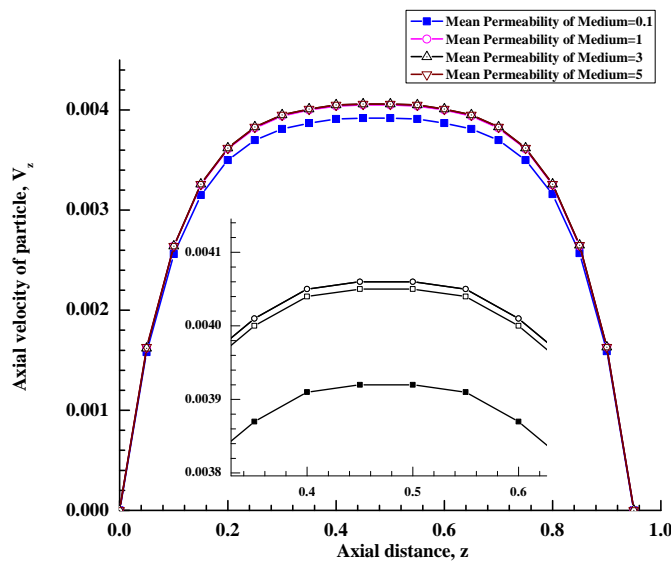
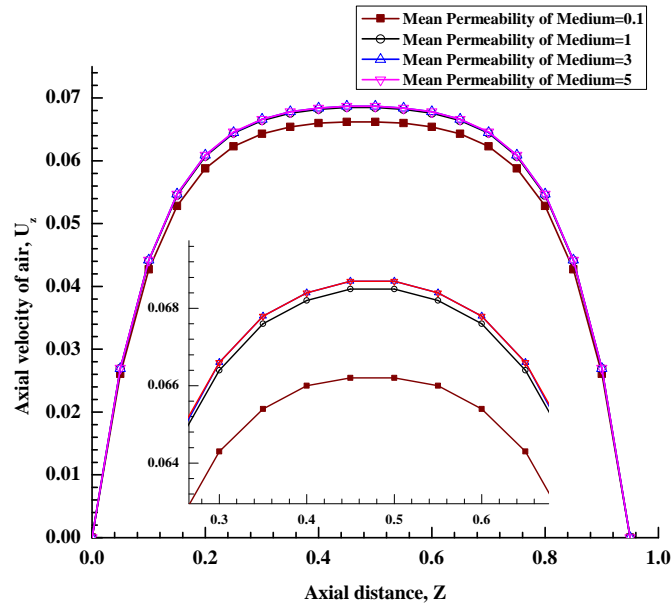


FIG. 3. Effect of mean permeability of porous media on axial velocity of (a) air and (b) particles at  $\tau = 0.5$ ,  $R = 0$ ,  $Z = [0, 1]$ ,  $Re = 10$ ,  $d = 50$  nm,  $a = 0.5$   $\mu$ m

We used following stability criteria for explicit finite difference scheme and found our results are accurate of order  $10^{-5}$  by using grid size  $100 \times 100 \times 10^5$  (i.e.  $M = 100$ ,  $N = 100$ ,  $O = 10^5$ ):

$$\max \left( \frac{\Delta \tau}{\Delta Z^2} \right) \leq 0.5. \tag{23}$$

#### 4.1. Model Validation and Grid Independency Test

Before analyzing the problem related to periodic permeability and sinusoidal pressure gradient due to periodic breathing, a grid independency test, together with a numerical code validation to find the predictive accuracy of the mathematical model is done by comparing outcomes produced by present study with the study of Saini et al. [7] and shown in Fig. 2 for grid sizes  $10 \times 10 \times 10^5$ ,  $50 \times 50 \times 10^5$  and  $100 \times 100 \times 10^5$ . Saini et al. [7] performed an extensive

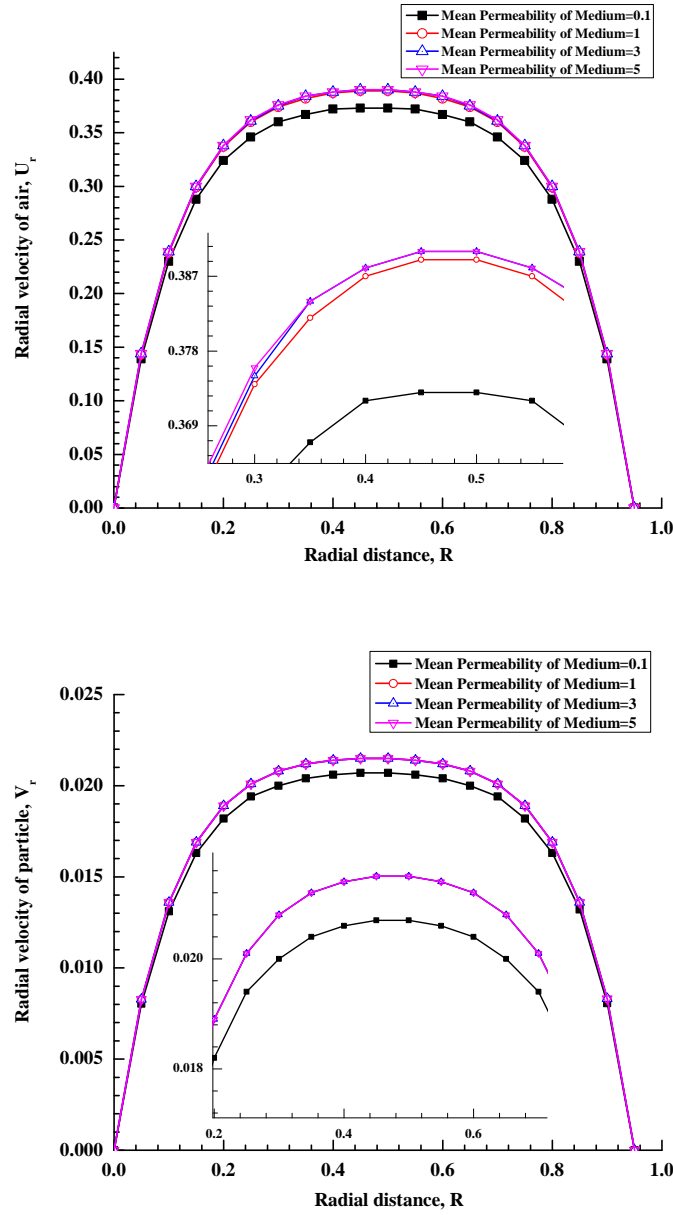


FIG. 4. Effect of mean permeability of porous media on radial velocity of (c) air and (d) particles at  $\tau = 0.5$ ,  $R = 0$ ,  $Z = [0, 1]$ ,  $Re = 10$ ,  $d = 50$  nm,  $a = 0.5$   $\mu$ m

quantitative study through numerical computations to study the flow of viscous air in alveolar region and calculated the location of deposition of the nanoparticles of diameter=100 nm inside the alveolar duct of the human lung. All the results are presented in graphical form in both radial and axial directions at various time points. However, in their study authors did not consider porosity of alveolar region, which an important factor for biological tissues. So, in the present study we include porosity of media and used periodic permeability due to an oscillation of velocity about a nonzero constant mean.

We compared result of present study with the result of Saini et al. [7] in Fig. 2 for velocity of air with respect to axial distance at  $\tau = 0.9$ ,  $R = 0$ ,  $Z = [0, 1]$  after removing porosity and relevant terms (Darcy term, periodic permeability) at  $Re = 10$ ,  $d = 100$  nm, and  $a = 125$   $\mu$ m. We found that our results did not change for grid size of  $100 \times 100 \times 10^5$  and higher. Hence, a grid size of  $100 \times 100 \times 10^5$  is chosen for all of our computations.

We compared result of present study with the result of Saini et al. [7] in Fig. 2 for velocity of air with respect to axial distance at  $\tau = 0.9$ ,  $R = 0$ ,  $Z = [0, 1]$  after removing porosity and relevant terms (Darcy term, periodic permeability) at  $Re = 10$ ,  $d = 100$  nm, and  $a = 125$   $\mu\text{m}$ . We found that our results did not change for grid size of  $100 \times 100 \times 10^5$  and higher. Hence, a grid size of  $100 \times 100 \times 10^5$  is chosen for all of our computations.

## 5. Results and discussion

In this work we aimed to find the effect of periodic permeability of the porous lung on air and particle velocity by varying the mean permeability of medium. A numerical computation is done by using following values [7, 18, 24–27]:

$$m = 0.0002 \text{ Kg/l}, \quad d = 50 \text{ nm}, \quad f = 0.3 \text{ hz}, \quad \rho_a = 1.145 \text{ kg/m}^3, \quad \rho_p = 0.02504 \cdot 10^{12} \text{ m}^{-3}, \\ r = 0.5 \text{ } \mu\text{m}, \quad a_0 = 1 \text{ Kg/m}^2 \text{ s}^2, \quad \nu = 1.71 \cdot 10^{-5} \text{ m}^2/\text{s}, \quad Re = 1 - 20, \quad \epsilon = 0.6, \quad K_0 = 0.1 - 5. \quad (24)$$

In Fig. 3, we obtained effect of periodic permeability of media by varying mean permeability  $K_0$  of medium from 0.1 to 5 on axial velocity of air and particle at  $\tau = 0.5$ ,  $R = 0$ ,  $Z = [0, 1]$ ,  $Re = 10$ ,  $d = 50$  nm,  $a = 0.5$   $\mu\text{m}$  respectively. We found from Fig. 3(a)–3(b), at  $K_0 = 0.1$  the velocity of air and particle in axial directions are lesser than velocities at  $K_0 = 5$ . However, by increasing value of mean permeability ( $K_0$ ) from 0.1 to 5 periodic permeability of airways increases and due to highly permeable walls, level of pressure inside airway tubes reduces, which increases velocity of air and particles in axial directions of flow periodically.

In Fig. 4, we obtained effect of periodic permeability of media by varying mean permeability  $K_0$  of medium from 0.1 to 5 on radial velocity of air and particle at  $\tau = 0.5$ ,  $R = 0$ ,  $Z = [0, 1]$ ,  $Re = 10$ ,  $d = 50$  nm,  $a = 0.5$   $\mu\text{m}$  respectively. We found from Fig. 4(a)–4(b), at  $K_0 = 0.1$  velocity of air and particle in radial directions are lesser than velocities at  $K_0 = 5$ . However, by increasing the value of mean permeability ( $K_0$ ) from 0.1 to 5 periodic permeability of airways increases and due to highly permeable walls, level of pressure inside airway tubes reduces, which increases velocity of air and particles in radial directions of flow periodically.

Consequently, we found that axial and radial velocity of air and particle influenced highly as compared to axial and radial velocity of particle and concluded that the increase in permeability,  $K_0$ , elevates airflow inside the lung airways.

## 6. Conclusion

A mathematical model characterizing the motion of nanoparticles, diameter 50 nm, with the laminar, sinusoidal flow of air through airway duct is developed. Porosity of tissue and periodic permeability of media due to rhythmic breathing is considered. It is found that periodic permeability affects the velocity of air and particles in axial and radial direction of flow such as the increment in the permeability of porous media,  $K_0$ , rises the flow of air inside the lung airways.

## Acknowledgment

One of the authors, Jyoti Kori, is thankful to Ministry of Human Resource Development India (Grant Code:-MHR-02-23-200-44) for providing fund and support while writing this manuscript.

## References

- [1] Heyder J. Deposition of Inhaled Particles in the Human Respiratory Tract and Consequences for Regional Targeting in Respiratory Drug Delivery. *Proc Am Thorac Soc.*, 2004, P. 315-320.
- [2] Kori J., Pratibha. Numerical Simulation of Dusty Air Flow and Particle Deposition Inside Permeable Alveolar Duct. *Int. J. Appl. Comput. Math.*, 2019, **5**, P. 1–13.
- [3] Tian L., Shang Y., Chen R., Bai R., Chen C., Inthavong K., Tu1 J. A combined experimental and numerical study on upper airway dosimetry of inhaled nanoparticles from an electrical discharge machine shop. *Particle and Fibre Toxicology*, 2017, **14**, P. 24.
- [4] Li D., Xu Q., Liu Y., Libao Y., Jun J. *Numerical Simulation of Particles Deposition in a Human Upper Airway*. Advances in Mechanical Engineering, 2014.
- [5] Sturm R. Theoretical deposition of carcinogenic particle aggregates in the upper respiratory tract. *Ann Transl Med.*, 2013, **1**, P. 25.
- [6] Sturm R. A computer model for the simulation of nanoparticle deposition in the alveolar structures of the human lungs. *Ann Transl Med.*, 2015, **3**, P. 281.
- [7] Saini A., Katiyar V.K., Pratibha. Two-dimensional model of nanoparticle deposition in the alveolar ducts of the human lung. *Applications & Applied Mathematics*, 2017, **12**, P. 305–318.
- [8] Haber S., Yitzhak D., Tsuda A. Gravitational deposition in a rhythmically expanding and contracting alveolus. *J. Appl. Physiol.*, 2013, **95**, P. 657–671.
- [9] DeGroot C.T., Straatman A.G. A porous media model of alveolar duct flow in the human lung. *Journal of Porous Media*, 2018.
- [10] Khanafer K., Cook K., Marafie A. The Role of Porous Media in Modeling Fluid Flow Within Hollow Fiber Membranes of The Total Artificial Lung. *J. Porous Media*, 2012, **15**, P. 113–122.
- [11] Cheng P. Heat Transfer in Geothermal Systems. *Advances in Heat Transfer*, 1979, **14**, P. 1–105.
- [12] Vafai K., Tien C.L. Boundary and Inertia Effects on Flow and Heat Transfer in Porous Media. *Int. J. Heat Mass Transfer*, 1981, **24**, P. 195–203.

- [13] Kuwahara F., Sano Y., Liu J., Nakayama A. A Porous Media Approach for Bifurcating Flow and Mass Transfer in a Human Lung. *J. Heat Transfer*, 2009, **131**, P. 101013-5.
- [14] Saini A., Katiyar V.K., Pratibha. Numerical simulation of gas flow through a biofilter in lung tissues. *World Journal of Modelling and Simulation*, 2015, **11**, P. 33–42.
- [15] Balashazy I., Hofmann W., Farkas A., Madas B.G. Three-dimensional model for aerosol transport and deposition in expanding and contracting alveoli. *Inhalation Toxicology*, 2008, **20**, P. 611–621.
- [16] Sturm R., Hofmann W. A theoretical approach to the deposition and clearance of fibers with variable size in the human respiratory tract. *J. of Hazardous Materials*, 2009, **170**, P. 210–218.
- [17] Darcy H. *Les Fontaines Publiques de la Ville de Dijon*. Dalmont, Paris, 1856.
- [18] Singh K.D., Verma G.N. Three-Dimensional Oscillatory Flow through a Porous Medium with Periodic Permeability. *Z. Angew. Math. Mech.*, 1995, **75**, P. 599–604.
- [19] Kori J., Pratibha. Numerical Simulation of Mucus Clearance inside Lung Airways. *Journal of Applied Fluid Mechanics*, 2018, **11**, P. 1163–1171.
- [20] Kori J., Pratibha. Simulation and Modeling for Aging and Particle Shape Effect on Airflow Dynamics and Filtration Efficiency of Human Lung. *Journal of Applied Fluid Mechanics*, 2019, **12**, P. 1273–1285.
- [21] Smith S., Cheng U.S., Yeh H.C. Deposition of ultrafine particles in human tracheobronchial airways of adults and children. *Aerosol Sci. Tech.*, 2010, **35**, P. 697–709.
- [22] Seraa T., Uesugib K., Yagib N., Yokotac H. Numerical simulation of airflow and microparticle deposition in a synchrotron micro-CT-based pulmonary acinus model. *Computer Methods in Biomechanics and Biomedical Engineering*, 2013, **18**, P. 1427-1435.
- [23] Koullapis P.G., Kassinos S.C., Bivolarova M.P., Melikov A.K. Particle deposition in a realistic geometry of the human conducting airways: Effects of inlet velocity profile, inhalation flowrate and electrostatic charge. *J Biomech.*, 2016, **49**(11), P. 2201–2212.
- [24] Ismail Z., Abdullah I., Mustapha N., Amin N. A power-law model of blood flow through a tapered overlapping stenosed artery. *Appl. Math. Comput.*, 2007, **195**, P. 669–680.
- [25] Kapur J.N. *Mathematical Models in Biology and Medicine*. East-West Press, Pvt. Ltd., New Delhi, 1985.
- [26] Mandal P.K. An unsteady analysis of non-Newtonian blood flow through tapered arteries with a stenosis. *Int. J. Non-Linear Mech.*, 2005, **40**, P. 151–164.
- [27] Singh P., Misra J.K., Narayan K.A. Free convection along a vertical wall in a porous medium with periodic permeability variation. *Int. J. Numer. Anal. Methods Geomech.*, 1989, **13**.

## Appendix

Nomenclature is defined in Table 1.

TABLE 1. Nomenclature

Variable	Description	Variable	Description
$r$	radial direction of flow	$z$	axial direction of flow
$u_r$	air velocity radial direction	$v_r$	particle velocity radial direction
$u_z$	air velocity axial direction	$v_z$	particle velocity axial direction
$\rho_p$	density of particles	$\rho_a$	density of air
$\nu$	kinematic viscosity	$k_f$	Stokes drag force
$K$	permeability of tissue	$K_0$	Mean permeability of medium
$P_l$	particle load	$Da$	Darcy number
$a_0$	amplitude	$f$	breathing frequency
$\mu$	dynamics viscosity	$Re$	Reynolds number
$t$	time	$\epsilon$	media porosity
$d$	diameter of spherical particle of unite density		

## Orientalional order parameter of liquid crystalline nanocomposites by Newton's rings and image analysis methods

M. Munavar Hussain<sup>1\*</sup>, B. H. Doreswamy<sup>2</sup>, N. C. Shobha<sup>3</sup>, V. N. Vijayakumar<sup>4</sup>, K. Fakruddin<sup>5</sup>

<sup>1</sup>Department of Physics, KNS Institute of Technology, Bengaluru, India

<sup>2</sup>Department of Physics, SJB Institute of Technology, Bengaluru, India

<sup>3</sup>Department of Physics, APS College of Engineering, Bengaluru, India

<sup>4</sup>Department of Physics, Bannari Amman Institute of Technology, Sathyamangalam, India

<sup>5</sup>Department of Physics, Ghousia College of Engineering, Ramanagara, India

\*munavar.phd@gmail.com

DOI 10.17586/2220-8054-2019-10-3-243-254

Liquid crystalline nanocomposites are prepared by dispersing TiO<sub>2</sub>, ZnO, Fe<sub>2</sub>O<sub>3</sub> and Fe<sub>3</sub>O<sub>4</sub> nanoparticles separately in 4-Cyano 4'-Propoxy-1, 1'-Biphenyl (3O-CB) liquid crystal in a 1:100 ratio. The characteristic textures exhibited are captured at different liquid crystalline phases by using POM. The phase transition temperatures are measured by both polarizing optical microscope (POM) and differential scanning calorimeter (DSC). The optical textures are analyzed by using MATLAB software to compute birefringence and order parameter of samples. The birefringence and order parameter also measured by conventional Newton's rings technique, the results are discussed.

**Keywords:** liquid crystals, nanocomposites, optical textures, phase transition temperatures, birefringence, order parameter.

*Received: 12 November 2018*

*Revised: 19 April 2019*

### 1. Introduction

Liquid crystal technology has a major effect on many areas of science and technology. Applications of this kind of materials are being discovered and continued to provide effective solution to many different problems. For modern industrial application, wide temperature range of liquid crystal phase, high optical and dielectric anisotropy and fast switching time are required. By composing liquid crystalline mixtures or using guest materials in host liquid crystals are two basic methods for obtaining liquid crystals with enhanced properties. Metal oxide nanoparticles are novel type of guest materials. Doping nanomaterials in liquid crystals enhances the properties of liquid crystals. Different types of metal oxide nanoparticles are used to achieve this purpose [1].

Liquid crystals, being anisotropic media, provide good support for self-assembly of nanomaterials into large organizing structures in multiple dimensions. Therefore, doping of nanoparticle into liquid crystals has emerged as a fascinating area of applied research. Nano objects (Guests) are embedded in the liquid crystals (Hosts) that can trap the ion concentration, electrical conductivity and improve the electro-optical response of the host [2].

Incorporation of metal oxide nanoparticles into liquid crystals makes it easier to obtain better display parameter profiles [3]. The metal oxide nanoparticles embedded in liquid crystal bases have attracted much interest not only in the field of magnetic recording media but also in the area of medical care. The medical applications, which include radio frequency, hyperthermia, photo magnetic and magnetic resonance imaging, cancer therapy, sensors and high frequency applications, were reported [4–7].

In the present work, an effort has been made to study the effect of metal oxide nanoparticles on the orientation order parameter of 4-Cyano 4'-Propoxy-1, 1'-Biphenyl liquid crystal by image analysis and Newton's ring techniques. There are several techniques for studying the temperature dependence of liquid crystal properties [8–11]. But they involve technical difficulties in measuring required parameters.

In this paper, we have explored image analysis-computer program technique to find orientation order parameter of liquid crystalline nanocomposites. In the image analysis technique, textures of liquid crystal samples are captured from crystal to isotropic phase by using POM. The changes in textural feature as a function of temperature are useful to compute thermo-optical properties of liquid crystals. By this technique, it is possible to extract as much information as possible from the textural image by means of applying computational algorithms on image data or intensity values. MATLAB software [12, 13] is used for the analysis of liquid crystal textures and to estimate the orientational order parameter.

TABLE 1. Liquid crystalline compound and its nanocomposites

S <sub>l</sub> . No.	Liquid crystalline compound (100 mg)	Metal oxide nanoparticles (1 mg)	Liquid crystalline nanocomposites
1	4-Cyano 4'-Propoxy-1, 1'-Biphenyl (C <sub>16</sub> H <sub>15</sub> NO)	—	S <sub>1</sub>
2	4-Cyano 4'-Propoxy-1, 1'-Biphenyl (C <sub>16</sub> H <sub>15</sub> NO)	ZnO	S <sub>11</sub>
3	4-Cyano 4'-Propoxy-1, 1'-Biphenyl (C <sub>16</sub> H <sub>15</sub> NO)	TiO <sub>2</sub>	S <sub>12</sub>
4	4-Cyano 4'-Propoxy-1, 1'-Biphenyl (C <sub>16</sub> H <sub>15</sub> NO)	Fe <sub>3</sub> O <sub>4</sub>	S <sub>13</sub>
5	4-Cyano 4'-Propoxy-1, 1'-Biphenyl (C <sub>16</sub> H <sub>15</sub> NO)	Fe <sub>2</sub> O <sub>3</sub>	S <sub>14</sub>

## 2. Materials and methods

In this present work 4-Cyano 4'-Propoxy-1, 1'-Biphenyl liquid crystal was purchased from TCI, Ltd. and ZnO, TiO<sub>2</sub>, Fe<sub>3</sub>O<sub>4</sub> and Fe<sub>2</sub>O<sub>3</sub> nanoparticles were obtained from VTU-PG centre, Muddenahalli, Chikkaballapura District, Bengaluru, India. Liquid crystalline nanocomposites are prepared using sonication method and its composition names are given in the Table 1. Textural features are studied using POM to confirm its liquid crystalline behavior. Then the transition temperature is measured with DSC studies for reliable information. Optical parameters like birefringence and order parameters of such nanocomposites are studied using conventional newton's ring method as well as computational methods using MATLAB program.

## 3. Results and discussions

### 3.1. Polarizing optical microscope

The liquid crystalline nanocomposites are characterized by different liquid crystalline phases due to the changes in local molecular order with temperature [14]. The characterization of these mesophases will provide very important information on the pattern and textures of LCs. The transition temperatures and optical textures observed by polarizing optical microscope is shown in Figs. 1–5. As a representative case, the schelieren texture of nematic phase from isotropic phase is observed at 61.5 °C then it is grown to curved brushes texture observed at 54 °C and finally at 47.5 °C the crystalline texture is formed which is not transparent hence look dark, all this textures are represented in the set of Fig. 1.

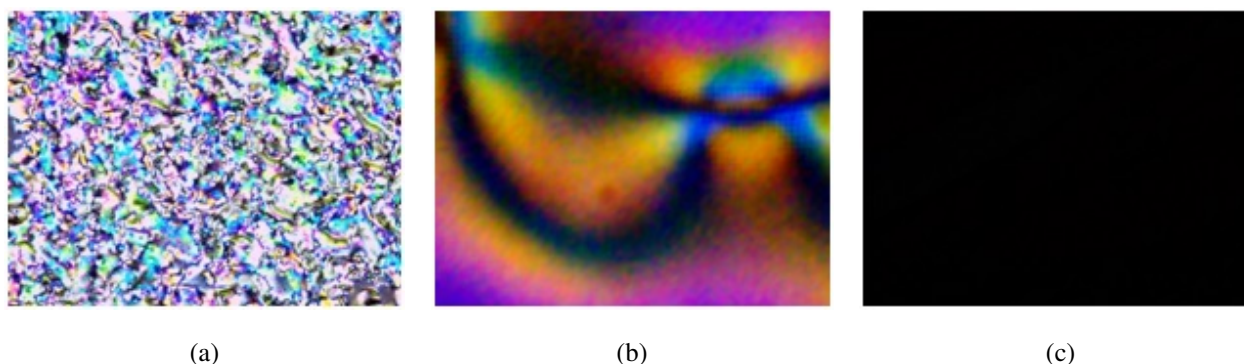


FIG. 1. POM Textures of sample S<sub>1</sub>: Isotropic – Nematic Transition Phase @ 61.5 °C (a); Nematic Phase @ 54 °C (b); Solid Phase @ 47.5 °C (c)

Dispersion of nanoparticles with liquid crystal influenced the textural features of the sample at different phases with respect to temperature and nanomaterial is observed in POM textures. The surface to volume ratio of sample liquid crystal increases due to surface restructuring by nanoparticle dispersion. This phenomenon of molecular restructuring varies as a function of temperature and nanoparticle composition. It is observed that orientational order of liquid crystal molecules are further strengthened heavily at isotropic to nematic phase and strengthened less at

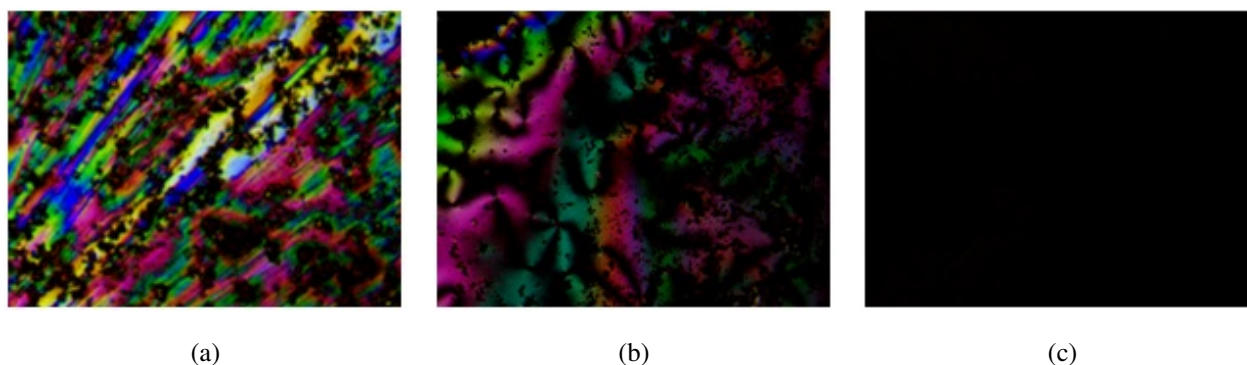


FIG. 2. POM Textures of sample  $S_{11}$ : Isotropic – Nematic Transition Phase @  $60.5\text{ }^{\circ}\text{C}$  (a); Nematic Phase @  $56.5\text{ }^{\circ}\text{C}$  (b); Solid Phase @  $46\text{ }^{\circ}\text{C}$  (c)

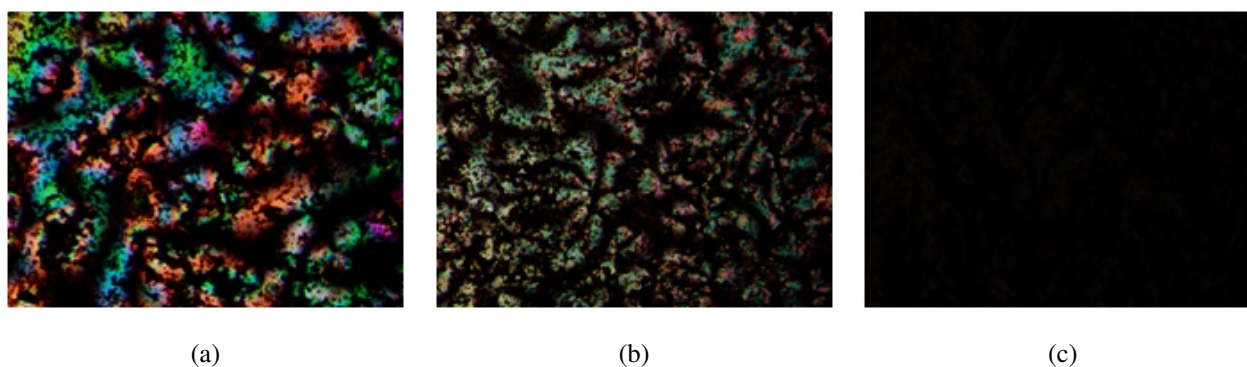


FIG. 3. POM Textures of sample  $S_{12}$ : Isotropic – Nematic Transition Phase @  $60.5\text{ }^{\circ}\text{C}$  (a); Nematic Phase @  $56.5\text{ }^{\circ}\text{C}$  (b); Solid Phase @  $46\text{ }^{\circ}\text{C}$  (c)

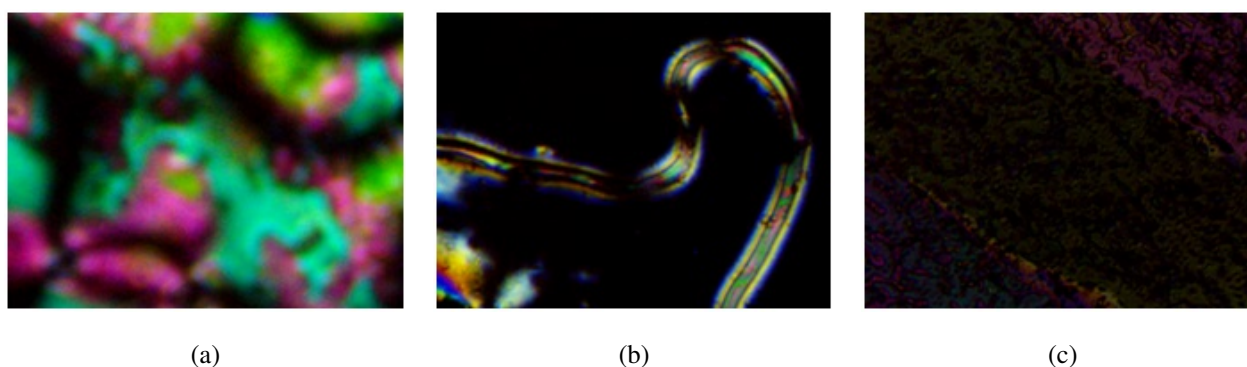


FIG. 4. POM Textures of sample  $S_{13}$ : Isotropic – Nematic Transition Phase @  $59.5\text{ }^{\circ}\text{C}$  (a); Nematic Phase @  $54\text{ }^{\circ}\text{C}$  (b); Solid Phase @  $50\text{ }^{\circ}\text{C}$  (c)

crystalline phase by the nanoparticles with shifting transition temperature. This is because possibility of increasing its surface area and decreasing its volume. It is also observed that molecular weight of nanoparticles plays vital role in restructuring liquid crystal molecules. The observation of POM shows that restructuring of molecules leads to defective textural images at various instances.

Phase transition temperatures observed for liquid crystalline nanocomposites using POM and DSC shows that they are reduced due to the dispersion of nanoparticles. The nanoparticles  $\text{ZnO}$ ,  $\text{TiO}_2$ ,  $\text{Fe}_3\text{O}_4$  and  $\text{Fe}_2\text{O}_3$  influences the liquid crystal and reduces the transition temperature by  $1\text{ }^{\circ}\text{C}$ ,  $1\text{ }^{\circ}\text{C}$ ,  $1\text{ }^{\circ}\text{C}$  and  $2\text{ }^{\circ}\text{C}$  respectively.

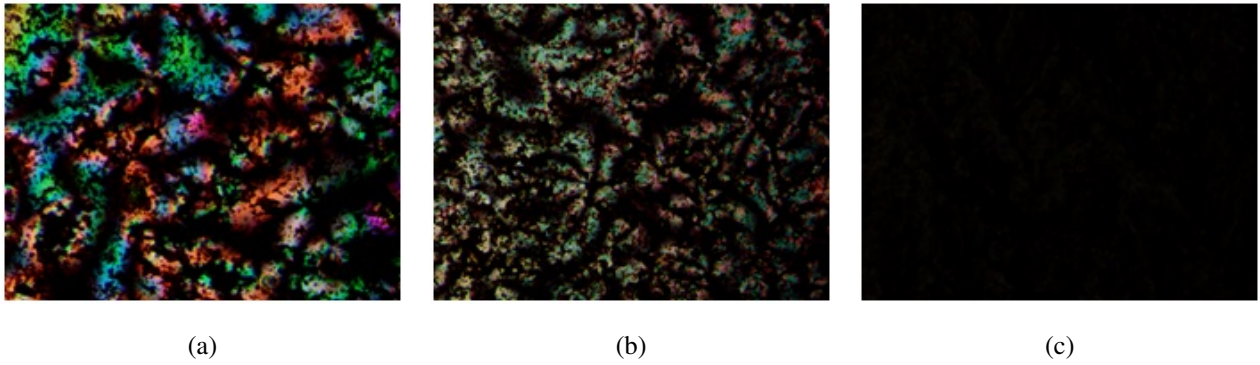


FIG. 5. POM Textures of sample  $S_{14}$ : Isotropic – Nematic Transition Phase @  $60.5\text{ }^{\circ}\text{C}$  (a); Nematic Phase @  $52\text{ }^{\circ}\text{C}$  (b); Solid Phase @  $49.5\text{ }^{\circ}\text{C}$  (c)

### 3.2. Differential scanning calorimeter (DSC) studies

The thermal analysis by DSC study provides data regarding the temperatures and heat capacity of different phases. DSC study reveals presence of phase transition in materials by detecting the enthalpy change associated with each phase transition. DSC study is used in conjunction with optical polarizing microscopy to determine the mesophase types exhibited by the materials. The different thermograms of liquid crystalline nanocomposites are recorded from DSC as shown in Figs. 6, 7.

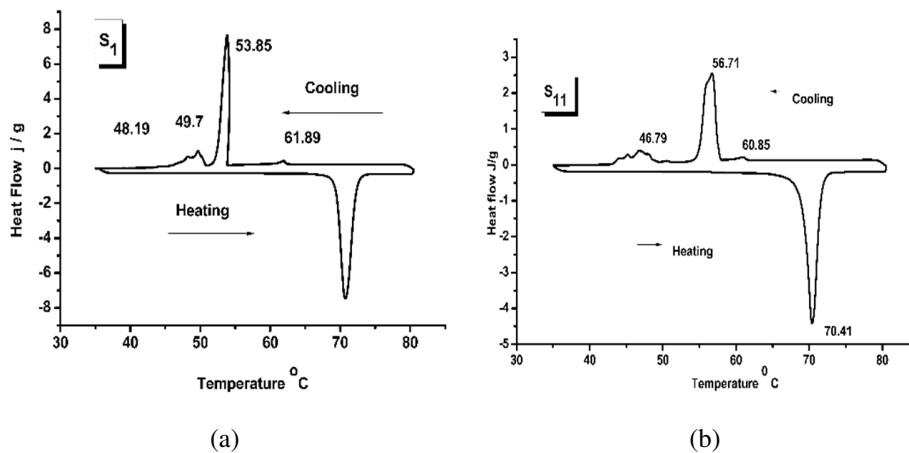


FIG. 6. DSC Thermogram of sample  $S_1$  (a) and  $S_{11}$  (b)

The phase transition temperatures obtained by POM and DSC are tabulated for pure and nanocomposites liquid crystals at different phases in Table 2. The samples show isotropic, nematic and crystalline phases. The phases of samples are confirmed with the help of POM images obtained and corresponding transition temperatures are considered with the help of DSC values. The temperatures are measured in degree centigrade ( $^{\circ}\text{C}$ ). The enthalpy jump at various phase is noted in the given table with in units of Joules per gram (J/g).

### 3.3. Birefringence studies by Newton's rings method

The experimental setup consists of plano-convex lens of small radius of curvature (13 mm) and plane glass plate which is being placed in hot stage connected to specially designed microcontroller based temperature and image capturing device. The LC sample is introduced between the glass plate and lens and set the polarizer and the analyzer in the crossed position. The hot stage along with LC sample mount is placed on the microscope stage and then adjust hot stage axis to coincide with the microscopic axis. Set the reflector of the microscope to pass the light through LC sample until the clear Newton's rings are formed on the monitor. These rings are formed due to the interference of ordinary and extra ordinary rays after passing through the analyzer. The diameter of various rings was measured. The experimental setup is shown in the Fig. 8 and ring pattern in Fig. 9.

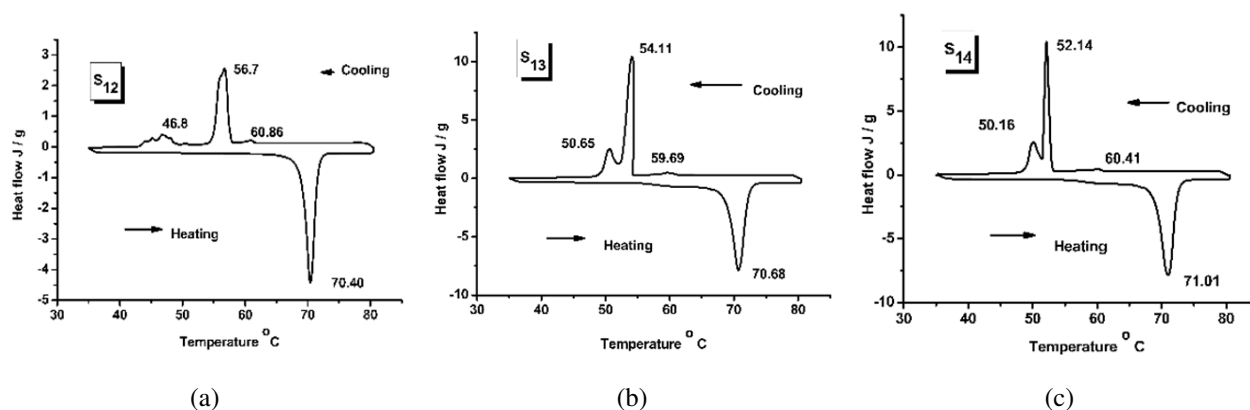

 FIG. 7. DSC Thermogram of sample S<sub>12</sub> (a), S<sub>13</sub> (b) and S<sub>14</sub> (c)

 TABLE 2. Phase transition temperature of S<sub>1</sub>, S<sub>11</sub>, S<sub>12</sub>, S<sub>13</sub> and S<sub>14</sub>

Nano Composite LC	Study	Unit	Phase Variance		
			I-N	N	N-Crystal state
S <sub>1</sub>	POM	°C	62	52	
	DSC	°C J/g	61.89 (0.22)	53.85 (7.23)	49.7 (30.11)
S <sub>11</sub>	POM	°C	61.21	56.98	
	DSC	°C J/g	60.85 (0.24)	56.71 (6.32)	46.79 (13.54)
S <sub>12</sub>	POM	°C	61.41	57.2	
	DSC	°C J/g	60.86 (0.26)	56.7 (6.51)	46.8 (14.22)
S <sub>13</sub>	POM	°C	60.32	55	
	DSC	°C J/g	59.69 (0.78)	54.11 (8.79)	50.65 (31.15)
S <sub>14</sub>	POM	°C	61.23	53.17	
	DSC	°C J/g	60.41 (0.86)	52.14 (8.14)	50.16 (30.55)

The optical path difference between e-ray (extra ordinary ray) and o-ray (ordinary ray) is given by  $y$ ,  $\delta n$  which corresponds to ring number  $k$  and wavelength  $\lambda$  for a bright fringe is given by:

$$\delta n = \frac{k\lambda}{y}, \quad (1)$$

$$y = \frac{x^2}{2R}. \quad (2)$$

From equations (1) and (2):

$$\delta n = (2R\lambda) \frac{k}{x^2}. \quad (3)$$

Since  $2R\lambda = c$ , cell constant for the given wavelength of light:

$$\delta n = \frac{ck}{x^2}, \quad (4)$$

where  $x$  is the radius of the ring and  $R$  – the radius of curvature of the lens used.

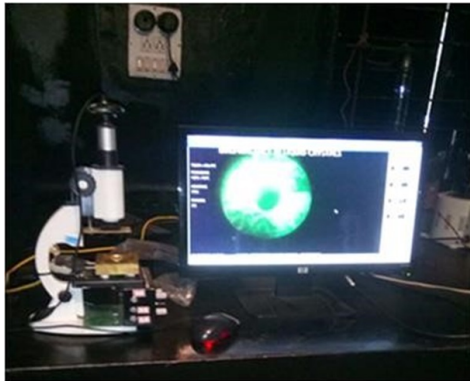


FIG. 8. Experimental setup to measure birefringence (Newtons rings method)

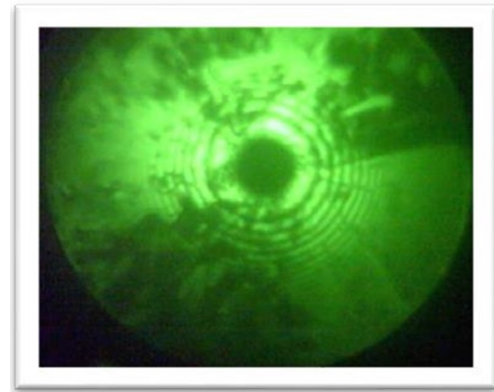


FIG. 9. Newtons Rings observed in samples  $S_1$  at temperatures  $59\text{ }^\circ\text{C}$

$\delta n$  can be measured with great accuracy by finding the slope of the straight line drawn between  $x^2$  versus the ring number  $k$  and shown in Figs. 10–12. We can obtain the same result by considering the dark rings also. The schematic diagram is shown in Fig. 13.

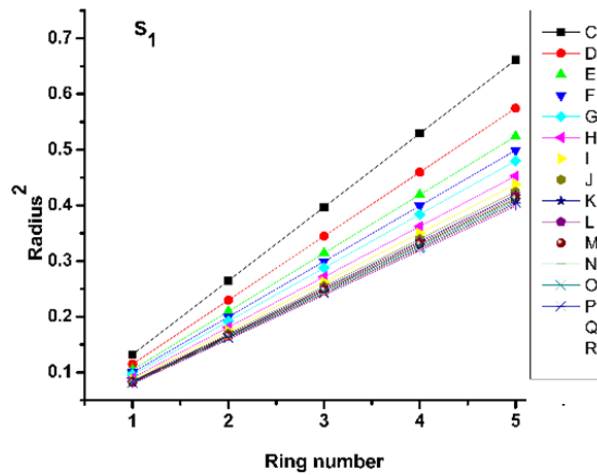


FIG. 10. The square of radius of ring Vs ring number at various temperature of sample  $S_1$

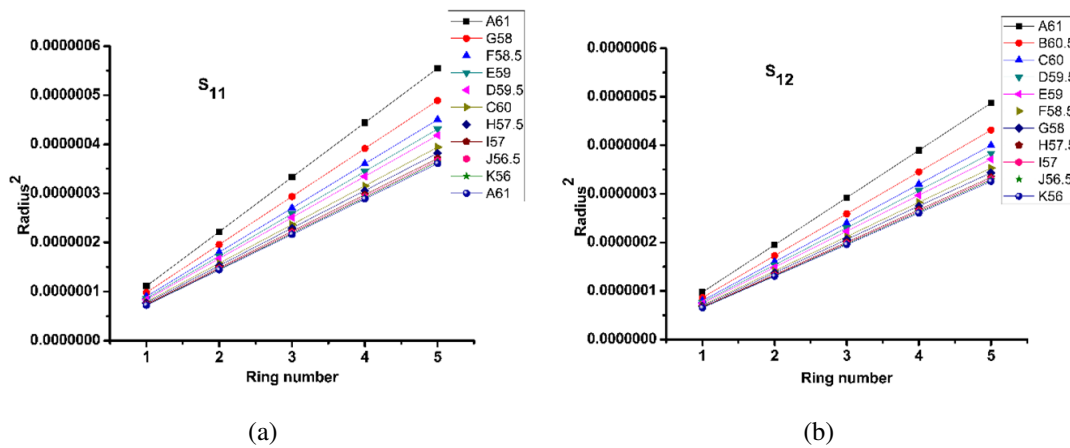


FIG. 11. The square of radius of ring Vs ring number at various temperature of sample  $S_{11}$  (a) &  $S_{12}$  (b)

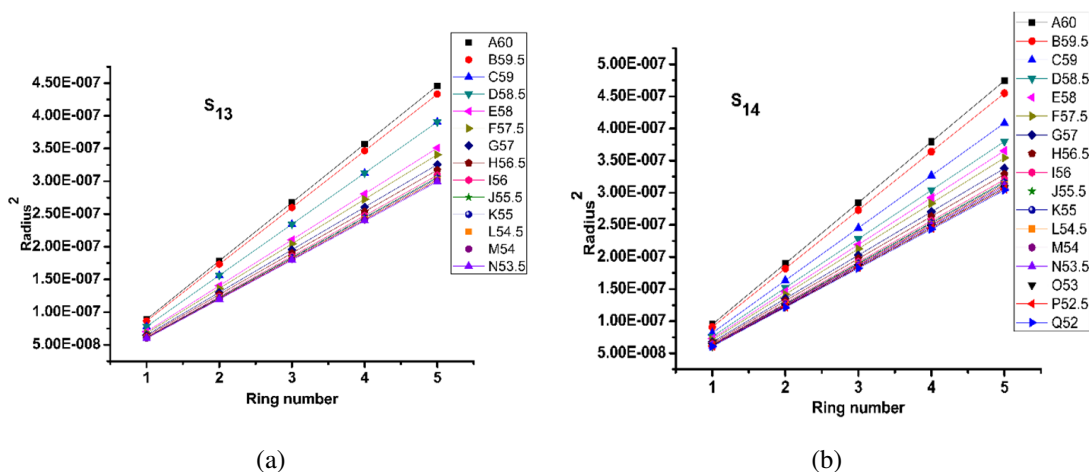


FIG. 12. The square of radius of ring Vs ring number at various temperature of sample S<sub>13</sub> (a) & S<sub>14</sub> (b)

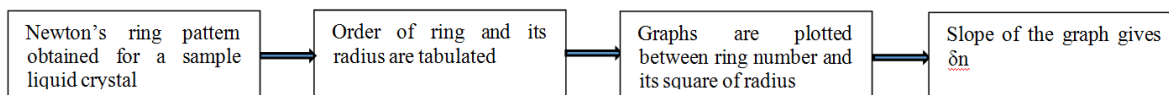


FIG. 13. Schematic diagram of Newtons Rings method for calculation of birefringence ( $\delta n$ )

As the temperature decreases, birefringence  $\delta n$  increases. The method adopted for the estimation of orientational order parameter from  $\delta n$  given by Kuczynski et al. as follows where  $\Delta n$  is birefringence at crystalline phase and is obtained by linear regression method shown in Figs. 14–16 [15, 16]:

$$S = \frac{\delta n}{\Delta n} \tag{5}$$

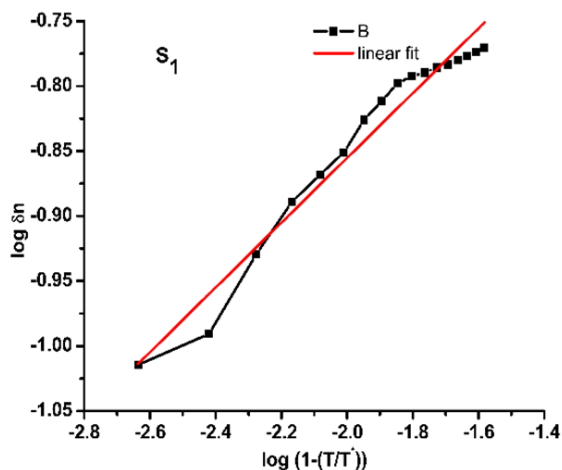
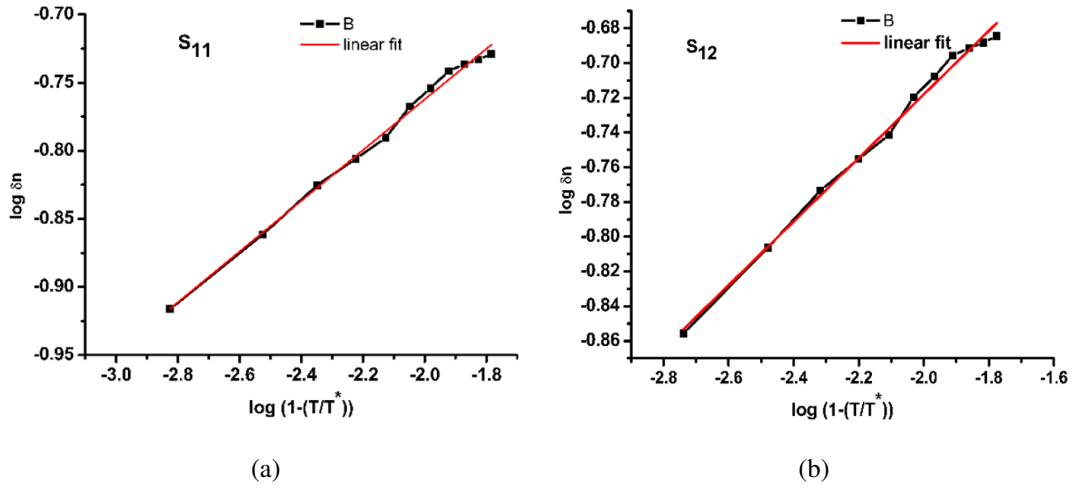
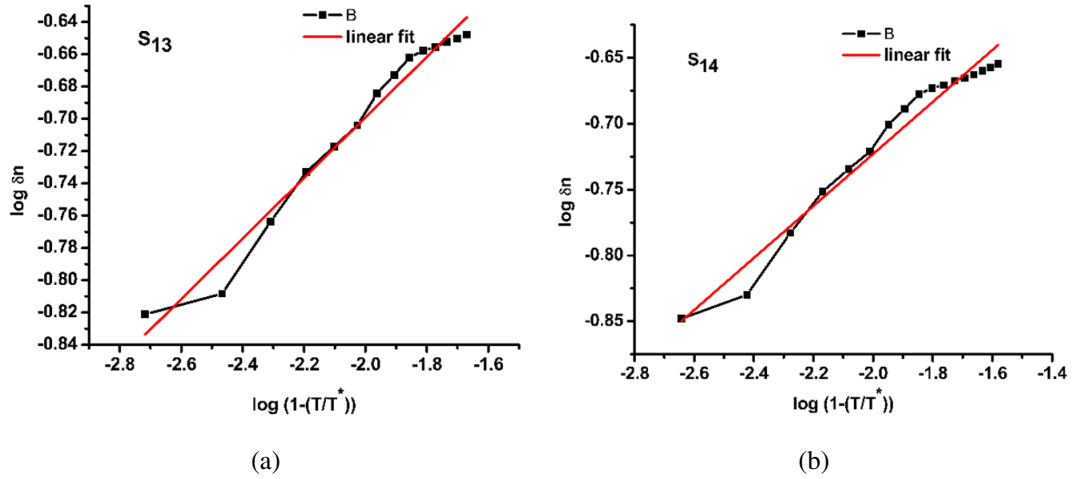


FIG. 14.  $\log \delta n$  and  $\log(1 - (T/T^*))$  graph of S<sub>1</sub> by Newtons rings method

FIG. 15.  $\log \delta n$  and  $\log(1 - (T/T^*))$  graph of  $S_{11}$  (a) and  $S_{12}$  (b) by Newtons rings methodFIG. 16.  $\log \delta n$  and  $\log(1 - (T/T^*))$  graph of  $S_{13}$  (a) and  $S_{14}$  (b) by Newtons rings method

### 3.4. Birefringence and order parameter by image analysis

Phase transitions are characterized by abrupt changes, discontinuities, breaking of symmetry and strong fluctuations of the molecules in a compound. The identification of transition temperatures is essential to study the physical properties of the LC materials. The transition also indicates the transformation from an ordered phase to relatively disordered phase and Vice versa as the temperatures are raised or cooled [17, 18].

The behavior of light with respect to temperature is known as the thermo-optical parameters. Optical birefringence and order parameters are the important thermo-optical parameters. Image analysis is the extraction of meaningful information from images (Textures) by applying computational techniques and algorithms to image data. Image analysis technique compute the statistics and measurement based on grey level intensities of the image pixels. In the present work, optical birefringence and order parameter are computed from the optical textures of samples as a function of temperatures by image analysis technique.

The birefringence of the liquid crystals was measured as a function of temperature by substituting the thickness  $d$  of liquid crystalline sample layer and wavelength of color in the following equation to calculate birefringence [8]:

$$I = I_0 \sin^2 \left( \frac{\pi d \delta n}{\lambda} \right), \quad (6)$$

where  $d$  is thickness of liquid crystal layer,  $I_0$  is the intensity of light observed when there is no sample (Liquid crystal layer) between light source and lens,  $I$  is the Intensity of light observed when there is sample (Liquid crystal layer).

The temperature dependent birefringence values of the samples are used to calculate the order parameter using Kuczynski equation given below [16, 19]:

$$S = \frac{\delta n}{\Delta n}, \tag{7}$$

where  $\Delta n$  is birefringence at crystalline state and is obtained by linear regression method using Newton's rings experiment.

In the image analysis technique, optical textures, thickness of the liquid crystal layer ( $d$ ) and birefringence in perfect order ( $\Delta n$ ) are given as input to obtain birefringence and order parameter. The birefringence and order parameter evaluated at different liquid crystalline phases by image analysis and Newton's rings methods are represented in Tables 3–7. The order parameter values are found to be same using both methods. The order parameter found to decrease with increase of temperature. The temperature variation of order parameter is depicted in Fig. 17.

TABLE 3. Birefringence and order parameter of sample S<sub>1</sub> by Newton's ring and image processing methods at various phases

$\Delta n = 0.35$			$\beta = 0.24$				
Temp (°C)	T (K)	Phase Variance	Newton's ring method		Image processing method		
			$\delta n$	$S = \frac{\delta n}{\Delta n}$	Thickness of sample layer ( $d$ ) in meter	$\delta n$	$S = \frac{\delta n}{\Delta n}$
61.5	334.5	I-N	0.09671	0.276314286	1.12E-6	0.0957982	0.273709
54	327	N	0.1684	0.481142857	1.01E-6	0.170262	0.486463
47.5	320.5	Cr	—	—	0.81E-6	0.307646	0.878989

TABLE 4. Birefringence and order parameter of sample S<sub>11</sub> by Newton's ring and image processing methods at various phases

$\Delta n = 0.391$			$\beta = 0.186$				
Temp (°C)	T (K)	Phase Variance	Newton's ring method		Image processing method		
			$\delta n$	$S = \frac{\delta n}{\Delta n}$	Thickness of sample layer ( $d$ ) in meter	$\delta n$	$S = \frac{\delta n}{\Delta n}$
60.5	333.5	I-N	0.13758	0.351867	1.45E-06	0.124618	0.318717
56.5	329.5	N	0.18492	0.472941	1.18E-06	0.185199	0.473655
46	319	Cr	—	—	0.72E-06	0.352115	0.90055

From our investigation it is observed that order parameter increases due to the dispersion of metal oxide nanoparticles in 4-Cyano 4'-Propoxy-1, 1'-Biphenyl liquid crystal. The percentage of increase of order parameter in nematic phase is 1.27 % to 4.5 %, 7.13 % to 15.81 %, 19.93 % to 23.1 % and 18.51 % to 19.03 % due the dispersion of ZnO, TiO<sub>2</sub>, Fe<sub>3</sub>O<sub>4</sub> and Fe<sub>2</sub>O<sub>3</sub> nanoparticles respectively.

TABLE 5. Birefringence and order parameter of sample S<sub>12</sub> by Newton's ring and image processing methods at various phases

$\Delta n = 0.347$			$\beta = 0.186$				
Temp (°C)	T (K)	Phase Variance	Newton's ring method		Image processing method		
			$\delta n$	$S = \frac{\delta n}{\Delta n}$	Thickness of sample layer (d) in meter	$\delta n$	$S = \frac{\delta n}{\Delta n}$
60.5	333.5	I-N	0.15611	0.449885	1.30E-06	0.15156	0.431796
56.5	329.5	N	0.20503	0.590865	1.05E-06	0.195764	0.557733
46	319	Cr	—	—	0.79E-6	0.311774	0.888244

TABLE 6. Birefringence and order parameter of sample S<sub>13</sub> Newton's ring and image processing methods at various phases

$\Delta n = 0.324$			$\beta = 0.188$				
Temp (°C)	T (K)	Phase Variance	Newton's ring method		Image processing method		
			$\delta n$	$S = \frac{\delta n}{\Delta n}$	Thickness of sample layer (d) in meter	$\delta n$	$S = \frac{\delta n}{\Delta n}$
59.5	332.5	I-N	0.15548	0.479877	1.00E-06	0.163524	0.504705
54	327	N	0.22365	0.690278	9.70E-07	0.222162	0.685685
50	323	Cr	—	—	0.788E-6	0.291083	0.898404

TABLE 7. Birefringence and order parameter of sample S<sub>14</sub> by Newton's ring and image processing methods at various phases

$\Delta n = 0.329$			$\beta = 0.197$				
Temp (°C)	T (K)	Phase Variance	Newton's ring method		Image processing method		
			$\delta n$	$S = \frac{\delta n}{\Delta n}$	Thickness of sample layer (d) in meter	$\delta n$	$S = \frac{\delta n}{\Delta n}$
60	333	I-N	0.141953	0.431468	1.1E-06	0.152654	0.463995
52	325	N	0.221508	0.673277	1.02E-06	0.220937	0.671541
49.5	322.5	Cr	—	—	0.78E-6	0.295959	0.899572

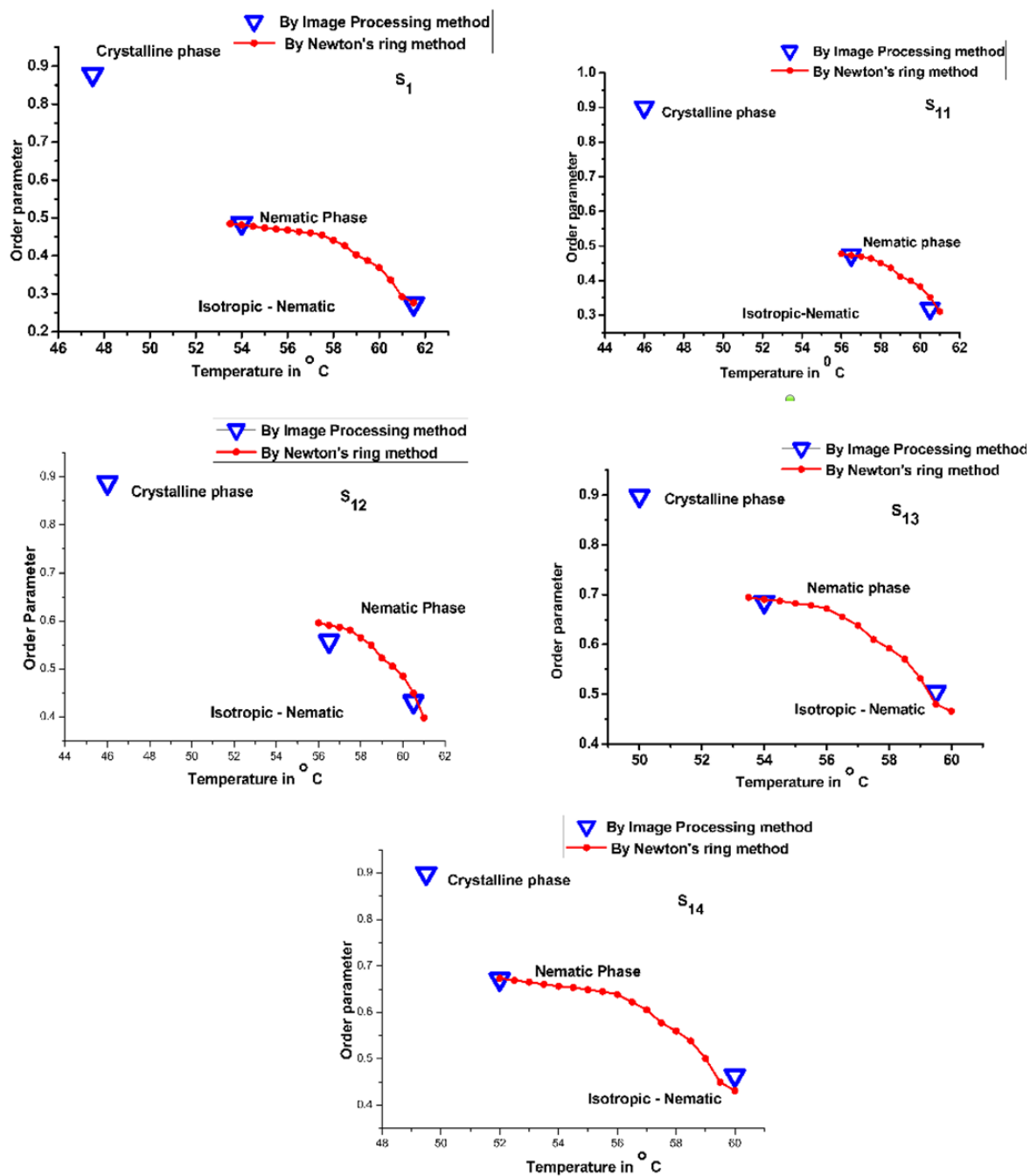


FIG. 17. Order parameter with respect to temperature by Newtons rings method and Image analysis method in samples S<sub>1</sub>, S<sub>11</sub>, S<sub>12</sub>, S<sub>13</sub> and S<sub>14</sub>

#### 4. Conclusion

The advantage of the image analysis method is that it is simple, less complex, efficient and reliable in this type of studies, unlike other techniques, there is no need to arrange different experimental setup except to arrange POM. By conventional techniques, the order parameter can be estimated in the nematic and smectic phases only; however, in the image analysis method, the order parameter can be evaluated in the crystalline phase in addition to the nematic and smectic phases. By the image analysis technique, the order parameter can be estimated in all liquid crystalline phases such as nematic, smectic and crystalline phases, whereas in Newton's rings method it can be evaluated only in nematic, smectic phases. Due to the dispersion of Nano particles, the birefringence anisotropy increases. Therefore, the view angle increases and this can be most advantageous in liquid crystal display devices, to produce large panel LC displays with good depth.

#### Acknowledgements

The authors are very much thankful to the management of Ghousia College of Engineering, Ramanagara, India and Bannari Amman Institute of Technology, Sathyamangalam, India for providing lab facilities to carry out this work. The authors also thankful to Dr. Dinesh Rangappa, VTU-PG centre, Muddenahalli, chikkaballapura Dist, Bengaluru, India for sponsoring nanoparticles.

#### References

- [1] Kobayashi S., Miyama T., et al. Dielectric Spectroscopy of Metal Nanoparticle Doped Liquid Crystal Displays Exhibiting Frequency Modulation Response. *J. Display Technology*, 2006, **2**, P. 121–129.
- [2] Garbovskiy Y., Glushchenko I. Nano-Objects and Ions in Liquid Crystals: Ion Trapping Effect and Related Phenomena. *Crystals*, 2015, **5** (4), P. 501–533.
- [3] Goel P. Arora M., Biradar A.M. Electro-optic switching in iron oxide nanoparticle embedded paramagnetic chiral liquid crystal via magneto-electric coupling. *Journal of Applied Physics*, 2014, **115** (12), P. 124905(1–6).
- [4] Silva J.B., de Brito W., Mohallem N.D.S. Influence of heat treatment on cobalt ferrite ceramic powders. *Materials Science and Engineering: B*, 2004, **112** (2–3), P. 182–187.
- [5] Sun S., Murray C.B., et al. Monodisperse FePt nanoparticles and ferromagnetic FePt nanocrystal super lattices. *Science*, 2000, **287** (5460), P. 1989–92.
- [6] Pankhurst Q.A., Connolly J., Jones S.K., Dobson J. Applications of magnetic nanoparticles in biomedicine. *Journal of Physics D: Applied Physics*, 2003, **36**, P. R167–R181.
- [7] Ito A., Shinkai M., Honda H., Kobayashi T. Medical application of functionalized magnetic nanoparticles. *J. BiosciBioeng*, 2005, **100** (1), P. 1–11.
- [8] Avci N., Nesrullajev A., Oktik S. Nonlinear thermotropic and thermo-optical behaviour of planar oriented textures in nematic liquid crystals at phase transitions. *Brazilian Journal of Physics*, 2010, **40**, P. 224–227.
- [9] Shin-Tson Wu, Uzi Efron, LaVerne D. Hess. Birefringence measurements of liquid crystals. *Applied Optics*, 1984, **23** (21), P. 3911–3915.
- [10] Fakruddin K., Jeevan Kumar R., Datta Prasad P.V., Pisipati V.G.K.M. Orientational Order Parameter – I A Birefringence Study. *Molecular Crystals and Liquid Crystals*, 2009, **511**, P. 133–146.
- [11] Pardhasaradhi P., Datta Prasad P.V., et al. Orientational order parameter studies in two symmetric dimeric liquid crystals – an optical study. *Phase Transitions*, 2012, **85** (12), P. 1031–1044.
- [12] Gonzalez R.C., Woods R.E., Eddins S.L. *Digital Image Processing Using MATLAB*, 2nd Edition, Gates mark Publishing, Natick, 2009.
- [13] Solomon C., Breckon T. *Fundamentals of Digital Image Processing: A Practical Approach with Examples in Matlab*, Wiley-Blackwell, Chichester, U.K., 2011.
- [14] Priestley E.L., Wojtowicz P.J., Sheng P. *Introduction to Liquid Crystals*, RCA Laboratories, Princeton, NJ, 1974.
- [15] Kuczynski W., Zywuicki B., Malecki J. Determination of orientational order parameter in various liquid-crystalline phases. *Mol. Cryst. Liq. Cryst.*, 2002, **381**, P. 1–19.
- [16] Zywicki B.J., Kuczynski W. IEEE transactions on optical phenomena – The orientational order in nematic liquid crystals from birefringence measurements. *Dielectr. Electr. Insul.*, 2001, **8**, P. 512–515.
- [17] Chandra Sekhar S. *Liquid Crystals*, Cambridge University Press: New York, 1992.
- [18] Singh S. Phase transitions in liquid crystals. *Phys. Rep.*, 2000, **324**, P. 107–269.
- [19] De Jeu W.H. *Physical Properties of Liquid Crystalline Materials*, Gordon and Breach, New York, 1980.

## Tunable multiferroic properties of cerium doped bismuth ferrite

Rozina Patel<sup>1\*</sup>, Pratibha Sawadh<sup>2</sup>

<sup>1</sup>Department of Physics, New Arts, Commerce and Science college, Wardha, India

<sup>2</sup>Department of Physics, Bapurao Deshmukh College of Engineering, Wardha, India

\*patel.rozina84@gmail.com

DOI 10.17586/2220-8054-2019-10-3-255-265

Multiferroic  $\text{Bi}_{1-x}\text{Ce}_x\text{FeO}_3$  ( $x = 0.05, 0.1, 0.15, 0.2$ ) nanoparticles were prepared using an auto-combustion method. The effect of cerium substitution on the crystal structure, electrical and magnetic properties of  $\text{BiFeO}_3$  (Bismuth Ferrite) was studied. X-ray diffraction spectra revealed that Ce substitution increases the lattice parameters. The average particle size estimated from TEM images is less than 50 nanometers. According to the magnetic hysteresis loops, it was found that the enhanced magnetization which results from increasing Ce concentration is attributed to the nanoparticle size and enhanced ferroelectric polarization. The magnetization and ferroelectric polarization were found to exhibit an exotic mutual relationship. The samples were found to exhibit relaxation of dielectric polarization. This rare combination of Ce doped  $\text{BiFeO}_3$  by auto-combustion method has not been reported before.

**Keywords:** Multiferroic, nano particles, X-ray diffraction, ferroelectric, ferromagnetic .

*Received:* 9 March 2019

*Revised:* 24 May 2019

### 1. Introduction

One of the reasons for fabricating novel materials for attaining rich functionality is to unite different physical properties in single material. Magnetic and Ferroelectric materials are enduring subject of study and have led to notable progress in the development of technology to date. These apparently distinct phenomena can coexist in certain unusual substances, termed as multiferroics which are of key importance, both from research as well as technological perspective.

Multiferroic materials exhibit the phenomena of ferroelectricity (FE), ferromagnetism (FM) and ferroelasticity simultaneously in their single phase [1–3]. Although the possibility of coupling or interaction between ferromagnetic and ferroelectric order parameters is known for quite long time, its existence and practical applications were realized only after the discovery of multiferroicity in  $\text{BiFeO}_3$ .

Bismuth ferrite is found to be one such material which demonstrate a coupling between magnetic and ferroelectric order, having Curie temperature  $T_C \approx 1100$  °K and antiferromagnetic temperature  $T_N \approx 640$  °K [4, 5]. Bismuth ferrite possesses G-type antiferromagnetic ordering because of its complex cycloidal spin structure with a wavelength of 62 nm with [110] spiral direction and (110) spin rotation plane [6]. However  $\text{BiFeO}_3$  suffers from several major issues like phase defects such as oxygen vacancies and impurity, high leakage current, spiral spin structure, large difference in transition temperature ( $T_C$  &  $T_N$ ). The leakage current rises in  $\text{BiFeO}_3$  due to its nonstoichiometry. This is particularly because of the difficulty in obtaining stoichiometric single phase  $\text{BiFeO}_3$  materials. In order to reduce leakage current density efforts have been made by using different fabrication methods. Several techniques have also been recently adopted to eliminate secondary phases and oxygen vacancies [7–11]. Particle size also plays a vital role in controlling the structural and magnetic properties of  $\text{BiFeO}_3$  [12]. The authors [13] described the necessity to lower the sintering time during the increase in synthesis temperature to confine the formed  $\text{BiFeO}_3$  crystals within the nanosize range. The current trend is to avoid brute force methods in order to have a better control of stoichiometry, structure, and phase purity of metal oxides. The authors [14] reported cerium-substituted  $\text{BiFeO}_3$  powders using hydrothermal method revealed the lattice contraction and decrease of grain size. Synthesis of Ce substituted  $\text{BiFeO}_3$  nanoflakes [15] using sol-gel method has resulted in enhancement of electrical properties. The combustion or fire synthesis is quite simple, fast, and economical. It is possible to control the particle size of solid combustion product to nano-range by using suitable fuels that control the nature of combustion. Urea is documented as an ideal fuel for the combustion synthesis of high temperature oxides [16]. In this work, auto combustion method was used for synthesis as it has not been reported for the synthesis of Ce doped  $\text{BiFeO}_3$  and urea was chosen as the fuel, which act as a self-catalyst and generates heat as its melting point is very low, which further helps in increasing the reactivity of the samples yielding a good result as compared to solid state process.

Attempts to improve the electrical properties have been made by doping it with rare earth elements such as lanthanum (La), samarium (Sm), gadolinium (Gd) and dysprosium (Dy) etc. [17, 18]. Efforts have also been made to

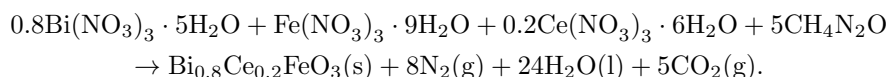
overcome these issues by doping transition metals [19] into BiFeO<sub>3</sub>, also modifying material by including solid solution of BiFeO<sub>3</sub> with BaTiO<sub>3</sub> etc. [20, 21]. Difficulties also prevail in the practical realization of BiFeO<sub>3</sub>, resulting from weak ferromagnetism exhibited by BiFeO<sub>3</sub>, as the spiral spin modulation, superimposed on G-type antiferromagnetic spin ordering [22, 23], cancels out any possible net magnetization. One means for suppressing spiral spin modulation in BiFeO<sub>3</sub> is the chemical substitution in the A-sublattice [24–29]. Diamagnetic substitution at A-site in BiFeO<sub>3</sub> has been shown to enhance the net magnetization of parent material because of the kind of diamagnetic dopant element [30, 31].

In the present work, we have incorporated the compositional variations which have permitted the attainment of improved multiferroic properties. Cerium was chosen to substitute at A-site of BiFeO<sub>3</sub> because the ionic radius of Ce<sup>3+</sup> is comparable with that of Bi<sup>3+</sup>. The electronic configuration of Ce<sup>3+</sup> also causes hybridization resulting in formation of Ce–O bond [32] leading to a noncentrosymmetrically distorted structure and a suppressed spiral spin structure, probably improving the ferroelectric and magnetic properties. The partial substitution of Bi<sup>3+</sup> ions by rare earth ions are reported to improve multiferroic properties of BiFeO<sub>3</sub> [33–37].

## 2. Experimental

The samples with the composition Bi<sub>1-x</sub>Ce<sub>x</sub>FeO<sub>3</sub> ( $x = 0.05, 0.1, 0.15, 0.2$ ) were prepared by an auto combustion method using urea as a fuel. The prime basis of auto combustion method depends on the proficiency of highly exothermic reactions to be self-sustaining and, therefore, energetically efficient. The exothermic reaction is initiated at the ignition temperature, and generate heat which is displayed in a maximum or combustion temperature ( $T_{comb}$ ), which can volatilize low boiling point impurities, and therefore result in purer products than those produced by more conventional techniques.

The precursor materials used for the synthesis of Bi<sub>1-x</sub>Ce<sub>x</sub>FeO<sub>3</sub> ( $x = 0.05, 0.1, 0.15, 0.2$ ) by the auto combustion route were analytical reagent grade bismuth nitrate pentahydrate (Bi(NO<sub>3</sub>)<sub>3</sub>·5H<sub>2</sub>O), ferric nitrate nonahydrate (Fe(NO<sub>3</sub>)<sub>3</sub>·9H<sub>2</sub>O), Cerium(III) nitrate hexahydrate (Ce(NO<sub>3</sub>)<sub>3</sub>·6H<sub>2</sub>O) with a purity of more than 99%. Analytical grade urea in a powder form with purity more than 99% was used as fuel in the synthesis of the Bi<sub>1-x</sub>Ce<sub>x</sub>FeO<sub>3</sub> powder. Appropriate quantities of materials were weighed in microbalance according to the stoichiometry to obtain (0.05, 0.1, 0.15, 0.2) trivalent Ce<sup>3+</sup> dopant concentrations to replace trivalent Bi<sup>3+</sup>. Stoichiometry of their mixture for combustion is calculated based on the total oxidizing and reducing valencies of oxidizer and fuel. So that the equivalent oxidizer to fuel ratio becomes unity which results in release of maximum heat [38, 39]:



According to propellant chemistry, the valencies of the elements carbon, hydrogen, nitrogen and oxygen are +4, +1, 0 and –2 respectively. The valency of nitrogen is taken as zero because of its conversion to molecular nitrogen during combustion. The valencies of metal depend upon metal ions in that compound. The valencies of the metals bismuth, iron and cerium are +3, +3 and +3 respectively. Thus, a mixture of (Bi(NO<sub>3</sub>)<sub>3</sub>·5H<sub>2</sub>O), (Fe(NO<sub>3</sub>)<sub>3</sub>·9H<sub>2</sub>O), Ce(NO<sub>3</sub>)<sub>3</sub>·6H<sub>2</sub>O and urea in an appropriate molar proportion were thoroughly mixed by grinding using agate mortar and pestle to form a homogeneous mixture. This homogeneous mixture was then poured into a crucible and was introduced into a 500 °C preheated muffle furnace, which undergoes self-propagating, gas producing combustion reaction to yield voluminous metal oxide in less than 5 minutes, which is a porous and foamy product [40]. The porous powder was ground in a mortar and pestle to obtain a fine powder. The ground powder was again placed into the furnace for sintering at 400 °C for 3 hours.

The samples were then characterized by using various techniques. X-ray powder diffraction data was collected using an XPERT-PRO diffractometer with CuK $\alpha$  radiation ( $\lambda = 0.15456$  nm) at step of 0.02 in the range  $2\theta = 200$  to 800. The magnetic properties were measured by a vibrating sample magnetometer (Lakeshore VSM 7410) at room temperature. Dielectric measurements were performed on an impedance analyzer (Weynn Kerr 6500B) for which the sintered samples were mechanically pressed in a hydraulic press and an Ag paste was applied to both sides of the polished pellets. Ferroelectric hysteresis loops were studied by a P–E loop tracer.

## 3. Result and discussion

Room temperature powder x-ray diffraction was then carried out on Bi<sub>1-x</sub>Ce<sub>x</sub>FeO<sub>3</sub> ( $x = 0.05, 0.1, 0.15, 0.2$ ). Rhombohedral perovskite structure is retained even after substituting Ce<sup>3+</sup> ions for Bi<sup>3+</sup> in BiFeO<sub>3</sub>. The profile fit for the Rietveld refinement of Bi<sub>1-x</sub>Ce<sub>x</sub>FeO<sub>3</sub> ( $x = 0.05, 0.1, 0.15, 0.2$ ) samples are shown in Fig. 1(a,b,c,d) respectively. Ce doping causes the peaks to shift toward lower  $2\theta$  value this indicates that Ce is getting substituted in the BiFeO<sub>3</sub> lattice.

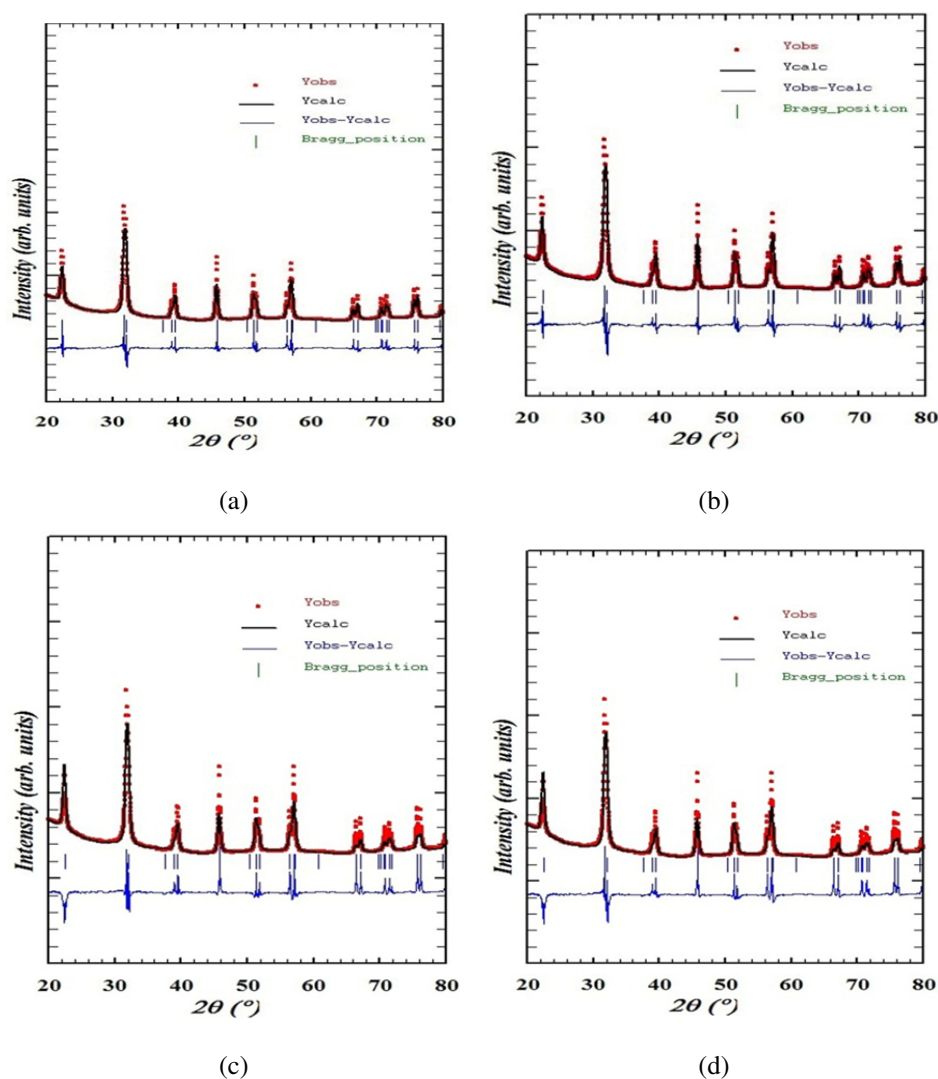


FIG. 1. The fit for the Rietveld refined profile for the  $\text{Bi}_{0.95}\text{Ce}_{0.05}\text{FeO}_3$  (a);  $\text{Bi}_{0.9}\text{Ce}_{0.1}\text{FeO}_3$  (b);  $\text{Bi}_{0.85}\text{Ce}_{0.15}\text{FeO}_3$  (c) and  $\text{Bi}_{0.8}\text{Ce}_{0.2}\text{FeO}_3$  (d) samples

The lattice parameters are found to increase with Ce doping because ionic radii of  $\text{Ce}^{3+}$  (radius = 1.01 Å) is more than that of  $\text{Bi}^{3+}$  (radius = 1.03 Å) ion [41]. The crystallite sizes of all the samples  $\text{Bi}_{1-x}\text{Ce}_x\text{FeO}_3$  ( $x = 0.05, 0.1, 0.15, 0.2$ ) were found to be 16 nm, 19 nm, 22 nm and 27 nm respectively obtained by considering the most intense diffraction peak in the pattern using Scherer's formula.

The simulated XRD patterns of sample coincide well with the measured XRD pattern with generally small  $R$ -values as illustrated in Table 1. The lattice parameters and other refined parameter are also tabulated in Table 1.

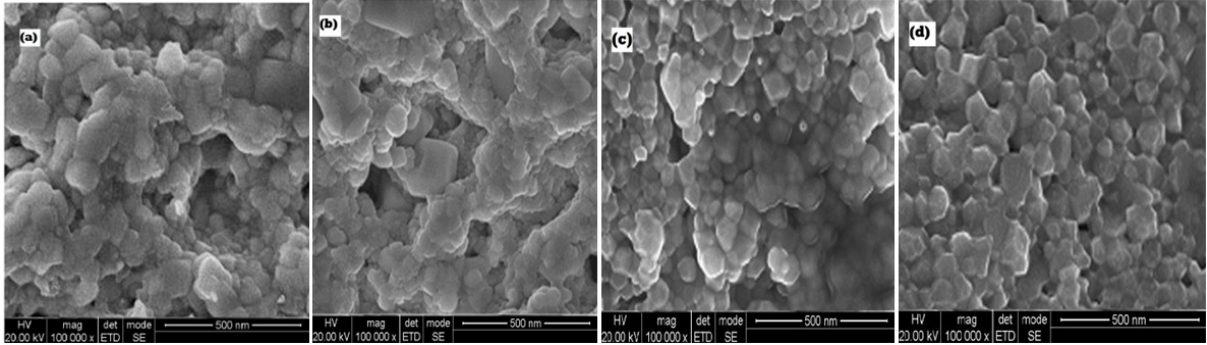
SEM micrograph of Ce doped samples exhibits finegrained structure with sharp grain boundaries with almost uniform diameter as shown in Fig. 2. The micrographs of the samples showed relatively greater homogeneity in the microstructure. Also the grain size of the samples decreases with increasing cerium in  $\text{BiFeO}_3$  which is a clear indication of incorporation of cerium into  $\text{BiFeO}_3$ .

Typical TEM images of  $\text{Bi}_{1-x}\text{Ce}_x\text{FeO}_3$  ( $x = 0.05, 0.1, 0.15, 0.2$ ) samples prepared by the auto combustion method is shown in Fig. 3 respectively.

The average particle size estimated from TEM images for  $\text{Bi}_{1-x}\text{Ce}_x\text{FeO}_3$  ( $x = 0.05, 0.1, 0.15, 0.2$ ) were found to be 15 nm, 20 nm, 24 nm and 27 nm respectively, which is in accordance with XRD analysis. The particles are well connected with each other and are found to be approximate lyspherical in shape. The average particle size is found to decrease with Ce doping. Thus we can conclude that the substitution of Bismuth by rare-earth in multiferroic material  $\text{BiFeO}_3$  is accompanied by a significant decrease in particle size [42].

TABLE 1. Details of Rietveld refined XRD parameters for  $\text{Bi}_{1-x}\text{Ce}_x\text{FeO}_3$ 

Parameters	$\text{Bi}_{0.95}\text{Ce}_{0.05}\text{FeO}_3$	$\text{Bi}_{0.9}\text{Ce}_{0.1}\text{FeO}_3$	$\text{Bi}_{0.85}\text{Ce}_{0.15}\text{FeO}_3$	$\text{Bi}_{0.8}\text{Ce}_{0.2}\text{FeO}_3$
$2\theta$ range (deg.)	20° to 80°	20° to 80°	20° to 80°	20° to 80°
Step size (deg.)	0.02	0.02	0.02	0.02
Wavelength	1.5406 AA	1.5406 Å	1.5406 Å	1.5406 Å
Space group	R3c	R3c	R3c	R3c
$a$ (Å)	5.587 Å	5.613 Å	5.643 Å	5.659 Å
$b$ (Å)	5.587 Å	5.613 Å	5.643 Å	5.659 Å
$c$ (Å)	13.876 Å	13.902 Å	13.932 Å	13.948 Å
Volume (Å <sup>3</sup> )	375.09 Å <sup>3</sup>	379.3 Å <sup>3</sup>	384.19 Å <sup>3</sup>	386.82 Å <sup>3</sup>
$R_F$	1.7	2.1	2.5	2.8
$R_{Bragg}$	2.95	2.8	2.6	2.35
$R_{wp}$	16	15.6	14.5	13.0
$R_{exp}$	13.8	14.0	15.6	17.6
$R_p$	12.4	13.5	14.4	15.4
$\chi^2$	1.924	1.804	1.423	1.34

FIG. 2. SEM images of  $\text{Bi}_{1-x}\text{Ce}_x\text{FeO}_3$  nanoparticles (a)  $x = 0.05$ ; (b)  $x = 0.1$ ; (c)  $x = 0.15$  and (d)  $x = 0.2$ 

Thermal analysis of  $\text{Bi}_{1-x}\text{Ce}_x\text{FeO}_3$  ( $x = 0.05, 0.1, 0.15, 0.2$ ) samples sintered at 400 °C has been carried out with DTA (600 – 900 °C) to study the transition temperatures. DTA results for temperature range (800 – 900 °C) are shown in Fig. 4. For  $\text{Bi}_{1-x}\text{Ce}_x\text{FeO}_3$  respectively. A peak is observed for all the samples. Kaczmarek et al. [43] have attributed the peak observed in DTA near 830 °C to ferroelectric phase transition (Curie temperature,  $T_C$ ) of bulk  $\text{BiFeO}_3$ . This clear endothermic peak is of chief interest here.

The peak is shifted towards higher temperature with increase in Ce concentration. This increase in  $T_C$  can be due to the decrease in pressure with increase in the cell volume. In  $\text{BaTiO}_3$ , the various transition temperatures shift down on compression [44]. Similarly, lowering of ferroelectric transition temperature is observed when doped with smaller atoms [45].

The room temperature magnetic hysteresis loops for  $\text{Bi}_{1-x}\text{Ce}_x\text{FeO}_3$  ( $x = 0.05, 0.1, 0.15, 0.2$ ) samples are shown in Fig. 5 recorded at 300 K. It is noted that saturation is achieved in all the samples for an applied field of <10 KOe.

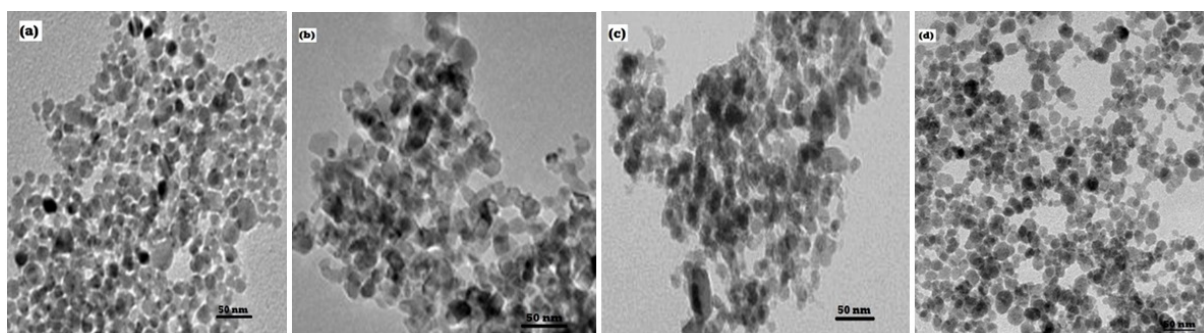


FIG. 3. TEM images of  $\text{Bi}_{1-x}\text{Ce}_x\text{FeO}_3$  nanoparticles (a)  $x = 0.05$ ; (b)  $x = 0.1$ ; (c)  $x = 0.15$  and (d)  $x = 0.2$

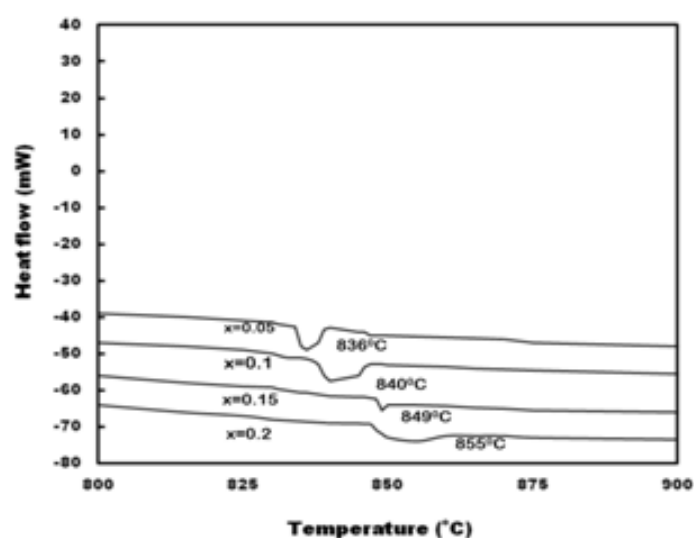


FIG. 4. DTA curve of  $\text{Bi}_{1-x}\text{Ce}_x\text{FeO}_3$  sintered at  $400\text{ }^\circ\text{C}$

All the samples exhibited ferromagnetic ordering at room temperature. Owing to finite size the nanoparticles usually show unusual magnetic behaviors distinct from that of their bulk counterparts. In antiferromagnetic nanoparticles, due to the large surface to volume ratio, the contribution of uncompensated spins at the surface becomes higher.

Nèel [46–48] proposed that the finite magnetic moment of nanoparticles of antiferromagnetic materials is due to the presence of the seun compensated spin sat the surface of the particles. Apart from uncompensated spins at the surface, canting of spins in antiferromagnetic sublattices also plays an important role in the magnetic properties of the nanostructures [49, 50]. Ce doping could have increased the canting angle, which in turn has resulted in enhanced magnetic properties. Another reason for the observed ferromagnetism is the suppression of spirals pin structure characteristic of  $\text{BiFeO}_3$ . When the particle size is on the order of or  $<62\text{ nm}$ , this spiral spin structure changes so as to result in enhancement in magnetic properties. The variation of magnetic parameters and crystallite size is tabulated in Table 2. It is clear that Ce doping has strengthened the magnetic properties of  $\text{BiFeO}_3$  significantly.

Figure 6 shows P–E hysteresis loops for the  $\text{Bi}_{1-x}\text{Ce}_x\text{FeO}_3$  ( $x = 0.05, 0.1, 0.15, 0.2$ ) as a function of electric field. Ferroelectric parameters at room temperature for  $\text{Bi}_{1-x}\text{Ce}_x\text{FeO}_3$  ( $x = 0.05, 0.1, 0.15, 0.2$ ) samples are given in Table 3. All samples show typical ferroelectric behavior. According to Wang et al. [51], the ferroelectricity of the  $\text{BiFeO}_3$  samples originated from the displacements of Bi with respect to the  $\text{FeO}_6$  cages along the (111) plane. Experimental results suggested that partial doping of Ce ions in  $\text{BiFeO}_3$  acts as donor in oxygen octahedron and force the reduction of oxygen vacancies by restricting the formation of  $\text{Fe}^{3+}$  to  $\text{Fe}^{2+}$  ions, resulting in a great suppression of leakage current.

It is found that remanent polarization is found to increase with an increase in crystallite size. As the grain boundary is a low permittivity region, it has weak ferroelectricity. Therefore, polarization of grain boundary may be little or

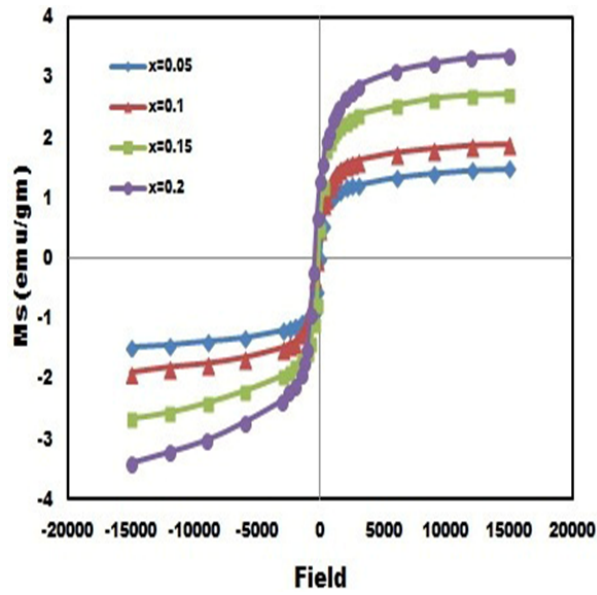


FIG. 5. The M–H plot of  $\text{Bi}_{1-x}\text{Ce}_x\text{FeO}_3$  ( $x = 0.05, 0.1, 0.15, 0.2$ ) at 300 K

TABLE 2. Details of Magnetic Parameters at Room Temperature for  $\text{Bi}_{1-x}\text{Ce}_x\text{FeO}_3$  samples

Sample	Remanent Magnetization (emu/g)	Saturation Magnetization (emu/g)	Crystallite Size (nm)
$\text{Bi}_{0.95}\text{Ce}_{0.05}\text{FeO}_3$	0.5	1.48	16
$\text{Bi}_{0.9}\text{Ce}_{0.1}\text{FeO}_3$	0.7	1.89	19
$\text{Bi}_{0.85}\text{Ce}_{0.15}\text{FeO}_3$	1.3	2.71	22
$\text{Bi}_{0.8}\text{Ce}_{0.2}\text{FeO}_3$	1.6	3.38	27

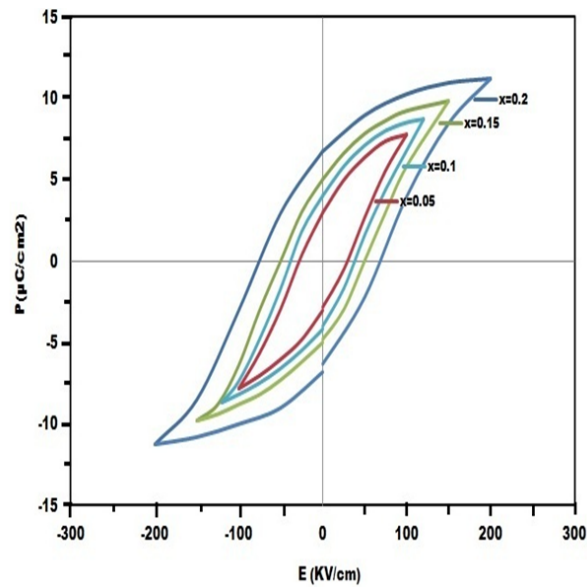


FIG. 6. Ferroelectric hysteresis loop of  $\text{Bi}_{1-x}\text{Ce}_x\text{FeO}_3$  ( $x = 0.05, 0.1, 0.15, 0.2$ ) at 50 Hz

TABLE 3. Details of Ferroelectric Parameters at Room Temperature for  $\text{Bi}_{1-x}\text{Ce}_x\text{FeO}_3$  samples

Sample	Electric field, $E_c$ (KV/cm)	Remnant polarization $P_r$ ( $\mu\text{C}/\text{cm}^2$ )	Crystallite Size (nm)
$\text{Bi}_{0.95}\text{Ce}_{0.05}\text{FeO}_3$	25	3.08	16
$\text{Bi}_{0.9}\text{Ce}_{0.1}\text{FeO}_3$	38	4.21	19
$\text{Bi}_{0.85}\text{Ce}_{0.15}\text{FeO}_3$	46	5.02	22
$\text{Bi}_{0.8}\text{Ce}_{0.2}\text{FeO}_3$	63	6.8	27

even nonexistent. On the other hand, space charges in grain boundary exclude polarization charge on grain surface and depletion layer on grain surface can be formed. That results in polarization discontinuity on grain surface to form depolarization field and polarization decreases. The number of grain boundary increases as crystallite size decreases. Consequently, the remanent polarization increases as the crystallite size increases [52]. Also the remanent polarization is found to increase with Ce concentration, hence we may anticipate that replacement of highly volatile  $\text{Bi}^{3+}$  with  $\text{Ce}^{3+}$  reduces the concentration of oxygen vacancies giving reduced leakage current and thus improves ferroelectric properties.

The measured temperature dependence of dielectric constant  $\varepsilon$  and loss for  $\text{Bi}_{1-x}\text{Ce}_x\text{FeO}_3$  ( $x = 0.05, 0.1, 0.15$  and  $0.2$ ) samples at 100 Hz frequency are shown in Fig. 7(a,b), respectively. The peak in the dielectric constant is attributed to a transformation from the antiferromagnetic order to the paramagnetic order, indicating an effect of disappearing magnetic order as compared to electric order and attests to magneto-electric coupling in the samples. This type of anomaly near the Néel temperature has also been predicted by several studies [53–58]. Here, the peaks show a diffuse nature. The substitution of cerium shifts the dielectric peak to low temperature region and a diffuse dielectric peak results. The peak shift may be attributed to the slightly larger ionic radii of  $\text{Ce}^{3+}$  which replaces  $\text{Bi}^{3+}$  due to which tolerance factor decreases which in turn reduces the Néel temperature. Another significant result is peak broadening with increased cerium concentration.

Figure 7(b) shows the variation in dielectric loss  $\tan \delta$  for  $\text{Bi}_{1-x}\text{Ce}_x\text{FeO}_3$  ( $x = 0.05, 0.1, 0.15, 0.2$ ) samples. Further as noted in the dielectric constant, anomalies are observed at 390, 380, 374 and 352 °C for  $x = 0.05, 0.1, 0.15$  &  $0.2$  respectively. In addition, the peaks in dielectric constant  $\varepsilon$  and dielectric loss  $\tan \delta$  shifted towards a lower temperature with increased  $\text{Ce}^{3+}$  substitution, which indicates a decrease in the antiferromagnetic ordering temperature upon  $\text{Ce}^{3+}$  substitution.

Frequency (100 Hz – 1 MHz) dependence of real part of dielectric constant  $\varepsilon'$  and loss for the  $\text{Bi}_{1-x}\text{Ce}_x\text{FeO}_3$  ( $x = 0.05, 0.1, 0.15, 0.2$ ) samples at 300 K is shown in Fig. 8(a,b) respectively. For all samples, the  $\varepsilon'$  decreases with the increase in frequency and is consistent with combined response of orientational relaxation of dipoles and conduction of charge carriers. It may be attributable to the fact that the intra well hopping probability of charge carriers dominates and dipoles are unable to follow the field reversal in such a small interval of time at higher frequencies. It has been observed that  $\varepsilon'$  is increasing with substitution of Ce. Variation in  $\tan \delta$  with frequency at 300 K for  $\text{Bi}_{1-x}\text{Ce}_x\text{FeO}_3$  ( $x = 0.05, 0.1, 0.15, 0.2$ ) samples is shown in Fig. 8(a,b).

It is evident that  $\tan \delta$  also decreases with an increase infrequency. The increase in the dielectric constant may be attributed to the suppression of oxygen vacancies due to the substitution of  $\text{Ce}^{3+}$  at  $\text{Bi}^{3+}$  site. Since the substitution of Ce at Bi site is ascribed to compensation of the volatile Bi component in  $\text{BiFeO}_3$ , which causes reduction in the oxygen vacancies, which could have been generated to compensate the positive charge deficiency caused by the volatilization of Bi [59,60]. As a result, the number of oxygen vacancies decrease, therefore  $\text{Bi}_{0.8}\text{Ce}_{0.2}\text{FeO}_3$  has the highest  $\varepsilon$  value among all the Ce doped compositions.

#### 4. Conclusions

It can be concluded from the present work that auto-combustion synthesis technique can be an advantageous method to prepare single phase cerium-doped  $\text{BiFeO}_3$ . The XRD pattern showed rhombohedrally distorted perovskite structure for cerium-doped  $\text{BiFeO}_3$ . The crystallite size is found to increase with increasing cerium concentration. Magnetization is found to increase considerably in all doped samples due to canting of spins and particle size less than 62 nm, which is less than the periodicity of  $\text{BiFeO}_3$ . Also cerium-doped  $\text{BiFeO}_3$  sample shows fairly good ferroelectric behavior with increased remanent polarization with increasing crystallite size. Increasing the cerium concentration is found to reduce the Néel temperature, which is observed from the temperature dependant dielectric

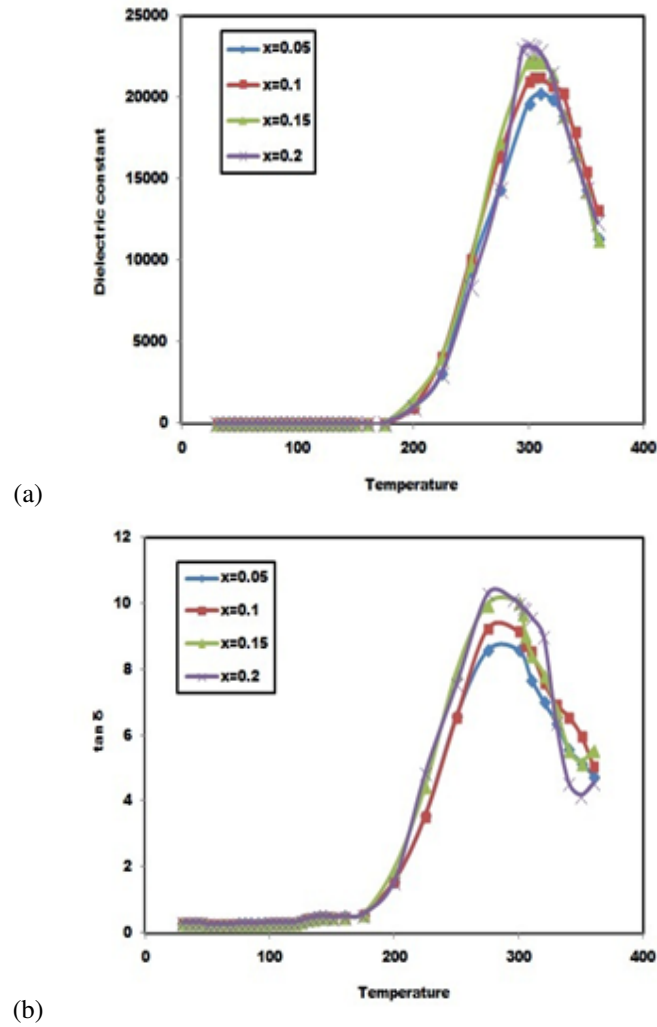


FIG. 7. (a) Temperature dependent dielectric constant at 50 Hz; (b) Dielectric loss of  $\text{Bi}_{1-x}\text{Ce}_x\text{FeO}_3$  ( $x = 0.05, 0.1, 0.15, 0.2$ ) at 50 Hz

anomaly. This dielectric anomaly observed in all the samples is a signature of magneto-electric coupling. Dielectric constant also shows strong frequency dependence for all the samples, indicating the usual dielectric dispersion. It is anticipated that appropriate doping at A Site of  $\text{BiFeO}_3$  can enhance the intrinsic magnets and ferroelectric properties as well as generating novel functionalities.

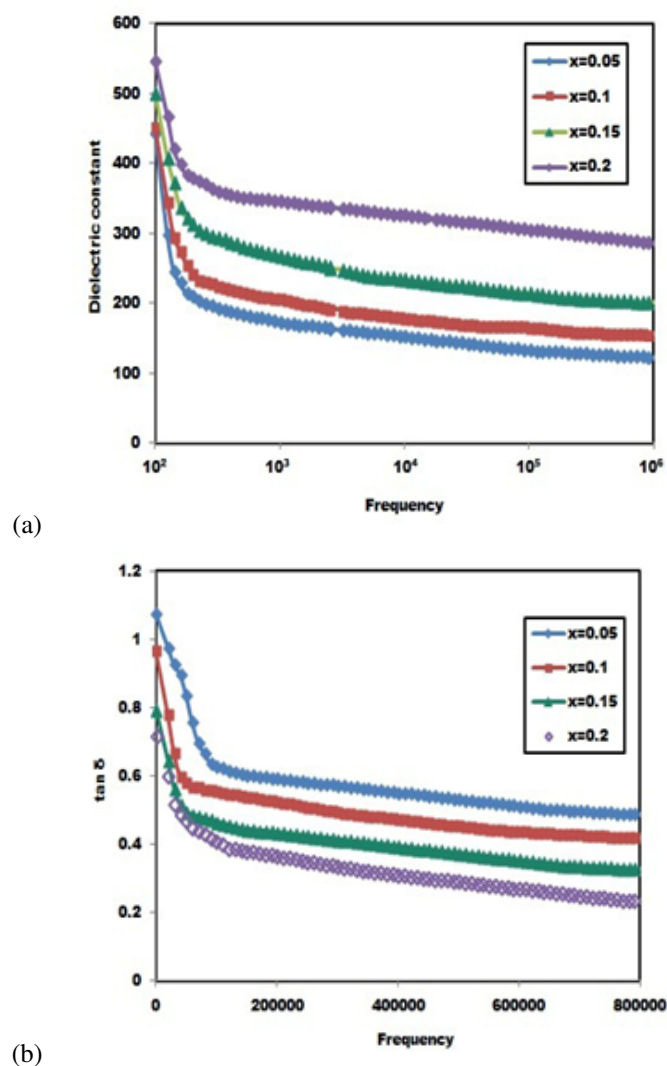


FIG. 8. (a) Real part of Frequency dependent dielectric constant; (b) Dielectric loss of  $\text{Bi}_{1-x}\text{Ce}_x\text{FeO}_3$  ( $x = 0.05, 0.1, 0.15, 0.2$ ) at 300 K

## References

- [1] M. Fiebig, T. Lottermoser, et al. Observation of coupled magnetic and electric domains. *Nature (London)*, 2002, **419**, P. 818–820.
- [2] J. Wang, J.B. Neaton, et al. Epitaxial  $\text{BiFeO}_3$  multiferroic thin film heterostructures. *Science*, 2003, **299**, P. 1719–1722.
- [3] Rajasree Das, Gobinda Gopal Khan, Kalyan Mandal. Enhanced ferroelectric, magnetoelectric, and magnetic properties in Pr and Cr co-doped  $\text{BiFeO}_3$  nanotubes fabricated by template assisted route. *J. Appl. Phys.*, 2012, **111**, P. 104115 (1–6).
- [4] Nguyen Van Minh, Nguyen Gia Quan. Structural, optical and electromagnetic properties of  $\text{Bi}_{1-x}\text{Ho}_x\text{FeO}_3$  multiferroic materials. *J. Alloys Compd.*, 2011, **509**, P. 2663–2666.
- [5] Deepti Kothari, V. Raghavendra Reddy, et al. Eu doping in multiferroic  $\text{BiFeO}_3$  ceramics studied by Mossbauer and EXAFS spectroscopy. *J. Phys.: Condens. Matter*, 2010, **22**, P. 356001.
- [6] Sosnowska I., Loewenhaupt M., David W.I.F., Ibberson R.M. Investigation of the unusual magnetic spiral arrangement in  $\text{BiFeO}_3$ . *Physica B: Condensed Matter*, 1992, **180–181**, P. 117–118.
- [7] Dho J., Qi X., et al. Large Electric Polarization and Exchange Bias in Multiferroic  $\text{BiFeO}_3$ . *ADV. Mater.*, 2006, **18**, P.1445–1448.
- [8] Xiaoding Qi, Joonghoe Dho, et al. Greatly reduced leakage current and conduction mechanism in aliovalent-ion-doped  $\text{BiFeO}_3$ . *Appl. Phys. Lett.*, 2005, **86**, P. 062903.
- [9] Can Wang, Mitsue Takahashi, et al. Leakage current of multiferroic  $(\text{Bi}_{0.6}\text{Tb}_{0.3}\text{La}_{0.1})\text{FeO}_3$  thin films grown at various oxygen pressures by pulsed laser deposition and annealing effect. *Journal of Applied Physics*, 2006, **99**, P. 054104.
- [10] Xiao X.H., Zhu J., et al. Greatly reduced leakage current in  $\text{BiFeO}_3$  thin film by oxygen ion implantation. *Journal of Physics D: Applied Physics*, 2007, **40**, P. 18.
- [11] Chen Y.B., Katz M.B., Pan, Ferroelectric domain structures of epitaxial (001)  $\text{BiFeO}_3$  thin films. *Appl. Phys. Lett.*, 2007, **90**, P. 072907.
- [12] Samar Layek, Soumen Kumar Bag, Verma H.C. Preparation And Studies On  $(1 - X)\text{BiFeO}_3 - X\text{Li}_{0.5}\text{Fe}_{2.5}\text{O}_4$  ( $X = 0.25$  and  $0.5$ ) Multiferroic Nano-Composites. *'ICNANO 2011'*, 2013, **4**, P. 26–30.

- [13] Lomanova N.A., Gusarov V.V. Influence of synthesis temperature on BiFeO<sub>3</sub> nanoparticles formation. *Nanosystems: Physics, Chemistry, Mathematics*, 2013, **4** (5), P. 696–705.
- [14] Mao J., Cao L., et al. Experimental and first principles investigation of Bi<sub>1-x</sub>Ce<sub>x</sub>FeO<sub>3</sub>: Structure, electronic and optical properties. *Journal of Alloys and Compound*, 2017, **721**, P. 638–645.
- [15] El-Lateef H., Khalaf M., Ibrahim E.M.M. Magnetic and DC electric properties of sol-gel synthesized Ce-doped BiFeO<sub>3</sub> nanoflakes. *Applied Physics A*, 2017, **123**, P. 533.
- [16] Patil K.C., Hegde M.S., Rattan T., Aruna S.T. *Chemistry of nanocrystalline oxide materials – combustion synthesis: Properties and Applications*, World Scientific, (2008).
- [17] Gurmeet Singh Lotey, Verma N.K. Multiferroism in rare earth metals-doped BiFeO<sub>3</sub> nanowires. *Superlattices and Microstructures*, 2013, **60**, P. 60–66.
- [18] Yao Y.B., Liuc W.C., Mak C.L. Pyroelectric properties and electrical conductivity in samarium doped BiFeO<sub>3</sub> ceramics. *Journal of Alloys and Compounds*, 2012, **527**, P. 157–162.
- [19] Kumar M., Yadav K.L. Rapid liquid phase sintered Mn doped BiFeO<sub>3</sub> ceramics with enhanced polarization and weak magnetization. *Appl. Phys. Lett.*, 2007, **91**, P. 242901.
- [20] Ueda K., Tabata H., Kawai T. Coexistence of ferroelectricity and ferromagnetism in BiFeO<sub>3</sub>-BaTiO<sub>3</sub> thin films at room temperature. *Appl. Phys. Lett.*, 1999, **75**, P. 555.
- [21] Mahesh Kumar M., Srinivas A., Suryanarayan. Structure property relations in BiFeO<sub>3</sub>/BaTiO<sub>3</sub> solid solutions. *Journal of Applied Physics*, 2000, **87**, P. 855–862.
- [22] Sosnowska I., Peterlin-Neumaier T., Steichele E. Spiral magnetic ordering in bismuth ferrite. *J. Phys. C: Solid State Phys.*, 1982, **15**, P. 4835–4846.
- [23] Przenioso R., Palewicz A., et al. Does the modulated magnetic structure of BiFeO<sub>3</sub> change at low temperatures? *J. Phys.: Condens. Matter*, 2006, **18**, P. 2069–2075.
- [24] Yuan G.L., Or S.W., Chan H.L.W. Structural transformation and ferroelectric/paraelectric phase transition in Bi<sub>1-x</sub>La<sub>x</sub>FeO<sub>3</sub> ( $x = 0-0.25$ ) multiferroic ceramics. *J. Phys. D: Appl. Phys.*, 2007, **40**, P. 1196–1200.
- [25] Yuan G.L., Or S.W. Enhanced piezoelectric and pyroelectric effects in single-phase multiferroic Bi<sub>1-x</sub>Nd<sub>x</sub>FeO<sub>3</sub> ( $x = 0-0.15$ ) ceramics. *Appl. Phys. Lett.*, 2006, **88**, P. 062905.
- [26] Khomchenko V.A., Kiselev D.A., et al. Effect of diamagnetic Ca, Sr, Pb, and Ba substitution on the crystal structure and multiferroic properties of the BiFeO<sub>3</sub> perovskite. *Journal of Applied Physics*, 2008, **103**, P. 024105.
- [27] Fujino S., Murakami M., et al. Combinatorial discovery of a lead-free morphotropic phase boundary in a thin-film piezoelectric perovskite. *Appl. Phys. Lett.*, 2008, **92**, P. 202904.
- [28] Yan Z., Wang K.F., et al. Processing and properties of Yb-doped BiFeO<sub>3</sub> ceramics. *Appl. Phys. Lett.*, 2007, **91**, P. 082906.
- [29] Mishra R.K., Pradhan D.K., Choudhary R.N.P., Banerjee A. Effect of yttrium on improvement of dielectric properties and magnetic switching behavior in BiFeO<sub>3</sub>. *J. Phys.: Condens. Matter*, 2008, **20**, P. 045218(1–6).
- [30] Khomchenko V.A., Kiselev D.A., et al. Synthesis and multiferroic properties of Bi<sub>0.8</sub>A<sub>0.2</sub>FeO<sub>3</sub> (A=Ca,Sr,Pb) ceramics. *Appl. Phys. Lett.*, 2007, **90**, P. 242901.
- [31] Khomchenko V.A., Kiselev D.A., et al. Effect of diamagnetic Ca, Sr, Pb, and Ba substitution on the crystal structure and multiferroic properties of the BiFeO<sub>3</sub> perovskite. *Journal of Applied Physics*, 2008, **103**, P. 024105.
- [32] Schaffer J.P., Saxena A., et al. *The Science and Design of Engineering Materials*, McGrawHill, New York, 1999.
- [33] Lotey G.S., Verma N.K. Structural, magnetic, and electrical properties of Gd-doped BiFeO<sub>3</sub> nanoparticles with reduced particle size. *Journal of Nanoparticle Research*, 2012, **14** (3), P. 742.
- [34] Lotey G.S., Verma N.K. Phase-dependent multiferroism in Dy-doped BiFeO<sub>3</sub> nanowires. *Superlattices and Microstructures*, 2013, **53**, P. 184–194.
- [35] Lotey G.S., Verma N.K. Multiferroic properties of Tb-doped BiFeO<sub>3</sub> nanowires. *Journal of nanoparticle research*, 2013, **15** (4), P. 1553.
- [36] Das R., Khan G.G., Mandal K. Pr and Cr co-doped BiFeO<sub>3</sub> nanotubes: an advance multiferroic oxide material. *EPJ Web of Conferences*, 2013, **40**, P. 15015.
- [37] Wang J., Li M., et al. Synthesis and ferroelectric properties of Nd doped multiferroic BiFeO<sub>3</sub> nanotubes. *Chin. Sci. Bull.*, 2010, **55**, P. 1594–1597.
- [38] Prakash A.S., Khadar A.M.A., Patil K.C. Hegde M.S. Hexamethylenetetramine: A New Fuel for Solution Combustion Synthesis of Complex Metal Oxides. *J. Mater. Synth. Process*, 2002, **10**, P. 135–141.
- [39] Jain S.R., Adiga K.C., Pai Verneker V.R. A new approach to thermochemical calculations of condensed fuel-oxidizer mixtures. *Combust. Flame*, 1981, **40**, P. 71–79.
- [40] Patil K.C. Advanced ceramics: Combustion synthesis and properties. *Bull. Mater. Sci.*, 1993, **16**, P. 533–541.
- [41] Shannon R.D. Revised effective ionic radii and systematic studies of interatomic distances in halides and chalcogenides. *R. D. Acta Cryst. A*, 1976, **32**, P. 751.
- [42] Zhang Xingquan, Sui Yu, et al. Influence of diamagnetic Pb doping on the crystal structure and multiferroic properties of the BiFeO<sub>3</sub> perovskite. *Journal of Applied Physics*, 2009, **105**, P. 07D918.
- [43] Kaczmarek W., Pajak Z., Polomska M. Differential thermal analysis of phase transitions in Bi<sub>1-x</sub>La<sub>x</sub>FeO<sub>3</sub> solid solution. *Solid State Commun.*, 1975, **17**, P. 807–810.
- [44] Ishidate T., Abe S. Phase Diagram of BaTiO<sub>3</sub>. *Physical Review Letters*, 1997, **78**, P. 2397–2400.
- [45] Sahu J.R., Rao C.N. Beneficial modification of the properties of multiferroic BiFeO<sub>3</sub> by cation substitution. *Solid State Sciences*, 2007, **9**, P. 950–954.
- [46] Néel L. Superparamagnetisme des Grains Tres Fins Antiferromagnetiques. *C. R. Hebd. Sean. Acad. Sci.*, 1961, **252**, P. 4075–4080.
- [47] Néel L. Proprietes Magnetiques des Grains Fins Antiferromagnetiques: Superparamagnetisme et Superantiferromagnetisme. *J. Phys. Soc. Jpn.*, 1962, **17**, P. 676–689.
- [48] Néel L. Antiferromagnetic Hysteresis. In Selected Works of Louis Néel. Edited by N. Kurti. Gordon and Breach, New York, 1988, P. 467–488.
- [49] Dzyaloshinskii I.E. Thermodynamic Theory of Weak Ferromagnetism in Antiferromagnetic Substances. *Sov. Phys. JETP*, 1957, **5**, P. 1259–1272.

- [50] Moriya T. Anisotropic Superexchange Interaction and Weak Ferromagnetism. *Phys. Rev.*, 1960, **120** (1), P. 91–98.
- [51] Wang J., Neaton J.B., et al. Epitaxial BiFeO<sub>3</sub> multiferroic thin film heterostructures. *Science*, 2003, **299**, P. 1719–1722.
- [52] Mudinepalli V.R., Feng L., WenChin L.I.N., Murty B.S. Effect of grain size on dielectric and ferroelectric properties of nanostructured Ba<sub>0.8</sub>Sr<sub>0.2</sub>TiO<sub>3</sub> Ceramics. *Journal of Advanced Ceramics*, 2015, **4** (1), P. 46–53.
- [53] Chaudhari Y.A., Mahajan C.M., Jagtap P., Bendre S.T. Structural, Magnetic and Dielectric Properties of Nano-Crystalline Ni-Doped BiFeO<sub>3</sub> Ceramics Formulated by Self Propagating High Temperature Synthesis. *Journal of Advanced Ceramics*, 2013, **2**, P. 135.
- [54] Kumar M., Yadav K.I. Study of Dielectric, Magnetic, Ferroelectric and Magnetolectric Properties in the PbMn<sub>x</sub>Ti<sub>1-x</sub>O<sub>3</sub> system at Room Temperature. *Journal of Physics:Condensed Matter*, 2007, **19**, P. 242202.
- [55] Uniyal P., Yadav K.I. Room Temperature Multiferroic Properties of Eu doped BiFeO<sub>3</sub>. *Journal of Applied Physics*, 2009, **105**, P. 07D914.
- [56] Singh H., Yadav K.L. Effect of Nb Substitution on the Structural, Dielectric and Magnetic Properties of Multiferroic BiFe<sub>1-x</sub>Nb<sub>x</sub>O<sub>3</sub> ceramics. *Materials Chemistry and Physics*, 2012, **17**, P. 132.
- [57] Chaudhari Y.A., Singh A., et al. Multiferroic Properties in BiFe<sub>1-x</sub>Zn<sub>x</sub>O<sub>3</sub> ( $x = 0.1-0.2$ ) Ceramics by solution combustion Method (SCM). *Journal of Alloys and compounds*, 2008, **518**, P. 51.
- [58] Tripathy S.N., Pradhan D.K., et al. Phase Transition and Enhanced Magneto-Dielectric Response in BiFeO<sub>3</sub>-DyMnO<sub>3</sub> Multiferroics. *Journal of Applied Physics*, 2015, **117**, Article ID: 144103.
- [59] Jo S.H., Lee S.G., Lee S.H. Structural and pyroelectric properties of solgel derived multiferroic BFO thin films. *Material Research Bulletin*, 2012, **47** (2), P. 409–412.
- [60] Makhdoom A.R., Akhtar M.J., Rafiq M.A., Hassan M.M. Investigation of transport behavior in Ba doped BiFeO<sub>3</sub>. *Ceramics International*, 2012, **38**, P. 3829–3834.

## Resonant dielectric waveguide-based nanostructure for efficient interaction with color centers in nanodiamonds

O. N. Sergaeva, I. A. Volkov, R. S. Savelev

ITMO University, St. Petersburg 197101, Russia

r.savelev@metalab.ifmo.ru

PACS 42.25.Fx, 42.79.-e, 42.82.Gw

DOI 10.17586/2220-8054-2019-10-3-266-272

Diamond nanoparticles containing single color centers are considered to be one of the most promising realizations of the sources of single photons required for many potential applications in quantum telecommunication and quantum computing systems. Their implementation in practical schemes, however, requires a sufficient increase in their brightness, including the enhancement of both emission and collection efficiency. In this work, we propose a design of a compact planar structure composed of a dielectric periodic cavity coupled with a strip waveguide that is particularly suitable for improving optical characteristics of color centers embedded in a nanodiamond placed inside the structure. We numerically demonstrate that such scheme permits the achievement of simultaneous increase of emission rate of color centers by  $\approx 50$  times in a spectral range  $\approx 2$  nm, and up to  $\approx 85\%$  out-coupling efficiency of emission to the dielectric strip waveguides. We analyze the main factors that decrease the performance of the proposed arrangement and discuss the possible ways for restoring it.

**Keywords:** nanodiamonds, color centers, dielectric cavity, Purcell effect, zero-phonon-line emission.

*Received: 9 May 2019*

Color centers in diamonds are recognized as one of the most propitious platforms for development of single photon sources [1,2], for creating nanoscale sensors [3], for magnetometry [4,5], and thermometry [6,7] due to the possibility of their manipulation at room temperature and quite long electronic spin coherence times. The main problem that prevents their implementation in practical schemes is their relatively low brightness, i.e., the number of photons that a defect emits in a certain period of time, and that can be further collected, is relatively small [2].

The brightness of a source is determined by several factors: its luminescence rate, emission collection efficiency, internal quantum efficiency of the source and radiative efficiency of the surrounding environment. Moreover, creation of coherent sources of indistinguishable single photons based on color centers for quantum applications requires them to emit predominantly into the zero phonon line (ZPL), while, for instance, for negatively charged NV centers at room temperature about 96% of the energy is emitted through the phonon side-band [1]. Some other types of color centers, e.g., SiV<sup>-</sup> defects, exhibit much higher fraction of ZPL emission, however, they suffer from low internal quantum efficiency [1, 8]. Another essential problem is the efficient collection of the luminescence. For instance, the fraction of emission from color centers in bulk diamond or diamond films that can be detected by a confocal microscope is limited by only several percents due to high refractive index contrast between the diamond and vacuum. Emission from color centers in nanodiamonds does not suffer from such a problem, but being dipole-like in nature, it slightly differs from the isotropic one. Consequently, the development of optical devices based on color centers requires a sufficient increase of their brightness, which implies the increase of both emission rate and collection efficiency.

Conventionally, the emission rate of color centers can be enhanced by exploiting the Purcell effect, which manifests itself as a modification of emission properties, when an emitter is placed in the vicinity of a cavity with a resonant frequency that coincides with the ZPL of the color center [9]. High emission rate is usually achieved either by using plasmonic cavities that are characterized by ultrasmall mode volume, or dielectric cavities that can be designed to have very large quality factors ( $Q$ -factors) [10]. In the plasmonic structures [11–13], the strength of the Purcell effect, however, substantially depends on the position of the emitter, and strong Ohmic losses in metals may result in low radiation efficiency. Therefore, most of the studies are focused on coupling color centers to dielectric cavities, which can be divided into two main groups based on the type of the considered geometry.

The first one relies on color centers embedded in bulk diamond or diamond films. A scenario of their interaction with dielectric cavities is realized by fabrication of the resonant structures from the diamond itself [14–19]. Although such an approach allows for the control over the orientation of the color center symmetry axis, it is not very common, because fabrication of high-quality diamond nanostructures presents major technological difficulties [9, 14].

In this study, we focus on the second type of diamond-based sources in the form of small diamond nanoparticles with the size of several tens of nanometers containing single or multiple defects. Such nanoparticles can be experimentally tested after the fabrication, and then the ones with the desired properties (e.g., containing a single defect

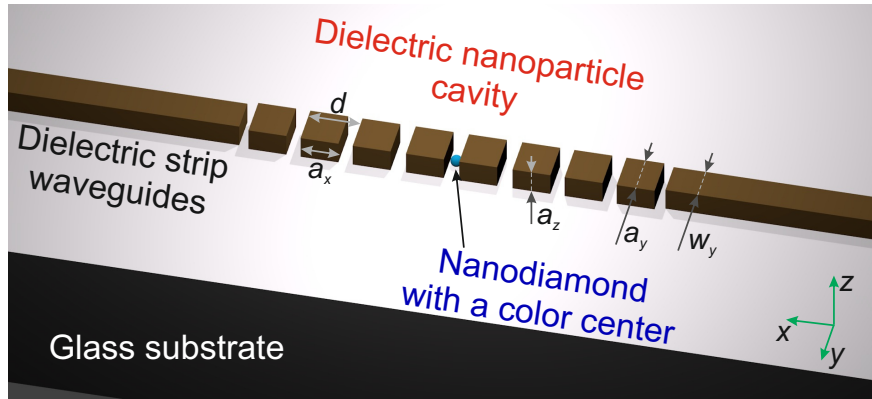


FIG. 1. (a) Scheme of the considered structure: a diamond nanoparticle with an embedded color center is placed in the middle of the cavity formed by dielectric particles with high refractive index. The single-mode homogeneous dielectric waveguides butt-coupled to the cavity serve as channels for efficient photon extraction. Parameters of the system are given in the text

with high quantum efficiency and absence of photo-bleaching) can be placed at the appropriate position using different techniques [11, 13, 20–22], usually by a pick-and-place method with atom-force microscopy tip. Coupling of an emitter in a diamond nanoparticle to a dielectric cavity is usually achieved by placing it on the surface of a dielectric cavity [20, 21, 23–26]. In this case, however, the interaction occurs only via evanescent tails of the cavity field, which is far from ideal, because the electric field in dielectric cavities is typically concentrated inside the dielectric material. Therefore, one of the specific problems is to design a proper cavity that will ensure its efficient interaction with a color center embedded in a nanodiamond located in such structure [27].

Another important problem is the efficient collection of the emission from the color centers. Typically, in experiments the emission is collected by using far-field optical microscopes. While this might be a convenient approach for the experiments in a laboratory, for the practical advancement in the scalable photonic and quantum integrated circuits, the more favorable scheme is the coupling of the emission into a mode of a planar single-mode ridge/strip waveguide or a nanowire [28–30]. However, coupling of a defect in a nanodiamond directly to the homogeneous dielectric waveguide or optical fiber is also a quite inefficient process, because similarly to dielectric cavities, coupling occurs only through the evanescent field of a guided mode [22, 31–34].

The approach, exploited in this study, is based on the use of periodic waveguides with high local density of optical guided modes, which provides a substantial increase in the rate of emission that is directed into the waveguide modes. Namely, we consider a system composed of a waveguide-type cavity made of high-refractive-index nanoparticles butt-coupled to a single mode homogeneous optical waveguide (see Fig. 1), that allows improvement of both the ZPL emission rate and the collection efficiency of the emission from the color center in a nanodiamond at the same time. First, we calculate the properties of the designed cavity, then we analyze its coupling with single-mode homogeneous strip waveguide, and after that we discuss the main issues that deteriorate the performance of considered structure and suggest different modifications that can partially restore it.

The designed cavity operates on the quasi-dark mode of the subwavelength array of mutually coupled magnetic dipole resonances of single dielectric nanoparticles with high refractive index [35, 36]. Interaction of a dipole emitter with such cavity is similar to the interaction with photonic-crystal waveguides and is based on the excitation of the slow light guided modes of a periodic system, i.e. modes which are characterized with a group velocity that tends to zero at the edge of the Brillouin zone and, consequently, a high density of optical states [37]. Photonic crystal waveguides, however, exhibit maximum field distribution of the guided mode inside the dielectric layer [38], which is the reason why such structures work well for emitters embedded inside the waveguide slab [19, 39]. In contrast, the cavity suggested in this work, interacts efficiently with emitters placed in the gap between the dielectric particles. This can be seen from the calculated dispersion of the infinite periodic system along with the field distribution of the corresponding mode, shown in Fig. 2(a-c) for the following parameters of the system: dimensions of the particles  $a_x = 160$  nm,  $a_y = 180$  nm,  $a_z = 100$  nm, material of the particles is lossless dielectric with  $\varepsilon = 14$ , period of the structure  $d = 225$  nm, and the refractive index of the substrate is  $n = 1.45$ . All numerical simulations were performed in a commercial software Computer Simulation Technology (CST). Fig. 2(a) shows that the dispersion of the fundamental waveguide mode is characterized by zero group velocity and, consequently, with the Purcell factor (PF) that diverges near the frequency  $\approx 410$  THz. Calculation of the PF, defined as the emission rate of a point-like

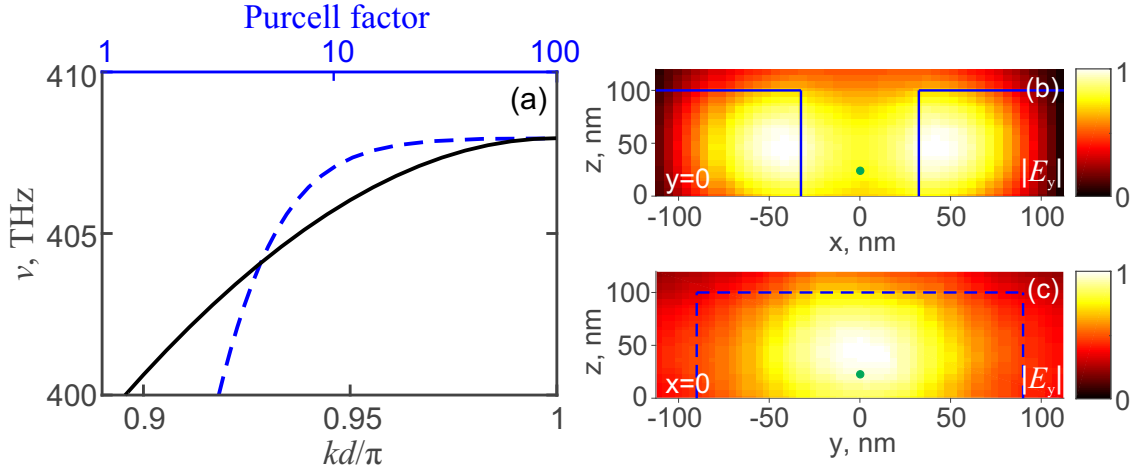


FIG. 2. (a) Dispersion diagram of an infinite periodic (in  $x$  direction) chain of cubic nanoparticles (bottom horizontal axis) and Purcell factor (PF) (top horizontal axis in logarithmic scale) calculated for the source placed in the infinite periodic system at the point shown with a green circle in (b,c);  $k$  is the Bloch wavenumber,  $d$  is the period of the array. (b,c) Distribution of the  $y$ -component of electric field in the single unit cell for the eigenmode at the edge of the Brillouin zone in the plane (b)  $x = 0$ , (c)  $z = 0$ . Blue lines indicate the position of the dielectric nanoparticles. Geometrical parameters of the system are given in the text

dipole normalized by the emission rate of the same source in vacuum, was performed based on the eigenmode field distribution [37], assuming that a dipole is placed exactly in the middle of the gap between the particles at the distance of 25 nm above the substrate and its orientation coincides with the orientation of the electric field of the excited mode. From Figs. 2(b,c) we can notice that the interaction of the electric dipole source with such waveguide mode is strong when it is placed between the two central particles. Since the gap between the particles in our calculations was equal to 65 nm, the arrangement is particularly suitable for placing a nanodiamond with a size of 30-50 nm in it.

Further, we calculate the properties of the finite-size structure, shown in Fig. 1. In order to extract the radiation from such a cavity it was butt-coupled to homogeneous strip waveguides with the same height  $a_z = 100$  nm and different width  $w_y = 130$  nm and made from the same material as the nanoparticles. The size of a homogeneous waveguide was chosen so that the propagation constant of its mode coincides with the propagation constant of the periodic waveguide-cavity. In calculations we assume that an electric dipole source is oriented in  $y$  direction and located in the center of spherical diamond nanoparticle (refractive index  $n = 2.4$ ) with radius  $r_{ND} = 25$  nm, which is, in turn, placed on the substrate between the two middle particles.

The distribution of the power flow in the investigated structure is schematically shown in Fig. 3(a). In the absence of material losses, the main characteristics are determined by the  $\beta$ -factor, defined as the power emitted into the modes of the strip waveguides  $P_{WG}$  normalized by the total power emitted by the source  $P_{tot} = P_{WG} + P_{fs}$  (where  $P_{fs}$  is the power emitted into free space or substrate), and by the PF, defined here as the power emitted by the point dipole in the structure  $P_{tot}$  divided by the power emitted by the same source in the nanodiamond in vacuum  $P_0$ . Such characteristics calculated for the system with 24 particles are presented in Fig. 3(b,c) with solid black curves, respectively. The arrangement allows for almost 40-fold enhancement of the power emitted by the source, while at the same time almost 90% of this power is directed into the modes of the strip waveguides. The quality factor of the structure consisting of 24 particles was  $\approx 300$ , with the linewidth  $\approx 2$  nm. At low temperature, the ZPL of color centers can be very narrow (close to the transform-limited line), and the interaction strength can be further increased by implementing a composition of larger number of particles and consequently higher  $Q$ -factor. The parameters of the considered structure were tuned in such a way that the finite size system exhibits a resonance at the wavelength  $\approx 737$  nm, which corresponds to the ZPL of the  $\text{SiV}^-$  color centers in diamond [8]. However, we emphasize that the proposed dielectric structure can be easily tuned to the desired wavelength by adjusting the geometrical parameters. An example of the scheme designed for the  $\text{NV}^-$  centers is considered further.

In the basic symmetric arrangement in Fig. 1 photons are emitted in both directions. A unidirectional emission can be straightforwardly achieved by placing a Bragg mirror on one of the sides of the structure. The Bragg reflector consisted of 10 particles (in order to ensure the sufficient reflection coefficient) with adjusted width  $a_y$ . Since the Bloch wavelength of the periodic waveguide is close to  $2d$ , the reflected wave should be almost in-phase with the emitted

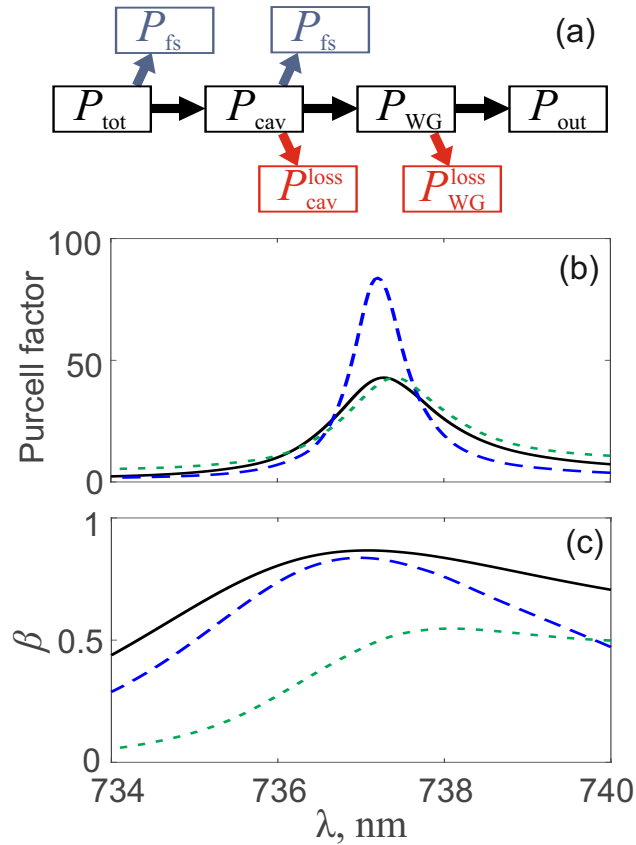


FIG. 3. (a) Power flow distribution in the considered system. (b) Purcell factor and (c)  $\beta$ -factor calculated for the finite structure shown in Fig. 1 made of material with permittivity  $\varepsilon = 14$ . Solid black curve corresponds to the symmetric arrangement, long-dashed blue curves correspond to the design with Bragg reflector put on one of the sides of the structure, and short-dashed green curves – to the system composed of two structures rotated by  $\pi/2$  angle in the plane of substrate with respect to each other. Geometrical parameters of the structure are given in the text

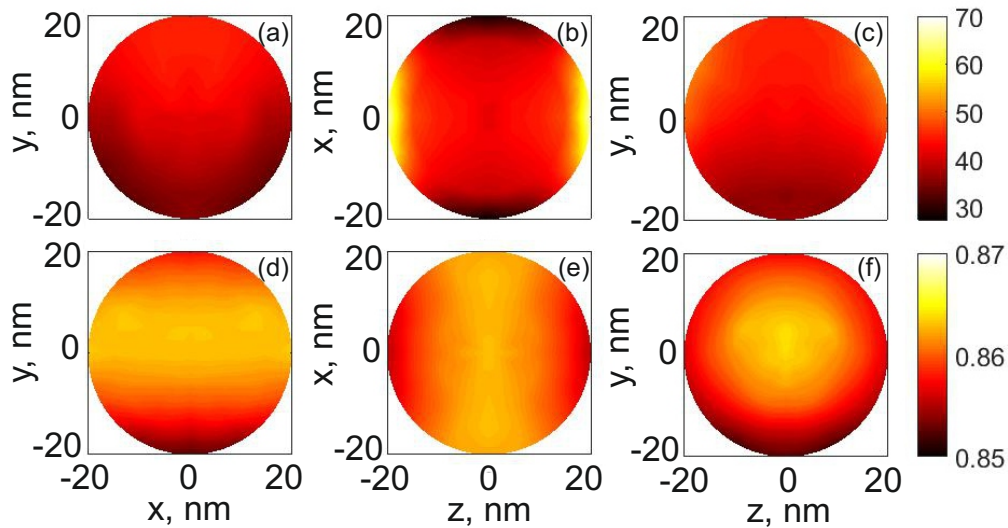


FIG. 4. (a-c) Purcell factor and (d-f)  $\beta$ -factor calculated for different positions of the dipole source within the nanodiamond in (a,d)  $x = 0$  plane, (b,e)  $y = 0$  plane, (c,f)  $z = 0$  plane

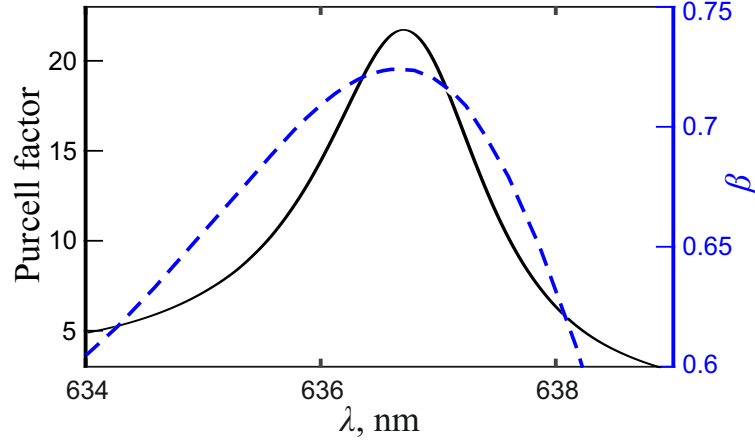


FIG. 5. Purcell factor (left vertical axis) and  $\beta$ -factor (right vertical axis) for the structure shown in Fig. 1 made of gallium phosphide with real part of permittivity  $\varepsilon = 10.95$  and zero imaginary part; other parameters are given in the text. The operational wavelength of the structure matches the ZPL transition of  $\text{NV}^-$  color centers  $\approx 637$  nm

one, regardless of the number of particles in the cavity. The calculated PF and  $\beta$  factor for the system with reflector, shown in Fig. 3(b,c) with dashed blue curves, confirm this: the power emitted by the source has almost doubled, while approximately the same fraction  $\approx 85\%$  is channeled into one remaining strip waveguide. This can be potentially beneficial for the development of scalable quantum optical circuits with different elements connected via single-mode dielectric strip waveguides. The extraction of propagating photons from the nanowaveguide with high efficiency can be achieved by well-established methods of far-field [40] or nanowaveguide/fiber [41] grating out-coupling.

There are several main factors that can substantially affect the performance of considered structure, including position of the source, orientation of its dipole moment, and material losses in dielectric. One of the essential issues is related to the orientation of the dipole source. In fact, the designed system works well only for the  $y$ -oriented source. Therefore, if, for example, the symmetry axis of the  $\text{NV}^-$  center in a nanodiamond placed inside the structure happens to be oriented along the  $y$  direction, its dipole moment can be oriented either along  $x$  or along  $z$  direction. Consequently, the coupling of such source to the cavity mode vanishes. In order to overcome this problem, we consider a “2D” structure, that is composed of two considered “1D” structures shown in Fig. 1, one of which is rotated by 90 degrees in  $x - y$  plane, thus achieving identical performance characteristics for arbitrary orientation of a dipole source in the plane of the substrate. Because the gap between the particles is small as compared to their width, four central particles become noticeably overlapped with each other, which leads to overall decreased performance of the structure. In order to restore approximately the same value of  $Q$ -factor and PF as for the “1D” structure, we have increased the number of particles in the system to 36 and have slightly adjusted the four central particles by changing  $a_x$  from 160 to 150 nm. The results of calculations show that such “2D” structure with 36 particles maintains the same  $Q$ -factor and PF as “1D” structure [see black solid and green dashed curves in Fig. 3(b)]. Although the  $\beta$ -factor has dropped down to  $\approx 50\%$  [green dashed curves in Fig. 3(c)], in this geometry all characteristics remain the same for any orientation of the dipole source in  $x - y$  plane.

Further, we consider the effect of small deviations of the position of the source on the emission and extraction efficiency. The change in the PF is determined mainly by the interaction with the cavity mode, in which strength is proportional to the electric field intensity at the point of the source location. According to eigenmode calculations shown in Fig. 2(b,c), the dependence is quite weak. We have confirmed this by performing the exact numerical calculations for the finite system. Colormaps plotted in Figs. 4(a-c) show the values of PF for different positions of the color center at the distances up to 20 nm from the center of the nanodiamond in  $x - y$  and  $x - z$  and  $y - z$  planes. The variation of PF is observed only in the range from  $\approx 30 - 60$ , which shows that for almost arbitrary position of a defect in a nanodiamond the emission rate remains as high as in the center.

The similar maps in Figs. 4(d-f) show the dependence of  $\beta$ -factor on the position of the dipole source. Since in the absence of losses in the system  $\beta$ -factor is determined as  $\beta = P_{\text{WG}} / (P_{\text{fs}} + P_{\text{WG}})$  (see Fig. 3(a)), it can be modified in two ways. First, the decrease (increase) of PF reduces (enhances) the  $\beta$ -factor directly. And, second, the increase of  $P_{\text{FS}}$ , which occurs when the dipole source gets closer to the substrate [42], also reduces  $\beta$ -factor. The combination of these two factors gives the result shown in Figs. 4(d-f). Overall, we can expect approximately the same characteristics of the system (PF and  $\beta$ -factor) for almost arbitrary position of the color center in the small nanodiamond (40–50 nm).

We stress here that because the optical size of a nanodiamond is much smaller than the wavelength, its form and size also do not noticeably affect emission properties [27, 43]. We also note, that further tolerance to the position of the emitter can be achieved by designing a similar structure with smaller height  $a_z$ . Our calculations show (not presented here) that e.g. for  $a_z = 50$  nm field distribution in the gap between the particles becomes even more homogeneous, and, consequently, dependence of emission properties on the position becomes even more negligible.

Finally, we consider the effect of material losses in the system. For instance, crystalline silicon, the most exploited material with high refractive index at visible frequency range, has an imaginary part of permittivity of about 0.065 at the wavelength  $\lambda \approx 737$  nm [44]. Our calculations revealed that taking into account the material losses in silicon results in following changes. The  $Q$ -factor of the resonance and, consequently, the PF and  $P_{\text{tot}}$  are reduced by  $\approx 3$  times and the fraction of power lost in the cavity  $P_{\text{cav}}^{\text{loss}}/P_{\text{cav}}$  [see Fig. 3(a)] reaches almost 60%. Moreover, the total radiation efficiency also depends on the losses in the strip waveguides  $P_{\text{WG}}^{\text{loss}}$ , which grow with the increase of the length of the waveguide. E.g. for the  $4\mu\text{m}$ -size waveguides we have estimated the radiative PF ( $P_{\text{out}}/P_0$ ) to be only  $\approx 10$ , while the  $\beta$ -factor (which is defined as  $P_{\text{out}}/P_{\text{tot}}$  for the system with losses) dropped down to 10%. For color centers with ZPL at lower wavelengths radiation efficiency is expected to be even lower due to higher losses in silicon.

This problem can be overcome by using different materials with lower losses. E.g. gallium phosphide with refractive index  $n \approx 3.5$  or materials with lower refractive index, such as  $\text{TiO}_2$  or  $\text{SiN}$  [45]. To illustrate the possibility of engineering structures tuned at different operational frequencies and fabricated from different materials, we have developed a similar system made from GaP, that is suitable for operation with NV color centers with ZPL at  $\approx 637$  nm. The numerical simulation results, shown in Fig. 5 demonstrate, that it is indeed possible to have similar values of PF and  $\beta$  for considered structure. In this case the radiation efficiency of this composition is limited only by the internal quantum efficiency of the color center, which in the case of the nanodiamond, can be estimated before the placement in the nanostructure.

In summary, we have proposed a design of a dielectric structure composed of a nanoparticle waveguide-cavity butt-coupled to dielectric strip waveguide for efficient interaction with the color centers embedded in small nanodiamonds with linear size up to  $\approx 50$  nm. We have studied numerically optical properties of considered arrangement and have shown that it allows one to increase the emission rate of color centers by several orders of magnitude in  $\approx 2$  nm spectral range and at the same time to provide out-coupling of emission to planar strip waveguide with up to 85% efficiency. We have shown that tuning of the system can be realized in a straight-forward way by adjusting the geometrical parameters of nanostructures, which makes them a promising platform for creating bright single photon sources based on nanodiamonds containing color centers for quantum optical integrated circuits.

## Acknowledgements

This work was supported by the Russian Science Foundation Grant No. 17-72-10280. Authors would like to acknowledge D. Zuev and I. Shadrivov for fruitful discussions.

## References

- [1] Aharonovich I., Castelletto S., Simpson D.A., Su C.-H., Greentree A.D., Prawer S. Diamond-based single-photon emitters. *Reports on Progress in Physics*, 2011, **74**, P. 076501.
- [2] Aharonovich I., Englund D., Toth M. Solid-state single-photon emitters. *Nature Photonics*, 2016, **10**, P. 631–641.
- [3] Schirhagl R., Chang K., Loretz M., Degen C.L. Nitrogen-Vacancy Centers in Diamond: Nanoscale Sensors for Physics and Biology. *Annual Review of Physical Chemistry*, 2014, **65**, P. 83–105.
- [4] Maze J.R., Stanwix P.L., Hodges J.S., Hong S., Taylor J.M., Cappellaro P., Jiang L., Gurudev Dutt M.V., Togan E., Zibrov A.S., et al. Nanoscale magnetic sensing with an individual electronic spin in diamond. *Nature*, 2008, **455**, P. 644–647.
- [5] Hong S., Grinolds M.S., Pham L.M., Le Sage D., Luan L., Walsworth R.L., Yacoby A. Nanoscale magnetometry with NV centers in diamond. *MRS Bulletin*, 2013, **38**, P. 155–161.
- [6] Kucsko G., Maurer P., Yao N.Y., Kubo M., Noh H., Lo P., Park H., Lukin M.D. Nanometre-scale thermometry in a living cell. *Nature* 2013, **500**, P. 54–58.
- [7] Toyli D.M., de las Casas C.F., Christle D.J., Dobrovitski V.V., Awschalom D.D. Fluorescence thermometry enhanced by the quantum coherence of single spins in diamond. *Proceedings of the National Academy of Sciences*, 2013, **110**, P. 8417–8421.
- [8] Neu E., Hepp C., Hauschild M., Gsell S., Fischer M., Sternschulte H., Steinmüller-Nethl D., Schreck M., Becher C. Low-temperature investigations of single silicon vacancy colour centres in diamond. *New Journal of Physics*, 2013, **5**, P. 043005.
- [9] Aharonovich I., Greentree A.D., Prawer S. Diamond photonics. *Nature Photonics*, 2011, **5**, P. 397–405.
- [10] Pelton M. Modified spontaneous emission in nanophotonic structures. *Nature Photonics*, 2015, **9**, P. 427.
- [11] Schietinger S., Barth M., Aichele T., Benson O. Plasmon-Enhanced Single Photon Emission from a Nanoassembled Metal-Diamond Hybrid Structure at Room Temperature. *Nano Letters*, 2009, **9**, P. 1694–1698.
- [12] Andersen S.K., Kumar S., Bozhevolnyi S.I. Ultrabright Linearly Polarized Photon Generation from a Nitrogen Vacancy Center in a Nanocube Dimer Antenna. *Nano Letters*, 2017, **17**, P. 3889–3895.
- [13] Siampour H., Kumar S., Davydov V.A., Kulikova L.F., Agafonov V.N., Bozhevolnyi S.I. On-chip excitation of single germanium vacancies in nanodiamonds embedded in plasmonic waveguides. *Light: Science & Applications*, 2018, **7**, P. 397–405.

- [14] Bayn I., Meyler B., Lahav A., Salzman J., Kalish R., Fairchild B.A., Praver S., Barth M., Benson O., Wolf T., et al. Processing of photonic crystal nanocavity for quantum information in diamond. *Diamond and Related Materials*, 2011, **20**, P. 937–943.
- [15] Faraon A., Barclay P.E., Santori C., Fu K.-M.C., Beausoleil R.G. Resonant enhancement of the zero-phonon emission from a colour centre in a diamond cavity. *Nature Photonics*, 2011, **5**, P. 301–305.
- [16] Riedrich-Möller J., Kipfstuhl L., Hepp C., Neu E., Pauly C., Mücklich F., Baur A., Wandt M., Wolff S., Fischer M., et al. One- and two-dimensional photonic crystal microcavities in single crystal diamond. *Nature Nanotechnology*, 2012, **7**, P. 69–74.
- [17] Faraon A., Santori C., Huang Z., Acosta V.M., Beausoleil R.G. Coupling of Nitrogen-Vacancy Centers to Photonic Crystal Cavities in Monocrystalline Diamond. *Phys. Rev. Lett.*, 2012, **109**, P. 033604.
- [18] Evans R.E., Sipahigil A., Sukachev D.D., Zibrov A.S., Lukin M.D. Narrow-Linewidth Homogeneous Optical Emitters in Diamond Nanostructures via Silicon Ion Implantation. *Phys. Rev. Applied*, 2016, **5**, P. 044010.
- [19] Sipahigil A., Evans R.E., Sukachev D.D., Burek M.J., Borregaard J., Bhaskar M.K., Nguyen C.T., Pacheco J.L., Atikian H.A., Meuwly C., et al. An integrated diamond nanophotonics platform for quantum-optical networks. *Science*, 2016, **354**, P. 847–850.
- [20] Gregor M., Henze R., Schröder T., Benson O. On-demand positioning of a preselected quantum emitter on a fiber-coupled toroidal microresonator. *Applied Physics Letters*, 2009, **95**, P. 153110.
- [21] Wolters J., Schell A.W., Kewes G., Nüsse N., Schoengen M., Döschner H., Hannappel T., Löchel B., Barth M., Benson O. Enhancement of the zero phonon line emission from a single nitrogen vacancy center in a nanodiamond via coupling to a photonic crystal cavity. *Applied Physics Letters*, 2010, **97**, P. 141108.
- [22] Liebermeister L., Petersen F., Münchow A.V., Burchardt D., Hermelbracht J., Tashima T., Schell A.W., Benson O., Meinhardt T., Krueger A., et al. Tapered fiber coupling of single photons emitted by a deterministically positioned single nitrogen vacancy center. *Applied Physics Letters*, 2014, **104**, P. 031101.
- [23] van der Sar T., Heeres E.C., Dmochowski G.M., de Lange G., Robledo L., Oosterkamp T.H., Hanson R. Nanopositioning of a diamond nanocrystal containing a single nitrogen-vacancy defect center. *Applied Physics Letters*, 2009, **94**, P. 173104.
- [24] Barclay P.E., Santori C., Fu K.-M., Beausoleil R.G., Painter O. Coherent interference effects in a nano-assembled diamond NV center cavity-QED system. *Opt. Express*, 2009, **17**, P. 8081–8197.
- [25] Englund D., Shields B., Rivoire K., Hatami F., Vučković J., Park H., Lukin M.D. Deterministic Coupling of a Single Nitrogen Vacancy Center to a Photonic Crystal Cavity. *Nano Letters*, 2010, **10**, P. 3922–3926.
- [26] Gould M., Schmidgall E.R., Dadgostar S., Hatami F., Fu K.-M.C. Efficient Extraction of Zero-Phonon-Line Photons from Single Nitrogen-Vacancy Centers in an Integrated GaP-on-Diamond Platform. *Phys. Rev. Applied*, 2016, **6**, P. 011001.
- [27] Alagappan G., Krivitsky L.A., Png C.E. Diamond in a Nanopocket: A New Route to a Strong Purcell Effect. *ACS Omega*, 2018, **3**, P. 4733–4742.
- [28] Silverstone J.W., Bonneau D., Ohira K., Suzuki N., Yoshida H., Iizuka N., Ezaki M., Natarajan C.M., Tanner M.G., Hadfield R.H., et al. On-chip quantum interference between silicon photon-pair sources. *Nature Photonics*, 2014, **8**, P. 104–108.
- [29] Lodahl P., Mahmoodian S., Stobbe S. Interfacing single photons and single quantum dots with photonic nanostructures. *Reviews of Modern Physics*, 2015, **87**, P. 347–400.
- [30] Johnson S., Dolan P.R., Smith J.M. Diamond photonics for distributed quantum networks. *Progress in Quantum Electronics*, 2017, **55**, P. 129–165.
- [31] Fu K.-M.C., Santori C., Barclay P.E., Aharonovich I., Praver S., Meyer N., Holm A.M., Beausoleil R.G. Coupling of nitrogen-vacancy centers in diamond to a GaP waveguide. *Applied Physics Letters*, 2008, **93**, P. 234107.
- [32] Schröder T., Fujiwara M., Noda T., Zhao H.-Q., Benson O., Takeuchi S. A nanodiamond-tapered fiber system with high single-mode coupling efficiency. *Opt. Express*, 2012, **20**, P. 10490–10497.
- [33] Liebermeister L. *Photonic Waveguides Evanescently Coupled with Single NV-centers*. Fakultät für Physik der Ludwig-Maximilians-Universität München, 2015.
- [34] Fujiwara M., Neitzke O., Schröder T., Schell A.W., Wolters J., Zheng J., Mouradian S., Almqvist M., Takeuchi S., Englund D., et al. Fiber-Coupled Diamond Micro-Waveguides toward an Efficient Quantum Interface for Spin Defect Centers. *ACS Omega*, 2017, **2**, P. 7194–7202.
- [35] Krasnok A., Glybovski S., Petrov M., Makarov S., Savelev R., Belov P., Simovski C., Kivshar Y. Demonstration of the enhanced Purcell factor in all-dielectric structures. *Applied Physics Letters*, 2016, **108**, P. 211105.
- [36] Savelev R.S., Sergaeva O.N., Baranov D.G., Krasnok A.E., Alù A. Dynamically reconfigurable metal-semiconductor Yagi-Uda nanoantenna. *Phys. Rev. B*, 2017, **95**, P. 235409.
- [37] Yao P., Manga Rao V., Hughes S. On-chip single photon sources using planar photonic crystals and single quantum dots. *Laser & Photonics Reviews*, 2010, **4**, P. 499–516.
- [38] Javadi A., Mahmoodian S., Söllner I., Lodahl P. Numerical modeling of the coupling efficiency of single quantum emitters in photonic-crystal waveguides. *J. Opt. Soc. Am. B*, 2018, **35**, P. 514–522.
- [39] Arcari M., Söllner I., Javadi A., Lindskov Hansen S., Mahmoodian S., Liu J., Thyrrstrup H., Lee E.H., Song J.D., Stobbe S., et al. Near-Unity Coupling Efficiency of a Quantum Emitter to a Photonic Crystal Waveguide. *Phys. Rev. Lett.*, 2014, **113**, P. 093603.
- [40] Wang Y., Wang X., Flueckiger J., Yun H., Shi W., Bojko R., Jaeger N.A.F., Chrostowski L. Focusing sub-wavelength grating couplers with low back reflections for rapid prototyping of silicon photonic circuits. *Opt. Express*, 2014, **22**, P. 20652–20662.
- [41] Zhu L., Yang W., Chang-Hasnain C. Very high efficiency optical coupler for silicon nanophotonic waveguide and single mode optical fiber. *Opt. Express*, 2017, **25**, P. 18462–18473.
- [42] Novotny L., Hecht B. *Principles of Nano-optics*. Cambridge University Press, New York, 2006.
- [43] Rogobete L., Schniepp H., Sandoghdar V., Henkel C. Spontaneous emission in nanoscopic dielectric particles. *Opt. Lett.*, **2003**, **28**, P. 1736–1738.
- [44] Green M.A. Self-consistent optical parameters of intrinsic silicon at 300K including temperature coefficients. *Solar Energy Materials and Solar Cells*, 2008, **92**, P. 1305–1310.
- [45] Baranov D.G., Zuev D.A., Lepeshov S.I., Kotov O.V., Krasnok A.E., Evlyukhin A.B., Chichkov B.N. All-dielectric nanophotonics: the quest for better materials and fabrication techniques. *Optica*, 2017, **4**, P. 814–825.

## A theoretical study of the propagation of light soliton produced by semiconductor quantum dots through optical fibers

O. P. Swami<sup>1</sup>, V. Kumar<sup>2</sup>, B. Suthar<sup>3</sup>, A. K. Nagar<sup>2</sup>

<sup>1</sup>Department of Physics, Government College, Loonkaransar, Bikaner, Rajasthan, 334001, India

<sup>2</sup>Department of Physics, Government Dungar College, Bikaner, Rajasthan, 334001, India

<sup>3</sup>Department of Physics, MLB Government College, Nokha, Bikaner, Rajasthan, 334803, India

omg1789@gmail.com, vijendrasaini2009@gmail.com, bhuvneshwer@gmail.com, ajaya.nagar@gmail.com

PACS 42.65.-k, 42.65.Tg, 78.67.Hc

DOI 10.17586/2220-8054-2019-10-3-273-281

In this paper, the propagation of light soliton is studied in nonlinear optical fiber. We propose the external excitation of semiconductor quantum dot (SQD) waveguides through an optical source which allows the generation of solitonic pulses. These solitonic pulses are propagated through a nonlinear optical fiber. Soliton formation is investigated by the interaction between the external optical excitation and SQDs. Here, the SQDs are considered as a quantum system of three energy levels. In this study, the Fourier Split-Step (FSS) method is used to solve the numerically continuous nonlinear Schrödinger equation (NLSE) for evolution of the soliton pulse emitted by the SQDs inside an optical fiber with real physical parameters. The effect of a SQD's density and electric field on the pulse width is also studied. Phase plane portraits are drawn to observe the stability of soliton in fiber and SQDs.

**Keywords:** quantum dots, nonlinear optics, optical solitons, nonlinear guided waves.

*Received: 13 March 2019*

*Revised: 1 April 2019*

*Final revision: 10 May 2019*

### 1. Introduction

Semiconductor quantum dots (SQDs) are model systems for investigating nonlinear light-matter interaction that have attracted much interest. SQDs are referred to zero-dimensional systems that restrict the movement of charge carriers in the three spatial dimensions, which results in atom-like discrete energy spectra and strongly enhanced carrier lifetimes [1]. These atoms like structures have been proposed for the use as qubits in quantum information processing [2] as well as for laser devices [3]. Some of the most recent investigations indicate that these types of heterostructures can undergo abrupt changes in the spectral response with minimal variations in their size and morphology, offering important applications for optics, among which are next-generation lasers, diodes, light emitters, optical multiplexers, biosensors, spectral tuners, quantum computing, logic gates, among others [4–12]. Due to their large dipole moments, reaching values on the order of  $10^{-17}$  esu cm [13], the interaction between SQDs and optical light fields is strongly enhanced in comparison with atomic systems, making them good candidates for the study of nonlinear optical propagation effects. Recently, it has become possible to combine nanostructures with other polymeric materials such as optical fibers, giving rise to nanocomposites, which are generally composed of several phases such as SiO<sub>2</sub>, where one or more of its dimensions are found at the nanoscale [14–22]. The optical fibers are important elements for the propagation of light wave signals with water and for the propagation of electromagnetic waves in the visible, ultraviolet and infrared range. In an optical fiber, it is necessary to consider a theory of wave propagation in dispersive media. The nonlinear Schrödinger equation (NLSE) gives a complete description of a variety of the localized non-linear effects that have been extensively studied in various contexts of the sciences and that the theory can directly link with the propagation of intense optical pulses in non-linear optical fibers that give rise to the optical solitons. Although there are many experimental advances in the propagation of solitons in optical fibers, in practice, the propagation of solitary pulses across large distances at a commercial level has not been possible due to the different technical functions [23–26]. The study allows us to propose a general model which permits the coupling of solitons from a set of quantum dots with specific characteristics in an optical fiber that has non-linear optical characteristics. As a result, a numerical simulation is developed to study the evolution of the soliton inside a non-linear optical fiber with the Fourier Split-Step numerical technique with the real parameters associated with the SQD and the optical fiber. The effect of soliton density and electric field on the full width at half maximum (FWHM) of re-emitted solitonic pulse is studied. Phase planes represent the stability/instability of solitons.

2. Theoretical analysis

SQDs can confine the movement of charge carriers in all dimensions due to their zero dimensional nanosized structures, which exhibits a discrete energy system. We consider a two-dimensional sheet of inhomogeneously broadened SQDs which forms a transition layer on one of the surfaces of the planar waveguide. The waveguide soliton satisfies the Maxwell–Bloch equations with nonlinear boundary conditions. The purpose of the present article is to theoretically investigate the formation processes of optical solitons under the condition of SIT in a semiconductor waveguide.

A SQD of three-level energy system is considered, whose ground state is  $|\psi_1\rangle$  and has energy  $\varepsilon_{\psi_1} = 0$ . The states  $|\psi_2\rangle$  and  $|\psi_3\rangle$  have energies  $\varepsilon_{\psi_2} = h\nu_0 = \varepsilon_x + \frac{\delta_x}{2}$  and  $\varepsilon_{\psi_3} = h\nu'_0 = 2\varepsilon_x - \delta_{xx}$ , respectively. Where the quantities  $\varepsilon_x = (\varepsilon_{\psi_2} + \varepsilon'_{\psi_2})/2$  and  $\varepsilon_{\psi_3}$  describe the energies of the single-excitonic and biexcitonic states, respectively.

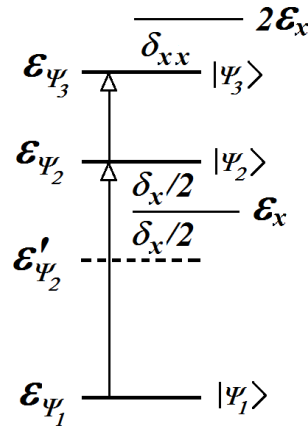


FIG. 1. Schematic diagram of energy structures of semiconductor quantum dots

The energy of exciton fine structure splitting is denoted by  $\delta_x = \varepsilon_{\psi_2} - \varepsilon'_{\psi_2}$  and biexciton binding energy is denoted by  $\delta_{xx}$ .  $h$  is Planck constant. The Hamiltonian of system is described by:

$$H = H_0 + H'_0, \tag{1}$$

where  $H_0 = h\nu_0|\psi_2\rangle\langle\psi_2| + \frac{1}{2}h\nu'_0|\psi_3\rangle\langle\psi_3|$  is called the Hamiltonian of single excitonic state  $|\psi_2\rangle$  and biexcitonic state  $|\psi_3\rangle$ . The additional term  $H'_0$  in the Hamiltonian is present due to the interaction of the light pulse with SQDs and  $H'_0 = -\vec{P} \cdot \vec{E}$ . During the excitation of the SQDs, an external light source is considered, composed of a linearly-polarized, high intensity optical wave from a laser and we will study the formation of non-linear optical waves that are re-emitted by the SQDs. Fig. 2 represents a schematic of a linearly-polarized plane wave incident on SQDs. In the process, due to the interaction of the light with the SQDs, the light is re-emitted in the form of a non-linear wave with special characteristics that will depend on the morphology of the quantum dot and the incident wave.

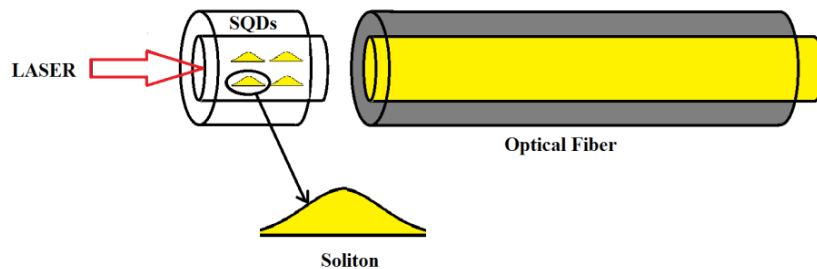


FIG. 2. Schematic arrangement of SQDs and optical fiber with an external light source

In the analytical treatment the electric field vector of incident light beam is taken as below:

$$\vec{E}(z, t) = \sum_{l=\pm 1} \vec{e}_l \hat{E}_l \varphi_l, \quad (2)$$

where:

$$\vec{e} = \frac{1}{\sqrt{2}} (\vec{x} + i\vec{y}), \quad (3)$$

is the complex polarization vector.  $\vec{x}$  and  $\vec{y}$  are unit vector along the  $x$  and  $y$  axes.  $\varphi_l = e^{il(kz-v_l t)}$  is a periodic wave function and  $\hat{E}$  is the slowly changing amplitude of the electric field. The incident light is considered linearly-polarized in TE mode and has a width  $T$  and angular frequency  $\omega \gg T^{-1}$  propagating along  $z$  direction. When an external light beam interacts with SQDs, then a secondary dipolar field is produced in same direction as incident field and can be written as:

$$-c^2 \frac{\partial^2 \vec{E}(z, t)}{\partial z^2} + \eta^2 \frac{\partial^2 \vec{E}(z, t)}{\partial t^2} = -4\pi \frac{\partial^2 \vec{P}(z, t)}{\partial t^2}, \quad (4)$$

where the polarization component of ensemble of SQDs is the following:

$$\vec{P}(z, t) = \frac{1}{2} n_0 \int g(v_{01}) \vec{e} (\mu_{12} \rho_{21} + \mu_{23} \rho_{32})(v, z, t) dv + c.c., \quad (5)$$

which is determined by the interband transitions occurring in the quantum dots between the three energy levels. The quantities  $\mu_{12}$  and  $\mu_{23}$  are the dipole moments for the corresponding transitions which we assume to be parallel to each other.  $g(v_{01})$  is an inhomogeneous broadening function which arises due to the quantum dot size fluctuations. Because the energy levels depend on the size of dots, the exciton frequency  $\nu_0$  and detuning quantity  $\nu_{01} = \nu_0 - \nu_1$  are also size dependent.  $\eta$  is the refractive index of semiconductor and  $n_0$  is the density of Quantum Dots.  $\rho_{ij}$  are the matrix elements of the density matrix and  $\rho$  can be determined from Liouville equation:

$$i\hbar \dot{\rho}_{mn} = \sum (\langle n|H|l\rangle \rho_{lm} - \rho_{nl} \langle l|H|m\rangle), \quad (6)$$

where  $n, m, l = 1, 2, 3$ .

The density matrix of the pulse is considered of the form:

$$\rho_{21} = \hat{\rho}_{21} \varphi_3, \quad \rho_{32} = \hat{\rho}_{32} \varphi_1, \quad \rho_{31} = \hat{\rho}_{31} \varphi_2, \quad (7)$$

where  $\hat{\rho}_{nm}$  is the slowly varying complex amplitudes of the elements of density matrix.  $\varphi_{1,2,3}$  is taken in for envelope function. To guarantee that  $E$  is a real number we choose slow envelope approach, it is considered that amplitude  $\hat{E}_l$  of pulse is very smooth in space and time and can be written as:

$$\left| \frac{\partial \hat{E}_l}{\partial t} \right| \ll \nu_l |\hat{E}_l|, \quad (8)$$

and

$$\left| \frac{\partial \hat{E}_l}{\partial z} \right| \ll k |\hat{E}_l|, \quad (9)$$

then nonlinear carrier wave equation can be written as following form:

$$\sum_{l=\pm 1} \varphi_l \left[ l^2 (c^2 k^2 - \eta^2 \nu_l^2) \hat{E}_l - 2iklc^2 \frac{\partial \hat{E}_l}{\partial z} - 2il\eta^2 \nu_l \frac{\partial \hat{E}_l}{\partial t} \right] = -2\pi l^2 \nu_l^2 n_0 [\mu_{12} \hat{\rho}_{21} + \mu_{23} \hat{\rho}_{32}] e^{i(kx - \nu_l t)} + c.c. \quad (10)$$

The diagonal elements  $\rho_{12}$ ,  $\rho_{22}$  and  $\rho_{33}$  give rise to the populations in the states  $|\psi_1\rangle$ ,  $|\psi_2\rangle$  and  $|\psi_3\rangle$  respectively. Non-diagonal elements  $\rho_{mn} (n \neq m)$  contain the relative phase between the states that describe the atomic coherence. In the absence of phase modulation  $\hat{E}_l = \hat{E}_{-l} = \hat{E}_l^* = \hat{E}$ . Therefore, the system of equations for the slowly varying amplitudes:

$$\begin{aligned} i\hbar \dot{\rho}_{11} &= (\hat{\rho}_{21}^* - \hat{\rho}_{21}) \mu_{12} \hat{E}, \\ i\hbar \dot{\rho}_{22} &= (\hat{\rho}_{21} - \hat{\rho}_{21}^* + \delta \hat{\rho}_{32}^* - \delta \hat{\rho}_{32}) \mu_{12} \hat{E}, \\ i\hbar \dot{\rho}_{33} &= (\hat{\rho}_{32} - \hat{\rho}_{32}^*) \mu_{12} \hat{E}, \\ i\hbar \dot{\rho}_{21} &= h(\nu_0 - \nu) \hat{\rho}_{21} - [(\hat{\rho}_{11} - \hat{\rho}_{22}) + \delta \hat{\rho}_{31}] \mu_{12} \hat{E}, \\ i\hbar \dot{\rho}_{32} &= h(\nu_0^l - \nu_0 - \nu) \hat{\rho}_{32} + [\delta(\hat{\rho}_{33} - \hat{\rho}_{22}) + \hat{\rho}_{31}] \mu_{12} \hat{E}, \\ i\hbar \dot{\rho}_{31} &= h(\nu_0^l - 2\nu) \hat{\rho}_{31} + [\hat{\rho}_{32} - \delta \hat{\rho}_{21}] \mu_{12} \hat{E}. \end{aligned} \quad (11)$$

In the above equations, the rotating wave approximation has been applied and  $\delta = \frac{\mu_{23}}{\mu_{12}}$ . The solution of the system of equations (11), allows the calculation of the elements of the right side of equation (10). As the diagonal elements of matrix give rise to the populations in the states, for ground state  $\rho_{11} = 1$ ,  $\rho_{11} = 0$  and  $\rho_{33} = 0$ , the equations (11) take the form:

$$\begin{aligned}\hat{\rho}_{21} &= \frac{i}{2d^3} (\sin 2Ad + 2\delta^2 \sin Ad), \\ \hat{\rho}_{32} &= \frac{i\delta}{2d^3} (\sin 2Ad - 2\sin Ad),\end{aligned}\quad (12)$$

where  $d = \sqrt{(1 + \delta^2)}$  and  $A = \frac{2\pi\mu_{12}}{h} \int_{-\infty}^t E(z, t) dt$ , which is called the area of nonlinear optical pulse.

Applying the dispersion law for linear wave guide modes, wave equation (4) will take following form:

$$(2\psi)_{tt} + \frac{c}{\eta}(2\psi)_{zt} + \frac{2\pi^2\nu\mu_{12}^2n_0}{h\eta^2} \sin(2\psi) = 0, \quad (13)$$

where

$$\psi = Ad. \quad (14)$$

Equation (13) can be written in the form of electric field as below:

$$\left(\frac{d\hat{E}}{d\xi}\right) = \frac{\hat{E}^2}{T^2} - \frac{\pi^2\mu_{12}^2\hat{E}^4}{h^2}, \quad (15)$$

with  $\xi = t - \frac{z}{V}$  and constant phase velocity  $V$ . The solution of equation (15) for the envelope function has the form:

$$\hat{E} = \frac{h}{\sqrt{2\pi\mu_{12}T}} \operatorname{sech} h \left(\frac{\xi}{T}\right), \quad (16)$$

which is well-known solitonic solution, with width of the pulse remitted by SQD:

$$T = \sqrt{\frac{h\eta^2}{4\pi^2\nu n_0\mu_{12}^2} \left(\frac{c - \eta V}{\eta V}\right)}. \quad (17)$$

These soliton became stable when the speed of light (phase velocity) in SQD media  $c/\eta$  remains greater than the phase velocity  $V$ .

### 3. Result and discussion

The theoretical result of wave equation (4) is presented as a soliton. In other words, the excitation of SQDs from an intense nonlinear wave can produce optical solitons as a result of light-SQDs interaction. During the nonlinear interaction process, the SQDs are considered as a three-level energy quantum system, in which the optical transitions are given from the ground state to the biexcitonic and excitonic states. The allowed transitions between the ground state to the biexcitonic and excitonic states have very low dipole moment compared to the transition between the ground state and the background of the exciton band. On the other hand, the characteristics of the light re-emitted by the sheets of quantum dots in the form of optical solitons depend on the intensity of the incident light, whose minimum value to form the optical solitons can be specifically determined depending on the nature of the SQDs. In this way, the soliton remitted will depend on the refractive index of the semiconductor  $\eta$ , the dipole moment corresponding to the transitions between the ground state and the excitonic state or between the biexcitonic state and the excitonic state  $\mu_{12}$ . In order to study the propagation of short optical pulses through nonlinear optical fibers, the non-linear Schrodinger equation (NLSE) is used, which takes into account the effects of the length of the fiber, the dispersion effect of group speed and non-linear optical effects as a consequence of the high intensity of light. The Fourier Split-Step method is a pseudo-spectral technique that is extremely useful due to its rapidity and high accuracy in calculations. In general, this method obtains an approximate solution of the propagation equation, assuming that dispersion effects and non-linear effects act independently along the fiber in very small steps. This technique was used to simulate the evolution of solitons that are re-emitted by the SQD.

In the results, it is observed that as the density of SQD increases, the peak intensity also increases. Because as the number of QDs per unit volume increases, absorption will also increase. Therefore the intensity of re-emitted beam will increase. Due to this the pulse width (FWHM) will also decrease. Same concept is applies for electric field verses FWHM. In the mathematical modelling of proposed work, the interactions of QDs in the Hamiltonian are omitted. For the simulation, we have proposed SQDs with pyramidal morphology of In as manufactured with a cylindrical symmetry with the parameters  $\eta = 2.11$ ,  $\mu_{12} = 1.92 \times 10^{-28}$  C·m and  $V = 1.37 \times 10^8$  m/s.

Figures 3(a–d) represent the simulation of solitons created by SQDs arrays with different densities of SQDs according to following table. It is clear from equation (17) that the pulse width decreases as  $n_0$  increases. In many optical fiber communications systems, FWHM is required 1 ps or below, which can be achieved by increasing the density of SQDs. Simulated data are summarized in Table 1.

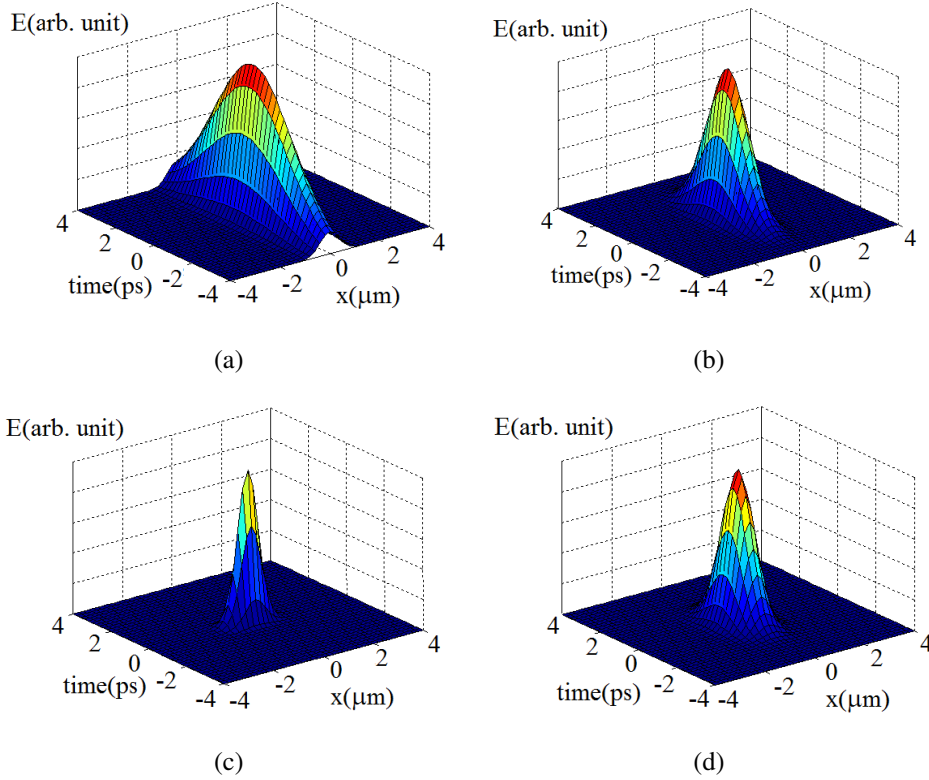


FIG. 3. Simulation of soliton generated by SQDs system with different densities of QDs.(a)  $n_0 = 2.59 \times 10^{12} \text{ cm}^{-3}$ ; (b)  $n_0 = 8.00 \times 10^{12} \text{ cm}^{-3}$ ; (c)  $n_0 = 23.35 \times 10^{12} \text{ cm}^{-3}$  and (d)  $n_0 = 99.12 \times 10^{12} \text{ cm}^{-3}$

TABLE 1. Relation between the density of SQDs and FWHM of solitons

S.No.	Density of SQD( $10^{12} \text{ cm}^{-3}$ )	FWHM(ps)
1.	2.59	6.18
2.	8.00	3.52
3.	23.35	2.06
4.	99.12	1.00

Figures 4(a–d) represent that the soliton width as determined from equation (16) is decreased as electric field  $E$  is increased. According to Table 2, it is clear that when the amplitude of the electric field is increased, then the FWHM of TM mode of wave decreases, which is a basic requirements for many optical fiber communications systems.

Figures 5(a–d) represent the evolution of soliton profiles in SQDs for different values of refractive index of material of SQDs as taking  $V = 1.37 \times 10^8 \text{ m/s}$ .

Figures 6(a–d) represent the phase plane portraits for Figs. 5(a–d) respectively for stability analysis. Closed limit cycles of phase plane structures clearly indicate a stable soliton, while spiral-like phase plane structures indicate an unstable soliton. It is clear from below Table 3 that as  $c/\eta$  become less than  $V$ , the soliton become unstable, which is summarised in Table 3.

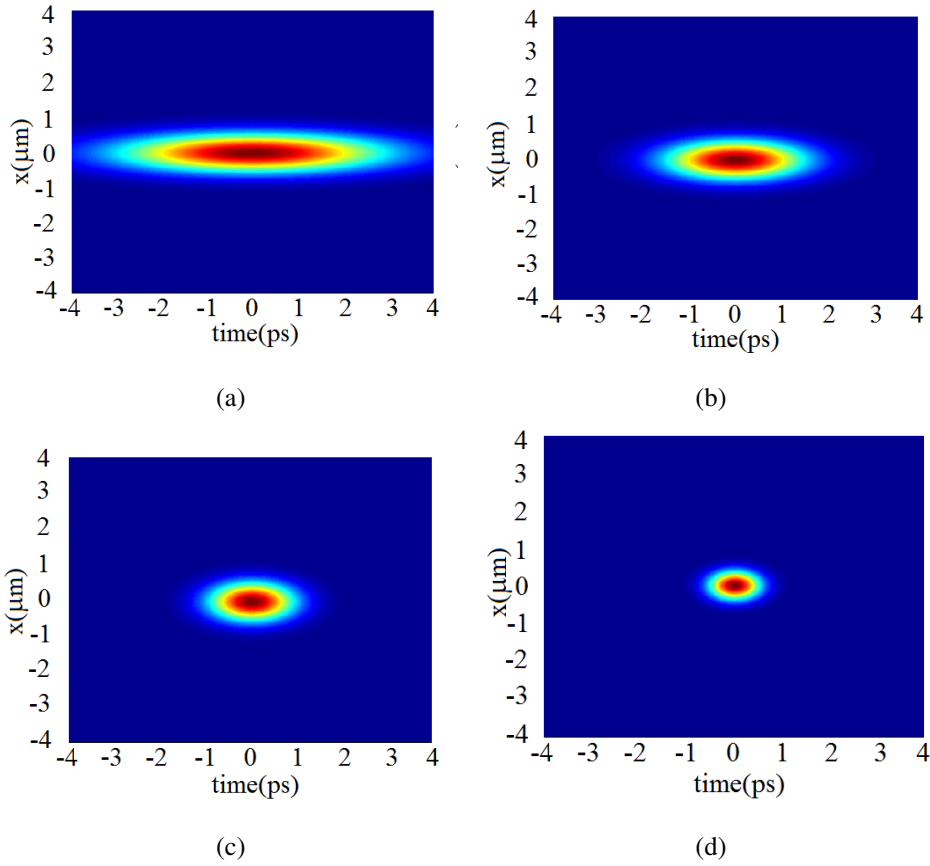


FIG. 4. Transverse view of soliton in SQD with electric field (a)  $E = 0.96 \times 10^8$  V/m; (b)  $E = 1.73 \times 10^8$  V/m; (c)  $E = 2.86 \times 10^8$  V/m and (d)  $E = 6.00 \times 10^8$  V/m

TABLE 2. Relation between the amplitude of Electric field and FWHM of TM mode of solitons

S.No.	Amplitude of electric field( $10^8$ V/m)	FWHM(ps)
1.	0.96	6.26
2.	1.73	3.46
3.	2.86	2.10
4.	6.00	1.00

TABLE 3. Relation between refractive index of material of SQDs and (in)stability of soliton

S. No.	Refractive index( $\eta$ ) of SQDs	$c/\eta$ (m/s)	Nature of soliton
1	2.05	$1.46 \times 10^8$	Stable
2	2.11	$1.42 \times 10^8$	Stable
3	2.40	$1.25 \times 10^8$	Unstable
4	3.50	$0.86 \times 10^8$	Unstable

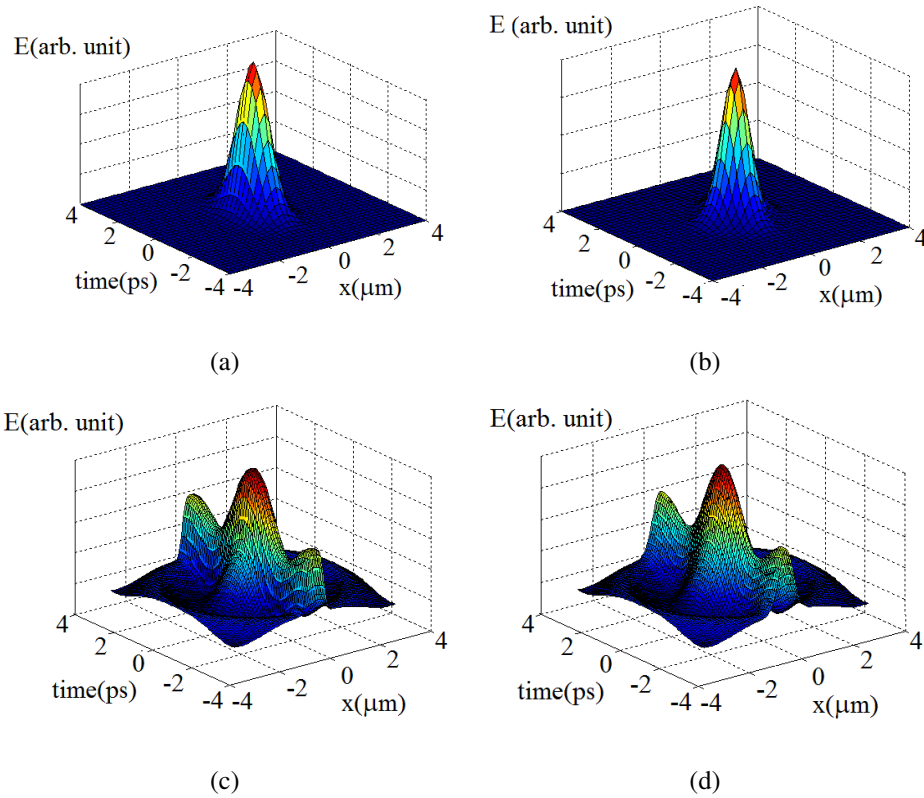


FIG. 5. Simulation of soliton generated by SQDs system with different refractive indices of QDs. (a) 2.05; (b) 2.11; (c) 2.40 and (d) 3.50 taking  $V = 1.37 \times 10^8$  m/s

Figure 7(a) represents the soliton profiles for input pulse in optical fiber and the Fig. 7(b) represents the pulse in optical fiber after travelling the distance of  $z = 1000$  m. Simulations are made using split-step Fourier method with the parameters: nonlinear fiber parameter  $\gamma = 0.32$  W/m, fiber attenuation constant  $\alpha = 0.2$  dB/km and second order dispersion coefficient  $\beta = -2 \times 10^{-26}$  s<sup>2</sup>/m.

#### 4. Conclusions

In this paper, we have investigated the formation of optical solitonic pulses in three level semiconductor quantum dots embedded in nonlinear optical fibers for propagation of fields without losses over long distances. Light solitons are produced in semiconductor quantum dots by the interaction of laser field with SQDs. The FWHM of solitonic pulses can be modulated according to densities of SQDs and field intensity. If the density of SQD is increased, the peak intensity is also increased. Because as the number of QDs per unit volume is increased, absorption will also be increased. Therefore the intensity of re-emitted beam will be increased. Due to this, the pulse width (FWHM) will also be decreased. The same concept is applied for electric field versus FWHM. The stability/instability of generated solitons is dependent on the refractive indices of SQDs material. Likewise, it is proposed the manufacture of these types of nanostructures with different morphologies inserted in optical fibers that allow the propagation of solitons without losses over the long distances.

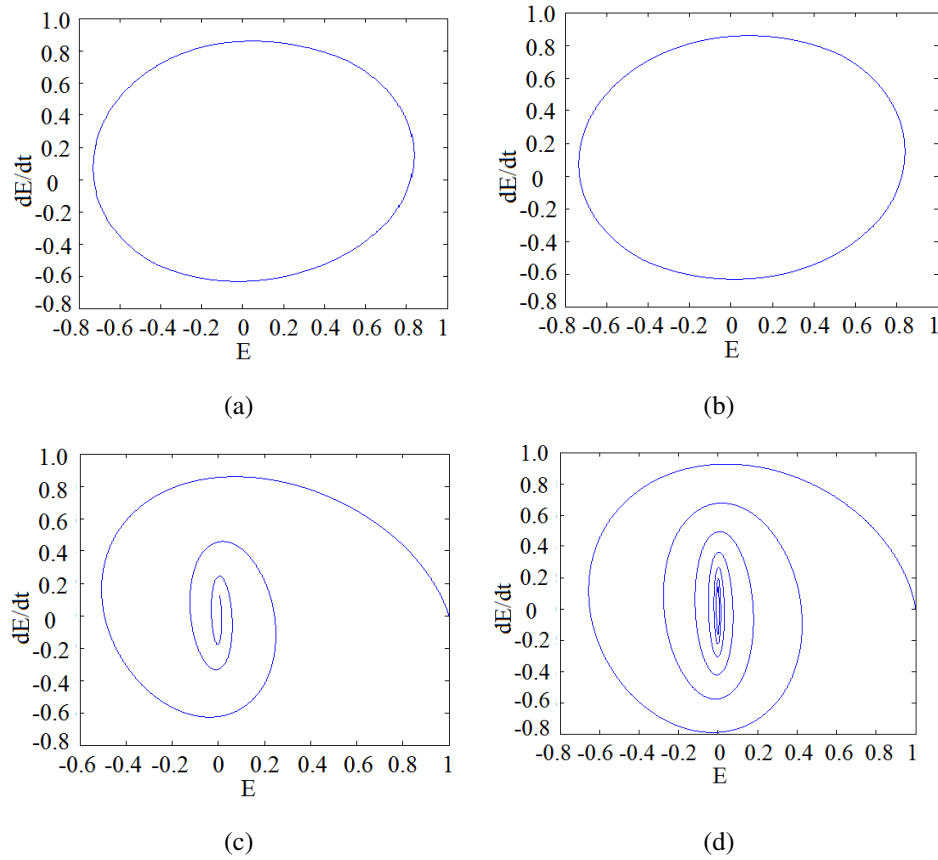


FIG. 6. Phase plane portraits for solitons for different refractive indices of QDs.(a) 2.05; (b) 2.11; (c) 2.40 and (d) 3.50 taking  $V = 1.37 \times 10^8$  m/s

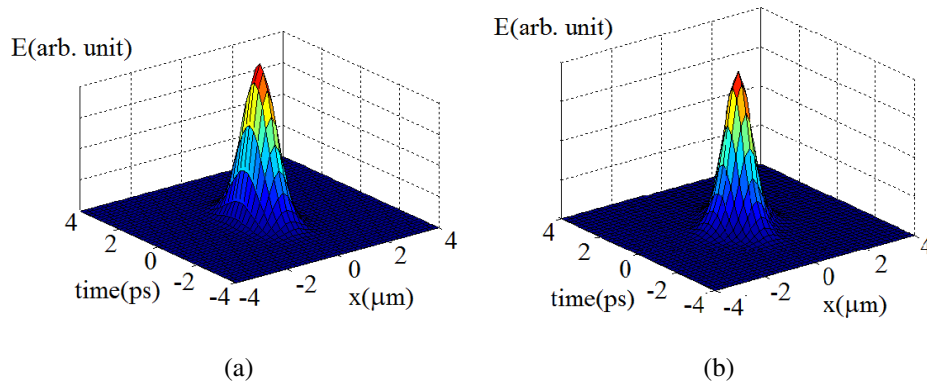


FIG. 7. Evolution of soliton through nonlinear optical fiber at (a)  $z = 0$  m and (b)  $z = 1000$  m

## References

- [1] Pavese L., Dal Negro L., et al. Optical gain in silicon nanocrystals. *Nature*, 2000, **408**, P. 440–444.
- [2] Hu Y.M., Yang W.L., Feng M., Du J.F. Distributed quantum-information processing with fullerene-caged electron spins in distant nanotubes. *Phys. Rev. A*, 2009, **80**, P. 022322(1–13).
- [3] Máximo L., Mendez V.H. Autoensamblado de puntos cúnticos. *Cinvestav*, 2008, **27**, P. 44–49.
- [4] Hanewinkel B., Knorr A., Thomas P., Koch S.W. Optical near-field response of semiconductor quantum dots. *Phys. Rev. B*, 1997, **55**, P. 13715(1–10).
- [5] Akmnanov S.A., Vislough V.A., Chirkin A.S. *Optics of Femtosecond Laser Pulses*. New York, American Institute of Physics, 1992.
- [6] Klimov V.I., Mikhailovsky A.A., et al. Optical gain and stimulated emission in nanocrystal quantum dots. *Science*, 2000, **290**, P. 314–317.
- [7] Yang W.X., Chen A.X., Lee R.K., Wu Y. Matched slow optical soliton pairs via biexciton coherence in quantum dots. *Phys. Rev. A*, 2011, **84**, P. 013835(1–11).

- [8] Hu L., Wu H., et al. The effect of annealing and photoactivation on the optical transitions of band-band and surface trap states of colloidal quantum dots in PMMA. *Nanotechnology*, 2011, **22**, P. 125202(1–8).
- [9] Adamashvili G.T., Weber C., Knorr A. Optical nonlinear waves in semiconductor quantum dots: Solitons and breathers. *Phys. Rev. A*, 2007, **75**, P. 1–9.
- [10] Newell A.C. *Solitons in Mathematics and Physics*. Philadelphia, Society for Industrial and Applied Mathematics, 1985.
- [11] Ajayan P.M., Schadler L.S., Braun P.V. *Nanocomposite science and technology*. Weinheim, Germany, Wiley, 2003.
- [12] Rothenberg J.E., Grischkowsky D., Balant A.C. Observation of the Formation of the  $0\pi$  Pulse. *Phys. Rev. Lett.*, 1984, **53**, P. 552–555.
- [13] Chen M., Kaup D.J., Malomed B.A. Three-wave solitons and continuous waves in media with competing quadratic and cubic nonlinearities. *Phys. Rev. E*, 2004, **69**, P. 056605(1–17).
- [14] Bimberg D., Grundmann M., Ledentsov N.N. *Quantum Dot Heterostructures*. Chichester, Wiley, 1999.
- [15] Schneider S., Borri P., et al. Self-induced transparency in InGaAs quantum-dot waveguides. *Appl. Phys. Lett.*, 2003, **83**, P. 3668–3670.
- [16] Panzarini G., Hohenester U., Molinari E. Self induced transparency in semiconductor quantum dots. *Phys. Rev. B*, 2002, **65**, P. 165322(1–6).
- [17] Klimov V.I. Nanocrystal quantum dots. *Los Alamos Science*, 2003, **28**, P. 214–220.
- [18] Chen Y., Herrnsdorf J., et al. Colloidal quantum dot random laser. *Opt. Express*, 2011, **19**, P. 2996–3003.
- [19] Akhmediev N., Ankiewicz A. *Solitons, Nonlinear pulses and Beams*. London, Chapman and Hall, 1997.
- [20] Kevrekidis P.G., Rasmussen K.O., Bishop A.R. Two-dimensional discrete breathers: Construction, stability, and bifurcations. *Phys. Rev. E*, 2000, **61**, P. 2006(1–7).
- [21] Blum K. *Density Matrix Theory and Applications*, 2nd ed. New York, Plenum Press, 1996.
- [22] Adamashvili G.T., Weber C., Knorr A. Optical solitons in semiconductor Quantum dots. *Eur. Phys. J. D*, 2008, **47**, P. 113–117.
- [23] Malomed B.A., Kevrekidis P.G. Discrete vortex solitons. *Phys. Rev. E*, 2001, **64**, P. 026601(1–6).
- [24] Lamb Jr.G.L. *Elements of soliton theory*. New York, Wiley, 1980.
- [25] Lamb Jr.G.L. *Optical waves in crystals*. New York, Wiley, 1980.
- [26] Oster M., Johansson M. Stable stationary and quasiperiodic discrete vortex breathers with topological charge  $S = 2$ . *Phys. Rev. E*, 2006, **73**, P. 066608(1–6).

## Composite membranes based on geometrically constrained PIM-1 for dehumidification of gas mixtures

E. A. Chernova, I. V. Roslyakov, S. G. Dorofeev, A. V. Lukashin

Lomonosov Moscow State University, Leninskiye Gory, Moscow, 119991, Russia

wellastra@gmail.com, alexey.lukashin@gmail.com

PACS 81.05.Rm, 47.56.+r

DOI 10.17586/2220-8054-2019-10-3-282-288

Composite membranes based on polymer with intrinsic microporosity (PIM-1) confined in the pores of porous anodic alumina (AAO) supports were prepared by spin-coating method under vacuum suction. Water permeance of the membranes was measured at humidities ranging from 10 to 70 %. High permeance towards water vapors reaching the value of  $\sim 13700 \text{ l}/(\text{m}^2 \cdot \text{bar} \cdot \text{h})$  coupled with the  $\text{H}_2\text{O}/\text{N}_2$  selectivity of 1400 was observed at the humidity of 70 % for composite membranes due to the condensation in nanopores of polymer and anodic alumina channels. The obtained selectivity exceeds strongly that of bulk PIM-1 due to confinement of polymer chains mobility in AAO channels. The water vapor sorption capacity for composite membranes exceeds 7 % being governed both by condensation in polymer micropores and anodic alumina channels. Physical ageing of the membranes was monitored for a period of 6 months and then the membranes were subjected to activation in methanol. It was established that physical ageing substantially reduces the water permeance but activation in methanol allows one to partially rejuvenate water transport performance.

**Keywords:** dehumidification, polymer with intrinsic microporosity, geometric confinement, physical ageing.

*Received:* 16 May 2019

*Revised:* 25 May 2019

### 1. Introduction

Dehumidification of gas mixtures is of vital importance in industry, including natural gas purification in the petroleum industry and air conditioning for electronics, food industry and medicine [1]. For this purpose, membrane technology is of great demand, owing to its low cost and high performance [2–4]. Among membrane separation technologies, capillary transport of water vapor appears favorable as providing both high permeance and selectivity due to the blockage of membrane channels by the condensate. Membrane operation in the capillary transport regime has been previously reported for inorganic membranes, including Vycor glass [5], porous anodic alumina [6, 7], graphene oxide [8, 9], as well as microporous polymer membranes with thermodynamic (reverse) selectivity, including polysulfone, sulfonated polyether-etherketon (sPEEK) and poly-trimethylsilylpropyne (PTMSP) [10, 11]. Due to high solubility of water vapors in hydrophilic microporous polymers, it becomes possible to achieve outstanding membrane performance. Among the listed polymers, the highest permeance of 61000 Barrer coupled with high  $\text{H}_2\text{O}/\text{N}_2$  selectivity of  $10^7$  is exhibited by sulfonated polyether-etherketone [12]. On the other hand, polymer membranes are easily degradable due to the plasticization in the presence of water vapor; also, high  $\text{H}_2\text{O}$  sorption capacity usually demands a means of polymer regeneration. Another drawback is the implementation of bulk polymer membranes which are rather expensive. Thus, there is still a need for high-quality mechanically stable membranes for the dehumidification of gases.

A good decision is the design of composite polymer-inorganic membranes where the mechanically-stable highly-permeable support provides the robustness of the membrane, while the polymer thin selective layer provides high performance and selectivity. Recently, we have shown that geometric confinement of polymer chains in a rigid matrix can strongly hinder the transport of permanent gases [13, 14]. As a result, polymers confined in nanochannels illustrate significant reduction of permeance towards permanent gases, whereas the transport characteristics of condensable vapors are preserved due to polymer swelling. The effect enhances polymer selectivity, and is best pronounced for rigid polymers with large Kuhn segment. A good candidate for this purpose is polymer with intrinsic microporosity (PIM-1) with rigid ladder-like macromolecules and the size of Kuhn segment equal to the entire size of the macromolecule. Also, owing to the polar nature of its monomer unit due to the presence of nitrile groups and ether oxygen, PIM-1 exhibits elevated sorption capacity towards water vapor [4].

In the present paper, we apply the concept of geometric confinement to the preparation of PIM-1-based composite membranes for the dehumidification of gases. The composite membranes were obtained by spin-coating onto nanoporous anodic aluminum oxide (AAO) supports, their permeance and sorption capacity towards water vapors was

measured, the evolution of permeance and selectivity was monitored in time and the influence of membrane activation with methanol was tested.

## 2. Experimental section

Anodic alumina films, utilized as membrane supports, were prepared by anodic oxidation of high purity aluminum in 0.3 M oxalic acid at 40 V and in 0.3 M sulfuric acid at 25V. The detailed description of the AAO preparation can be found in [15–17]. Composite membranes were obtained by spin-coating of 1 wt.% polymer solution in chloroform onto AAO supports under vacuum suction. Detailed preparation procedure is described in [15].

The microstructure of AAO supports and composite membranes was studied using SEM Carl Zeiss NVision 40 (5 kV, InLens detector) electron microscope. The homogeneity of PIM-1 layer of composite membranes was examined with luminescence microscopy on Renishaw InVia spectrometer equipped with Leica DMLM optics (50× objective) with 20 mW 514 nm Ar laser excitation. Luminescence intensity distribution maps were acquired in streamline mode with line-focused laser beam (a length of  $\sim 50 \mu\text{m}$  and a thickness below  $1 \mu\text{m}$ ) with point accumulation time of 10 s. The obtained intensity distribution maps were treated in Wire 3.4 Renishaw software.

Sorption capacity towards  $\text{H}_2\text{O}$  for composite membrane PIM-1/AAO-40, AAO-40 membrane and PIM-1 thin film, was measured using quartz microbalance. The outer selective layer of the PIM-1/AAO-40 sample was preliminary removed using wipe with chloroform so that the sample include only geometrically-confined polymer. Then, composite membranes as well as AAO-40 membrane, were grinded into a fine powder and deposited onto both sides of the quartz resonators with the fundamental frequency of 12 MHz. PIM-1 polymer thin film was deposited on the surface of the quartz resonators from 0.05 wt.% solution in chloroform. Typical frequency shift after sample deposition was  $\sim 30$  kHz. The change of frequency of quartz resonators upon sorption of water vapors was calculated as follows:

$$\omega(\text{H}_2\text{O}) = \frac{\Delta f(\text{H}_2\text{O}) - \Delta f_0 - f_0}{\Delta f_0} \cdot 100 \%,$$

where  $\omega(\text{H}_2\text{O})$  – water sorption capacity of the sample, %,  $\Delta f_0$  – frequency shift of quartz resonator with deposited sample at zero humidity, MHz,  $\Delta f(\text{H}_2\text{O})$  – frequency shift of quartz resonator with deposited sample during the sorption of water, MHz.

The permeance of AAO supports and composite membranes was measured in two-compartment cross-flow cell using a permeance setup equipped with SLA5850 mass-flow controllers (Brooks, England), PD-100-DI pressure transducers (OVEN, Russia) and T-Station 75 vacuum system (BOC Edwards, England). The gas scheme of experimental setup has been described recently in [8]. The measurements were performed at ambient temperature ( $22 \pm 2$  °C). The flux and humidity of air was controlled with two mass-flow controllers SLA5850 (Brooks, USA). To control the humidity one of inlet air streams was saturated with water vapor in humidifier by direct air-water contact. Air temperature and humidity on the inlet and outlet of a composite membrane was monitored by HIH-4000 (Honeywell, USA) sensors. Dew point temperature of the outlet air was also determined by a chilled mirror dew-point hygrometer TOROS-3VY (Ukraine). The permeance of water was calculated using the following equation:

$$F = \frac{J(\text{He}) \cdot RH_{out}}{S \cdot P_{sat} \cdot (RH_{in} - RH_{out})},$$

where  $J(\text{He})$  – helium carrier flux,  $RH_{in}$  and  $RH_{out}$  – inlet and outlet relative humidity,  $P_{sat}$  – saturated water vapor pressure at a given temperature (calculation was performed by Antoine Equation with coefficients determined by Stull [18]), and  $S$  – membrane area.

## 3. Results and discussion

According to SEM, the microstructure of the composite membranes comprises a few m-thick dense outer layer and porous AAO support with partly infilled pores (Fig. 1). The thickness of the external polymer selective layer is somewhat lower for PIM-1/AAO-40 membrane which can result from more effective infiltration of macromolecules (Table 1). The inner selective layer is represented by polymer nanofibers formed during infiltration of polymer solution into the AAO channels. The polymer replica obtained from the PIM-1/AAO-40 sample after the dissolution of the AAO support in 0.3 V NaOH, clearly evidences the formation of partly hollow polymer fibers and directly proves the polymer infiltration into the AAO supports.

To prove the uniformity of the polymer selective layers and quantify the amount of polymer in composite membranes, the maps of polymer luminescence intensity were recorded (Fig. 2). As it has been shown recently, the photoluminescence (PL) intensity of thin PIM-1 films can be used as semiquantitative characteristics of PIM-1 content [14].

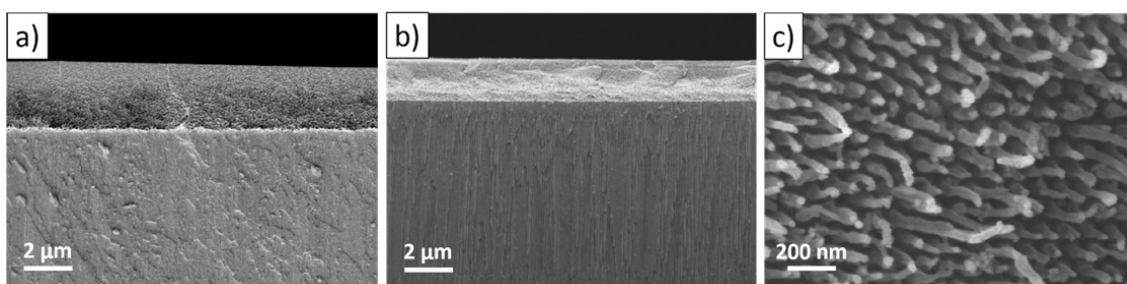


FIG. 1. SEM-images of composite membranes: a) cross-section of PIM-1/AAO-25 membrane; b) cross-section of PIM-1/AAO-40 membrane; c) polymer replica of the selective layer of PIM-1/AAO-40 membrane

TABLE 1. Microstructure characteristics and statistical analysis of luminescence intensity maps for PIM-1-based composite membranes

Sample	Thickness of the external selective layer (SEM), $\mu\text{m}$	Pore diameter of the AAO support, nm	Average PL intensity, $\text{cps}\cdot 10^4$	PL intensity RSD, %	PL intensity interval for $P_{90}$ , $\text{cps}\cdot 10^4$
PIM-1/AAO-25	$2.6 \pm 0.1$	$21 \pm 5$	2.82	10.2	2.44 – 3.41
PIM-1/AAO-40	$2.0 \pm 0.1$	$36 \pm 5$	3.50	5.77	3.16 – 3.81

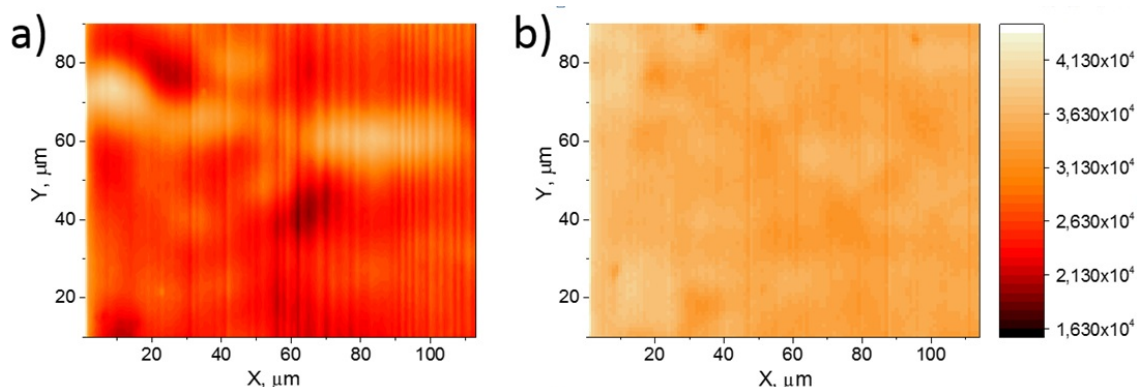


FIG. 2. Luminescence intensity distribution maps for a) PIM-1/AAO-25; b) PIM-1/AAO-40 membranes

According to the obtained results, the luminescence intensity is uniform enough across the whole thickness of the selective coatings indicating polymer macromolecules are homogeneously distributed on the surface of the AAO support. The statistical analysis has shown (Table 1) that the relative standard deviation (RSD) of luminescence intensity along the membrane for PIM-1/AAO-25 sample is nearly 2 times higher than for PIM-1/AAO-40 sample, indicating more uneven distribution of macromolecules in PIM-1/AAO-25 which also can be associated with hindrances of macromolecules incorporation into small-diameter nanochannels. Note that the average luminescence intensity of the PIM-1/AAO-40 sample is greater as compared to the PIM-1/AAO-25 membrane, while the thickness of the external layer for this sample is smaller (see Table 1). This suggests that the greater quantity of the polymer is introduced into AAO under vacuum suction for the substrate with larger diameter of the channels. This stays in line with increasing liquid permeance of AAO membranes with pore diameters [17].

To get detailed understanding of water vapor transport in composite membranes, the sorption capacity of PIM-1/AAO-40 sample as well as anodic alumina AAO-40 and pure PIM-1 thin film was measured as a function of partial water vapor pressure using quartz microbalance method (Fig. 3).

According to the obtained results, all the isotherms include 3 standard regions: the Henry region (up to  $0.3 P_0$ ), the Langmuir region ( $0.3 - 0.6 P_0$ ) and the region of capillary condensation (over  $0.6 P_0$ ).

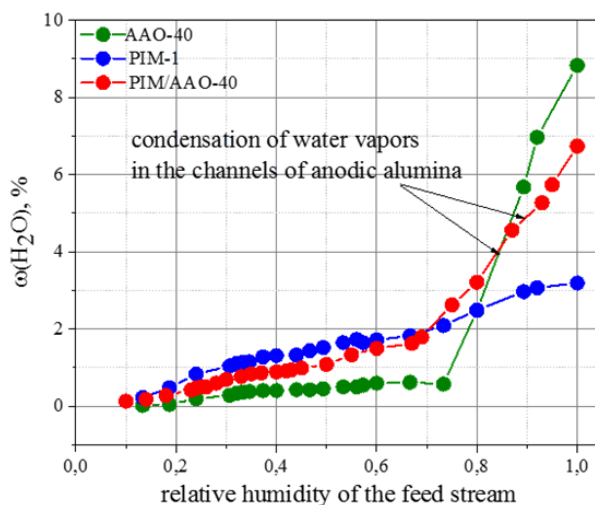


FIG. 3. Sorption isotherms of water vapor on the composite membrane PIM-1/AAO-40, anodic alumina AAO-40 and thin PIM-1 polymer film

A significant increase in sorption capacity of the AAO-40 substrate is observed at the humidity of 75 % which can be attributed to the capillary condensation of water vapor in nanometer-sized channels of the AAO [7, 19, 20]. According to the Kelvin equation, the capillary radius can be estimated as:

$$r = \frac{2\sigma M}{\rho RT \cdot \ln(p_c/p_0)}$$

where  $\sigma$  is the surface tension of liquid water,  $p_c$  and  $p_0$  are the pressure of condensation in the pore with radius  $r$  and the pressure of water vapors condensation on a flat surface, respectively,  $M$  and  $\rho$  are the molecular mass and density of water.

Taking the beginning of the capillary condensation in the AAO-40 film at the relative pressure of  $0.75 P_0$ , the condensation diameter can be estimated as 7.4 nm which differs dramatically from the diameter of AAO channels ( $\sim 35 \pm 5$  nm). The value can be attributed to the presence of small-sized mesopores in AAO walls, accessible to the condensation of water, those were evidenced during examination of thermal properties of AAO membranes [21].

The sample of PIM-1 polymer exhibits maximal sorption capacity of 3.2 % manifesting the filling of polymer free volume elements with water molecules. At  $\sim 0.4 P_0$ , the first kink at the isotherm is observed, corresponding likely to beginning of filling of free-volume elements with water molecules. The average diameter of the microvoids in PIM-1 according to the Kelvin equation was estimated as 4 nm. According to the data obtained from NMR, PALS, and low-temperature nitrogen adsorption, the average diameter of spherical microvoids in PIM-1 polymer ranges from 0.6 to 1 nm [22,23]. The discrepancy in the derived values can be regarded to some variation of the accessible porosity in PIM-1 for water vapors, governed by hydrophilicity of polymer and its local structure [4].

The sorption capacity of PIM-1/AAO-40 sample can be regarded as a result of cooperative sorption in the AAO-40 matrix and the PIM-1 polymer. In the range  $0.1 - 0.7 P_0$  it follows the behavior of the PIM-1 sorption curve, while at  $\sim 0.7 P_0$  the in-channel condensation of water vapors begins. At low humidity range the sorption curve for the PIM-1/AAO-40 is located significantly higher than that for the AAO-40 substrate, suggesting that the sorption of water vapors is provided mainly by the polymer inside the AAO channels. Besides, the condensation in PIM-1/AAO-40 composite membrane begins at lower pressure compared to AAO-40 support which can be attributed to the facilitated condensation in the free volume elements generated by polymer in the AAO pores. Thus, the porosity, available for water condensation in composite membrane inherits both the features of PIM-1 and AAO, while high enough  $H_2O$  vapor sorption capacity allows their application in dehumidification processes.

Figure 4 (a, b) represents the dependencies of water vapor permeance on the humidity of the feed stream for PIM-1/AAO-25 and PIM-1/AAO-40 composite membranes, respectively. An increase in permeance with the elevation of humidity level is observed owing to the growth of the sorption capacity. At a humidity of 70 %, the maximum permeance value of  $19000 \text{ L}/(\text{m}^2 \cdot \text{bar} \cdot \text{h})$  is achieved for the membrane PIM-1/AAO-40 accompanied with the  $H_2O/N_2$  selectivity of 600 (Table 2). The permeance of the PIM-1/AAO-25 composite membrane is lower ( $13700 \text{ L}/(\text{m}^2 \cdot \text{bar} \cdot \text{h})$ ), due to the smaller channels of the AAO-25 support which hinder polymer chains mobility and elevates the vapors flow resistance. This effect allows one to reach greater  $H_2O/N_2$  selectivity for PIM-1/AAO-25 (see Table 2). The maximum

membrane selectivity of 1400 is achieved for the PIM-1/AAO-25 composite membrane at the feed humidity of 70 % which, coupled with the high permeance, is favorable for air dehumidification processes.

According to Fig. 4, the significant reduction of permeance of composite membranes is observed with time which can be attributed to the physical ageing of polymer structure. To quantitatively show the decay of the membrane permeance, the permeance reduction coefficient was calculated  $P^L$  (see Table 2):

$$P^L = \frac{P_{ref} - P_C}{P_{ref}} \cdot 100 \%,$$

where  $P_C$  – the permeance of composite membrane under physical ageing,  $L/(m^2 \cdot \text{bar} \cdot \text{h})$ ,  $P_{ref}$  – the permeance of freshly prepared membrane,  $L/(m^2 \cdot \text{bar} \cdot \text{h})$ .

TABLE 2. The permeance, ideal selectivity and permeance reduction coefficients for the PIM-1-based composite membranes at the feed flow humidity of 70 %

Sample	Permeance, $L/(m^2 \cdot \text{bar} \cdot \text{h})$		Selectivity $H_2O/N_2$	Permeance reduction coefficients at the humidity of 70 %, %
	$H_2O$	$N_2$		
<b>PIM-1, bulk 50 <math>\mu\text{m}</math> [4]</b>	<b>1590</b>	<b>20</b>	<b>80</b>	—
<b>PIM-1/AAO-25</b>	<b>13700</b>	<b>10</b>	<b>1400</b>	—
PIM-1/AAO-25-2m	9700	7	1390	30
PIM-1/AAO-25-6m	3100	4	770	80
PIM-1/AAO-25-6m- $\text{CH}_3\text{OH}$	9970	30	330	30
<b>PIM-1/AAO-40</b>	<b>19000</b>	<b>30</b>	<b>600</b>	—
PIM-1/AAO-40-2m	10100	20	500	50
PIM-1/AAO-40-6m	4020	9	450	80
PIM-1/AAO-40-6m- $\text{CH}_3\text{OH}$	15250	40	400	25

During the first two months of physical ageing, composite membranes lose about 30 – 50 % of the initial permeance, and after 6 months, the permeance reduction achieves  $\sim 80$  % manifesting the significant compaction of selective polymer layers due to the relaxation of macromolecules to thermodynamically stable conformations (Table 2). The accelerated reduction of polymer permeance can be associated with the effect of geometric confinement in the channels of AAO. Nevertheless, the  $H_2O/N_2$  selectivity of physically-aged composite membranes stays nearly at the same level due to the synchronous reduction of polymer permeance towards water vapors as well as  $N_2$ . At the same time, the significant fall in permeance discounts this virtue.

It is well documented that the soaking of microporous polymers in methanol and ethanol can be considered as one of the ways to rejuvenate the polymer permeance [24, 25]. The specific interactions of alcohol molecules with polymer chains leads to the enhancement of local segmental mobility of the macromolecules and the most pronounced effect is observed when methanol is used. In this work, the composite membranes were activated by soaking in pure methanol for a few minutes. According to Fig. 4, the activation in methanol enables one to elevate the membrane permeance, but it does not allow one to reach the initial permeance level of fresh membranes. For activated PIM-1/AAO-25 and PIM-1/AAO-40 composite membranes, the water permeance achieves the values of 80 % of the initial permeances for freshly-prepared membranes. According to [26] and [4], water molecules can form stable water clusters inside the free-volume elements of the polymer which can hardly be removed from the structure. This phenomenon can be considered as one of the key reasons preventing the complete rejuvenation of polymer permeance during activation. Nevertheless, the achieved regeneration values can be considered as high enough for practical applications.

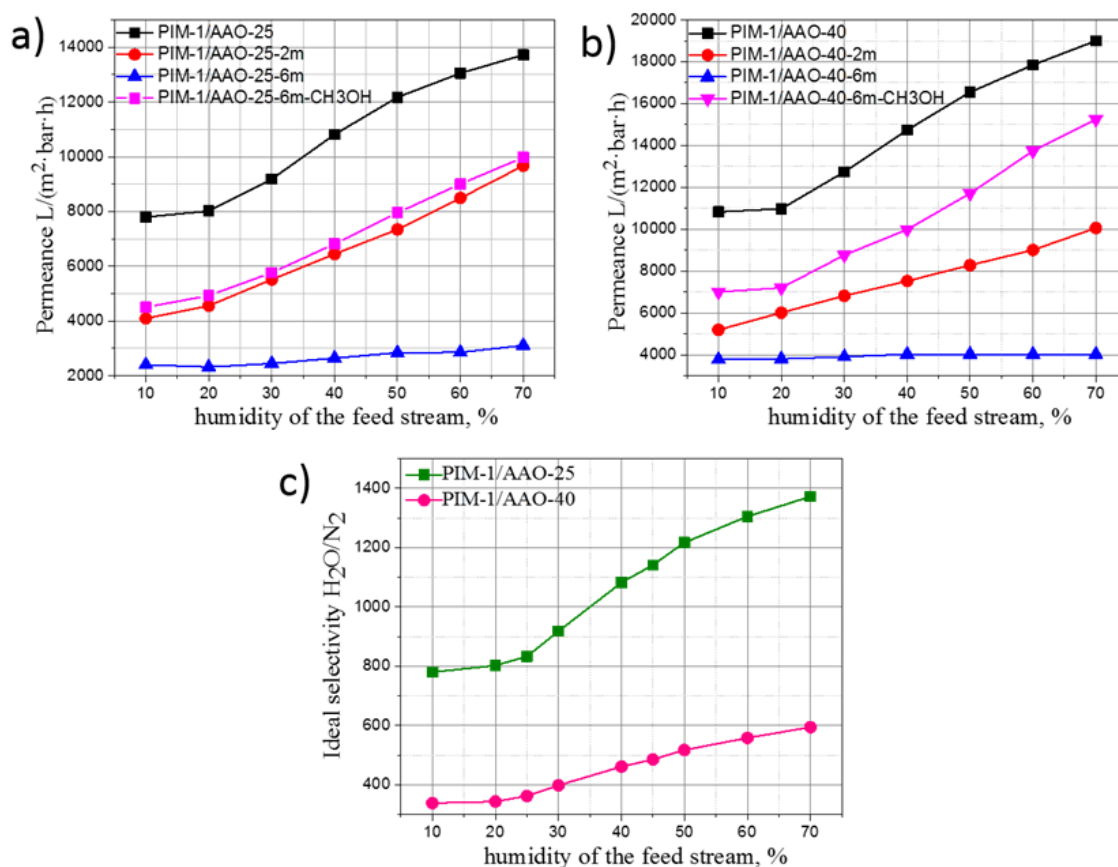


FIG. 4. The dependence of water vapor permeance on relative humidity of the feed gas for the composite membranes: a) PIM-1/AAO-25; b) PIM-1/AAO-40; c) the dependence of H<sub>2</sub>O/N<sub>2</sub> selectivity of composite membranes on the humidity of the feed gas for the freshly-prepared membranes

#### 4. Conclusions

Thus, composite membranes based on polymer with intrinsic microporosity (PIM-1) spatially confined in the pores of anodic alumina membranes with variable diameter have been considered as potential material for gas dehumidification processes. The H<sub>2</sub>O vapors sorption capacity of the composite membranes was found to be a result of the cooperative sorption in PIM-1 polymer and AAO support with the dominating role of PIM-1 in the water vapor transport. It is shown that for the freshly-prepared PIM-1-based composite membranes the H<sub>2</sub>O vapor permeance increases strongly with humidity, owing to the polar nature of the PIM-1. On the other hand, the confined polymeric phase exhibits strong hindrance for permanent gases transport giving rise to the enhancement of H<sub>2</sub>O/N<sub>2</sub> ideal selectivity up to 1400 compared to bulk polymer selectivity of 80. During 6 months of physical ageing, composite membranes lose about 80 % of their initial H<sub>2</sub>O vapor permeance accompanied by loss in selectivity. The activation in methanol allows to rejuvenate up to 80 % of the initial polymer permeance. According to the obtained results, PIM-1-based composite membranes are suitable candidates for water vapor extraction from gas streams, but regular activation in methanol is required in order to save optimal polymer performance.

#### Acknowledgements

The authors are grateful to A. A. Eliseev and D. I. Petukhov (Lomonosov Moscow State University) for the help in experimental work and discussion of the results. The work is supported by the Ministry of education and science of the Russian Federation within a Federal Targeted Programme for "Research and Development in Priority Areas of Development of the Russian Scientific and Technological Complex for 2014–2020" (Agreement No. 14.604.21.0177, unique Project Identification RFMEFI60417X0177).

## References

- [1] Yang B., Weixing Y., Gao F., Guo B. A review of membrane-based air dehumidification. *Indoor and Built Environment*, 2013, **24** (1), P. 11–26.
- [2] Baker R.W., Low B.T. Gas separation membrane materials: A perspective. *Macromolecules*, 2014, **47** (20), P. 6999–7013.
- [3] Sadilov I.S., Petukhov D.I., Eliseev A.A. Enhancing gas separation efficiency by surface functionalization of nanoporous membranes. *Separation and Purification Technology*, 2019, **221**, P. 74–82.
- [4] Scholes C.A., Jin J., Stevens G.W., Kentish S.E. Competitive permeation of gas and water vapour in high free volume polymeric membranes. *Journal of Polymer Science Part B: Polymer Physics*, 2015, **53** (10), P. 719–728.
- [5] Uchytíl P., Petrickovic R., Seidel-Morgenstern A. Study of capillary condensation of butane in a Vycor glass membrane. *Journal of Membrane Science*, 2005, **64** (1–2), P. 27–36.
- [6] Lira H. de L., Paterson R. New and modified anodic alumina membranes: Part III. Preparation and characterisation by gas diffusion of 5 nm pore size anodic alumina membranes. *Journal of Membrane Science*, 2002, **206** (1–2), P. 375–387.
- [7] Petukhov D.I., Berekchiian M.V., Eliseev A.A. Meniscus Curvature Effect on the Asymmetric Mass Transport through Nanochannels in Capillary Condensation Regime. *The Journal of Physical Chemistry C*, 2018, **122** (51), P. 29537–29548.
- [8] Petukhov D.I., Chernova E.A., et al. Thin graphene oxide membranes for gas dehumidification. *Journal of Membrane Science*, 2018, **577**, P. 184–194.
- [9] Eliseev An.A., Poyarkov A.A., et al. Operando study of water vapor transport through ultra-thin graphene oxide membranes. *2D Materials*, 2019, **6** (3), 035039.
- [10] Bolto B., Hoang M., Xie Z. A review of water recovery by vapour permeation through membranes. *Water Research*, 2012, **46** (2), P. 259–266.
- [11] Metz S.J., van De Ven W.J.C., et al. Transport of water vapor and inert gas mixtures through highly selective and highly permeable polymer membranes. *Journal of Membrane Science*, 2005, **251** (1–2), P. 29–41.
- [12] Shengzhou L., Feng W., Tianlu C. Synthesis of Poly(ether ether ketone)s with High Content of Sodium Sulfonate Groups as Gas Dehumidification Membrane Materials. *Macromolecular Rapid Communications*, 2001, **22** (8), P. 579–582.
- [13] Chernova E.A., Bermeshev M.A., et al. The effect of geometric confinement on gas separation characteristics of additive poly[3-(trimethylsilyl)tricyclononene-7]. *Nanosystems: Physics, Chemistry, Mathematics*, 2018, **9** (2), P. 252–258.
- [14] Chernova E., Petukhov D., et al. Enhanced gas separation factors of microporous polymer constrained in the channels of anodic alumina membranes. *Scientific Reports*, 2016, **6**, P. 31183.
- [15] Petukhov D.I., Napolskii K.S., et al. Comparative study of structure and permeability of porous oxide films on aluminum obtained by single- and two-step anodization. *ACS Applied Materials and Interfaces*, 2013, **5** (16), P. 7819–7824.
- [16] Petukhov D.I., Napolskii K.S., Eliseev A.A. Permeability of anodic alumina membranes with branched channels. *Nanotechnology*, 2012, **23** (33), P. 335601.
- [17] Petukhov D.I., Buldakov D.A., et al. Liquid permeation and chemical stability of anodic alumina membranes. *Beilstein Journal of Nanotechnology*, 2017, **8**, P. 561–570.
- [18] Stull D.R. Vapor Pressure of Pure Substances. Organic and Inorganic Compounds. *Industrial & Engineering Chemistry*, 1947, **39** (4), P. 517–540.
- [19] Petukhov D.I., Berekchiian M.V., et al. Experimental and Theoretical Study of Enhanced Vapor Transport through Nanochannels of Anodic Alumina Membranes in a Capillary Condensation Regime. *The Journal of Physical Chemistry C*, 2016, **120** (20), P. 10982–10990.
- [20] Petukhov D.I., Eliseev A.A. Gas permeation through nanoporous membranes in the transitional flow region. *Nanotechnology*, 2016, **27** (8), P. 85707.
- [21] Roslyakov I.V., Napolskii K.S., et al. Thermal properties of anodic alumina membranes. *Nanosystems: Physics, Chemistry, Mathematics*, 2013, **4** (1), P. 120–129.
- [22] Emmler T., Heinrich K., et al. Free Volume Investigation of Polymers of Intrinsic Microporosity (PIMs): PIM-1 and PIM1 Copolymers Incorporating Ethanoanthracene Units. *Macromolecules*, 2010, **43** (14), P. 6075–6084.
- [23] Shantarovich V.P., Suzuki T., et al. Structural heterogeneity in glassy polymeric materials revealed by positron annihilation and other supplementary techniques. *Physica status solidi*, 2007, **4** (10), P. 3776–3779.
- [24] Chaukura N. Interaction of a Polymer of Intrinsic Microporosity (PIM-1) with Penetrants. *American Journal of Applied Chemistry*, 2015, **3** (3), P. 139.
- [25] Yampolskii Y., Alentiev A., et al. Intermolecular Interactions: New Way to Govern Transport Properties of Membrane Materials. *Industrial & Engineering Chemistry Research*, 2010, **49** (23), P. 12031–12037.
- [26] Lasseguette E., Ferrari M.-C., Brandani S. Humidity Impact on the Gas Permeability of PIM-1 Membrane for Post-combustion Application. *Energy Procedia*, 2014, **63**, P. 194–201.

## Synergetic action of ceria nanoparticles and doxorubicin on the early development of two fish species, *Danio rerio* and *Puntius tetrazona*

E. Yu. Krysanov<sup>1</sup>, T. B. Demidova<sup>1</sup>, O. S. Ivanova<sup>2</sup>, K. G. Ordzhonikidze<sup>3</sup>, A. B. Shcherbakov<sup>4</sup>, V. K. Ivanov<sup>2,5</sup>

<sup>1</sup>Severtsov Institute of Ecology and Evolution, Russian Academy of Sciences, Moscow, 119071 Russia

<sup>2</sup>Kurnakov Institute of General and Inorganic Chemistry, Russian Academy of Sciences, Moscow, 119991 Russia

<sup>3</sup>Vavilov Institute of General Genetics, Russian Academy of Sciences, Moscow, 119991 Russia

<sup>4</sup>Zabolotny Institute of Microbiology and Virology, NAS of Ukraine, Kiev, D 03680 Ukraine

<sup>5</sup>National Research Tomsk State University, Tomsk, 634050 Russia

krysanov@sevin.ru, van@igic.ras.ru

PACS 87.18.h, 89.60.k

DOI 10.17586/2220-8054-2019-10-3-289-302

The combined action of ceria nanoparticles and doxorubicin on the early stages of ontogenesis of *Danio rerio* and *Puntius tetrazona* was studied. Results obtained indicate that there is a synergetic effect of CeO<sub>2</sub> nanoparticles and doxorubicin which is demonstrated by a high incidence of embryonic malformations in fish. This synergetic effect is more pronounced in tiger barbs than in zebrafish, and depends strongly on the synthetic route of ceria nanoparticles' preparation, the most notable effects being registered for citrate-stabilized nanoparticles.

**Keywords:** cerium dioxide, nanotoxicology, zebrafish, doxorubicin, embryotoxicity.

Received: 23 May 2019

Revised: 1 June 2019

### 1. Introduction

Nanoscale cerium oxide (nanoceria) is widely used in modern technological applications as a key component of catalysts, an abrasive, a corrosion inhibitor and a constituent of healthcare and cosmetics products [1, 2].

Nanoceria applications in biomedicine have been extensively discussed in several reviews [3–6]. It has been demonstrated that ceria nanoparticles are capable of playing the role of reactive oxygen species (ROS) level regulator and free radicals scavenger, both *in vitro* and *in vivo*. The usefulness of nanoceria for biomedical applications can be attributed to two main factors: its oxygen nonstoichiometry and its relatively low toxicity. The first factor determines the ability of nanoceria to affect the redox processes in the living cell, in particular under oxidative stress conditions caused by ROS. The second factor offers the prospect of comparative safety for *in vivo* applications of ceria nanoparticles.

Another specific property of nanoceria is the ability to regenerate its oxygen nonstoichiometry: after participating in a redox process, ceria nanoparticles are able to return to their initial state in a relatively short period of time; this feature is responsible for a prolonged therapeutic effect of nanosized ceria inside the living body [7].

Current data on nanoceria effects on living beings are still somewhat controversial. Some papers have reported on the pro-oxidant properties of nanoceria [8–10], while others have demonstrated its antioxidant behavior [11–14]. Recent *in vitro* experiments have demonstrated the fine interplay between the synthesis conditions of nanoceria and its toxicity [15].

The data on nanoceria's effects on aquatic organisms are also quite controversial [16]. Different aquatic species demonstrate different sensitivity rates towards nanoceria. For instance, nanoceria did not show any toxic effects in an acute test with *Daphnia magna* for concentrations from 10 to 1000 mg/l [17], yet it appeared to be toxic for two other genus representatives, with significant interspecies differences. Toxicity for *D. similis* was 350 times as high as for *D. pulex* [18].

No toxic effects were observed upon microinjection of nanoceria into yolk of *Danio rerio* embryos [17, 19]. A recent study [20] revealed that CeO<sub>2</sub> nanoparticles are non-hazardous to *D. rerio* embryos, both under visible light and UV-A irradiation; also, nanoceria does not exhibit any UV-A-induced phototoxic effects on zebrafish.

In the majority of papers, the toxic effects were only observed at high concentrations of nanoparticles. In turn, estimated nanoceria concentrations in the environment have been fairly low [21, 22], and in aquatic systems the majority of nanoparticles precipitate [23] and only 1.3 % remain suspended in water. For nanoceria concentrations below 1 mg/l, the toxicity has only been observed in one investigation [24]. The technique of suspension preparation also affects toxicity of nanoceria. Suspensions prepared using magnetic stirring did not show any toxic effects in *C. dubia*, while the same suspension prepared under sonication caused death (EC<sub>50</sub> = 11.9 – 25.3 mg/l) [25]. Another significant

factor that predetermines toxicity of nanoceria is the composition of precursors for CeO<sub>2</sub> synthesis. CeO<sub>2</sub> nanoparticles prepared with hexamethylenetetramine (HMT) caused toxic effects in *Daphnia* during a 48-hour test [26], while HMT itself did not. It should be noted that, in this case, the formation of ceria nanoparticles was accompanied by hydrolysis of HMT, with the release of harmful formaldehyde. Some authors have suggested that nanoceria effects on living organisms depend on the synthesis conditions [4] and type of stabilizers used [27]. For example, in the experiment with fibroblasts, CeO<sub>2</sub> nanoparticles stabilized by citrate species interacted more actively with cells and were able to penetrate them [27]. It is worth noting that, in the presence of dissolved organic substances, stability of ceria suspensions increases and aggregate size decreases [17, 28, 29]. It is fair to assume that synergetic effects of nanoceria and dissolved ecotoxic agents may also be observed in a natural water environment.

The present paper aims to investigate the synergetic action of CeO<sub>2</sub> nanoparticles and doxorubicin on the early stages of fish ontogenesis. The effects of antibiotics on the early stages of embryogenesis have been quite well investigated. Doxorubicin is a strong cardiotoxin, and the choice of doxorubicin in our experiments was due to the fact that its cardiotoxic effect is easily observable and can be distinguished from the effects caused by nanoparticles [30]. As the toxic effects of nanoceria-doxorubicin composition can exhibit interspecies differences, we used two fish species in our study, namely zebrafish (*Danio rerio*) and tiger barb (*Puntius tetrazona*), whose embryogenesis features are different.

## 2. Materials and methods

We used three types of ceria nanoparticle, including two aqueous sols and water-dispersible nanopowder. A non-stabilized 6 nm ceria aqueous sol was synthesized using a previously reported technique of hydrothermal–microwave treatment of the colloid solution formed upon anionite treatment of a cerium (III) nitrate aqueous solution [31]. Briefly, Amberlite IRA 410 CL ion-exchange resin (Aldrich, #216569), preliminarily converted to the OH-form, was gradually added to a 0.01 M cerium (III) nitrate (Aldrich, #238538) solution until pH reached 10.0. Sols formed in this way were separated from the resin by filtering, immediately transferred to 100 ml polytetrafluoroethylene autoclaves (filled to 50 %) and subjected to hydrothermal–microwave treatment in a Berghof Speedwave MWS-3+ setup at 190 °C for 3 h. Upon completion of the synthesis, the autoclaves were withdrawn from the microwave oven and cooled down to room temperature in air. A citrate-stabilized ceria sol was obtained from the “naked” one by addition of an equimolar quantity of citric acid, and through careful neutralizing of the solution with ammonia (Chimmed, Russia). In addition, a CeO<sub>2</sub> nanopowder was used (Sigma Aldrich, particle size < 25 nm).

Lyophilized doxorubicin hydrochloride powder (Pharmachemi, Netherlands) was purchased from a local distributor.

Particle size measurements by dynamic light scattering and ζ-potential measurements by automatic titration were carried out on the Malvern Zetasizer Nano ZS analyser (Malvern Instruments, UK). The light source used was a helium–neon laser, (the radiation wavelength was 632.8 nm).

Tests were carried out in zebrafish (*Danio rerio*) and tiger barb (*Puntius tetrazona*) embryos. The fish were kept under standard conditions in 20 litre aquaria at 26 °C with a 12 h light / 12 h dark time-schedule. The eggs were collected immediately after spawning; the quality was estimated under a stereomicroscope. The embryos were incubated in embryo media (5 mmol NaCl; 0.17 mmol KCl; 0.33 mmol CaCl<sub>2</sub>; 0.33 mmol MgSO<sub>4</sub>; pH = 7.2 – 7.3) in 24-well plates.

In a preliminary experiment, we assessed the action of pure doxorubicin (concentrations from 0.1 to 50 mg/l) on the development of zebrafish using ceria nanoparticles alone (0.001, 0.01, 0.1, 1.0 and 10 mg/l), doxorubicin alone (1.0, 5.0, 10, 20, 30 and 50 mg/l) and mixtures of nanoparticles and doxorubicin, wherein a single concentration of doxorubicin (10 mg/l) was used with nanoceria sols of different concentrations (from 0.001 to 10 mg/l), or a single concentration of nanoceria sols (10 mg/l) was used with 1.0 and 5.0 mg/l of doxorubicin.

For the preparation of the CeO<sub>2</sub> nanoparticle suspension, the necessary quantity of stock colloidal solution of CeO<sub>2</sub> was dispersed in an embryo medium by sonication for 10 min. Doxorubicin stock solution was prepared in distilled water. The nanoparticle suspension was mixed with fresh doxorubicin solution immediately after preparation, with subsequent sonication for 2 min.

The embryo development stages were examined using a stereomicroscope (Carl Zeiss, Stemi 2000C) and were matched according to [32].

### 2.1. Developmental biology of zebrafish and barb eggs

Barb eggs have a sticky layer, for substrate affixing, which hardens after fertilization. The eggs are transparent. Development up to hatching lasts for 24 h at 28 °C. The yolk sack resolves in 58 – 72 h after hatching. The embryogenesis period in barbs, when the embryo remains inside the egg and is protected by chorion, is shorter than with

zebrafish (24 h for the barb and 72 h for zebrafish). However, the larval period, when the larva swims but does not eat, is longer in tiger barbs than in zebrafish.

Fertilized eggs were collected in the first two hours after spawning. Embryos were transferred to a 24-well plate containing 2 ml of the solution being tested per well. Each embryo was transferred to a separate well and 24 embryos were used per test concentration. Embryos were incubated in a culture medium containing 0.29 g/l NaCl, 0.013 g/l KCl, 0.05 g/l  $\text{CaCl}_2 \times 7\text{H}_2\text{O}$ , 0.0365 g/l  $\text{CaCl}_2$ , 0.815 g/l  $\text{MgCl}_2 \times 6\text{H}_2\text{O}$ ; 7.0 – 7.5 pH. Embryos were kept in an incubator at 26 °C with a 14 h light / 10 h dark time-schedule. The medium was not replaced during the course of the experiment. Embryos were tested daily using a Zeiss Stemi 2000 stereomicroscope. Malformations and other teratogenic effects were scored. Survival rate, percentage of malformed embryos and rate of hatching were calculated at 96 hpf.

Statistical analysis was performed using a Chi-Square test in an SPSS 21 data analysis package.

### 3. Results

#### 4. Doxorubicin toxicity in fish

Doxorubicin toxicity was assessed for concentrations of 0.1 to 50 mg/l. A significant increase in embryo death was registered for concentrations of 40 mg/l and higher (Fig. 1(a)). The death rate was 91.7 % for a concentration of 40 mg/l. Embryonic abnormalities began to increase at concentrations starting from 30 mg/l (Fig. 1(b)). Pericardial edema was one of the most frequent types among the registered abnormalities. For this reason, for subsequent tests, we chose a doxorubicin concentration of 10 mg/l, for which the rate of embryonic abnormalities and mortality did not differ significantly from that for the control group.

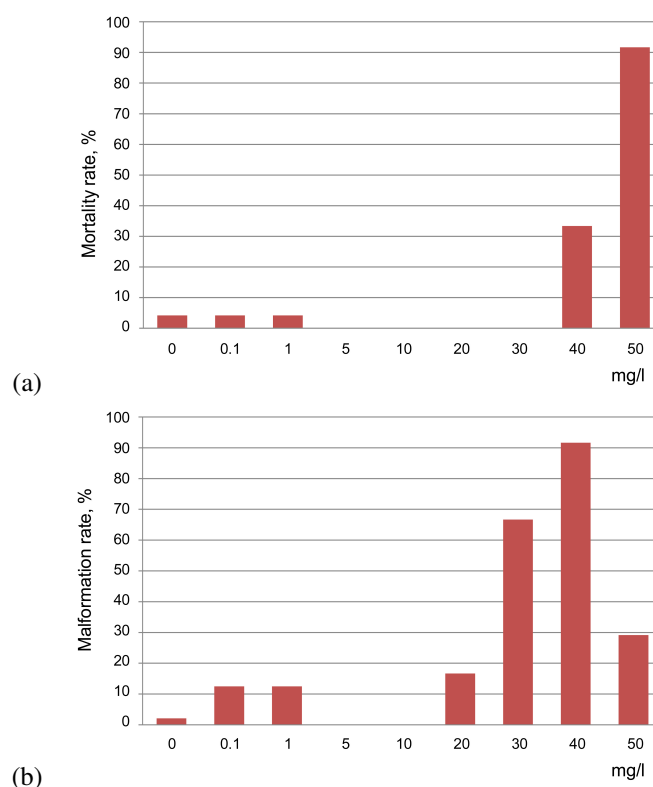


FIG. 1. Mortality rate (a) and malformation rate (b) of zebrafish embryos on exposure to different concentrations of doxorubicin

#### 5. CeO<sub>2</sub> nanoparticles colloids and suspensions toxicity for *Danio rerio* embryos

Our data indicate that CeO<sub>2</sub> nanoparticles in a concentration of 10 mg/l did not, themselves, affect zebrafish embryonic development (Fig. 2). The survival rate did not differ from that for the control group, and was independent of the method of nanoparticle preparation (Fig. 2(a)). The rate of malformations also did not exceed the control group

rate (Fig. 2(b)). Ceria nanoparticles also did not affect hatching time. Hatching started in 48 hours and finished in 72 hours. No significant differences between ceria-treated and control groups were registered (Fig. 3).

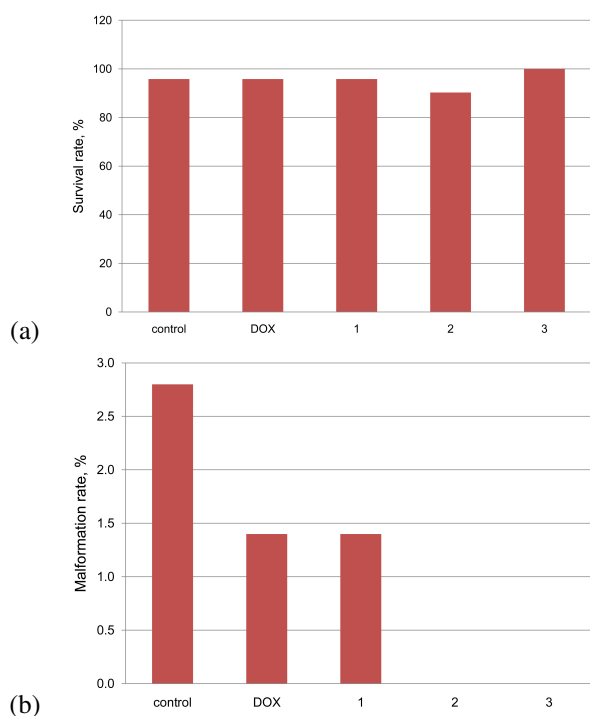


FIG. 2. *Danio rerio* embryo survival rates (a) and the rate of *Danio rerio* embryos with developmental abnormalities (b) on exposure to doxorubicin or ceria nanoparticles (10 mg/l). DOX – doxorubicin, 1 – citrate-stabilized ceria, 2 – non-stabilized ceria, 3 – ceria nanopowder

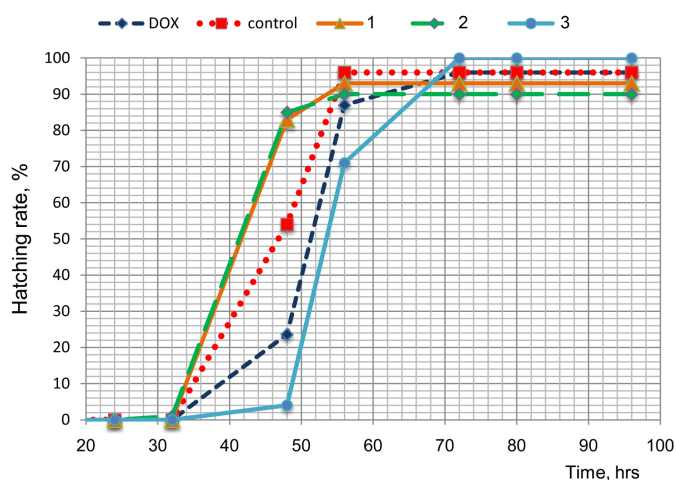


FIG. 3. Hatching rate of *Danio rerio* embryos upon exposure to doxorubicin or ceria nanoparticles (10 mg/l). DOX – doxorubicin, 1 – citrate-stabilized ceria, 2 – non-stabilized ceria, 3 – ceria nanopowder

### 5.1. The synergetic effects of various CeO<sub>2</sub> concentrations and fixed doxorubicin concentration (10 mg/l)

For the assessment of possible synergetic effects, CeO<sub>2</sub> nanoparticles in concentrations from 0.001 to 10 mg/l were mixed with doxorubicin (10 mg/l). Various combinations of nanoceria and doxorubicin had no significant effect on either zebrafish or tiger barb embryo survival rates (Fig. 4). In turn, the rate of malformations began to increase as

the ceria concentrations increased (Fig. 5). This effect was observed for all types of ceria nanoparticles and for both species of fish. The majority of abnormalities were represented by pericardial edema.

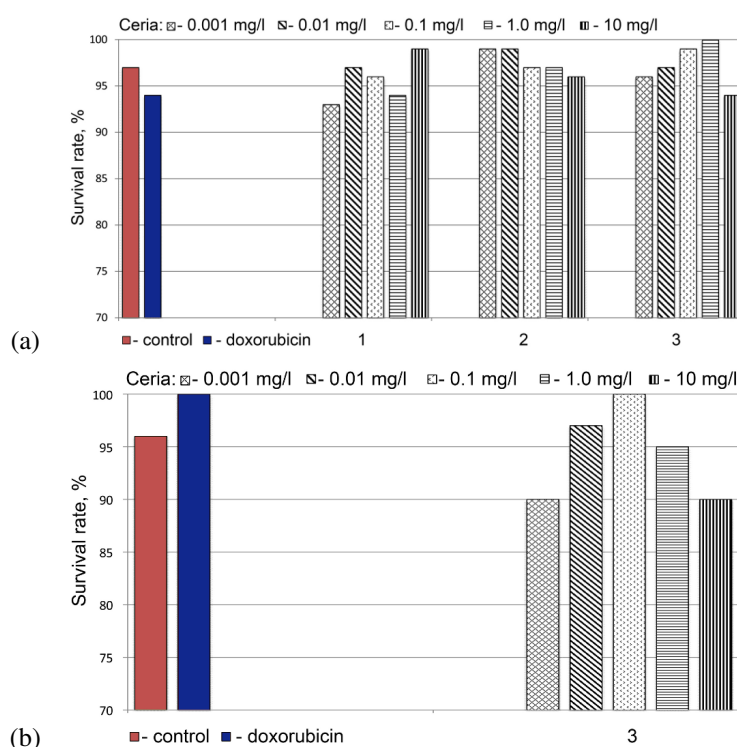


FIG. 4. The survival rate of zebrafish (*D. rerio*) (a) and of tiger barb (*P. tetrazona*) (b) embryos on exposure to doxorubicin alone (10 mg/l) and the mixture of ceria nanoparticles (0.001 – 10 mg/l) with doxorubicin (10 mg/l),  $N = 72$  (a),  $N = 40$  (b). 1 – citrate-stabilized ceria, 2 – non-stabilized ceria, 3 – ceria nanopowder

There was a significant difference between the effects of various types of ceria nanoparticles on zebrafish embryos. For the citrate-stabilized  $\text{CeO}_2$  sol, a significant increase in abnormalities was noted, even for a concentration of 1 mg/l (15.3 %), while, at a  $\text{CeO}_2$  concentration of 10 mg/l, the rate of malformations increased to 98.6 %. For the non-stabilized cerium dioxide sol at a concentration of 10 mg/l, the abnormality rate also increased, compared with the control group (51.4 %), but it was significantly lower than for citrate-stabilized nanoceria. The addition of the ceria nanopowder caused only minimal effects on the malformation rate; the malformation rate exceeded that caused by doxorubicin alone, but was lower than for  $\text{CeO}_2$  sols (31.9 %), with statistically significant differences.

In the experiments with the tiger barbs, only  $\text{CeO}_2$  nanopowder mixed with doxorubicin was used. Increasing the concentration of  $\text{CeO}_2$  to 10 mg/l caused a rise in embryonic abnormality rate to 90 %. Thus, significant differences in the ceria nanopowder-doxorubicin mixture effects were revealed for two different species of fish, with the malformation rate higher for the tiger barbs.

The high malformation rate did not affect the hatching of surviving embryos; the rate of hatched larvae exceeded 90 % for all groups (Fig. 6(a, b, c, d)). No significant differences were observed, either for the rate of hatched larvae or for the hatching time period.

## 5.2. Synergetic effects of a fixed concentration of ceria nanoparticles (10 mg/l) and various concentrations of doxorubicin (1 and 5 mg/l) on the embryonic development of zebrafish

For the next experimental series, ceria nanoparticles, at a concentration of 10 mg/l, were mixed with doxorubicin (1.0 or 5.0 mg/l). The data obtained demonstrate that survival and malformation rates and the hatching success of zebrafish upon exposure to low concentrations of doxorubicin mixed with ceria did not differ significantly from the control and doxorubicin alone groups (Table 1).

Thus, low doxorubicin concentrations in combination with high  $\text{CeO}_2$  nanoparticle concentrations had no significant effects on zebrafish embryo development.

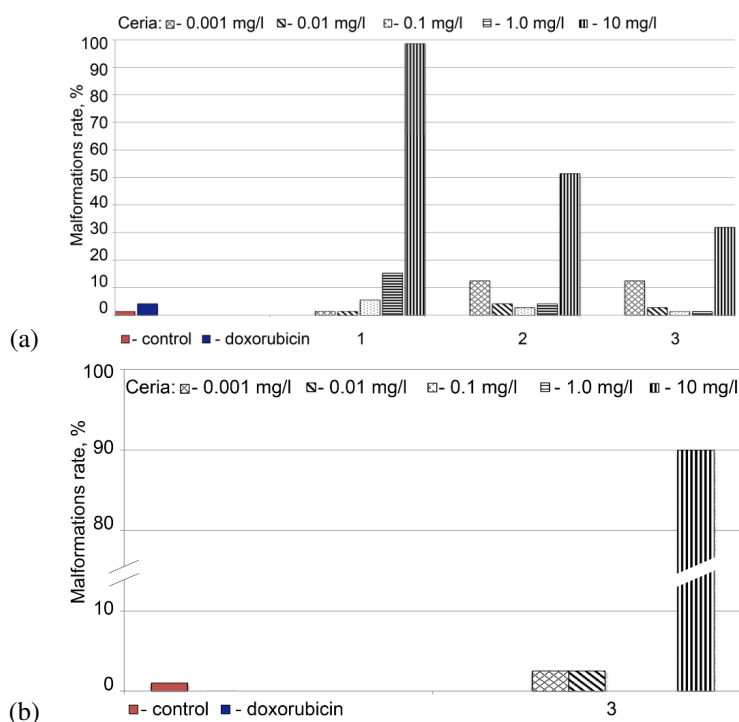


FIG. 5. The malformation rate in the embryonic development of zebrafish (a) and tiger barbs (b) on exposure to doxorubicin alone (10 mg/l) and the mixture of ceria nanoparticles (0.001 – 10 mg/l) with doxorubicin (10 mg/l),  $N = 72$  (a),  $N = 40$  (b). 1 – citrate-stabilized ceria, 2 – non-stabilized ceria, 3 – ceria nanopowder

## 6. Discussion

Data obtained indicate that, regardless of the preparation method and stabilizer type, ceria nanoparticles alone in concentrations ranging from 0.001 to 10 mg/l did not demonstrate any toxic effects during acute tests in zebrafish. The survival rate of embryos, hatching success and malformation rate did not exceed control significantly. The data

TABLE 1. The effects of different types of  $\text{CeO}_2$  nanoparticles (10 mg/l) and doxorubicin on zebrafish embryos

	Control	Doxorubicin	Citrate-stabilized ceria		Non-stabilized ceria		Ceria nanopowder		
			Without doxorubicin	With doxorubicin (1 mg/l)	Without doxorubicin	With doxorubicin (1 mg/l)	Without doxorubicin	With doxorubicin (1 mg/l)	With doxorubicin (5 mg/l)
$N$	72	72	48	48	48	48	24	24	24
mortality	4.2	1.4	4.2	8.3	4.2	2.1	0	5.6	5.6
malformations	1.4	0	2.1	0	0	0	0	2.8	1.4
hatching	95.1	97.9	89.6	91.7	95.8	95.8	100	93.1	94.4

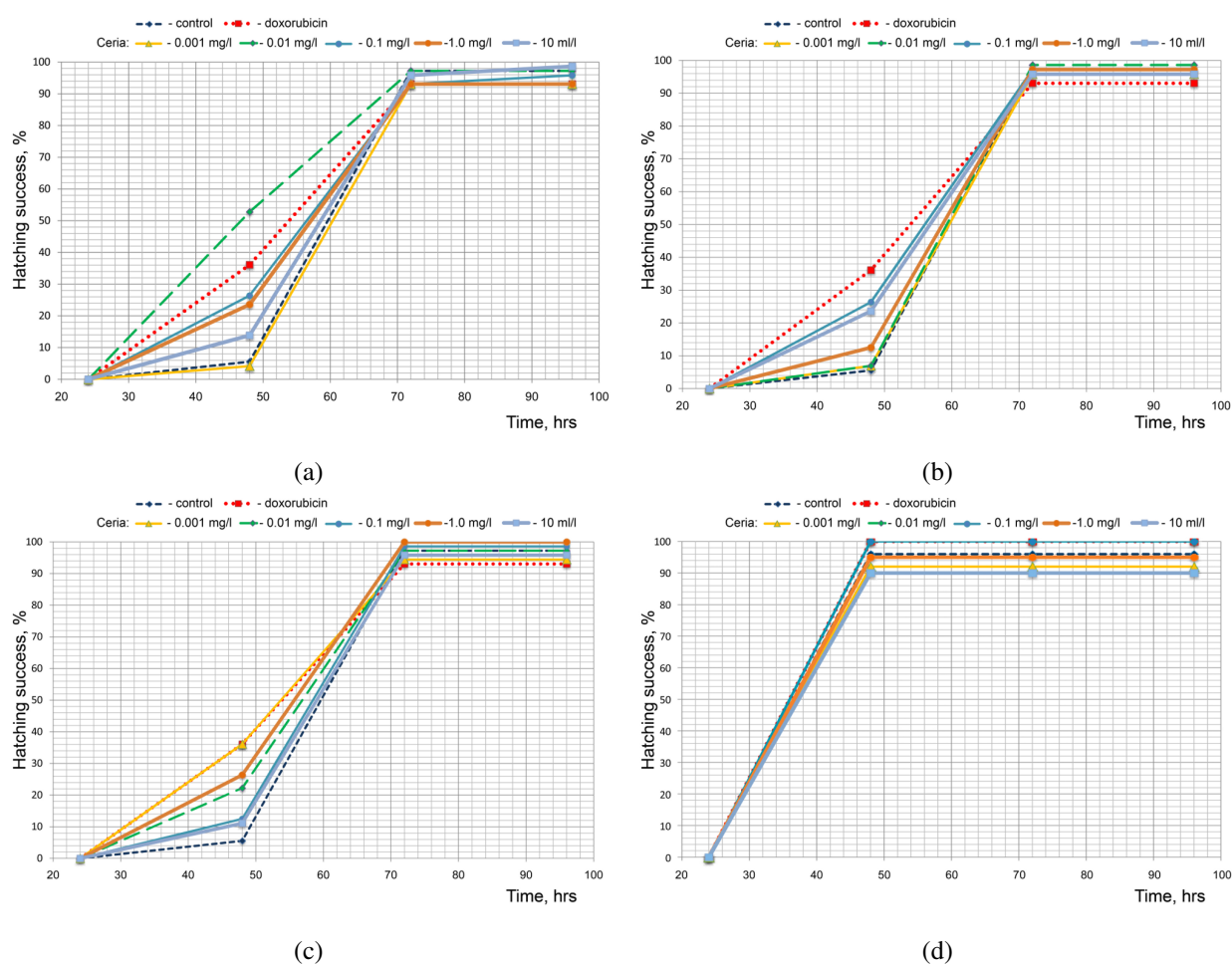


FIG. 6. The hatching success of zebrafish (a, b, c) and tiger barb (d) embryos on exposure to a mixture of citrate-stabilized ceria nanoparticles (0.001 – 10 mg/l) (a), non-stabilized ceria nanoparticles (0.001 – 10 mg/l) (b) and ceria nanopowder (0.001 – 10 mg/l) (c, d) with doxorubicin (10 mg/l) ( $N = 72$  for (a, b, c) and  $N = 40$  for (d))

obtained agree with data derived for zebrafish embryos and ceria nanoparticles at concentrations of 13 to 200 mg/l [17]. However, it was previously shown that  $\text{TiO}_2$  nanoparticles which were non-toxic in an acute test [33] influenced the behavior of larvae in a chronic test at nanoparticle concentrations of 1 mg/l [34]. Therefore, our data cannot exclude the possibility of chronic toxicity of nanoceria in fish.

The presence of ecotoxic agents in an aqueous environment can considerably influence the nanoparticle behavior and their effects on aquatic species. It has been shown in previous studies that metal oxide nanoparticles can increase the accumulation of diluted ecotoxicants in aquatic species or cause a synergetic effect. For example, in experiments on adult fish, the presence of  $\text{TiO}_2$  nanoparticles in water at a concentration of 10 mg/l increased As and Cd accumulation in carp (*Cyprinus carpio*) up to 30 – 140 % [35, 36]. However, in the experiments on zebrafish, with the same  $\text{TiO}_2$  nanoparticles, at concentrations of 5 – 20 mg/l, no pronounced influence on Cd bioaccumulation was observed [37]. Similar results were obtained in *Daphnia sp.* The presence of 2 mg/l  $\text{TiO}_2$  nanoparticles increased Cd accumulation six-fold in *D. magna*. For  $\text{TiO}_2$  nanoparticles, the increase in  $\text{Cu}^{2+}$  accumulation and toxicity was also observed for *D. magna* [38]; the same effect was registered for  $\text{As}^{5+}$  accumulation in *C. dubia* [39]. Similarly, the introduction of  $\text{CeO}_2$  nanoparticles increased atrazine accumulation in *Daphnia* due to herbicide adsorption and transfer by the nanoparticles [40].

In the present study, doxorubicin was used as a model ecotoxic agent. Doxorubicin is known to have cardiotoxic effects on zebrafish development [41], and leads to embryonic malformations, including pericardial edema, in concentrations exceeding 10 mg/l. Doxorubicin concentrations were used which do not affect zebrafish development. Addition of ceria nanoparticles did not lead to embryonic death, but had a significant effect on doxorubicin toxicity. When mixed with all types of ceria nanoparticles (10 mg/l), doxorubicin taken in 10 mg/l concentration caused a

significant rise in embryonic malformations, mainly pericardial oedema. Lower concentrations of ceria nanoparticles in the mixtures did not lead to such effects.

It is well known that metal oxide nanoparticles in aqueous solutions easily adsorb molecules and ions of various organic and inorganic substances. Due to its specific chemical properties, cerium dioxide appears to be a very good sorbent for several substances. For instance, CeO<sub>2</sub> nanoparticles adsorb 58 % of an initial concentration of Pb<sup>2+</sup>, which is considerably higher than for TiO<sub>2</sub> and Fe<sub>3</sub>O<sub>4</sub> nanoparticles [42]. Furthermore, CeO<sub>2</sub> nanoparticles are good adsorbents for various antibiotics, due to their affinity to hydrophilic molecules [43]. Apparently, in experiments conducted for the current research, ceria nanoparticles could adsorb doxorubicin and consequently promote the increase in its local concentration in zebrafish chorion. This effect was registered only for certain concentrations of doxorubicin and CeO<sub>2</sub> nanoparticles in the media.

Malformation rate in tiger barb embryos during embryogenesis was significantly higher than in zebrafish. Enhanced sensitivity of barb embryos is most likely to appear due to a shorter incubation period of the embryo in the egg: in contrast with zebrafish, the barb hatches within 24 hpf.

The question is still open as to whether the effects observed were caused by ceria nanoparticle penetration into the chorion. It has been established previously that silica nanoparticles do not penetrate zebrafish chorion [44]. Similarly, upon keeping zebrafish in the nanoceria-containing media, approximately 37 % of ceria nanoparticles bind with the chorion and only 0.07 % get through [45].

Citrate-stabilized cerium dioxide sols mixed with doxorubicin appeared to have the most toxic effect. A minimal effect was observed for suspended ceria nanopowders. An intermediate effect was registered for non-stabilized cerium dioxide sols.

Results obtained can be explained taking into account the peculiarities of doxorubicin adsorption on ceria nanoparticles. The interaction in the adsorption system depends on the charge of both adsorbent and adsorbate; the electrostatic difference potential of doxorubicin is unevenly distributed among functional groups, thus the position of functional groups will determine the orientation of the molecule. Calculations made indicate two possible orientations of a doxorubicin molecule on the ceria surface – vertical and planar (see Appendix, Fig. A1). In the first case, interaction with the surface proceeds via a nitrogen group, which has a positive charge when protonated. Obviously, this orientation will be favorable on the negatively charged surface. In the second case, interaction of the molecule with the surface proceeds via the  $\pi$ -electron system of fused aromatic rings and acidic –OH phenol groups, having a negative charge when doxorubicin is ionized. This “flat” orientation of doxorubicin is favorable on the positively charged surface, wherein the molecule occupies the area corresponding to about eight cerium atoms. According to calculations of the electronic structure [46], the sum of the atomic partial charges of the isolated molecule of doxorubicin is zero; in the aquatic environment, the total charge of the molecule is slightly positive, and in complex with DNA is slightly negative, but the overall pattern of the charge distribution is the same.

Unlike weak electrostatic adsorption on gold [47], citric acid is strongly chemisorbed on the ceria surface and cannot be substituted by doxorubicin; the interaction of doxorubicin with citrate-stabilized ceria occurs via the layer of citric acid molecules. The citrate adsorbs on the surface in an ordered manner (see Appendix, Fig. A2(A)), and the grafting density is one citrate molecule per 3 – 4 Ce atoms. Our data indicate that “citrate-stabilized” ceria nanoparticles have negative  $\zeta$ -potential in the whole range of biologically relevant pH values. In turn, for “naked” ceria nanoparticles, the  $\zeta$ -potential typically has a positive charge in the range of pH < 8 (see Appendix, Fig. A3). Several authors have shown that the interaction of various citrate-coated nanoparticles with organic molecules including doxorubicin can proceed by formation of hydrogen bonds [48] or by more complicated surface interactions [49]. According to the calculation referred to above, the doxorubicin molecule would preferably have a vertical orientation on the surface of a nanoparticle coated with dissociated carboxylic groups. In this case, the nitrogen atom of the antibiotic interacted with the carboxyl group of the citrate. Fig. A2(B) shows that the grafting density of doxorubicin on a citrate-coated ceria surface is one molecule per 4 – 5 Ce atoms. Some of the citric acid molecules did not participate in the interaction with the antibiotic; these molecules assure the colloidal stability of ceria nanoparticles.

The fraction of atoms located on the surface of a nanoparticle strongly depends on its size. The corresponding dependence for nanoceria is shown in Figs. A4 and A5. For 6 nm ceria nanoparticles, the proportion of surface-located atoms is about 40 %; for 25 nm nanoceria, about 12 %. The amount of adsorbed doxorubicin molecules for these types of nanoparticles varies correspondingly. For example, 10 mg of citrate-coated ceria nanoparticles can adsorb 2.8 mg of doxorubicin; 10 mg of the same “naked” ceria nanoparticles can adsorb 1.58 mg of doxorubicin; 10 mg of ceria nanopowder can adsorb 0.47 mg of doxorubicin (see Appendix). As the present work has demonstrated, the toxicity of doxorubicin-ceria conjugated changes in the same manner: citrate-coated nanoceria > “naked” nanoceria > ceria nanopowder.

Results obtained demonstrated that there exists a synergetic effect of ceria nanoparticles and doxorubicin action; the effect was expressed in a high incidence of embryonic malformations in fish. This effect was more pronounced in

tiger barbs than in zebrafish, which, in the authors' opinion, was due to some peculiarities of their embryogenesis. It was also found that differently prepared CeO<sub>2</sub> nanoparticles demonstrated different efficiency. Thus, CeO<sub>2</sub> stable sols application had a stronger effect than a suspended nanopowder. The method of nanoceria stabilization also played a considerable role in the synergetic action of nanoparticles and doxorubicin. Citrate-stabilized cerium dioxide nanoparticles had significantly higher effects than non-stabilized nanoparticles. A certain minimum ratio of nanoparticles and doxorubicin had to be reached to provide a synergetic effect, which substantially depended on the cerium surface atoms available, i.e. on the nanoparticles' size and on the presence of the stabilizer.

Ceria nanoparticles (both non-stabilized and citrate-stabilized aqueous colloid solutions and water redispersible ceria nanopowder) have no embryotoxic effect on *Danio rerio* and *Puntius tetrazona*. Nevertheless, nanoceria has been shown to increase greatly the toxic effect of doxorubicin on fish embryogenesis. This synergetic effect of ceria nanoparticles and doxorubicin depends strongly on the concentration of components, as well as on particle size and the presence of a stabilizer.

## Acknowledgements

This work was partially supported by research grants of Russian foundation for Basic Research No. 18-29-05023 mk.

## References

- [1] Adachi G., Imanaka N., Kang Z.C. *Binary Rare Earth Oxides*. Kluwer Academic Publishers, Dordrecht, 2005, 133 p.
- [2] Trovarelli A. *Catalysis by Ceria and Related Materials*. Imperial College Press, London, 2002, 58 p.
- [3] Ivanov V.K., Shcherbakov A.B., Usatenko A.V. Structure-Sensitive Properties and Biomedical Applications of Nanodispersed Cerium Dioxide. *Russ. Chem. Rev.*, 2009, **78** (9), P. 855–871.
- [4] Karakoti A., Singh S., et al. Redox-Active Radical Scavenging Nanomaterials. *Chem. Soc. Rev.*, 2010, **39** (11), 4422.
- [5] Shcherbakov A.B., Ivanov V.K., et al. Nanocrystalline Ceria Based Materials – Perspectives for Biomedical Application. *Biophysic (Oxf.)*, 2011, **56** (6), P. 987–1004.
- [6] Das S., Dowding J.M., et al. Cerium Oxide Nanoparticles: Applications and Prospects in Nanomedicine. *Nanomedicine*, 2013, **8** (9), P. 1483–1508.
- [7] Shcherbakov A.B., Zholobak N.M., Spivak N.Y., Ivanov V.K. Advances and Prospects of Using Nanocrystalline Ceria in Cancer Theranostics. *Russ. J. Inorg. Chem.*, 2014, **59** (13), P. 1556–1575.
- [8] Park E.-J., Choi J., Park Y.-K., Park K. Oxidative Stress Induced by Cerium Oxide Nanoparticles in Cultured BEAS-2B Cells. *Toxicology*, 2008, **245** (1–2), P. 90–100.
- [9] Horie M., Nishio K., et al. Cellular Responses Induced by Cerium Oxide Nanoparticles: Induction of Intracellular Calcium Level and Oxidative Stress on Culture Cells. *J. Biochem.*, 2011, **150** (4), P. 461–471.
- [10] Tseng M.T., Lu X., et al. Alteration of Hepatic Structure and Oxidative Stress Induced by Intravenous Nanoceria. *Toxicol. Appl. Pharmacol.*, 2012, **260** (2), P. 173–182.
- [11] Lee S.S., Song W., et al. Antioxidant Properties of Cerium Oxide Nanocrystals as a Function of Nanocrystal Diameter and Surface Coating. *ACS Nano*, 2013, **7** (11), P. 9693–9703.
- [12] Karakoti A.S., Monteiro-Riviere N.A., et al. Nanoceria as Antioxidant: Synthesis and Biomedical Applications. *JOM*, 2008, **60** (3), P. 33–37.
- [13] Hirst S.M., Karakoti A., et al. Bio-Distribution and in Vivo Antioxidant Effects of Cerium Oxide Nanoparticles in Mice. *Environ. Toxicol.*, 2013, **28** (2), P. 107–118.
- [14] Chigurupati S., Mughal M.R., et al. Effects of Cerium Oxide Nanoparticles on the Growth of Keratinocytes, Fibroblasts and Vascular Endothelial Cells in Cutaneous Wound Healing. *Biomaterials*, 2013, **34** (9), P. 2194–2201.
- [15] Karakoti A.S., Munusamy P., et al. Preparation and Characterization Challenges to Understanding Environmental and Biological Impacts of Ceria Nanoparticles. *Surf. Interface Anal.*, 2012, **44** (8), P. 882–889.
- [16] Cassee F.R., van Balen E.C., et al. Exposure, Health and Ecological Effects Review of Engineered Nanoscale Cerium and Cerium Oxide Associated with Its Use as a Fuel Additive. *Crit. Rev. Toxicol.*, 2011, **41** (3), P. 213–229.
- [17] Van Hoecke K., De Schampelaere K.A.C., et al. Aggregation and Ecotoxicity of CeO<sub>2</sub> Nanoparticles in Synthetic and Natural Waters with Variable PH, Organic Matter Concentration and Ionic Strength. *Environ. Pollut.*, 2011, **159** (4), P. 970–976.
- [18] Artells E., Issartel J., et al. Exposure to Cerium Dioxide Nanoparticles Differently Affect Swimming Performance and Survival in Two Daphnid Species. *PLoS One*, 2013, **8** (8), e71260.
- [19] Arnold M.C., Badireddy A.R., et al. Cerium Oxide Nanoparticles Are More Toxic than Equimolar Bulk Cerium Oxide in Caenorhabditis Elegans. *Arch. Environ. Contam. Toxicol.*, 2013, **65** (2), P. 224–233.
- [20] Jemec A., Djinović P., Črnivec I.G.O., Pintar A. The Hazard Assessment of Nanostructured CeO<sub>2</sub>-Based Mixed Oxides on the Zebrafish Danio Rerio under Environmentally Relevant UV-A Exposure. *Sci. Total Environ.*, 2015, **506–507**, P. 272–278.
- [21] O'Brien N., Cummins E. Nano-Scale Pollutants: Fate in Irish Surface and Drinking Water Regulatory Systems. *Hum. Ecol. Risk Assess. An Int. J.*, 2010, **16** (4), P. 847–872.
- [22] Johnson A.C., Park B. Predicting Contamination by the Fuel Additive Cerium Oxide Engineered Nanoparticles within the United Kingdom and the Associated Risks. *Environ. Toxicol. Chem.*, 2012, **31** (11), P. 2582–2587.
- [23] Zhang P., He X., et al. Distribution and Bioavailability of Ceria Nanoparticles in an Aquatic Ecosystem Model. *Chemosphere*, 2012, **89** (5), P. 530–535.
- [24] Bottero J.-Y., Auffan M., et al. Manufactured Metal and Metal-Oxide Nanoparticles: Properties and Perturbing Mechanisms of Their Biological Activity in Ecosystems. *Comptes Rendus Geosci.*, 2011, **343** (2–3), P. 168–176.

- [25] Manier N., Garaud M., et al. Behaviour of Ceria Nanoparticles in Standardized Test Media – Influence on the Results of Ecotoxicological Tests. *J. Phys. Conf. Ser.*, 2011, **304**, 012058.
- [26] García A., Espinosa R., et al. Acute Toxicity of Cerium Oxide, Titanium Oxide and Iron Oxide Nanoparticles Using Standardized Tests. *Desalination*, 2011, **269** (1–3), P. 136–141.
- [27] Ould-Moussa N., Safi M., et al. In Vitro Toxicity of Nanoceria: Effect of Coating and Stability in Biofluids. *Nanotoxicology*, 2014, **8** (7), P. 799–811.
- [28] Quik J.T.K., Lynch I., et al. Effect of Natural Organic Matter on Cerium Dioxide Nanoparticles Settling in Model Fresh Water. *Chemosphere*, 2010, **81** (6), P. 711–715.
- [29] Schwabe F., Schulin R., et al. Influence of Two Types of Organic Matter on Interaction of CeO<sub>2</sub> Nanoparticles with Plants in Hydroponic Culture. *Chemosphere*, 2013, **91** (4), P. 512–520.
- [30] Han Y., Zhang J., Qian J., Hu C. Cardiotoxicity Evaluation of Anthracyclines in Zebrafish ( *Danio Rerio* ). *J. Appl. Toxicol.*, 2015, **35** (3), P. 241–252.
- [31] Ivanov V.K., Polezhaeva O.S., et al. Microwave-Hydrothermal Synthesis of Stable Nanocrystalline Ceria Sols for Biomedical Uses. *Russ. J. Inorg. Chem.*, 2010, **55** (1), P. 1–5.
- [32] Kimmel C.B., Ballard W.W., et al. Stages of Embryonic Development of the Zebrafish. *Dev. Dyn.*, 1995, **203** (3), P. 253–310.
- [33] Zhu X., Zhu L., et al. Comparative Toxicity of Several Metal Oxide Nanoparticle Aqueous Suspensions to Zebrafish (*Danio Rerio*) Early Developmental Stage. *J. Environ. Sci. Heal. Part A*, 2008, **43** (3), P. 278–284.
- [34] Chen T.-H., Lin C.-Y., Tseng M.-C. Behavioral Effects of Titanium Dioxide Nanoparticles on Larval Zebrafish (*Danio Rerio*). *Mar. Pollut. Bull.*, 2011, **63** (5–12), P. 303–308.
- [35] Sun H., Zhang X., et al. Enhanced Accumulation of Arsenate in Carp in the Presence of Titanium Dioxide Nanoparticles. *Water. Air. Soil Pollut.*, 2007, **178** (1–4), P. 245–254.
- [36] Zhang X., Sun H., et al. Enhanced Bioaccumulation of Cadmium in Carp in the Presence of Titanium Dioxide Nanoparticles. *Chemosphere*, 2007, **67** (1), P. 160–166.
- [37] Hu X., Chen Q., et al. Combined Effects of Titanium Dioxide and Humic Acid on the Bioaccumulation of Cadmium in Zebrafish. *Environ. Pollut.*, 2011, **159** (5), P. 1151–1158.
- [38] Fan W., Cui M., et al. Nano-TiO<sub>2</sub> Enhances the Toxicity of Copper in Natural Water to *Daphnia Magna*. *Environ. Pollut.*, 2011, **159** (3), P. 729–734.
- [39] Wang D., Hu J., Irons D.R., Wang J. Synergistic Toxic Effect of Nano-TiO<sub>2</sub> and As(V) on *Ceriodaphnia Dubia*. *Sci. Total Environ.*, 2011, **409** (7), P. 1351–1356.
- [40] Han Z., Li J., Bao W., Wang J. Enhanced Toxicity of Atrazine to *Daphnia Magna* in the Presence of Nano-CeO<sub>2</sub>. *Chinese J. Geochemistry*, 2012, **31** (3), P. 297–302.
- [41] Chang C., Wu S.L., et al. Developmental Toxicity of Doxorubicin Hydrochloride in Embryo-Larval Stages of Zebrafish. *Biomed. Mater. Eng.*, 2014, **24** (1), P. 909–916.
- [42] Recillas S., Garca A., et al. Use of CeO<sub>2</sub>, TiO<sub>2</sub> and Fe<sub>3</sub>O<sub>4</sub> Nanoparticles for the Removal of Lead from Water. *Desalination*, 2011, **277** (1–3), P. 213–220.
- [43] Brigante M., Schulz P.C. Adsorption of the Antibiotic Minocycline on Cerium(IV) Oxide: Effect of PH, Ionic Strength and Temperature. *Microporous Mesoporous Mater.*, 2012, **156**, P. 138–144.
- [44] Fent K., Weisbrod C.J., Wirth-Heller A., Pielele U. Assessment of Uptake and Toxicity of Fluorescent Silica Nanoparticles in Zebrafish (*Danio Rerio*) Early Life Stages. *Aquat. Toxicol.*, 2010, **100** (2), P. 218–228.
- [45] Felix L.C., Ortega V.A., Ede J.D., Goss G.G. Physicochemical Characteristics of Polymer-Coated Metal-Oxide Nanoparticles and Their Toxicological Effects on Zebrafish (*Danio Rerio*) Development. *Environ. Sci. Technol.*, 2013, **47** (12), P. 6589–6596.
- [46] Poudel L., Wen A.M., et al. Electronic Structure and Partial Charge Distribution of Doxorubicin in Different Molecular Environments. *Chem. Phys. Chem.*, 2015, **16** (7), P. 1451–1460.
- [47] Curry D., Cameron A., et al. Adsorption of Doxorubicin on Citrate-Capped Gold Nanoparticles: Insights into Engineering Potent Chemotherapeutic Delivery Systems. *Nanoscale*, 2015, **7** (46), P. 19611–19619.
- [48] Nawara K., Romiszewski J., et al. Adsorption of Doxorubicin onto Citrate-Stabilized Magnetic Nanoparticles. *J. Phys. Chem. C*, 2012, **116** (9), P. 5598–5609.
- [49] Auffan M., Masion A., et al. Long-Term Aging of a CeO<sub>2</sub> Based Nanocomposite Used for Wood Protection. *Environ. Pollut.*, 2014, **188**, P. 1–7.

**Appendix**

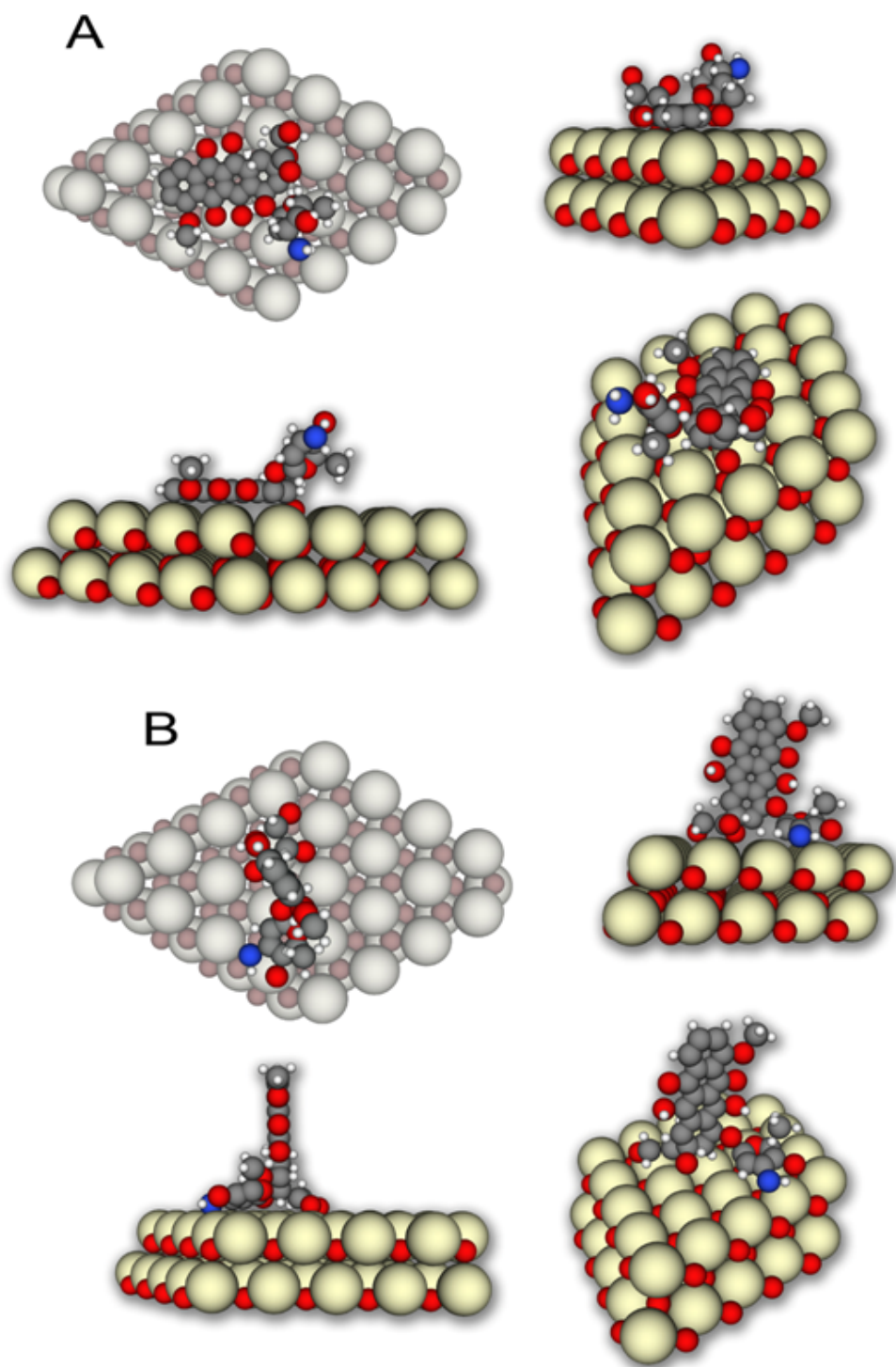


FIG. A1. The calculated adsorption of a doxorubicin molecule on the surface of a ceria cluster: A – planar orientation; B – vertical orientation

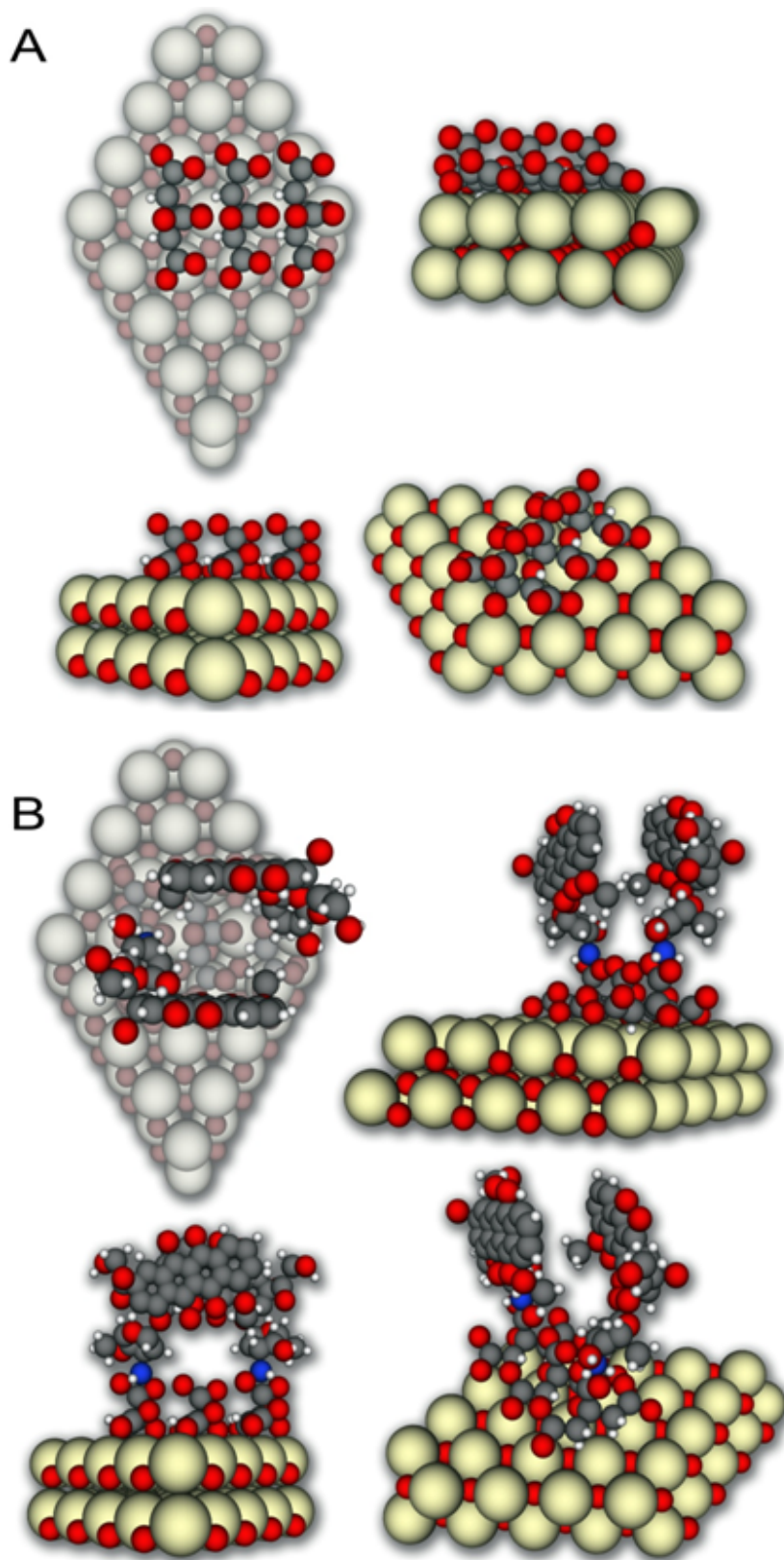


FIG. A2. The calculated adsorption of citrate molecules on the surface of a ceria cluster (A) and doxorubicin molecules on a citrate-coated surface of a ceria cluster (B)

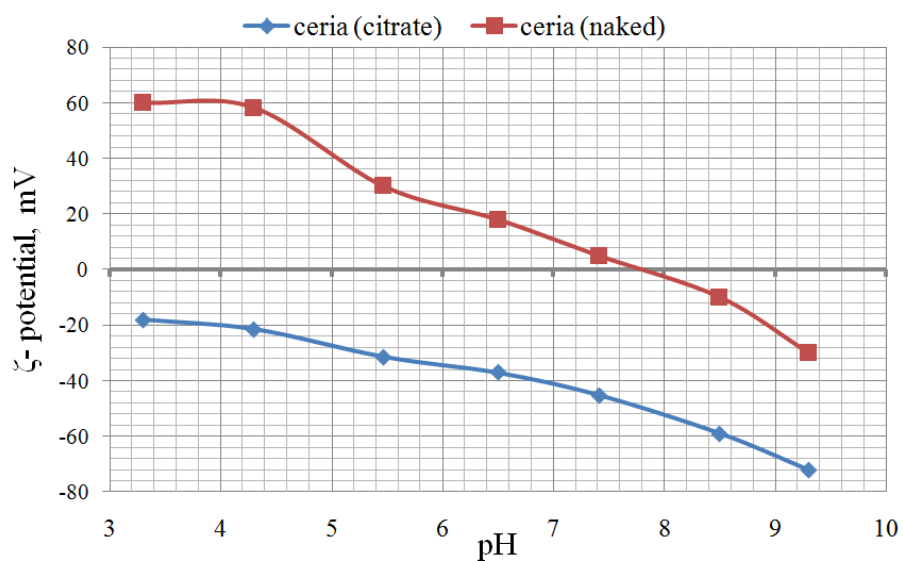


FIG. A3. The dependence of the  $\zeta$ -potential of the “naked” and citrate-stabilized ceria nanoparticles on pH

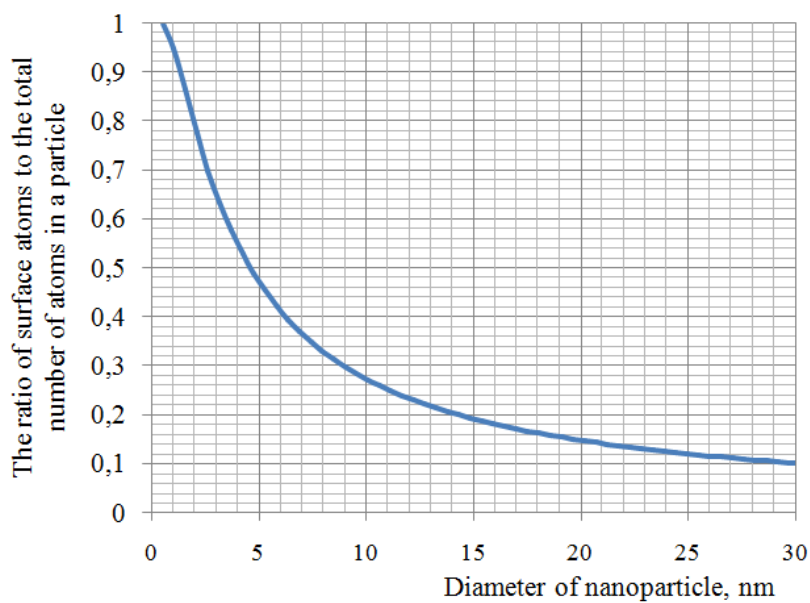


FIG. A4. The calculated ratio of surface atoms to the total number of atoms as a function of ceria particle size

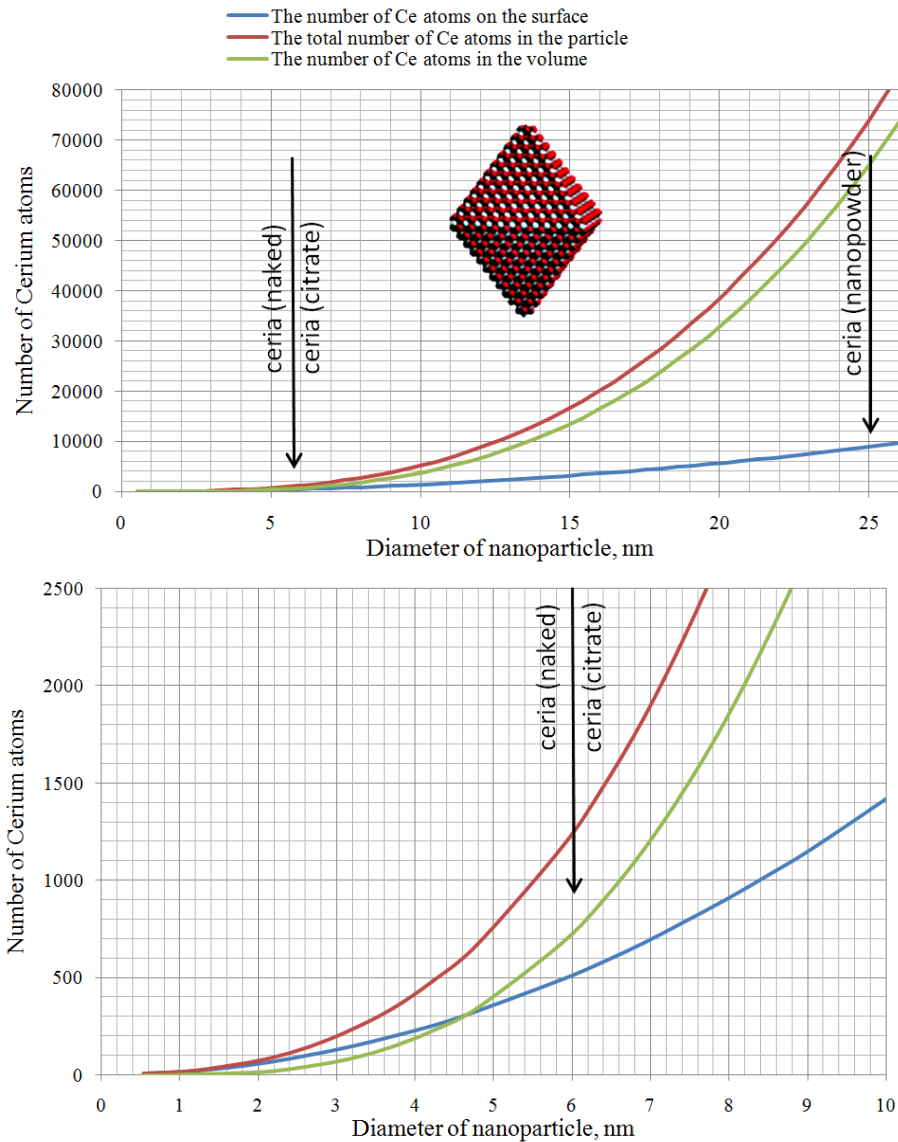


FIG. A5. The calculated number of surface and bulk cerium atoms in octahedral-shaped CeO<sub>2</sub> nanoparticles as a function of particle size

Calculation of doxorubicin amount which could be adsorbed on 10 mg of cerium dioxide particles.

$$M = 10/MW_{\text{CeO}_2} \cdot R/S \cdot MW_{\text{Dox}} = 31.6 \cdot R/S,$$

where

$M$  – the amount of doxorubicin, mg;

$MW_{\text{CeO}_2}$  – the molecular weight of ceria, 172 g/mol;

$R$  – the fraction of the cerium atoms at the surface of the particle;

$S$  – the “landing area” (the number of cerium atoms occupied by one molecule or grafting density) of doxorubicin;

$MW_{\text{Dox}}$  – the molecular weight of doxorubicin, 543.5 g/mol.

“ceria (citrate)” (size 6 nm),  $R = 0.4$ ,  $S = 4 - 5$ ,  $M \approx 2.8$  mg of doxorubicin;

“ceria (naked)” (size 6 nm),  $R = 0.4$ ,  $S = 8$ ,  $M = 1.58$  mg of doxorubicin;

“ceria (nanopowder)” (size 24 nm),  $R = 0.12$ ,  $S = 8$ ,  $M = 0.47$  mg of doxorubicin.

## Nano- and micro-scales structure and properties of the liquid-permeable piezoactive polyvinylidene fluoride films

I. S. Kuryndin, I. Yu. Dmitriev, V. K. Lavrentyev, N. N. Saprykina, G. K. Elyashevich

Institute of Macromolecular Compounds, Russian Academy of Sciences,  
Bolshoy pr., 31, St. Petersburg, 199004, Russia

isk76@mail.ru, ivan-dmitriev-email@yandex.ru, lavrentev1949@mail.ru, elmic@hq.macro.ru, elya@hq.macro.ru

PACS 82.35.x, 61.41.+e

DOI 10.17586/2220-8054-2019-10-3-303-312

Liquid-permeable piezoactive polyvinylidene fluoride films were produced as porous membranes using preparation process including melt extrusion, annealing, cold/hot extension and poling consequent operations. The effect of technological control parameter at extrusion stage (melt draw ratio) on the characteristics of the film structure (overall porosity, liquid permeability and polymorphous composition) was investigated. The values of melt draw ratio which provides the permeability to liquids were established. The structure elements of nano- and micro- levels were determined by a number of experimental techniques. It was proved that the samples contain the pores with sizes 10 – 50 nm. The dependence of polymorphous composition and content of piezoactive crystalline modification on preparation conditions was analyzed. Permeable polyvinylidene fluoride films were successfully poled, and the stable piezoelectric response of the samples was demonstrated.

**Keywords:** polyvinylidene fluoride, porous films, permeability, structure scale levels, piezoelectric properties.

*Received: 3 April 2019*

*Revised: 13 May 2019*

### 1. Introduction

Polyvinylidene fluoride (PVDF) attracts great attention as a membrane material because it has several advantages for filtration and separation processes such as chemical and thermal stability, flexibility and mechanical strength [1–7]. PVDF films have been extensively applied in industrial sectors including environmental, electronic, energy, chemical and biotechnologies areas. However, fabrication of high performance PVDF materials remains challenging and has remained difficult to be achieved.

Permeable to liquids, porous PVDF films can be prepared using techniques based on the mechanism of phase inversion and thermally induced phase separation [4, 8, 9]. In these methods, the pores are generated by the extraction of a solvent. Extraction is carried out as the solution is evaporated, and a solid porous film is formed. By controlling the morphology, it is possible to produce PVDF films with various pore sizes and permeability. A mean pore diameter in the range of 20 – 100 nm was reported for such materials. Membrane production based on the phase separation method has two main drawbacks: solvent contamination and expensive solvent recovery.

Permeable films of semicrystalline polymers may be produced by a so-called “dry method” which is less expensive, more productive and reduces the environmental impact because no solvents (as a rule, they are generally toxic ones) are needed [10–12]. This technique is based on the extension of a film containing a highly oriented stacked lamellar structure. It has been successfully employed for fabricating microporous polypropylene and polyethylene microporous films. There are three consecutive stages of the process: (1) melt extrusion to produce the precursor film with an oriented lamellar morphology, (2) annealing of this film to thicken the lamellae due to involving of macromolecular chains from amorphous regions into the crystals, and (3) uniaxial extension of the film at room temperature to create voids between lamellae, and then thermal stabilization of the porous structure. Stage (1) is a complex process because the film should be produced under high melt draw ratios and cooling rates. Stages (1) and (2) provide the specific morphology formed by stacks of flat lamellar crystallites arranged perpendicularly to the orientation direction of the macromolecular chains. Due to this structure, the effective pore creation is possible as a result of lamellae separation during extension at stage (3). It was proved that the 3-step process (melt extrusion–annealing–uniaxial extension) gives the possibility to obtain microporous PVDF films [13–17]. The porous structure of the PVDF membranes containing open to the surface and closed in the volume pores and permeable for water vapor have been produced [16]. At the same time, liquid-permeable PVDF membranes produced by melt extrusion technology haven't been reported to the best of our knowledge.

It should be noted, that PVDF is widely used not only in the membrane industry but also as the most common non-ceramic piezoelectric material in the electrical industry [18, 19]. Recently, it was shown [20–23] that electrical excitation of the piezoelectrically vibrating membranes (as PVDF, as inorganic piezomembranes, both) could increase

the flux and markedly reduce membrane fouling. The results of the filtration experiments of Darestani [20, 21] using the piezoelectric PVDF materials showed that the vibrations delayed membrane fouling significantly while the membrane flux was maintained close to its initial value. Another innovating point is design of oscillatory resonant devices for gravimetric biosensors (microbalances) based on porous PVDF piezofilms as an alternative for piezoelectric quartz crystals [24]. A new concept was also introduced for self-charging power cells (piezocapacitors) based on piezoactive PVDF separators, in which the mechanical energy is directly converted into electrochemical energy through a piezoelectric effect and is directly stored in a Li-ion battery [25–27]. All of these investigations involve the use of porous piezoactive PVDF films, therefore elaboration of new synthetic approaches seems relevant.

PVDF is a crystallising polymer, and it has at least four crystalline modifications ( $\alpha$ ,  $\alpha_c$ ,  $\beta$  and  $\gamma$ ) [28]. The all-trans  $\beta$ -phase is ferroelectric and mainly responsible for its piezoelectric properties. At the same time, melt processing techniques yield only  $\alpha$ -phase and the polymorphic transition from  $\alpha$ - to  $\beta$ -modification can be efficiently implemented using the orientation drawing at temperatures between 60 and 90 °C or under increased pressure [28, 29]. Therefore, the development of an approach that enables the formation of piezoactive  $\beta$ -crystallites in porous PVDF materials is an important task for practical application of PVDF.

It is important to note that for transformation of PVDF films into a piezoelectrically active state an electrical poling must be carried out. Poling involves the application of an electric field at elevated temperatures to orient the polar axis of the  $\beta$ -phase domains in the field direction. This allows alignment of the  $\beta$ -phase crystals and converts an inactive  $\beta$ -PVDF film into an electromechanically active material. In order to achieve a large piezoelectric response in PVDF materials, the poling process usually requires an external field of higher than 30 MV/m at temperatures of 70 – 100 °C. Poling can also result in partly conversion of the  $\alpha$ -phase to the  $\beta$ -phase [28]. However, there is the technological obstacle to polish porous structures because the voids are able to promote breakdown [29, 30]. To overcome this difficulty, the special method was elaborated. As an electrode the common aluminium adhesive tape was used. A thin adhesive layer played the role of an additional insulator protecting from electrical breakdown. The advantage of this approach is in its simplicity. Aluminium adhesive tapes provide satisfactory DC poling of PVDF at increased temperature and can be easily peeled off after the poling, and porous structure is not damaged. A poled porous film is a ready to use piezoactive membrane.

A liquid metal (eutectic gallium–indium–tin alloy) was used as an electrode for piezoelectric modulus measuring in this work. It can be easily rubbed in the surface of the PVDF porous films without permeation inside them. The liquid metal can be easily erased from the surface of the porous film. Thus, the proposed method of the poling technique is a universal approach which gives an opportunity to produce the materials with stable piezoelectric response. Specific applications of this approach may lay in the field where large-area piezoactive films are needed (much more than 10 cm<sup>2</sup>). The applicability of “dry method” for through porous PVDF films preparation and their piezoelectric performance has not been investigated yet to the full extent.

The applicability of “dry method” for through porous PVDF films preparation and their piezoelectric performance has not been investigated yet to the full extent. The goal of this study was to obtain the porous liquid-permeable and, at the same time, having piezoactive PVDF films in the process including the stages of melt extrusion/annealing/extension/poling and determine the permeability, porous structure characteristics, content of piezoactive  $\beta$ -crystallite modification and piezoelectric modulus.

The goal of this study was as follows:

- to obtain the porous liquid-permeable and, at the same time, piezoactive PVDF films using a melt extrusion process;
- to perform poling of these films by electric voltage;
- to determine the porous structure characteristics, content of piezoactive  $\beta$ -crystallite modification and piezoelectric modulus.

## 2. Materials and Methods

Commercial PVDF grades Kynar 720 (Atofina Chemicals Inc., USA) with melt index 10 g/10 min (230 °C, 5 kg) and melting temperature 168 °C were used. The PVDF films were formed on a laboratory single screw extruder (Scamia, France) with a slit die. Two processing parameters were controlled at this stage: die gap and extruder screw speed. Other parameters such as uptake speed (3.2 meters per minute) and melt extrusion temperature (die temperature 200 °C) were kept constant. The melt draw ratio was varied by adjusting of screw speed and die gap (Table 1) and calculated as:

$$\lambda = S \cdot \rho \cdot l / m,$$

where  $S$  – the die gap area (cm<sup>2</sup>),  $\rho$  – density of the extruded film (1.78 g·cm<sup>-3</sup>),  $m$  and  $l$  – weight (g) and length (cm) of the extruded film piece. In this work  $\lambda$  was varied from 55 to 157 (Table 1).

TABLE 1. The effect of extrusion parameters on characteristics of the extruded PVDF films

Die gap, mm	Screw speed, s <sup>-1</sup>	Melt draw ratio	Thickness, μm
1.0	0.75	55	22
1.0	0.50	84	15
1.5	0.75	103	18
1.5	0.50	157	12

The extruded films were annealed under isometric conditions (at fixed ends of the sample to avoid the shrinkage of an oriented film at heating) during 1 h at a temperature near the melting point of the polymer (167 °C). The uniaxial extension of the annealed films was carried out in air in the orientation direction at a velocity of 40 mm/min. The first (“cold”) extension was carried out at room temperature up to 40 % elongation. However, cold drawing alone leads to the formation of porous structure, permeable to vapors and gases but not permeable to liquids because it has low porosity and does not contain through flow channels. To enlarge the number and sizes of pores the second (“hot”) extension stage was carried out at 100 °C up to 50 %. After the “hot” extension, the films were subjected to thermal stabilization under isometric conditions for 1 h at 100 °C to prevent shrinkage after stress relief and to take off the inner stress initiated by orientation.

The stress–strain curves were obtained at uniaxial extension of the annealed samples with sizes 5 × 50 mm at the rate 50 mm·min<sup>-1</sup> in a 2166 R-5 tensile test machine (Tochpribor, Russia). The stress-strain curves were used to determine yield stress, breaking strength, elastic modulus and break elongation. For each sample no less than five measurements were performed. The measurement error calculated as the standard deviation did not exceed 10 % of the average value of the determined characteristic. The annealed films were characterized by the value of elastic recovery  $ER_{50}$  which was measured at cyclic loading of the samples up to extension 50 % at velocity 50 %·min<sup>-1</sup>.  $ER_{50}$  was calculated in percents as ratio of recovery deformation of the sample to its total deformation at the first cycle.

The overall porosity of the samples was calculated by the Eq.:

$$P = [(\rho - \rho_p) / \rho] \times 100 \%,$$

where  $\rho_p$  is the density of the porous film, which was measured gravimetrically.

The permeability of the porous films to liquids was estimated by filtration porosimetry based on the flow of a liquid through the PVDF sample. This method is a nondestructive one and, in addition, it is similar to the operation conditions under which microfiltration membranes are usually used. Permeability measurement was performed in a filtration cell under a pressure of 0.5 MPa. Ethanol was used as a wetting liquid in the experiment. To measure the permeability of water, which is nonwetting liquid for PVDF, it was necessary previously to wet the sample previously by ethanol and then to flow water through the sample. The permeability value is inversely to liquid viscosity. Viscosities of ethanol and water at 20 °C are 1.197 and 1.006 mPa/s, respectively. It was tested that permeability to water is on 15 % higher than to ethanol for all porous samples.

The wide-angle X-ray scattering studies were performed using a DRON 2.0 diffractometer (Burevestnik, Russia) with CuK $\alpha$  radiation. Recording was carried out in a transmission mode. To determine the degree of orientation of the samples, azimuthal curves of intensity of reflection (110) were obtained. The degree of orientation was estimated by calculating the orientation factor through the following Eq. [31]:

$$f_c = \frac{3 \langle \cos^2 \varphi \rangle - 1}{2},$$

where  $\varphi$  is the angle between the extrusion direction and the crystalline chain axis.

It is known that, as a rule, the crystalline structure of PVDF samples contains the mixtures of polymorphous modifications, mainly,  $\alpha$  and  $\beta$  crystals. To characterize the sample, it is necessary to determine the portions of these crystalline phases. At the same time, the structural methods such as Infrared Spectroscopy (IR) and Differential Scanning Calorimetry (DSC) cannot be used to determine the percentage of crystalline phases in PVDF films: the IR spectra permit to characterize these phases qualitatively but not quantitatively because of difficulties in peaks resolution [28]. The same can be said about melting peaks on DSC. In the previous works (for example, 16, 17, 28), X-ray scattering was used to identify the crystalline phases in PVDF by recording the equatorial reflections located in the vicinity of  $2\theta = 20^\circ$ ,  $17.66^\circ$ ,  $18.30^\circ$ ,  $26.56^\circ$  for  $\alpha$ - and  $20.26^\circ$  for  $\beta$ - phases, respectively. It was shown that the diffraction peaks for the phases partially overlap with each other, and therefore, it is impossible to separate correctly

these reflections. In the present work, the meridian reflections disposed at 39° and 35° for  $\alpha$ - and  $\beta$ - modifications [32], respectively, were recorded in the orientation direction of the film in transmission mode to estimate quantitatively the content of these crystalline phases.

The degree of crystallinity was determined by the Hermans–Weidinger method [31] using the samples prepared by stacking of randomly oriented pieces of the porous films. The thickness of lamellae was determined by the half-width of the meridional reflex using the Debae–Scherrer formula. In earlier work [15] we measured thickness of lamellae in the extruded and annealed samples by small-angle X-ray scattering, and the values obtained by these methods differ by no more than 10 – 20 %. Thickness of lamellae in the samples formed at the extrusion and subsequent annealing was measured by small-angle X-ray scattering [15].

The porous structure parameters were calculated from the N<sub>2</sub> adsorption/desorption isotherms, which were obtained using Surface area analyzer “Sorbometr-M” (Katakon, Russia). The standard sample holder was loaded with pieces of the porous film with the total mass 0.15 – 0.25 g. The samples specific surface area was estimated from the Brunauer–Emmett–Teller (BET) model. The pore size distribution was obtained using the isotherm measured over the relative pressure range of ( $P_s/P_o$ ) from 0.30 to 0.99.

The surface and cross-section morphology of the samples were studied using scanning electron microscopy ZEISS MERLIN (Germany) at the voltage of 10 kV. Film cleavages were obtained by the brittle failure technique in liquid nitrogen.

The PVDF porous films were poled by a contact method of thermal poling. Aluminum adhesive tape was used as an electrode material. For electrical poling, metalized PVDF membrane was sandwiched between two electrodes in the poling setup which was set in a thermostat at 90 °C. The voltage between the electrodes was increased step-wise from zero to 105 V· $\mu\text{m}^{-1}$  at a rate of 50 V·min<sup>-1</sup>. A DC power supply B5-24A (Russia) was used to generate the desired electric potential difference. After that, the film was cooled to room temperature under the electric field. The experiment was repeated at least three times for each sample.

After the sample poling, the aluminum adhesive tape was carefully removed from the film, the surfaces was thoroughly cleaned by ethanol and metalized again with a liquid metal (eutectic gallium–indium–tin alloy) which was applied on the sample surface manually. The reason for the second metallization is that the adhesive conductive tapes don't allow registering the piezoresponse because of isolating action of a thin glue layer. To the contrary, the liquid metal can't be used for thermal polarization of permeable membranes because of increased probability of breakdown as a result of metal penetration into the through channels. The thin isolation glue layer of the aluminum adhesion tape acts as a breakdown protector for porous film polarization, but it has to be substituted for an appropriate contact electrode layer after the poling procedure.

Transverse piezoelectric coefficient  $d_{31}$  was measured by static tension applied to the polarized films with the liquid metal contacts along the orientation axis. Mechanical stress of the sample was set from 5 to 20 N (12 – 40 MPa). The potential difference at the contact electrodes of the sample at its deformation was measured using a R-30 potentiostat (Elins, Russia). Piezoelectric coefficient  $d_{31}$  was calculated by equation [34]:

$$d_{31} = \frac{C \cdot \Delta U \cdot B}{A \cdot \Delta F},$$

where  $C$  is the sum of capacities of the sample and a reference capacitor (1  $\mu\text{F}$ ),  $A$  is area of the electrodes on the sample surfaces (cm<sup>2</sup>),  $B$  is the cross-section area of the film (cm<sup>2</sup>),  $\Delta U$  is the voltage values (V), and  $F$  is an applied tensile force (N).

### 3. Results and discussion

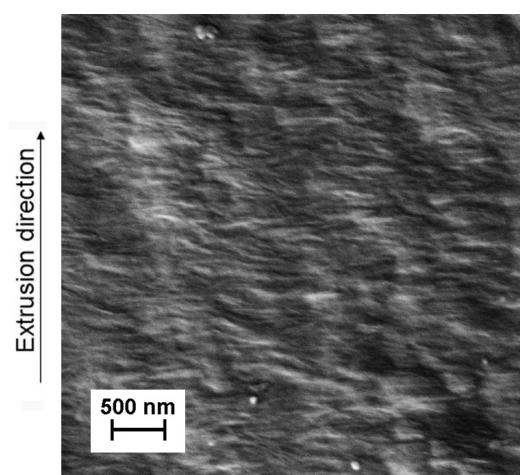
#### 3.1. Characterization of the extruded and annealed PVDF films

Due to melt drawing, the samples formed at extrusion stage have the oriented structure, and the orientation degree is determined by melt draw ratio  $\lambda$  (Table 2). This is displayed in the pictures of scanning electron microscopy (SEM) (Fig. 1), where the surface images of PVDF extruded films exhibits highly oriented lamellar stack morphology. It is known [10, 14, 15] that this structure is the most suitable for pores formation in the process of subsequent uniaxial extension which initiates moving apart of lamellae and appearance discontinuities between them. It was shown by X-ray data that the sizes of lamellae in PVDF extruded films were as 7 – 8 nm. These is values does not depend on  $\lambda$  because it is determined by crystallization temperature of the extruded films which was constant in the process of their solidification during film formation procedure.

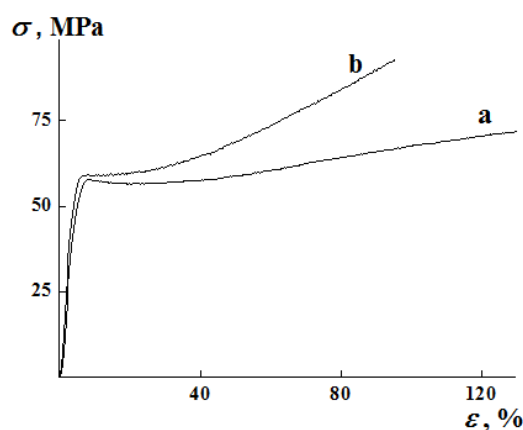
Isometric annealing of the extruded films at high temperature close to PVDF melting point is the important stage which makes it possible to enlarge orientation degree (annealing is carried out at the stress provided by fixation of the film ends) and also to increase considerably the thickness of lamellae which reaches 11 – 12 nm. As it can be seen from Table 2, the orientation factor of the annealed films increases from 0.90 to 0.97 as  $\lambda$  grows from 55 to 157.

TABLE 2. Orientation degree and mechanical characteristics of the annealed PVDF films

$\lambda$	$f_c$	Yield stress, MPa	Breaking strength, MPa	Young's modulus, MPa	Elongation at break, %	Elastic recovery, %
55	0.90	58	75	1460	130	71
84	0.93	59	81	1520	114	81
103	0.94	59	86	1570	94	87
157	0.97	60	98	1680	71	89

FIG. 1. SEM picture of surface for the extruded PVDF films formed at  $\lambda = 55$ 

Mechanical characteristics of the annealed films are also found to be dependent on melt draw ratio (Fig. 2). Breaking strength and elastic modulus increase with growth of  $\lambda$  (Table 2). At the same time, elongation at break decreases with increasing of  $\lambda$  that indicates a rising of their hardness.

FIG. 2. Stress-strain curves for annealed samples with  $\lambda = 55$  (a) and 103 (b)

Stress-strain curves analysis of the annealed PVDF films is useful for understanding of porous structure formation under uniaxial extension of the annealed samples (Fig. 2). The initial linear part of the stress-strain curves characterizes the elastic deformation of the samples up to the yield stress point. Yield stress is well pronounced for  $\lambda = 55$  but less and less observed for the samples as  $\lambda$  grows. In the second part of the curve, following an intermediate region, an almost linear increase in the stress (strain hardening) is observed. This increase is responsible for the elastic character of the lamellar deformation and growth of number and size of the pores. Fig. 2 demonstrates that the higher melt draw

ratio is the less pronounced the yield stress becomes, the higher the rupture strain and the more stronger the second slope which is responsible for the lamellar deformation. Thus at increasing of  $\lambda$  the annealed samples acquire “hard elastic” properties, namely, capability to large elastic reversible deformations. The cyclic loading (Fig. 3) demonstrates the “hard elasticity” of the annealed samples which were characterized by the value of elastic recovery  $ER_{50}$  as ratio of reversible deformation to total one. It is seen in Table 2 that  $ER_{50}$  increases with  $\lambda$ . It was shown [10,35] that hard elastic properties are the necessary condition for porous structure formation at subsequent extension.

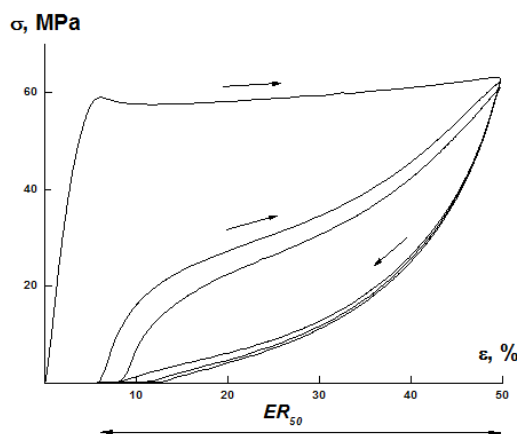


FIG. 3. Stressstrain curves for the annealed film with  $\lambda = 103$  under cyclic loading

### 3.2. Structure of the PVDF porous films

The influence of melt draw ratio on the structure of the porous PVDF films obtained by two-step – “cold” and then “hot” – uniaxial extension (40 and 50 %, respectively) is shown in Table 3. As it can be seen, the overall porosity of the film formed at  $\lambda = 55$  is 21 % while for the samples obtained at  $\lambda = 84 - 157$ , it reaches 26 – 28 %. According to the measurements by filtration porosimetry, the film prepared at  $\lambda = 55$  is impermeable while the samples extruded at  $\lambda = 84 - 157$  are permeable that is the evidence that these films contain through flow channels connecting two surfaces of the film providing them with through permeability. Thus, it can be concluded that the percolation threshold to reach the through permeability is found to lie around 25 % overall porosity that approximately corresponds to  $\lambda \sim 60 - 70$ . This result is in accordance with the porosity percolation threshold determined by percolation theory as 25 – 30 % [36]. It was confirmed for PE and PP porous films obtained by the same (“dry”) method [10, 35].

TABLE 3. Structure characteristics of PVDF porous films

Melt draw ratio	$\lambda = 55$	$\lambda = 84$	$\lambda = 103$	$\lambda = 157$
Thickness, $\mu\text{m}$	19	13	16	11
Overall porosity, %	21	26	27	28
Liquid permeability (ethanol), $\text{l}\cdot\text{m}^{-2}\cdot\text{h}^{-1}\cdot\text{atm}^{-1}$	Impermeable	1.1	0.9	1.3
Liquid permeability (water), $\text{l}\cdot\text{m}^{-2}\cdot\text{h}^{-1}\cdot\text{atm}^{-1}$	Impermeable	1.3	1.1	1.5
Degree of crystallinity, %	58	60	61	63
Content of $\beta$ -phase, %	38	31	20	15

It is seen in Table 3 that film permeability grows with increasing of  $\lambda$  and with decreasing of the die gap. This allows one to conclude that the optimal morphology for the effective through pores appearance at the stage of uniaxial extension is formed at the extrusion stage in the range of  $\lambda > 60 - 70$ .

Crystalline structure of the porous films was investigated by X-ray diffraction. According to the calculations of intensities of the meridional X-ray reflections, the crystalline phase of the extruded and annealed samples consists of

$\alpha$ -modification alone. It was found that all the microporous PVDF films contain a mixture of  $\alpha$ - and  $\beta$ -crystallites (Table 3 and Fig. 4).

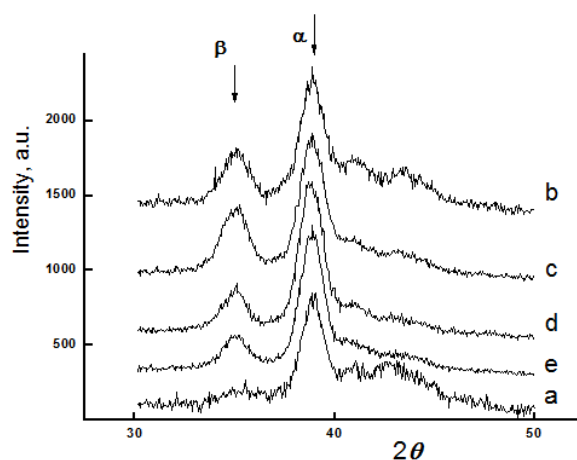


FIG. 4. Meridional X-ray diffractograms of the annealed (a) and porous PVDF films with  $\lambda = 55$  (b), 84 (c), 103 (d) and 157 (e)

In this preparation technique the porous structure formation and also  $\alpha > \beta$ -transition, both, are initiated by the uniaxial extension of the annealed PVDF films. Note that the data given in Table 3 demonstrates that the percentage of  $\beta$ -phase decreases with increasing of melt draw ratio. It may be explained by the fact that at lower orientation at the extrusion stage, the less perfect, weakly oriented crystals are formed (as compared with ones formed at higher  $\lambda$ ), and consequently it is easier to implement  $\alpha > \beta$ -transition on the subsequent uniaxial extension stage. At the same time, it was established in [29] that an increasing of orientation degree at extension leads to the growth of  $\beta$ -phase content for the films extruded at all  $\lambda$ .

### 3.3. Morphology of the porous PVDF films

The results of SEM investigations of the porous samples are presented at Fig. 5. The surface of the impermeable film ( $\lambda = 55$ , Fig. 5(a)) is filled with dense solidified structure elements, connected by fibrils. The surface structure is weakly oriented and has few ruptures (pores). In contrast, the permeable films surface ( $\lambda = 103, 157$ , Fig. 5(b,c)) has greater porosity and disrupted fibril-like ties inside the pores. This clearly illustrates the fact that at the extension of the annealed films obtained at the highest value of  $\lambda$  the mechanical stress leads to lamellar separation but not to reorientation, spherulites splitting and etc.

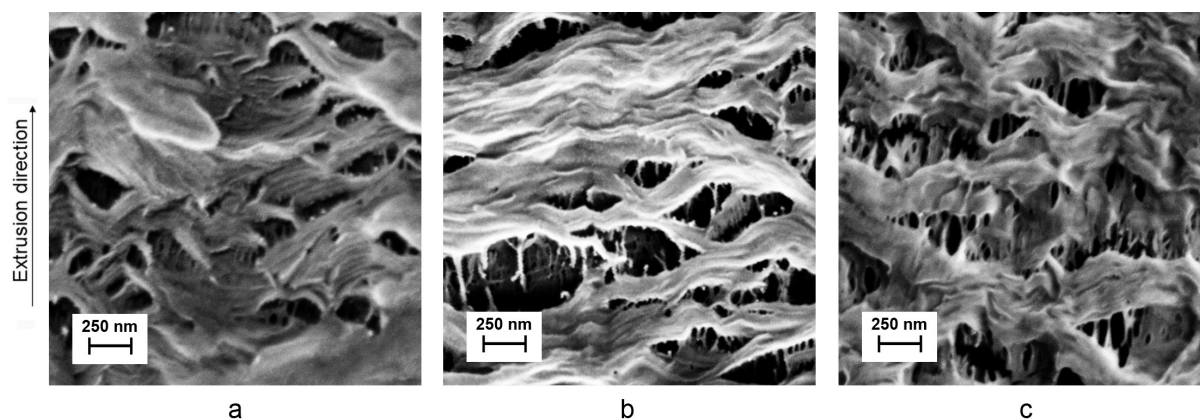


FIG. 5. SEM micrographs of surface of the PVDF porous films with  $\lambda = 55$  (a), 103 (b), 157 (c)

The denser structure with smaller pores can be noticed beneath the large, opened to surface pores (Fig. 5(b)). Electron microscopy of the porous films cross-section shows that the scale of surface structure elements differs from inner regions ones (Fig. 6). As it can be seen at Fig. 6, the morphology of the surface is characterized by the large

wavy structures which have a scale relief in submicro- and micrometer range  $0.1 - 1.0 \mu\text{m}$ . In contrast, in the inner part of the sample there are the smaller scale pores with the sizes less  $50 \text{ nm}$  located in the inter-lamellar regions (Fig. 6).

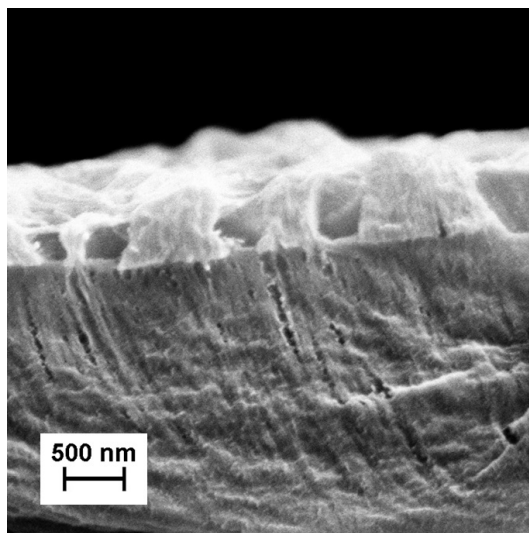


FIG. 6. SEM micrographs of cross-section of the permeable PVDF film ( $\lambda = 103$ )

Highly developed surface relief (Figs. 5–6) of the prepared porous films are able to produce a high specific surface area. Low-temperature gas adsorption method (method BET) gave specific surface of the permeable samples about  $37 \text{ m}^2 \cdot \text{g}^{-1}$ . Note that nonporous extruded and annealed films have specific surface in order  $10^{-3} \text{ m}^2 \cdot \text{g}^{-1}$ . The pores size distributions have a maximum in the range of diameters  $10 - 30 \text{ nm}$  (Fig. 7). Increasing of  $\lambda$  leads to a few shift of maximum of the curve to the larger sizes (at  $5 \text{ nm}$ ), and also to the growth of volume of pore space, i.e. number of pores. This provides evidence that the sizes  $10 - 50 \text{ nm}$  is a characteristic structural parameter for this system, and an increase in the permeability with orientation degree is mainly due to rising in the number of pores. It should be noted, that the pore size distribution calculated from adsorption isotherm (method Barrett–Joyner–Halenda) is in accordance with the SEM data of the sample cross-sections where the pores about  $15 - 50 \text{ nm}$  can be visually estimated (Fig. 6).

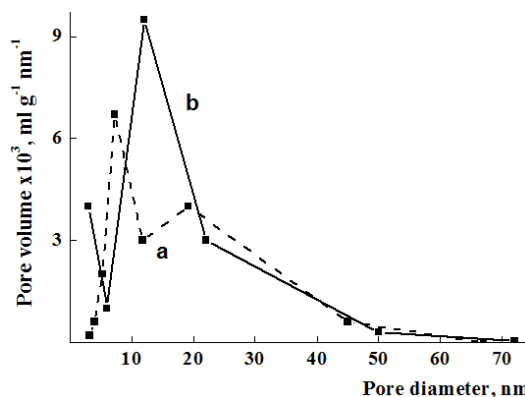


FIG. 7. Pores size distributions of the permeable porous PVDF film formed at  $\lambda = 55$  (a) and  $103$  (b)

Thus, investigations of permeable PVDF porous films performed by a number of experimental techniques demonstrate the complicated structure consisting of elements of different scale levels: surface relief is formed by structure details of micrometer scale, the sizes of pores are in the range of several tens of nanometers, and, at last, crystalline lamellae have the thickness of about  $10 \text{ nm}$ . However, the design of structure on the surface and inside the porous samples has the similar character that allows us to classify the sample structure as fractal.

Maximal permeability which have been reached in this work ( $1.3$  and  $1.5 \text{ l} \cdot \text{m}^{-2} \cdot \text{h}^{-1} \cdot \text{atm}^{-1}$  for flowing of ethanol and water, respectively) is rather small as compared with the PVDF films obtained by “wet method” which have the

larger pore sizes (50 – 300 nm) than our samples (Fig. 7). But the “wet method” process produces the membranes which are characterized by much wider pore size distribution, i.e. by low separation selectivity. And also, it is important to note, that “dry” technology is based on solvent-free and cost effective process comprising melt extrusion, thermal and mechanical treatments. Moreover, PVDF porous films prepared in this work have the additional functionality, namely, they demonstrate piezoactive properties.

### 3.4. Poling and stability of piezoelectric characteristics

To characterize the piezoelectric properties in porous PVDF films, the DC poling was performed for the impermeable ( $\lambda = 55$ ) and permeable ( $\lambda = 84$ ) ones. These samples possess the similar values of crystallinity but they have the different porosity and  $\beta$ -phase content (Table 3). It was found (Table 4) that the values of piezomodulus along the sample orientation ( $d_{31}$ ) are close to each other (10 – 11 pC·N<sup>-1</sup>) but have a tendency to decrease for the sample with lower content of piezoactive component. After the first month of storage at ambient conditions, the films' piezoelectric modulus decreased by  $\sim 15\%$  and  $27\%$  for impermeable and permeable samples, respectively. However after the next month of storage, both samples showed a high stability of polarization over time (Table 4). Note that the poling does not induce decreasing of permeability of the samples, which remains on the same level as it was before high voltage application (1.1 l·m<sup>-2</sup>·h<sup>-1</sup>·atm<sup>-1</sup>).

TABLE 4. Piezomodulus  $d_{31}$  (pC·N<sup>-1</sup>) of the microporous PVDF films with  $\lambda = 55$  and 84

Storage time	$\lambda = 55$ (impermeable)	$\lambda = 84$ (permeable)
Immediately after polarization	11.5	10.4
After 1 month	9.7	7.6
After 2 month	9.5	7.5

Thus, in this work, for the first time, for PVDF membranes were prepared by the a “dry method” the that attained both liquid permeability and piezoelectric response, both, are reached. These films may be used for electrically controlled systems design (piezosupercapacitors, piezobiosensors, oscillating fouling-resisted membranes and etc.).

## 4. Conclusions

Porous PVDF films which combine through permeability and also piezoactivity were successfully produced in the effective, ecologically safe manufacturing process based on polymer melt extrusion. The effect of melt draw ratio on the overall porosity and liquid permeability was investigated in this paper for the first time. Optimal operating parameters for melt extrusion were determined for successful pores nucleation and growth to reach the percolation threshold for the appearance of liquid permeability. The permeable membranes were obtained when extrusion process was performed at melt draw ratios higher than 60 – 70 which corresponds to the percolation threshold for overall porosity 23 %. At the higher melt draw ratios the permeability increases, but the overall porosity does not change. It was found that the films contained the pores with sizes 15 – 50 nm. The surfaces of the films were found to have a strongly developed relief with scale of relief in order 1 – 2  $\mu$ m. The content of  $\beta$ -phase in the permeable films having piezoproperties reaches more than 30 %. Hierarchy of structure elements on micro- and nano-scale levels have been investigated, and the possibility to regulate the characteristics of the samples by processing parameter at extrusion stage of the preparation process to reach the desired combination of properties was demonstrated. Also, new possibilities of poling were revealed for the permeable to liquids PVDF films which were successfully poled, and stable piezoelectric response was demonstrated. The “dry method” of porous PVDF piezoactive membranes preparation presented herein stimulates further research because the unique combination of their properties are of outstanding interest for a number of application fields such as membrane technology, storage, conversion and harvesting of energy.

## References

- [1] Davenport D.M., Gui M., Ormsbee L.R., Bhattacharyya D. Development of PVDF Membrane Nanocomposites via Various Functionalization Approaches for Environmental Applications. *Polymers*, 2016, **8** (32).
- [2] Ji J., Liu F., Hashim N.A., Abed M.R.M., Li K. Poly(vinylidene fluoride) (PVDF) membranes for fluid separation. *Reactive & Functional Polymers*, 2015, **86**, P. 134–153.
- [3] Kang G., Cao Y. Application and modification of poly(vinylidene fluoride) (PVDF) membranes – A review. *Journal of Membrane Science*, 2014, **463**, P. 145–165.

- [4] Liu F., Hashim N.A., et al. Progress in the production and modification of PVDF membranes. *Journal of Membrane Science*, 2011, **375**(1–2), P. 1–27.
- [5] Lai Ch.Y., Groth A., Gray S., Duke M. Nanocomposites for Improved Physical Durability of Porous PVDF Membranes. *Membranes*, 2014, **4** (1), P. 55–78.
- [6] Zhang Q., Lu X., Zhao L. Preparation of Polyvinylidene Fluoride (PVDF) Hollow Fiber Hemodialysis Membranes. *Membranes*, 2014, **4** (1), P. 81–95.
- [7] Liu F., Xu Y.Y., et al. Preparation of hydrophilic and fouling resistant poly(vinylidene fluoride) hollow fiber membranes. *Journal of Membrane Science*, 2009, **345** (1–2), P. 331–339.
- [8] Kima J.F., Jung J.T., et al. Microporous PVDF membranes via thermally induced phase separation (TIPS) and stretching methods. *Journal of Membrane Science*, 2016, **509**, P. 94–104.
- [9] Cui Z.Yu., Xu Y.Y., et al. Preparation of PVDF/PMMA blend microporous membranes for lithium ion batteries via thermally induced phase separation process. *Materials Letters*, 2008, **62** (23), P. 3809–3811.
- [10] Kuryndin I.S., Lavrentyev V.K., Bukoek V., Elyashevich G.K. Percolation transitions in porous polyethylene and polypropylene films with lamellar structures. *Polymer Science, Ser. A*, 2015, **57** (6), P. 717–722.
- [11] Lee S.Y., Park S.Y., Song H.S. Lamellar crystalline structure of hard elastic HDPE films and its influence on microporous membrane formation. *Polymer*, 2006, **47** (10), P. 3540–3547.
- [12] Johnson M.B., Wilkes G.L. Microporous membranes of isotactic poly(4-methyl-1-pentene) from a melt-extrusion process. I. Effects of resin variables and extrusion conditions. *J. Appl. Polym. Sci.*, 2002, **83** (10), P. 2095–2113.
- [13] Xu J., Johnson M., Wilkes G.L. A tubular film extrusion of poly(vinylidene fluoride): structure/process/property behavior as a function of molecular weight. *Polymer*, 2004, **45** (15), P. 5327–5340.
- [14] Du C.H., Zhu B.K., Xu Y.Y. A study on the relationship between the crystal structure and hard elasticity of PVDF fibers. *Macromol. Mater. Eng.*, 2005, **290** (8), P. 786–791.
- [15] Dmitriev I.Yu., Bukošek V., Lavrentyev V.K., Elyashevich G.K. Structure and Deformational Behavior of Poly(vinylidene fluoride) Hard Elastic Films. *Acta Chimica Slovenica*, 2007, **54** (4), P. 784–791.
- [16] Sadeghi F., Tabatabaei S.H., Ajji A., Carreau P.J. Effect of PVDF Characteristics on Extruded Film Morphology and Porous Membranes Feasibility by Stretching. *Journal of Polymer Science: Part B: Polymer Physics*, 2009, **47** (12), P. 1219–1229.
- [17] Hu B., Cai Q., et al. Influence of uniaxial cold stretching followed by uniaxial hot stretching conditions on crystal transformation and microstructure in extrusion cast and annealed polyvinylidene fluoride porous membranes. *Journal of Plastic Film & Sheeting*, 2015, **31** (3), P. 269–285.
- [18] Ramadan K.S., Sameoto D., Evoy S. A review of piezoelectric polymers as functional materials for electromechanical transducers. *Smart Mater. Struct.*, 2014, **23** (3), Article ID 033001.
- [19] Wan C., Bowen C.R. Multiscale-structuring of polyvinylidene fluoride for energy harvesting: the impact of molecular-, micro- and macro-structure. *J. Mater. Chem. A*, 2017, **5** (7), P. 3091–3128.
- [20] Darestani M.T., Coster H.G.L., et al. Piezoelectric membranes for separation processes: Fabrication and piezoelectric properties. *Journal of Membrane Science*, 2013, **434**, P. 184–192.
- [21] Darestani M.T., Coster H.G.L., Chilcott T.C. Piezoelectric membranes for separation processes: Operating conditions and filtration performance. *Journal of Membrane Science*, 2013, **435**, P. 226–232.
- [22] Mao H., Qiu M., et al. Self-cleaning Piezoelectric Membrane for Oil-in-water Separation. *ACS Appl. Mater. Interfaces*, 2018, **10** (21), P. 18093–18103.
- [23] Bae J., Baek I., Choi H. Efficacy of piezoelectric electrospun nanofiber membrane for water treatment. *Chemical Engineering Journal*, 2017, **307**, P. 670–678.
- [24] Lu X., Guo Q., et al. Biosensor platform based on stress-improved piezoelectric membrane. *Sensors and Actuators A: Physical*, 2012, **179**, P. 32–38.
- [25] Xue X., Wang S., et al. Hybridizing Energy Conversion and Storage in a Mechanical-to-Electrochemical Process for Self-Charging Power Cell. *Nano Lett.*, 2012, **12** (9), P. 5048–5054.
- [26] Song R., Jin H., et al. A rectification-free piezo-supercapacitor with a polyvinylidene fluoride separator and functionalized carbon cloth electrodes. *J. Mater. Chem. A*, 2015, **3** (29), P. 14963–14970.
- [27] Ghosh S.K., Sinha T.K., et al. Porous polymer composite membrane based nanogenerator: A realization of self-powered wireless green energy source for smart electronics applications. *J. Appl. Phys.*, 2016, **120** (17), Article ID 174501.
- [28] Martins P., Lopes A.C., Lanceros-Mendez S. Electroactive phases of poly(vinylidene fluoride): Determination, processing and applications. *Progress in Polymer Science*, 2014, **39** (4), P. 683–706.
- [29] Dmitriev I.Yu., Kuryndin I.S., Lavrentyev V.K., Elyashevich G.K. Structure and Piezoelectric Properties of Microporous Polyvinylidene Fluoride Films. *Physics of the Solid State*, 2017, **59** (5), P. 1041–1046.
- [30] Chen D., Zhang J.X.J. Microporous polyvinylidene fluoride film with dense surface enables efficient piezoelectric conversion. *Appl. Phys. Lett.*, 2015, **106** (19), Article ID 193901.
- [31] Hermans P.H., Weidinger A. On the determination of the crystalline fraction of polyethylenes from X-ray diffraction. *Macromol. Chem.*, 1961, **44** (1), P. 24–36.
- [32] Nakamura K., Sawai D., et al. Effect of annealing on the structure and properties of poly(vinylidene fluoride)  $\beta$ -form films. *Journal of Polymer Science: Part B: Polymer Physics*, 2003, **41** (14), P. 1701–1712.
- [33] Amoresi R.A.C., Felix A.A., et al. Crystallinity, Morphology and High Dielectric Permittivity of NiO Nanosheets Filling Poly(vinylidene fluoride). *Ceramics International*, 2015, **41**, P. 14733–14739.
- [34] Haghiashtiani G., Greminger M.A. Fabrication, polarization, and characterization of PVDF matrix composites for integrated structural load sensing. *Smart Mater. Struct.*, 2015, **24**, Article ID 045038.
- [35] Elyashevich G.K., Kuryndin I.S., et al. Porous Structure, Permeability, and Mechanical Properties of Polyolefin Microporous Films. *Physics of the Solid State*, 2012, **54** (9), P. 1907–1916.
- [36] Stauffer D., Aharony A. *Introduction to Percolation Theory*, Taylor and Francis, London, 1994, 192 p.

## Low coercivity microwave ceramics based on LiZnMn ferrite synthesized via glycine-nitrate combustion

K. D. Martinson<sup>1,2</sup>, S. S. Kozyritskaya<sup>1</sup>, I. B. Panteleev<sup>1</sup>, V. I. Popkov<sup>1,2,3</sup>

<sup>1</sup>Saint Petersburg State Institute of Technology (Technical University), Moskovskiy pr. 26, Saint Petersburg, 190013, Russia

<sup>2</sup>Ioffe Institute, Politechnicheskaya 26, Saint Petersburg, 194021, Russia

<sup>3</sup>Saint Petersburg University, 26 Universitetskii prospect, Saint Petersburg, 198504, Russia

[martinsonkirill@mail.ru](mailto:martinsonkirill@mail.ru)

DOI 10.17586/2220-8054-2019-10-3-313-317

Soft magnetic LiZnMn ferrite with low coercivity obtained via glycine-nitrate combustion was estimated in this work. According to SEM, the synthesized ceramics have a grain size ranging from 1.5 to 8  $\mu\text{m}$  and the EDX, AAS and XRD data show that the obtained samples correspond to  $\text{Li}_{0.45}\text{Zn}_{0.05}\text{Mn}_{0.06}\text{Fe}_{2.43}\text{O}_4$  structure. The hysteresis loops of LiZnMn ferrite ceramics provide evidence for the magnetically soft nature of the obtained materials. Basic magnetic characteristics, including remanent magnetization, saturation magnetization, and coercive force was also described. For a sample sintered at 1000 °C, the values of saturation magnetization ( $4\pi M_s$ ), residual magnetization ( $B_r$ ) and coercive force ( $H_c$ ) were 2644 G, 2139 G and 6.4 Oe, respectively, whereas the sample obtained at 1070 °C shows large values of saturation magnetization (3240 G) and residual magnetization (2459 G) and the coercive force is approximately half (3.4 Oe). Analysis of the influence of thermal treatment provided the possibility to determine necessary conditions for obtaining microwave ceramics based on LiZnMn ferrite via solution combustion method. Grain size distribution was examined to determine their influence on the properties of obtained ceramics.

**Keywords:** microwave ceramics, spinel ferrites, solution combustion synthesis, soft magnetics.

*Received:* 18 June 2019

*Revised:* 20 June 2019

### 1. Introduction

During the last few decades, the rapid development of microwave technologies has aroused an increased interest in classical high-frequency materials and imposed a new requirement on their electromagnetic parameters [1–3]. Some LiZnMn ferrites have been widely used in microwave devices due to their low coercive forces ( $H_c$ ), high remanent and saturation magnetizations ( $M_r$  and  $M_s$ ), great mechanical and chemical stabilities, rectangular hysteresis loop, etc. [4–7]. The electromagnetic properties of LiZnMn ferrites depend on factors such as the type of synthesis, degree of crystallinity, particle and grains size, degree of homogeneity for particle and grain sizes [8, 9]. There are many techniques to obtain lithium ferrites, for example, microwave sintering which is the most popular at the moment but has some significant flaws such as long synthesis time, the large grain size of the resulting product and high heterogeneity degree of their size, which negatively affects the final electromagnetic parameters of ceramics [10–13]. One of the more promising methods for obtaining ferrites, which allows improving the above parameters, is the solution combustion method. This method can result in the synthesis of ferrites with small particle and grain sizes, high density and conversion degree, excellent electromagnetic parameters and uniform microstructure [14–19].

In this work, the glycine-nitrate combustion process has been used for preparing initial LiZnMn ferrite powder using glycine as chelating reagent with ratio  $G/N = 1.5$  (where G is the glycine mole fraction and N is the nitrate mole fraction). There is the relatively large number of different chelating reagents, such as some organic acids, hydrazine, urea, and others but using the glycine can reduce the amount of residual organic compounds in the final product due to its lower molecular weight than other chelating agents have [20–22]. The received product of glycine-nitrate combustion was heat sintered at various temperatures (1000 and 1070 °C) as a result; microwave ceramics with low coercivity force were obtained.

## 2. Experimental

This work is devoted to the investigation of microwave ceramics based on the  $\text{Li}_{0.45}\text{Zn}_{0.05}\text{Mn}_{0.06}\text{Fe}_{2.43}\text{O}_4$  obtained via glycine-nitrate combustion method. The synthesis was performed under conditions of deficit of the chelating agent ( $G/N = 1.5$ ) in the reaction mixture. Initial lithium, zinc, manganese, and iron crystalline nitrates were dissolved in 100 ml of deionized water and 10 ml of 3M  $\text{HNO}_3$  with constant stirring for 2 hours and temperature of 50 °C. Then glycine was added to the reaction solution in an amount exceeding the stoichiometric ratio of 1.5. The solution prepared this way was heated to its autoignition point. During the autoignition process, the brown powder was obtained which was mechanically ground in an agate mortar. The final product was thermally treated at a temperature of 500 °C for 3 hours.

The obtained powder was mechanically processed in a vibration mill (ball diameter = 2 cm) for 2 hours with the addition of bismuth oxide ( $\text{LiZnMn:Bi}_2\text{O}_3$  to 95:5 wt. %) and polyethylene glycol as a binder. The addition of bismuth oxide reduces the sintering temperature, however, despite the fact that its effect on the sintering of lithium ferrites is well studied for solid-phase methods [4], due to the significantly smaller particle size of the original powder and, as a result, a higher specific surface area, the amount of bismuth oxide required to successfully lower the temperature is much higher. Sintering ceramics was carried out at two temperatures (1000 and 1070 °C). The two selected sintering temperatures are most common when lithium-zinc-manganese sintering a ferrite of the similar composition [8, 23].

Qualitative X-ray phase analysis and crystal structure refinement was performed using Rigaku SmartLab 3 powder diffractometer. The average crystallite size (coherent scattering area) was calculated from X-ray diffraction lines broadening using the Scherrer equation:

$$D = \frac{k \cdot \lambda}{\beta \cdot \cos \theta},$$

where  $k$  is the crystal shape factor (assumed to be 0.94 in the isometric approximation),  $\lambda$  is the X-ray emission wavelength ( $\text{CuK}_\alpha$ ,  $\lambda = 0.15406$  nm),  $\beta$  is the diffraction maximum broadening (in radians),  $\theta$  is the diffraction peak position (Bragg angle).

The chemical composition and morphology were determined using a TescanVega 3 SBN scanning microscope equipped with an Oxford INCA  $x$ -act  $x$ -ray spectral microanalysis device and atomic absorption spectrometer AA-7000. The measurement of the magnetic properties was conducted on the vibrating magnetometer Lake Shore 7400. The magnetic characteristics according to the hysteresis loop data were calculated using the vibration method built in the magnetometer's software on vibration magnetometer Lake Shore 7410. Dynamic light scattering and SEM microphotographs were used to determine the average grain size of  $\text{LiZnMn}$  ceramics obtained at different temperatures. The measurements were carried out using a Shimadzu SALD-7500 nano.

## 3. Results and discussion

The phase composition of the obtained  $\text{Li}_{0.45}\text{Zn}_{0.05}\text{Mn}_{0.06}\text{Fe}_{2.43}\text{O}_4$  powder and ceramics were determined by X-ray powder diffractometry. The obtained data show that initial ferrite powder consists of single-phase lithium-zinc-manganese ferrite (JCPDS card # 52-0278) with an average crystallite size of  $25 \pm 3$  nm (Fig. 1). The conversion degree of synthesized powder was determined to be 95% using an internal standard ( $\alpha$ -Si).

Diffractograms of the lithium-zinc-manganese ferrite sintered at 1000 and 1070 °C also show the absence of extraneous phases. The high intensity of the peaks indicates that the obtained ceramics have a high conversion. However, the peak intensities of the obtained sample at 1070 °C are higher than those for the sample sintered at 1000 °C, which indicates a more complete degree of sintering.

The elemental composition and morphology of the obtained lithium-zinc-manganese ferrite were determined by X-ray microanalysis, atomic absorption spectroscopy, and scanning electron microscopy. According to elemental analysis data, the obtained ferrite corresponds to the composition of  $\text{Li}_{0.45}\text{Zn}_{0.05}\text{Mn}_{0.06}\text{Fe}_{2.43}\text{O}_4$ . Fig. 2 shows the results of SEM for the  $\text{LiZnMn}$  ferrite ceramics samples sintered at 1000 and 1070 °C. The obtained data suggest that ceramics with grain size from 0.5–10  $\mu\text{m}$  are obtained at both temperatures. In the case of a sample sintered at a temperature of 1000 °C, porous ceramics are observed with an average grain size of 0.5–4.5  $\mu\text{m}$ . The presence of a large number of voids and the appearance of the grains is most likely due to the fact that the lithium-zinc-manganese ferrite ceramics is not completely sintered at a given temperature. In the case of a sample that was sintered at a temperature of 1070 °C the sintering passed completely, which indirectly confirms the XRD data. However, there is an increase in grain size, which ranges from 2–10  $\mu\text{m}$ .

The grain size distribution was determined by a dynamic light scattering method (Fig. 3c and Fig. 3d) and by the analysis of the micrographs in the OriginPro software package (Fig. 3a and Fig. 3b). The obtained data correlate well with each other and indicate that the average crystallite size ranges from 0.5–10  $\mu\text{m}$ . In the case of results obtained

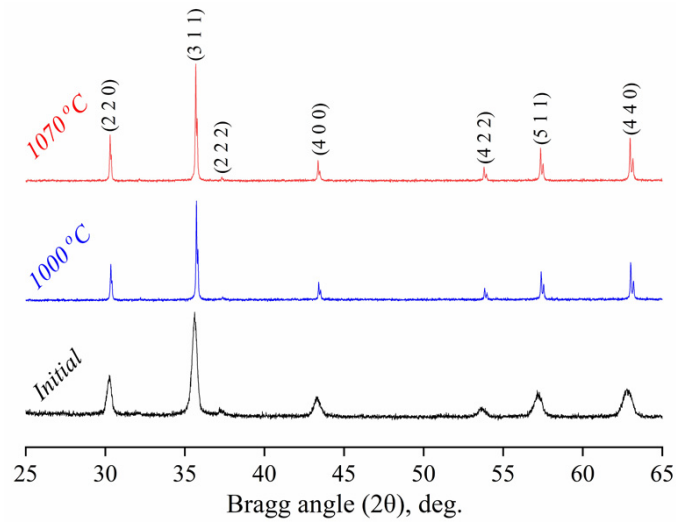


FIG. 1. X-ray diffraction patterns of  $\text{Li}_{0.45}\text{Zn}_{0.05}\text{Mn}_{0.06}\text{Fe}_{2.43}\text{O}_4$  initial powder and ceramics

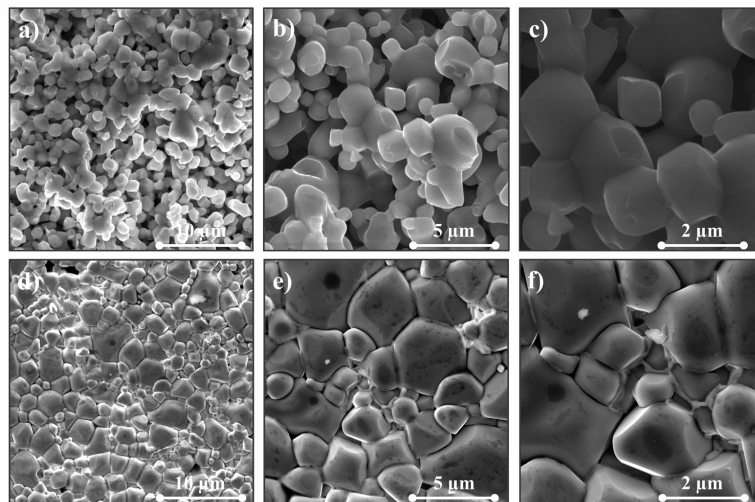


FIG. 2. SEM results of the LiZnMn ferrite ceramics sintered at 1000 and 1070 °C

by the method of dynamic light scattering, the distribution is shifted to the right side in relation to the results of micrographs analysis, which is associated with an insufficient degree of separation of one grain from another.

Figure 4 shows the saturated B–H hysteresis loops at 298 K for lithium-zinc-manganese samples sintered 1000 and 1070 °C. The obtained data indicate that the hysteresis loop of the sample sintered at 1070 °C degrees is approximately half that of the loop for the sample obtained at 1000 °C.

The data in Fig. 5 demonstrate that the saturation magnetization, residual magnetization, and coercive force depended on the sintering temperature.

The saturation magnetization is 2644 G and 3240 G for samples obtained at 1000 and 1070 °C, respectively. Residual magnetization is also higher for a sample sintered at a temperature of 1070 °C (2139 G vs 2458 G). However, the coercive force for a sample sintered at 1000 °C (6.4 Oe) is rough twice the size of the value obtained for a sample sintered at 1070 °C (3.4 Oe). These differences in the magnetic parameters of the obtained ceramic samples are related to both the grain size and to the incomplete degree of sintering of the sample obtained at 1000 °C.

#### 4. Conclusions

The present paper shows the possibility of producing a soft-magnetic low coercivity lithium-zinc-manganese ceramics based on ferrite powder obtained via glycine-nitrate combustion method. The obtained powder and ceramics are chemically and phase-pure and does not contain non-magnetic phases. The low coercivity force (6.4 and 3.4 Oe),

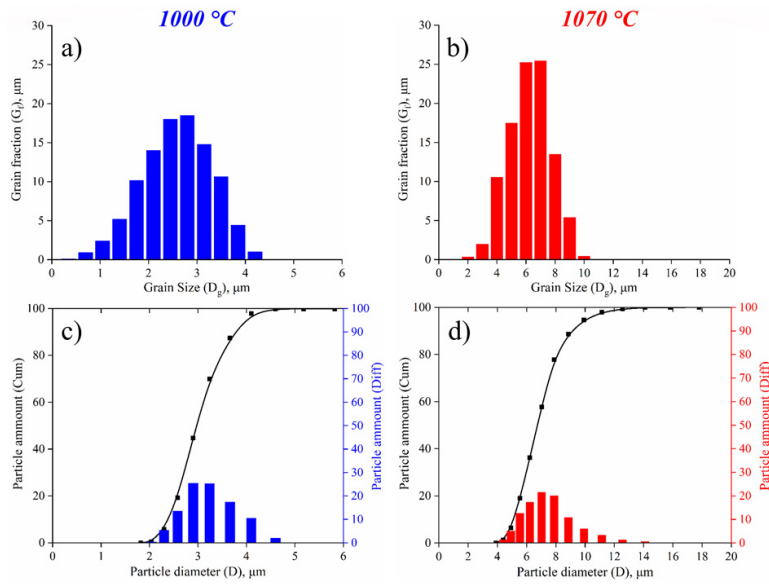


FIG. 3. The grain size distribution of the obtained samples of  $\text{Li}_{0.45}\text{Zn}_{0.05}\text{Mn}_{0.06}\text{Fe}_{2.43}\text{O}_4$  ceramics sintered at temperatures of 1000 and 1070 °C

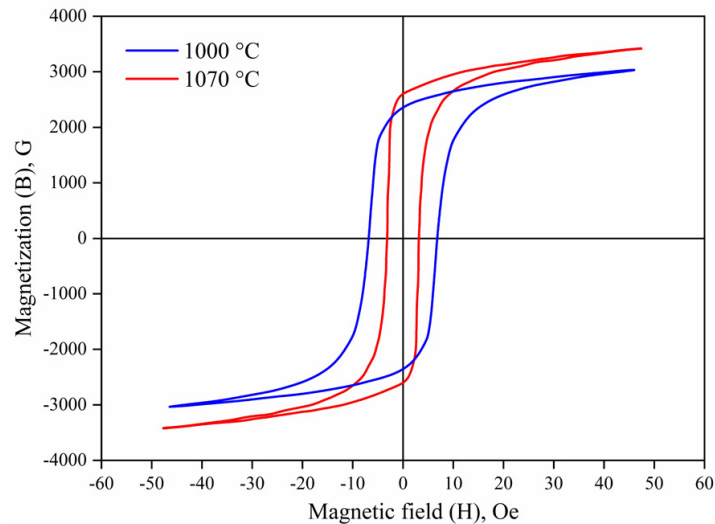


FIG. 4. B-H hysteresis loops of LiZnMn ceramics samples at 298 K

saturation magnetization (3240 and 2644 G) and residual magnetization (2459 and 2139 G) are at the same level as commercial high-frequency ceramics. It is shown that the sintering temperature strongly influences the magnetic characteristics of the obtained ceramics and allows a two-fold reduction in their coercive force.

## References

- [1] Asilqbal M., Islam M.U., Ali I., et. al. Study of physical, magnetic and electrical properties of rare-earth substituted Li-Mg ferrites. *Journal of alloys and compounds*, 2017, **692**, P. 322–331.
- [2] Lin Y., Don J.g, Dai J., et. al. Facile synthesis of flowerlike  $\text{LiFe}_5\text{O}_8$  microspheres for electrochemical supercapacitors. *Inorganic chemistry*, 2017, **56**, P. 14960–14967.
- [3] Abdel-Ghany A.E., Mauger A., Groult H., et. al. Structural properties and electrochemistry of  $\alpha\text{-LiFeO}_2$ . *Journal of Power Sources*, 2012, **197**, P. 285–291.
- [4] Guo R., Yu Z., Jiang X., et. al. Dispersion spectra of permeability and Permittivity for LiZnMn ferrite doped with  $\text{Bi}_2\text{O}_3$ . *IEEE Transactions of magnetics*, 2013, **49**, P. 4295–4298.
- [5] Guo R., Yu Z., Yand Y., et. al. Effects of  $\text{Bi}_2\text{O}_3$  on FMR linewidth and microwave dielectric properties of LiZnMn ferrite. *Journal of Alloys and Compounds*, 2014, **589**, P. 1–4.

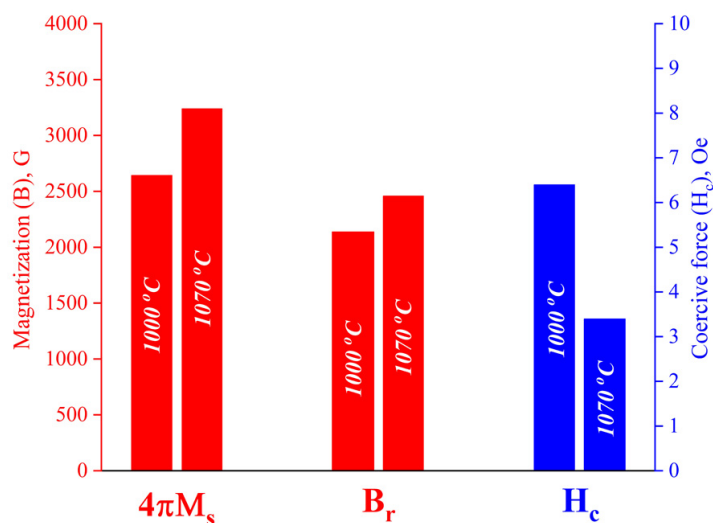


FIG. 5. Saturation magnetization, residual magnetization and coercive force of LiZnMn ceramics

- [6] Silakate S., Wannagon A., Nuntiya A. Influence of ferric oxide on the crystallization of Li-Zn ferrite anorthite and hematite phases at low-temperature ceramic glaze. *Journal of European Ceramic Society*, 2015, **35**, P. 2183–2188.
- [7] Kumar P., Juneja J.K., Prakash C., et. al. High DC resistivity in microwave sintered  $\text{Li}_{0.49}\text{Zn}_{0.02}\text{Mn}_{0.06}\text{Fe}_{2.43}\text{O}_4$  ferrites. *Ceramics International*, 2014, **40**, P. 2501–2504.
- [8] Sanatombi S., Sumitra S., Ibetombi S. Influence of sintering on the structural, electrical and magnetic properties of Li-Ni-Mn-Zn ferrite synthesized by citrate precursor method. *Iranian Journal of Science and Technology*, 2018, **42**, P. 2397–2406.
- [9] Teo M.L.S., Kong L.B., Li Z.W., et. al. Development of magneto-dielectric materials based on Li-ferrite ceramics. Densification behavior and microstructural development. *Journal of Alloys and Compounds*, 2008, **459**, P. 557–566.
- [10] Dai Y.M., Wang Y.F., Chen C.C. Synthesis and characterization of magnetic  $\text{LiFe}_5\text{O}_8$ - $\text{LiFeO}_2$  as a solid basic catalyst for biodiesel production. *Catalysis Communications*, 2018, **106**, P. 20–24.
- [11] Wu H., Li H., Sun G., et. al. Synthesis, characterization and electromagnetic performance of nanocomposites of graphene with  $\alpha$ - $\text{LiFeO}_2$  and  $\beta$ - $\text{LiFe}_5\text{O}_8$ . *Journal of Materials Chemistry*, 2015, **21**, P. 1–11.
- [12] Srivastava M., Layek S., Singh J., et. al. Synthesis, magnetic and mössbauer spectroscopic studies of Cr doped lithium ferrite nanoparticles. *Journal of Alloys and Compounds*, 2014, **591**, P. 174–180.
- [13] Sohn R.S., Macedo A.A.M., Costa M.M., et. al. Studies of the structural and electrical properties of lithium ferrite ( $\text{LiFe}_5\text{O}_8$ ). *Physica Scripta*, 2010, **82**, P. 1–6.
- [14] Martinson K.D., Kondrashkova I.S., Popkov V.I. Synthesis of  $\text{EuFeO}_3$  nanocrystals by glycine-nitrate combustion method. *Russian Journal of Applied Chemistry*, 2017, **90**, P. 1214–1218.
- [15] Bachina A., Ivanov V.A., Popkov V.I. Peculiarities of  $\text{LaFeO}_3$  nanocrystals formation via glycine-nitrate combustion. *Nanosystems: Physics, Chemistry, Mathematics*, 2017, **8**, P. 647–653.
- [16] Rubalajyothi P., Nehru L.C. Photoluminescence characterization of nanocrystalline  $\text{Ba}_{0.97}\text{Ca}_{0.03}\text{SO}_4$ :Eu by combustion method. *Nanosystems: Physics, Chemistry, Mathematics*, 2015, **3**, P. 561–565.
- [17] Martinson K.D., Cherepkova I.A., Sokolov V.V. Formation of cobalt ferrite nanoparticles via glycine-nitrate combustion and their magnetic properties. *Glass Physics and Chemistry*, 2018, **44**, P. 21–25.
- [18] Kondrashkova I.S., Martinson K.D., Zakharova N.V., Popkov V.I. Synthesis of nanocrystalline  $\text{HoFeO}_3$  photocatalyst via heat treatment of products of glycine-nitrate combustion. *Russian Journal of General Chemistry*, 2018, **88**, P. 2465–2471.
- [19] Popkov V.I., Almjasheva O.V., Nevedomskiy V.N., et. al. Crystallization behavior and morphology of  $\text{YFeO}_3$  nanocrystallites obtained by glycine-nitrate combustion. *Nanosystems: Physics, Chemistry, Mathematics*, 2015, **6**, P. 866–874.
- [20] Zhang D., McCartney D.G. Quantitatively evaluating the effect of oxygen/fuel ratio on  $\text{Fe}^{2+}$  content in HVOF-Sprayed Ni-Zn ferrite coatings. *ASM International*, 2009, **18**, P. 343–352.
- [21] Popkov, Almjasheva O.V. Yttrium Orthoferrite  $\text{YFeO}_3$  Nanopowders Formation under Glycine-Nitrate Combustion Conditions. *Russian Journal of Applied Chemistry*, 2014, **87**, P. 167–171.
- [22] Dyachenko S.V., Martinson K.D., Cherepkova I.A., Zhernovoi A.I. Particle size, morphology, and properties of transition metal ferrosinels of the  $\text{MFe}_2\text{O}_4$  (M = Co, Ni, Zn) type, produced by glycine-nitrate combustion. *Russian Journal of Applied Chemistry*, 2016, **89**, P. 535–539.
- [23] Zhao T., Qin Y., Zhang P., et. al. High-performance, reaction sintered lithium disilicate glass-ceramics. *Ceramics International*, 2014, **40**, P. 12449–12457.

## The use of nanocluster polyoxometalates in the bioactive substance delivery systems

A. A. Ostroushko<sup>1</sup>, I. D. Gagarin<sup>1</sup>, I. G. Danilova<sup>1,2</sup>, I. F. Gette<sup>1,2</sup>

<sup>1</sup>Ural Federal University named after the first President of Russia B. N. Yeltsin, Ekaterinburg, Russia

<sup>2</sup>Institute of Immunology and Physiology of the Ural Branch of the Russian Academy of Sciences,  
Ekaterinburg, Russia

alexander.ostroushko@urfu.ru

DOI 10.17586/2220-8054-2019-10-3-318-349

Nanoscale systems occupy the most important place among the vehicles intended for targeted drug delivery. Such vehicles are considered in this review. Attention is paid to the nanocluster polyoxometalate-based systems which are promising for transdermal iontophoretic transport. In this relation, and due to the characteristics of the skin as a transport medium, the problems of the transfer processes modeling are considered.

**Keywords:** nanocluster polyoxometalates, targeted drug delivery systems, transcutaneous iontophoretic transport.

*Received: 3 June 2019*

### 1. Introduction

The development of differently structured nanosystems for targeted delivery of bioactive substances and drugs [1–20] is currently receiving much attention. These systems can improve the drug action efficiency and selectivity, reduce side effects and decrease the dose used. This refers, for example, to cytostatics [21–26], to other drugs and substances, including those that work synergistically and are co-transported together [27–33]. It should be noted in general that the number of reviews and original publications that consider certain aspects of formation and use of the nanostructured targeted delivery systems is large globally and is constantly growing. In particular, Springer Publishing have released a series of books that widely address these matters [34–37]. The present review considers the classification of the organizational levels of the means of targeted drug delivery, including the nano-level, of passive and active methods for implementing delivery processes, and raises some issues related to obtaining these means. The peculiarities of the skin as a transport medium for nanoscale objects, the problems of physical chemistry and mathematical modeling of transcutaneous drug transport, including electrophoretic delivery, are considered. The prospects for using the targeted delivery systems are studied for developing such a class of compounds as polyoxometalates (POM), in particular, molybdenum-containing ones, and their physicochemical properties and metabolic impacts are assessed.

### 2. Organizational levels of targeted drug delivery systems

#### 2.1. Brief historical note, transition to nanosystems

In his review article [38], Allan S. Hoffman has distinguished three “eras” in the development of targeted drug delivery systems, namely the “MACRO”, “MICRO” and “NANO” eras. In the “MACRO era” times, such controlled release systems as patches, ophthalmic systems for antiglaucoma preparations, silicone-based devices containing contraceptive substances, and systems based on swelling polymer gels [38] were created. The “MICRO era” was characterized by the creation of systems with the sustained release of biodegradable microparticles and of the phase-separated depots. The development of the biodegradable suture polymers was underway in the 1960s and 1970s, and in the 1970s this technology was borrowed for targeted drug delivery and refined to make its clinical use possible in the 1980s. The pioneering work of Langer and Folkman, who showed that proteins could be released from non-degradable polymer matrices, has stimulated researchers to think about alternative ways of drug delivery by using biodegradable polymers [39].

The “NANO era” of targeted or site-controlled systems yielded three key technologies. The first concept is the creation of drugs conjugated to polyethylene glycol (PEG) molecules. The second technology is the “active targeting” of an antibody-conjugated drug to cellular receptors [38]. The third is the use of the “enhanced permeation and retention effect”, the essence of which is in the entrapment of nano-sized carriers within a solid tumor due to the leaky vasculature of a rapidly-growing tumor [40]. In this case, a nanoparticle can serve both as the directly acting agent and as a nanocontainer (core), that is, a carrier for an active agent. In both cases, the development of nanopreparations requires the solution of a number of issues, such as their stability in and safety for the body; delivery to pathological structures, penetration into them and effective impact; as well as elimination from the body (utilization). When

nanocontainers are used, such problems as the transferred agent protection from the destructive influence of the body environment, and the active agent release under the specified conditions arise.

## 2.2. Microencapsulation as a method preceding the nano-level

It follows from the above that there exist several organizational levels in targeted drug delivery in the body, while the delivery systems can be divided into passive with spontaneous processes of transport and release of active substances, and active (controlled) ones. Passive systems, in particular, protect drugs when administered orally, during their passage through the acidic gastric milieu, and ensure their release in the alkaline environment of the intestine. In this case, the dosed or prolonged release of the active component is possible, to which end various membranes or shells from natural and synthetic materials that form capsules are used. Microencapsulation is one of the trends in the organization of targeted effects of drugs on the body. As is stated above, the bioactive substances can be delivered orally, as well as by introduction into the bloodstream transcutaneously and by other methods. The use of all these delivery routes is usually associated with the creation of protective shells on the so-called nominal units of the delivered drugs (a nominal unit is understood as a spatially separated complex structure (formation) that includes biologically active molecules and/or protective polymer layers, the center of which is a POM particle). Polymeric films for micro- and nano-sized units, as well as the sorbed or chemically bound molecule protectors, serve as protective shells. To regulate the transportation of bioactive substances, e.g., transcutaneously, a special environment with the drug nominal units distributed in it is used. Ointment bases can serve as such an environment, for which hydrophobic, including lipophilic, hydrophilic or diphilic materials are chosen. When choosing ointment bases, their compatibility with drugs is necessary; in some cases, the problem of the ointment base component stability arises [41]. The effect of aprotic dipolar solvents, such as dimethyl sulfoxide, which are universal solvents, on the transcutaneous penetration ability and rate for a large number of substances is well known. Podands and cryptands, the so-called phase transfer catalysts, can be used as the drug transporting molecules. Cryptands are macrocyclic complexones (crown polyesters), while podands are their open-chain analogs [42].

In terms of structure, composition and protective shell, the drug delivery systems can be organized in various ways. Liposomal or vesicular capsules, phospholipid-based structures, e.g., lecithin shells, transport units with shells made of block copolymers or dendrimers, polyelectrolyte multilayer shells are considered promising. The simplest unilamellar liposome is a close to spherical, hollow structure formed by a bilayer of phospholipid molecules. The characteristic size varies from tens of nanometers to tens of micrometers. Humanity has encountered liposome-containing materials long before the formal discovery of these formations. For instance, the chicken egg-based colloidal systems, which contain lecithin, may include some spherical vesicles [43]. The direct discovery of liposomes was preceded by numerous studies. In particular, this is the work of T. N. Gobley, who studied the composition of a number of biological samples, such as chicken eggs, fish eggs, brain tissue of animals and humans, etc. and came to the discovery of lecithin [44]. The chemical nature of lecithin was established by A. Strecker [45]. Liposomes as such were discovered in the 1960s. When studying various blood components, in particular, peculiarities of the phospholipid dispersions behavior A. Bangham *et al.* used the results of electron microscopy to discover that the resulting multilayer structures have obvious similarities with cell membranes [43, 46, 47]. Moreover, this group studied the permeability of the obtained membrane structures and demonstrated that liposome membranes are poorly permeable for ions and large molecules, but are permeable for water and low-molecular weight non-electrolytes [43, 48].

Today, several different liposome types are known. In terms of the number of layers, unilamellar, oligolamellar and multilamellar liposomes are distinguished. In addition, there exist the so-called multi-vesicular liposomes that differ from the multilamellar ones by consisting of smaller liposomes enclosed in a common shell instead of a series of concentrically located layers. Unilamellar liposomes (vesicles) are subdivided into small (SUV) and large (LUV) ones, with a characteristic size of 20–100 for the former, and from 100 nm to several micrometers for the latter. A great multitude of techniques for their production have been developed. Most liposome production methods entail the dissolution of cholesterol, lecithin and the useful “cargo” in an organic solvent, drying to obtain a thin film, and its dispersal in an aqueous medium at a certain temperature to obtain a liposomal suspension [49].

The most common methods include the Bangham method, the reversed-phase evaporation method, and the solvent injection method. According to the thin film hydration method (Bangham method) [50, 51], the first stage involves lipid dissolution in an organic solvent, e.g., chloroform, ethanol, methanol, etc. Then, the solvent is evaporated, e.g., in a rotary evaporator, and a thin lipid film deposits on the vessel walls. The resulting film is dispersed in an aqueous medium. The active substance is loaded into liposomes by the addition to the lipid film (for lipophilic substances), or by the dissolving in the aqueous medium (for hydrophilic substances). This method has a relatively low loading efficiency of 5–15% for hydrophilic preparations. According to the reversephase evaporation method, water or an aqueous buffer solution is added to the lipids dissolved in an organic solvent. Then the organic solvent is evaporated at a reduced pressure. This is the way of obtaining large unilamellar and oligolamellar liposomes [52, 53]. The solvent

dispersion method [50] is mainly used for obtaining unilamellar liposomes. A solution of lipids is prepared in an organic solvent (e.g., in ethanol), and then the solution is quickly injected into the aqueous medium through a narrow channel under pressure [54]. The majority of methods for producing liposomes yield a non-uniform size dispersion of particles, while the Bangham method allows only the production of multilamellar vesicles. In order to reduce the size, to obtain more uniform sizes, as well as to obtain unilamellar liposomes, additional processing is used, in particular, ultrasonic dispersion and extrusion through a special membrane in a French press cell [55–58]. Among the advantages of liposomal systems are the possibility of introducing poorly soluble, lipophilic preparations bound with nonpolar tails of phospholipids forming a liposome; an increased penetrating capacity of drugs through cell membranes due to the affinity of phospholipid membranes of liposomes for cell membranes, and an increased drug bioavailability; and the possibility of extending the action of the rapidly metabolized drugs due to their sustained release. The possibilities of using liposomal means of targeted delivery are reflected in publications of various kinds and different years, e.g., in [2, 4, 5, 59–68]. Among the noted disadvantages of liposomes are their active capture by macrophages, which limits the possibility of drug delivery to a number of organs and tissues, and reduces the time of drug circulation in the body; as well as the liposome membrane degradation caused by lipoproteins. By now, techniques have been developed to circumvent some of the disadvantages of liposomes. Such techniques include the application of a layer of polyethylene glycol (PEG) on the liposome surface [69].

### 2.3. Nanostructured systems

Metallic and metal-containing nanoparticles form a large class of materials that differ in composition, size and production methods. Some of them have already found their application in biomedicine, and many are considered as promising materials. The presence of a metal core in nanocapsules can contribute to the activation of the drug release due to the local exposure to laser radiation absorbed by the said core with the release of heat (photodynamic, laser therapy). In some cases, the factor contributing to the release of the transported drug from the nanocapsules may be the changing pH of the medium into which they find themselves. By their composition, the metal-containing biomedical nanoparticles are usually divided into purely metallic, e.g., gold copper, silver, and nanoparticles with a complex composition, for example, based on oxides of iron, copper, zinc, titanium, tungsten, on cerium and zirconium dioxides, including those containing rare earth metals [70–86], etc.

There exist various methods for producing nanoparticles [78, 80, 87–102] and compositions on their basis. The most common methods for producing nanoparticles include “soft chemistry” methods, including microreactor [98–100] and hydrothermal [92–97] synthesis, and precipitation (sol-gel method) [87–91]. The methods that are also used include the conductor electric explosion when a high-density current pulse [103–115] is passed through it; direct laser ablation or ablation in a liquid medium [116–132]; methods of the Solution Combustion Synthesis group [133–139], etc. Depending on the role played in biomedicine, the composites can contain both non-magnetic and magnetic nanoparticles [140–162]. One of the trends in the biomedical use of nanoparticles for targeted drug delivery is the creation of compositions where nanoparticles can be used both as a core for attaching the active component and identification systems, and as active carriers. Another trend in nanoparticle application is the magnetic, photodynamic hyperthermia [163–167] of tumors. Magnetic nanoparticles are often used in this case, when they accumulate in a tumor and cause local overheating and destruction of the pathological formation under the influence of an external alternating electromagnetic field. Another function performed by nanoparticles in biomedicine is the visualization of normal and pathological processes, of pathological formations, and the use as biochemical and biophysical sensors.

Gold nanoparticles deserve special mention here, as in recent years they have been actively studied from the point of view of their possible use in biomedical applications. In fact, the attempts to use colloidal gold as a medicine can be found already in Arabic, Indian and Chinese sources dating back to the 5<sup>th</sup> – 4<sup>th</sup> centuries BC. Colloidal gold has not been overlooked in the medieval Europe either. With varying degree of success, attempts had been made to use it for treating a whole range of illnesses, from mental disorders to infectious diseases. In particular, the medical use of *quinta essentia auri* was mentioned already by Paracelsus (Philippus Aureolus Theophrastus Bombast von Hohenheim) [153]. One of the medieval literary sources that has survived until today and describes the process of obtaining colloidal gold and its medical application is a book by Dr. Francisci Antonii [168]. An important property of these nanoparticles is the inherent phenomenon of surface plasmon resonance, the essence of which is in the resonant absorption of incident radiation with a photon energy that corresponds to the energy of the surface plasmon. From the practical point of view, important is the essential dependence of this resonant frequency on what is found on the surface of a gold nanoparticle. Therefore, gold nanoparticles with the identifying molecules (e.g., antibodies) associated with their surface can serve as biochemical sensors by changing the frequency of the absorbed radiation depending on the presence of specific agents (e.g., antigens) in the analyzed medium.

Polymeric nanoparticles with the lipid (oily) core represent one of the subclasses of polymeric nanoparticles. They consist of a lipid core surrounded by a polymeric wall. Such particles have an average size of about 200–300 nm

with a narrow monomodal size distribution. The production of nanocapsules requires, in particular, such materials as polyethers and polyacrylates which are used as polymers, as well as triglycerides, polyatomic alcohols and mineral oils which are used as lipid cores [169]. One of the advantages of the oily-core nanocapsules, as compared to matrix systems, is the large drug loading capacity, especially in the case when the lipophilic nucleus is a good solvent for the loaded drug. Other advantages include the reduced effect of the drug explosive release, drug protection from degradation and the reduction of its side effects. Production of such nanocapsules employs a wide range of oils, including vegetable, mineral oils and individual compounds, such as ethyl oleate. In some cases, the oily core is represented by an active ingredient.

The criteria used to select a material for the oily core include the presence or absence of toxicity, the ability to decompose and/or dissolve the polymer, and the drug holding capacity [169]. Both synthetic and natural biodegradable polymers, including dendrimers, serve as the material for the polymeric nanocapsule walls. Among the polymeric materials are hydrophobic polyethers, such as poly(lactide) (PLA), poly(lactide-co-glycolide) (PLGA) and poly( $\epsilon$ -caprolactone) (PCL). Polymers have found wide application in targeted drug delivery due to their biocompatibility and ability to decompose to non-toxic products [169–175]. In addition, the associated drug release kinetics can be controlled by changing the polymer molecular weight. The kinetics of polyester decomposition *in vitro* and *in vivo*, as well as their biological action have been amply studied. They demonstrate slow decomposition by a catalyst, which can be a lipase that determines the lowest immunogenicity [169].

The next important aspect of nanocapsules creation is the surface functionalization. The techniques of surface functionalization can be divided into two groups, namely the attachment of a ligand to a nanocapsule during its creation or after it. In the first case, the polymer is chemically bound to the ligand, and this complex material is used as a raw material for nanocapsules production. In the second case, nonfunctionalized nanocapsules are first created, and then a ligand is attached to their polymer walls during a targeted physicochemical or chemical process. An example of the first approach are nanocapsules covalently bound to polyethylene glycol, the polymer walls of which are made of the diblock copolymer [176–183]. An example of the second approach is the introduction of entire antibodies and their fragments into the surface of the finished nanocapsules [169, 184–186].

Inorganic materials based on layered silicates, titanium oxide, zeolites, functionalized fullerenes and carbon nanotubes are also considered as drug transporting nanoparticles. It has already been noted that the development and use of such means of delivery is impossible without solving the problems of the further fate of sufficiently strong chemical carriers and their behavior in the body after performing their basic functions.

The literature describes hybrid supramolecular structures based on nanocluster polyoxometalates (to be discussed in more detail below) and organic molecules, namely polyelectrolytes. A technique of layer-by-layer synthesis of hybrid nanoparticles based on a latex suspension consisting of spherical polystyrene acrylic acid particles with a negative charge is presented in [187]. As polyelectrolytes, polyallylamine hydrochloride and poly(sodium 4-styrene sulfonate) were used, carrying a positive and negative charge, respectively. The layers of polyelectrolytes alternated with layers of  $\text{Mo}_{72}\text{Fe}_{30}^{n-}$ , an iron-molybdenum nanocluster with a negative charge. At the last stage, with all the layers formed, the polystyrene acrylic acid-based core was dissolved in tetrahydrofuran. A study of the obtained structures by scanning electron microscopy showed that they have a spherical structure before and after dissolution of the latex core [187]. It is supposed to use such systems as transport units delivered under the influence of a magnetic field, due to the presence of a magnetic polyoxometallate component in them.

#### 2.4. Carbon-based nanostructured systems

Thanks to their unique properties, carbon-based nanostructured materials attract attention from the point of view of their application in such industries as electronics, materials science, etc. Also, attempts are being made to find application for carbon nanomaterials in nanobiology and nanomedicine for diagnosing pathological conditions and targeted drug delivery. The matter is about three-dimensional (3D) carbon nanostructures (nanodiamonds, in particular), about two-dimensional (2D) structures (graphene), about one-dimensional (1D) structures (nanotubes), and also about zero-dimensional (0D) ones, which include fullerenes and their derivatives. Fullerenes (buckyballs) [188–192] are produced by carbon evaporation, e.g., in an electric arc between two graphite electrodes in helium or other inert gases, or by laser ablation, etc. As a rule, regardless of the method, a mixture of several types of fullerenes is obtained, which is contaminated with graphite, unstructured and cluster inclusions of different composition. Therefore, fullerenes require preliminary purification. Fullerenes can be functionalized by a wide range of molecules through external functionalization (molecules association with the fullerene outer surface) and by metals through internal functionalization (association to the inner surface during synthesis), as well as by replacing carbon atoms with heteroatoms. This aspect makes fullerenes promising candidates as means of targeted drug delivery. However, fullerenes are hydrophobic, which limits the possibilities of their direct use in biomedicine [193]. It is possible to obtain their aqueous dispersions [194–200] and associates with organic compounds [200–205]. One of the ways of modifying

the surface of fullerenes provides hydroxylated derivatives such as fullereneols [195, 200, 205, 206, 208]. The specific functionalization of their surface is achieved through the use of amphiphilic polymers, amino acids, carboxylic acids, and biologically active preparations that identify molecules [206, 207]. Fullerenes can be coated with biocompatible materials (encapsulation), e.g., with polyvinylpyrrolidone while conjugates including cytostatic preparations and antibodies to the corresponding cell type, can be used for delivering chemotherapeutic drugs to tumor cells. The absorption of such systems by cells can be realized through specific endocytosis. Another possible trend in the use of fullerenes is the creation of bioactive [203, 204, 206, 208] or contrast materials for nuclear magnetic resonance imaging (MRI) through internal functionalization by contrast agents, including  $Gd^{3+}$ ,  $Sc^{3+}$ ,  $Ho^{3+}$ ,  $Tm^{2+}$ ,  $Ga^{3+}$  and  $Tc^{2+}$  ions, with isolation of unstable and potentially toxic contrast materials from the internal medium of the body [209–212]. A similar solution for creating contrast materials is proposed in [213] for Keplerates, the non-carbon analogs of fullerenes which form ionic associates with cations of the above-mentioned metals.

Graphene [214–220], a single-layer (one atom thick) 2D nanostructure possesses high mechanical (high rigidity) and electric transport (high charge carrier mobility) properties, which have drawn attention to it as a material for semiconductor electronics, creating batteries and fuel cells. The use of graphene for biomedicine is studied [216, 218], including targeted drug delivery in the form of nanographene oxide (NGO). The discovery and creation of methods for producing carbon nanotubes (CNT) [221] is inextricably linked with the creation of fullerenes, since graphite dispersion in an arc yields not only fullerene molecules, but also one-dimensional CNT structures representing one or several rolled graphite layers [221–247]. The characteristic diameter of a CNT is from one to several nm, while the length reaches tens of  $\mu m$ . Among the CNT production methods [221–233] are pyrolytic synthesis, electric arc discharge, chemical vapor deposition, and laser ablation. Targeted CNT synthesis employs *d*-metal-based catalysts [226, 227, 239] (copper, iron, nickel, cobalt, etc.). Most often, the distance between CNT layers is 0.34 nm, which coincides with the distance between the layers in crystalline graphite. As a rule, both ends of a CNT have hemispheres the so-called “caps”, which include pentagons in addition to hexagons, thus making them similar to a half of the fullerene molecule [221, 224]. It is possible to open CNT ends by strong oxidizing agents such as nitric and perchloric acids, or ozone, which open access for various substances to the internal cavity for creating transport systems [237–249]. Methods for CNT size “calibration” using ultracentrifugation, dialysis, and “cutting” them to achieve the desired length have been developed. The synthesized CNTs also have foreign inclusions, including amorphous carbon, graphite and fullerenes. To remove impurities from CNT, technologies for their purification have been developed [235, 236]. By analogy with fullerenes, CNT functionalization can be divided into external and internal. In addition, the non-covalent and covalent types of functionalization are distinguished. Functionalization of the first type is, e.g., CNT surface coating with surfactants, polymers, lipids, etc. The second type includes the reactions of cycloaddition and oxidation under the influence of strong acids, which allow the CNT surface functionalization by carboxyl groups.

The biomedical aspect of nanodiamond use can also be considered [250–260]. The nanodispersed diamonds (or nanodiamonds) were obtained for the first time in the USSR in the 1960s [261], but the widespread interest in the research of this material arose in the 1990s due to several factors. Among them are the appearance of relatively affordable technologies for nanodiamond production, the use of nanodiamonds as quantum dots instead of toxic semiconductor materials, the development of nanoscale magnetic sensors based on nanodiamonds and some others [254, 262]. The methods of nanodiamond production, like those for producing a number of other superhard materials, are based on the shock compression of the source material. As a rule, the blasting of an explosive creates a shock wave, which makes it possible to achieve the pressure required for the nanodiamond crystal formation. Such synthesis conditions are called dynamic. The chamber in which the shock wave is created can be filled with an inert gas or liquid as a coolant hence, dry and wet synthesis methods exist, respectively. Both the explosive itself and graphite can serve as sources of carbon for the synthesis of nanodiamonds. The characteristic size of diamond crystals obtained by the above-described synthesis methods ranges from a few to tens of nm, and the crystals can also exist in the form of aggregates [264, 265]. Methods for disaggregating the obtained material are available [266–269]. In addition to dynamic synthesis, the research on the synthesis under static conditions is underway. The composition of impurities in the case with the detonation production method includes carbon in the form of graphite and non-combustible impurities (metals and oxides) [254, 261]. The areas of nanodiamonds application are determined by their inherent outstanding qualities, both characteristic of diamonds in general and specific to nanodiamonds. Such properties as exceptional hardness, the Young's modulus, specific optical properties, biocompatibility, chemical stability, and fluorescence ability make nanodiamonds a promising material for biomedical applications [250–263]. Among the possible areas of biomedical application is the use as a matrix for tissue engineering, creation of implants and, in particular, bioactive substances targeted delivery [250, 251, 253, 255, 259]. The latter is possible due to the ability of many bioactive substances (proteins, antibodies, nucleic acids, drugs) to bind to the surface of nanodiamonds [253–256, 259, 260, 263]. The use of nanodiamonds as a material for tissue engineering is possible due to their ability to bind to the cell surface, and in

this context studies are being conducted on the use of nanodiamonds as a means of cell delivery for cell therapy, in particular, for bone tissue regeneration [258,270].

### **2.5. Features of active drug delivery systems**

Active methods of drug delivery to biological targets include, among others, the impact of physical factors on the transported nominal units. These factors include, first of all, the magnetic and electric fields, which implies the creation of a means of delivery with relevant physical properties. The creation of units transported under the influence of a magnetic field is associated with the conjugation of bioactive substances and ferromagnetic particles at the nano- and micro levels. Associates may also include the above-mentioned protective shells in this case, too. The use of the magnetic phase-based associates should ensure not only targeted drug delivery to the correct location in the body, but also the subsequent safe removal of solid particles from it. This technique requires the use of magnetic fields of sufficiently high intensity. As is noted above, magnetic particles can be used for magnetic hyperthermia simultaneously with the delivery of drugs.

Electric field-assisted delivery (electrophoresis, iontophoresis) is acceptable for substances that form charged units at the level of ions or colloidal particles. It is well known that a fairly wide range of bioactive substances and drugs can be delivered to the body iontophoretically, including transcutaneous delivery. Such a delivery option significantly increases its efficiency and does not require the application of high intensity electric fields. Actually, the effect of iontophoresis on the skin increases its permeability to bioactive substances. In a number of cases, iontophoresis can be carried out directly for the drugs that form ions and amphiphilic molecules in solutions. Such substances include various groups of drugs transported either to the cathode or anode, namely antibiotics, vitamins, alkaloids, anti-inflammatory, antihistaminic and cardiotropic agents, analgesics, hormonal preparations, etc. Iontophoretic delivery of bioactive formulations is also possible when they associate with electrically charged effective transport units. Naturally, in this situation, it is advantageous to have a non-toxic transport units that can be easily removed from the body after performing their function. These carriers include biodegradable ones (e.g., due to natural metabolic processes), and biocompatible ones, especially those that have their own positive effects on the body. The considered options of iontophoretic drug delivery to the internal organs and lesion foci envisage their preliminary injection (including intracavitary) and external electrodes imposition on the corresponding zone. In view of the above-said, nanoscale systems have significant advantages.

### **3. Features of skin as a transport medium; transcutaneous transport models**

Skin is a very complex biological object that includes many heterogeneous layers that differ in mechanical and physico-chemical properties. The aforementioned layers contain polar (water, inorganic salts), non-polar (lipids, etc.) and amphiphilic (phospholipids, proteins) components. Skin consists of several types of cells which, in addition, are found at different stages of development (keratinization). In addition skin also has pores, hair follicles, blood vessels, and nerves [271–273]. The blood vessels in the skin are arranged as several plexuses found at different depths. There are superficial and deep arterial plexuses and two superficial venous ones. The deep subcutaneous arterial network is located at the subcutaneous fatty tissue and dermis boundary. The superficial (subpapillary) arterial network is located at the base of the papillary layer. Blood is evacuated from the skin capillary network by the papillary venous plexuses and the deep venous plexus, which is located between the dermis and hypodermic tissue [271–275]. Depending on the nature of the transported substance (hydrophilic, lipophilic), different transfer paths predominate. In particular, the question about the main route of substance transfer through the stratum corneum remains controversial [276–278]. Besides, a number of factors, such as skin moisture, lesions, chemical effects, pH, ultrasound, and electric field affect the parameters of transcutaneous transfer [279–287]. All this makes it quite difficult to create an adequate model of transcutaneous substance transfer. Since a model is a simplified representation of a real object, it is important to identify the most relevant skin properties from the point of view of transcutaneous substance transfer. Skin models are conventionally divided into macroscopic and microscopic ones (Table 1). The macroscopic models do not explicitly reflect the specificity of the skin microscopic structure, cell layers geometry, the presence and size of pores, etc. The skin is regarded as a single or multilayer membrane, which is characterized by the corresponding macroscopic parameters (diffusion coefficient, etc.). The microscopic models in turn provide a certain degree of detail when they take into account the skin structure at the micro level (the scale of cell layers and individual cells). Depending on the process type, the substance transfer models are divided into stationary and transitional ones. The stationary models describe a steady process with unchanging concentration profiles of transported substances in the skin, transcutaneous concentration gradients and other parameters of the simulated process. The transitional models characterize the non-stationary processes. One-dimensional (1D), two-dimensional (2D) and three-dimensional (3D) models of transcutaneous transport are distinguished. Their choice is mainly determined by such specific features of the problem as the geometric dimensions of the substance source and, in the case of iontophoresis, of the electrodes,

thickness and transverse dimensions of the skin, direction of concentration gradients and of the electric field. In the case when the transverse dimensions of the substance source significantly exceed skin (membrane) thickness, concentration and electric field gradients are directed perpendicular to the skin surface and all spatial parameters depend only on the coordinate perpendicular to skin surface, the problem can be regarded as one-dimensional. In a number of other cases, two-dimensional models are used, and in certain situations the use of three-dimensional models can be justified. In addition, transcutaneous substance transfer can be enhanced by additional external influences (iontophoresis, phonophoresis, etc.) [286, 287].

TABLE 1. Transcutaneous transfer models

Account of skin structure	Macroscopic	Microscopic
Process type	Stationary	Transitional
Additional impacts	Passive transfer	Iontophoresis, phonophoresis, etc

### 3.1. Simplified models of passive transcutaneous transfer

In [288], passive transport models are considered as the most simple case of transcutaneous transport. Conventionally, the four most significant processes (Fig. 1) that determine passive transcutaneous substance transfer can be named:

1. Molecular diffusion. The driving force of this process at a specified pressure and temperature is the difference in chemical concentration gradient of the transported substance at the opposite skin boundaries.
2. Separation. According to the Nernst's distribution law the dissolved substance distribution in two practically immiscible phases reaches in some time a value that is characteristic for each dissolved substance and solvent.
3. Metabolism and phase transitions. Examples of such processes are the dissolution, evaporation, cell metabolism and substance removal into the systemic circulation.
4. Adsorption and absorption. Many similar processes can occur in the skin. The binding of a number of substances with proteins (keratin, etc.) can serve as an example.

All the above processes follow the law of mass conservation, which is mathematically expressed by the following equation:

$$\frac{\partial C}{\partial t} + \operatorname{div} \vec{J} = \pi,$$

where  $C$  is the substance concentration  $t$  is time  $J$  is the substance flow and  $\pi$  is the sum of substance sources and sinks.

Diffusion, the first process, is usually described by the first Fick's equation, according to which a substance flow is proportional to its concentration gradient.

$J = -D\nabla C$  where  $C$  is the substance concentration,  $J$  is the substance flow,  $D$  is the coefficient of the given substance diffusion in the given medium.

In a particular case when the area under consideration has no sources and sinks of the substance, i.e., when  $\pi = 0$ ,

$$\frac{\partial C}{\partial t} + \operatorname{div} \vec{J} = 0$$

and, therefore:

$$\frac{\partial C}{\partial t} + \nabla \cdot [-D\nabla C] = 0.$$

The stationary regime can be achieved at constant conditions and only after some time, which is  $h^2/6D$  for the diffusion through a homogeneous membrane, where  $h$  is the membrane thickness and  $D$  is the diffusion coefficient [279, 287–292]. When several phases are available, as in the case with the transcutaneous substance transfer, the second process, that is, separation should be taken into account. This process is characterized by equilibrium at the boundary of two phases:

$K_{A/B}C_B = C_A$  where  $K_{A/B}$  is the separation coefficient  $C_A$  is the substance concentration at the  $A$  phase boundary, and  $C_B$  is the substance concentration at the  $B$  phase boundary.

Metabolism and removal from the system (the third process) are taken into account in term  $\pi$ . If only the processes the rate of which linearly depends on the substance concentration  $\pi = q - kC$  occur in the system, then:

$$\frac{\partial C}{\partial t} + \nabla \cdot [-D\nabla C] + kC = q,$$

where  $k$  is the process rate constant, which characterizes the amount of substance removed from the system or added into the system per unit of time, and the term  $q$  unites sources and sinks that do not depend on the substance concentration. Equations of this type form a system of equations for several substances undergoing mutual transformations. If there are only two substances, then:

$$\begin{aligned} \frac{\partial}{\partial t} C_A^0 + \Delta \cdot [-D_A^0 C_A^0] &= -k_A^0 C_A^0 + k_A^1 C_A^1, \\ \frac{\partial}{\partial t} C_A^1 + \Delta \cdot [-D_A^1 C_A^1] &= -k_A^0 C_A^0 - k_A^1 C_A^1. \end{aligned} \tag{1}$$

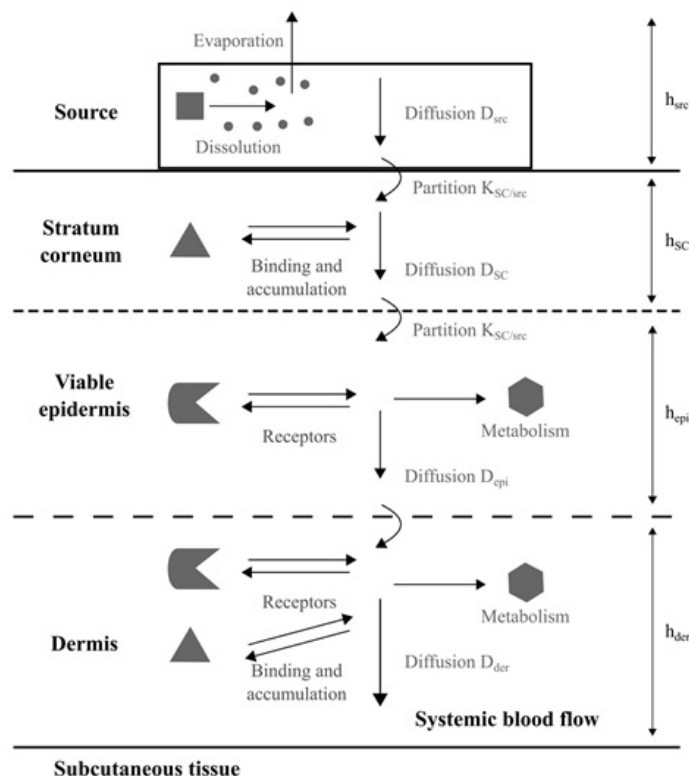


FIG. 1. Diagram of the processes occurring in the skin during the transcutaneous drug administration (based on the diagram from [288])

In this case, both types of particles are transferred by diffusion, however diffusion coefficients are different:  $D_A^0$  and  $D_A^1$ . The constants  $k_A^0$  and  $k_A^1$  describe the transformations between the two components. This description of the process is very similar to that of the fourth process, i.e., binding, if  $C_A^0$  and  $C_A^1$  denote concentrations of free and bound substances, respectively. Usually the bound particles are believed to be immobile, that is,  $D_A^1 = 0$ . It is a reversible adsorption process, the equilibrium condition of which is specified as:

$$k_A^0 C_A^0 = k_A^1 C_A^1. \tag{2}$$

The process is irreversible in the case when any of the constants becomes zero. It should be noted that the above diagram is a simplified one

In order to obtain a linear system of equations, it is necessary to accept several more simplifications. In particular, the role of the binding agent in the binding process is neglected. It is believed that the binding agent is present in excess and its capacity is not limited. Equations (1) describe the general case of binding. In the case of slow binding, the  $k_A^0$  and  $k_A^1$  constants are small and the binding can serve as a limiting stage of the transfer process. In the case of fast binding, the rate constants are large, which makes it possible to further simplify the system. In this case, equations (1) are replaced respectively by equation (2) and the following equation:

$$\frac{\partial}{\partial t} \left( \left( 1 + \frac{k_A^1}{k_A^0} \right) C_A^0 \right) + \nabla \cdot [-D_A^1 C_A^0] = 0.$$

The description of the processes will not be complete without defining the initial and boundary conditions. Their choice significantly depends on the particular situation. The most frequently accepted initial condition is the absence of a substance in the membrane, i.e.,  $C(0, x) = 0$  for all  $x$  points within the membrane. The ideal sink condition is represented as  $C(t, x) = C_{sink} = 0$  for any time instant  $t$  and for all points  $x$  that are in contact with the ideal sink [277, 288, 293].

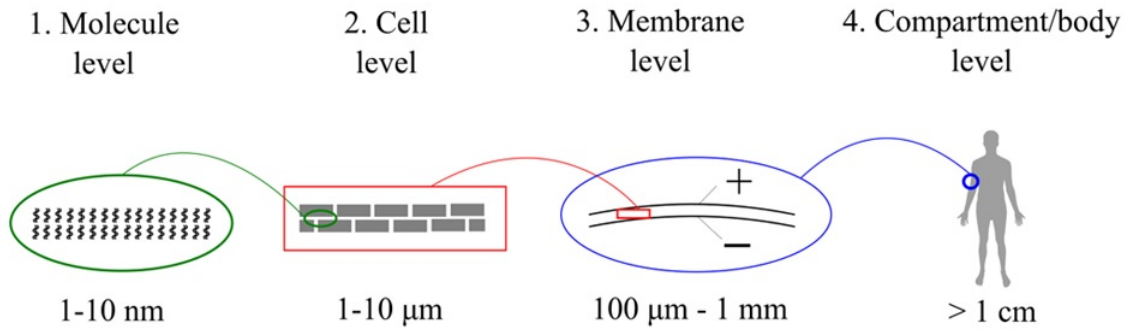


FIG. 2. Levels of detail in transcutaneous transfer models (based on the diagram from [288])

Different levels of skin description can be considered (Fig. 2).

1. Processes at the level of molecules (macromolecules) (1–10 nm), i.e. lipid bilayer level.
2. Processes at the subcellular (0.1 μm) or cellular (1–10 μm) level.
3. Processes at the membrane level (0.1–1 mm), i.e. analysis of the amount of substance that has reached a certain depth in experiments with a diffusion cell.
4. Processes at the compartment/organism level, i.e. the amount of substance that has passed through the membrane in experiments with a diffusion cell or into the body in *in vivo* experiments. Skin layers, as well as the substance source and sink that are seen as peculiar reservoirs are considered as compartments.

The models that describe the transfer process at the 3<sup>rd</sup> and 4<sup>th</sup> levels are called macroscopic. They describe the substance source and the skin as a sequence of homogeneous membrane layers (e.g., the substance source/ epidermis/ dermis) through which diffusion occurs. The parameters used in such models are averaged for the corresponding volume (layer, tissue, compartment). The description of the transfer process at the 1<sup>st</sup> and 2<sup>nd</sup> levels is done by microscopic models [288].

Thus, it is possible to identify the main classification parameters for the transcutaneous substance transfer models (Table 2). A separate subclass of macroscopic models is represented by pharmacokinetic (compartmental) models [294–296]. The transported substance concentration within one compartment is considered to be uniform throughout its volume. A simple 4 compartment pharmacokinetic model (Fig. 3) was considered as an example in [295] and included the drug source (on the skin surface), the stratum corneum, the viable skin layers, and blood vessels. In this case, each compartment is characterized by two parameters: the substance concentration and its volume. Each stage of the transfer process is characterized by the corresponding first-order rate constant ( $k_1, k_2, k_3, k_4$ ).

TABLE 2. Main classification parameters for the transport models

Scale of detail	Macroscopic	Microscopic	
Process type	Stationary (established)	Non-stationary (transition)	
Dimension	1D	2D	3D
Additional acting forces	Absent	Electrophoresis, phonophoresis, etc	

The  $k_1$  constant characterizes the drug absorption stage. It is supposed that its value is determined by diffusion through the stratum corneum and the numerical estimate for  $k_1$  can be obtained from the relation  $D_{SC}/h_{SC}^2$ , where  $D_{SC}$  is the coefficient of drug diffusion in the stratum corneum with  $h_{SC}$  thickness. Experimentally, the value of the  $k_1$  constant can be estimated in *in vitro* diffusion experiments on an isolated stratum corneum, including the use of labeled molecules (radioactive, fluorescent labels). The rate constant  $k_2$  characterizes the drug penetration through the skin layers following the stratum corneum, i.e., the viable epidermis layers that contain more water and the dermis

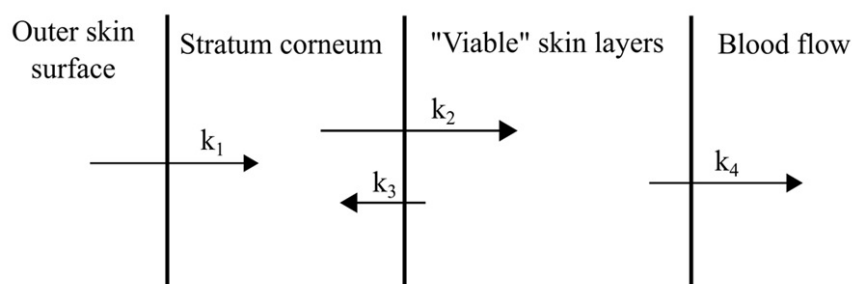


FIG. 3. Compartments in a simple transcutaneous transfer pharmacokinetic model (based on the diagram from [295])

upper part. Its value, by analogy with the  $k_1$  constant, is also associated with the diffusion coefficient related to the square of the diffusion path length, that is  $D_{VED}/h_{VED}^2$ , where  $D_{VED}$  is the diffusion coefficient in the viable epidermis and dermis, and  $h_{VED}$  is the considered skin layer thickness. The rate constant  $k_3$  is necessary for taking the effect of accumulation in the epidermis into account; its values are essential for drugs with high lipophilicity (greater affinity for the hydrophobic stratum corneum than for the deeper hydrophilic skin layers). In this model, the drug concentration in the subcutaneous capillaries and the systemic circulation are considered to be the same, so the rate constant  $k_4$  is actually the rate constant of the drug removal from the body. In this formulation, the problem is described by a system of ordinary first order differential equations:

$$\begin{aligned}\frac{dC_1}{dt} &= -k_1 C_1, \\ \frac{dC_2}{dt} &= \frac{V_1}{V_2} k_1 C_1 - k_2 C_2 + \frac{V_3}{V_2} k_3 C_3, \\ \frac{dC_3}{dt} &= \frac{V_2}{V_3} k_2 C_2 - (k_3 + k_4) C_3, \\ \frac{dC_4}{dt} &= \frac{V_3}{V_4} k_4 C_3,\end{aligned}$$

where  $V_i$  and  $C_i$  are the  $i^{\text{th}}$  compartment volume and drug concentration in it, respectively. The system can be solved analytically; the concentrations in each compartment can be expressed as functions of time [294, 295].

### 3.2. Improved models of transcutaneous transport

An example of a more complex approach is the hybrid diffusion/pharmacokinetic model suggested in [297]. The model diffusion medium is represented by two skin layers; in addition there are two separate areas (compartments) described pharmacokinetically, i.e., the central and peripheral vessels. This model also takes into account binding processes and drug metabolism in the skin. This model is schematically represented in Fig. 4. The introduced drug concentration at the surface of the epidermis stratum corneum is considered constant.

Though the real skin structure is multi-layered, this model treats it as if it consists of two layers. Such a simplification is deemed acceptable, in particular, on the basis of the data presented in [295, 296]. It can be then concluded that the epidermis stratum corneum and viable epidermis differ significantly from each other in properties that determine drug distribution. At the same time, the differences in drug distribution between the viable epidermis and dermis are not significant. Thus, it is possible to distinguish two layers: the first includes the epidermis stratum corneum (SC), the second includes the layers of viable epidermis and dermis (usually referred to as VS (from viable skin) or VED (from viable epidermis + dermis)). Let's consider the processes taken into account in this model in more detail. The introduced drug undergoes separation at the stratum corneum outer boundary and penetrates into it. It can also become partially bound in the stratum corneum. The binding process in the framework of this approach is described by a double sorption model based on the Langmuir isotherm [298–301]. Furthermore, the drug undergoes separation at the stratum corneum/viable skin boundary. Metabolic processes take place in the viable skin. The  $A \rightarrow B \rightarrow C$  transformation sequence is accepted in the considered model. As a rule, enzyme reactions follow the Michaelis-Menten kinetics, and simple competitive inhibition is also taken into account.  $B$  and  $C$  metabolites produced in the viable skin diffuse both into the receiving compartment (into the bloodstream) and back into the stratum corneum; this process is described by the first Fick's equation. In general, the rate of reverse diffusion back into the stratum corneum is rather low due to the low diffusion coefficient in the stratum corneum. However, the reverse diffusion is still taken

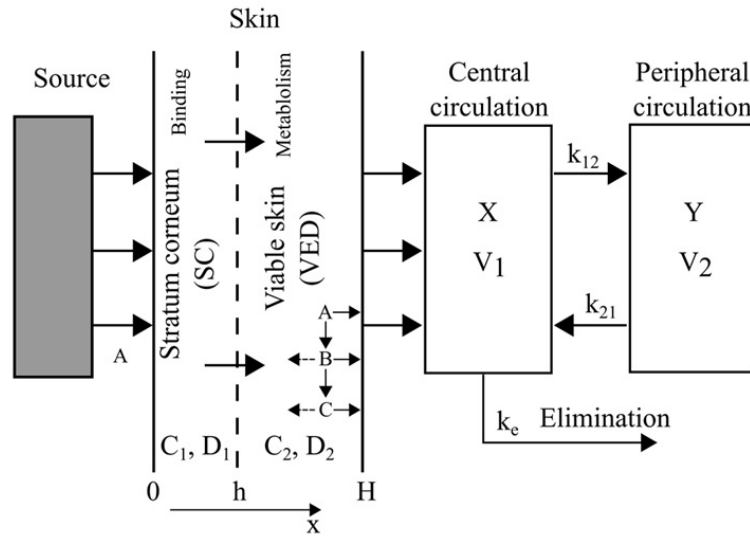


FIG. 4. Compartments in the hybrid diffusion/pharmacokinetic transcutaneous transfer model (based on the diagram from [288])

into account, since it is the stratum corneum that largely determines the drug accumulation in the skin. The drugs that have passed through the viable skin get into such compartments as the bloodstream and tissues. The considered model uses two compartments, and the kinetics of drugs removal from the body is described by the first-order equations. The mass balance of A, B and C metabolites in the skin is described by a system of differential equations:

$$\left(1 + \frac{p_a}{(1 + q_a C_a)^2}\right) \frac{\partial C_a}{\partial t} = \frac{\partial}{\partial x} \left( D_a \frac{\partial C_a}{\partial x} \right) - \frac{M_a C_a}{B_a + C_a}, \quad (3)$$

$$\left(1 + \frac{p_b}{(1 + q_b C_b)^2}\right) \frac{\partial C_b}{\partial t} = \frac{\partial}{\partial x} \left( D_b \frac{\partial C_b}{\partial x} \right) + \frac{M_a C_a}{B_a + C_a} - \frac{M_b C_b}{\left(1 + \frac{C_a}{K_i}\right) B_b + C_b}, \quad (4)$$

$$\left(1 + \frac{p_c}{(1 + q_c C_c)^2}\right) \frac{\partial C_c}{\partial t} = \frac{\partial}{\partial x} \left( D_c \frac{\partial C_c}{\partial x} \right) + \frac{M_b C_b}{\left(1 + \frac{C_a}{K_i}\right) B_b + C_b}. \quad (5)$$

Here  $p$  and  $q$  are the binding rate constants from the double sorption model,  $C$  is the substance concentration in the skin,  $t$  is time,  $x$  is the spatial coordinate,  $D$  is the diffusion coefficient,  $M$  and  $B$  are the Michaelis-Menten kinetic parameters, and  $K_i$  is the inhibition constant.

Equations (3), (4) and (5) are applicable both to the stratum corneum ( $0 \leq x \leq h$ ) without metabolism, and to the viable skin ( $h < x \leq H$ ) without binding ( $p = q = 0$ ). At a low substance  $A$  concentration, equations (3), (4) and (5) can be reduced as follows:

$$\begin{aligned} \left(1 + \frac{p_a}{(1 + q_a C_a)^2}\right) \frac{\partial C_a}{\partial t} &= \frac{\partial}{\partial x} \left( D_a \frac{\partial C_a}{\partial x} \right) - k_1 C_a, \\ \left(1 + \frac{p_b}{(1 + q_b C_b)^2}\right) \frac{\partial C_b}{\partial t} &= \frac{\partial}{\partial x} \left( D_b \frac{\partial C_b}{\partial x} \right) + k_1 C_a - k_2 C_b, \\ \left(1 + \frac{p_c}{(1 + q_c C_c)^2}\right) \frac{\partial C_c}{\partial t} &= \frac{\partial}{\partial x} \left( D_c \frac{\partial C_c}{\partial x} \right) + k_2 C_b. \end{aligned}$$

Here  $k$  are the enzymatic reaction rate constants in the viable skin.

In the general case, the diffusion coefficient is a function of the spatial coordinate ( $x$ ), time ( $t$ ) and concentration ( $C$ ):  $D = f(x, t, C)$ . However, this and most other models use the assumption that the diffusion characteristics of the skin do not change during the experiment. Thus, the diffusion coefficient is a function of only the spatial coordinate:

$$D_i = \begin{cases} D_{1i} & (0 \leq x \leq h; SC), \\ D_{2i} & (h < x \leq H; VS). \end{cases}$$

In this case, the diffusion coefficient  $D$  should be considered as an effective value due to the heterogeneity of the structure, especially of the stratum corneum. In the general case, the constants  $k_1$  and  $k_2$  of the  $A \rightarrow B \rightarrow C$  enzymatic reactions rate depend on time, which can especially manifest itself in *in vitro* experiments. This dependence may be associated with the processes of enzymes inactivation. In the considered model from [298], it is assumed that the rate constant exponentially decreases with time:

$$k_i = Z_i \exp(-A_i t), \quad i = 1, 2.$$

The rate of drug transfer through the skin can be expressed as:

$$\left(\frac{dQ}{dt}\right)_i = -D_i \left(\frac{dC_i}{dx}\right)_{x=H}.$$

The amount of substance that has transited through a unit of skin area will be expressed as:

$$Q_i = \int_0^t \left(\frac{dQ}{dt}\right)_i dt = \int_0^t \left(-D_i \frac{dC_i}{dx}\right)_{x=H} dt.$$

In the two-compartment model (Fig. 4), the administered drug concentration in the blood plasma will be expressed for the central vessels as:

$$\frac{d(XV_1)}{dt} = \left(\frac{dQ}{dt}\right) S_a + k_{21}YV_2 - k_{12}XV_1 - K_eXV_1,$$

where  $X$  is the concentration in central vessels  $Y$  is the concentration in peripheral vessels  $V_1$  and  $V_2$  are concentrations in central and peripheral vessels, respectively  $S_a$  is the skin surface area through which the drug is administered.

For the peripheral compartment,

$$\frac{d(YV_2)}{dt} = k_{12}XV_1 - k_{21}YV_2 \quad [297].$$

The so-called QSPR (quantitative structure-permeation relationship) models are also worth mentioning. This model class cannot be fully attributed to macroscopic or, moreover, to microscopic models. The essence of the QSPR method is in predicting the kinetics of the transcutaneous transfer of a certain substance with a known molecular structure. The prediction is based on statistical analysis of the experimentally determined kinetics parameters for a number of other substances. To this end, large sets of experimental data are used, such as the Flynn's dataset [302–304], which includes data on the transcutaneous transport for 94 substances, and a number of other data sets [305–307]. In recent years, this model class has received a new aid to development thanks to significant progress in the artificial intelligence methods, in particular, in the widespread introduction of the artificial neural networks (ANN) into the practice.

#### 4. Some features of biological target identification systems

The development of modern targeted drug delivery systems includes solving the problems of biochemical target identification in the body. For instance, the so-called homing peptides [308,309], which, while in the bloodstream and capillaries, can selectively stick to the transformed (tumor) cell membranes. A similar property is demonstrated by compounds of other classes, e.g., the water-soluble folic acid (B9 vitamin) and some other substances. At the same time, the homing peptides can transport bioactive substances associated with them, or chemotherapy drugs. When conjugation of homing peptides with quantum dots occurs, accumulation of the latter in the tumor region and its luminescent diagnostics using primary IR radiation, as well as dynamic laser therapy become possible. There exists a problem of quantum dot toxicity for the organism, in particular, of those based on nanoparticles of transition metal chalcogenides. The protective shell function for toxic quantum dots with a transition layer between the chalcogenide and peptide molecules can be performed by the above-mentioned biocompatible PEG polymer. The possibility of targeted, homing peptide-assisted transport to and accumulation in the tumor area of magnetic particles, which further exert therapeutic effect through hyperthermia, cannot be excluded. The presence of transport units that are mobile in the electric field and carry drug molecules or ions does not exclude the combination of such units with homing peptides, folic acid and other bioactive molecules with affinity to certain cell membranes. Potentially, it makes it possible to create a drug, the transport units of which can be controlled by an electric field, as well as selectively adhere to the transformed cells. The drugs (conjugates) that include folic acid can be absorbed together with their contents by the cells through endocytosis. The so-called receptor-mediated endocytosis that employs various kinds of protein vectors (hormones, enzymes, specific peptides, antibodies, glycoproteins, glycolipids, and viruses) occupies a significant place in ongoing studies worldwide [310–323]. Drugs bind to protein vectors by molecular linkers. The autologous blood cells, such as leukocytes and erythrocytes, are used as carriers for targeted delivery. The undoubted

advantage of the carriers in the latter case is their complete biological compatibility, the body's ability to utilize such "containers". Among the disadvantages is a relatively large volume of carriers that are not always able to penetrate tissues to biological targets. In addition to the delivery of drugs to the cell surface, intracellular targeted drug transport systems are being developed [324–328]. The matter is about an even more precise hitting the specified compartments directly in cells of a certain type by the nominal transport units.

## 5. The possibilities of using nanocluster polyoxometalates for the bioactive substances delivery

### 5.1. The structure and properties of molybdenum-containing polyoxometalates

Molybdenum can form a large number of different compounds; it belongs to the structural elements for polyanions. The ability of oxygen-containing molybdenum compounds to condense and form nanocluster polyoxoanions is due to its properties, such as the relatively large radius of  $\text{Mo}^{6+}$  cation (0.062 nm according to Pauling) [329], which allows it to have a coordination number of 6 in oxygen-containing compounds, as well as 7 (pentagonal bipyramid of oxygen atoms). For comparison, the  $\text{Cr}^{6+}$  cation with a radius of 0.052 nm [329] has a coordination number for oxygen equal to 4. The second property that determines the ability of oxygen-containing molybdenum compounds to form nanoclusters is that molybdenum is a good acceptor of oxygen electrons. The relatively simple oxygen-containing molybdenum compounds are, for instance,  $\text{MoO}_3$ ,  $\text{Mo}_5\text{O}_{14}$ , and  $\text{Mo}_{17}\text{O}_{47}$ . In the last two compounds, molybdenum is simultaneously found in two oxidation states (5+ and 6+). The behavior of oxygen-containing molybdenum ions in solution depends on the conditions: for example, molybdic acids with the general formula of  $\text{H}_x\text{Mo}_y(\text{O}_{6y+2x})/2 \cdot \text{H}_2\text{O}$  dissociate in an aqueous medium in different ways, depending on the medium's acidity. In the case of acid-type dissociation, the end product is the molybdate ion. Polymerized and protonated molybdates can be regarded as intermediate products. Since acid-type dissociation is a reversible process, molybdate acid solutions represent a complex system of various molybdenum ionic species. The basic-type dissociation yields molybdenyl ions.

Polyoxometalates (POM) is a class of inorganic compounds that represent by themselves multicenter anionic groups of transition metals, which also include oxygen atoms and, quite often, some other elements. POM nanoclusters are a vast array of complex compounds, the structural blocks of which are polyoxometallate molecules. Molybdenum is one of the elements that can form POM nanoclusters, namely polyoxomolybdates. The initial components for polyoxoanion nanoclusters are molybdate or heptamolybdate ions. These compounds are considered as promising materials in many scientific and applied fields, in particular, as catalysts for fine organic synthesis of the so-called templates for creating composite structures. There are indications of the possibility of POM application in biomedicine. For instance, their anti-cancer activity was reported in [330, 331], especially for the compound  $[\text{NH}_3\text{Pri}]_6[\text{Mo}_7\text{O}_{24}] \cdot 3\text{H}_2\text{O}$  (isopropyl ammonium heptamolybdate, designated as PM-8) in the examples with breast cancer, sarcoma and adenocarcinoma. PM-8 is water soluble; its structure is preserved in aqueous solutions at pH 5–7. POM can be isolated in the form of metal-ammonium or organometallic salts. A study on mice with tumors showed that some POM, such as PM-8, PM-17, PM-26 and PM-32, show anti-cancer activity against human cancer. It was also reported that  $[\text{NH}_4]_6[\text{Mo}_7\text{O}_{24}] \cdot 4\text{H}_2\text{O}$  and  $\text{K}_6[\text{Mo}_7\text{O}_{24}] \cdot 4\text{H}_2\text{O}$  were found to be effective, while  $[\text{NH}_3\text{Pri}]\text{Cl}$  ineffective against mouse sarcoma. A particularly noticeable suppression of the sarcoma growth was demonstrated by PM-8. According to the results the polyoxoanionic structure of  $\text{Mo}_7\text{O}_{24}$  is crucial for the anticancer activity [331]. From the point of view of biomedical application, the use of POM as part of complexes based on them seems to be promising. Reference [332] describes the creation of a number of conjugates of biological substances and organic compounds with a POM with the Anderson structure and the formula  $\text{MnMo}_6\text{O}_{18}[(\text{OCH}_2)_3\text{CNH}_2]_2^{3-}$ , which has a proven antitumor effect. Among the above-mentioned organic compounds are the cholic dehydrocholic and adipic acids; cholesterol, and diacetone-D-galactose (pretreated with succinic anhydride to obtain derivatives containing the carboxylic group). These substances are selected from the group of identifier molecules specific to certain tissues or cells. It was demonstrated in the paper that the correct choice of ligands can ensure a synergistic effect. Thus, the best result was achieved when a POM cluster was conjugated with cholic and dehydrocholic acids. Such conjugates demonstrated an increased antitumor activity and selectivity in comparison with the initial cluster and ligands [332–334].

Among the most interesting types of POM nanoclusters are the spherical polyoxomolybdates with a fullerene-like structure, which are called Keplerates. These POM were discovered by the research group of Prof Achim Müller [335]. The first obtained POM nanocluster contains 132 molybdenum atoms ( $\text{Mo}_{132}$ ), of which 72 have an oxidation state of 6+, and 60 of 5+. Molybdenum oxygen polyhedra that form Keplerates are octahedral configurations and pentagonal pyramids connected by edges and tops (Fig. 5) Such compounds are stabilized by ligands (in particular, acetate groups) and water molecules. Compounds belonging to the class of Keplerate-type POM nanoclusters attract attention both by the uniqueness of their structure and by the relative simplicity of their synthesis [336]. Their formation occurs through self-assembly from the initial molybdenum compounds under the conditions of medium acidity regulation and in presence of a specified amount of reducing agent. POM show stability in weakly acidic solutions, and can be isolated

in crystalline or amorphized state. Due to the presence of an internal cavity and pores in the structure of Keplerales, it is possible to introduce various substances inside them, both ions and molecules [337, 338], including bioactive substances, which makes them promising in the context of creating nanocapsules for targeted drug delivery [339]. Fig. 5 shows structure of a POM with pentavalent molybdenum replaced by iron(III) ions in the initial  $\text{Mo}_{132}$  cluster. The absence of toxic Mo(V) in its structure and its electron-transport properties [340] make this compound particularly interesting. It has the following chemical formula:  $[\text{Mo}_{72}\text{Fe}_{30}\text{O}_{252}(\text{CH}_3\text{COO})_{12}\{\text{Mo}_2\text{O}_7(\text{H}_2\text{O})\}_2\{\text{H}_2\text{Mo}_2\text{O}_8(\text{H}_2\text{O})\}(\text{H}_2\text{O})_{91}] \sim 150\text{H}_2\text{O}$  and its common abbreviation is  $\text{Mo}_{72}\text{Fe}_{30}$  [341]. In dilute aqueous solutions or at an increase in the medium pH, the POM clusters decompose over time into simpler compounds [342, 343].  $\text{Mo}_{72}\text{Fe}_{30}$  decomposes into compounds that are relatively harmless to the body. Toxicity studies did not reveal any significant adverse effect of  $\text{Mo}_{72}\text{Fe}_{30}$  on the animal subjects [344]. Studies of the acute and subacute effects of  $\text{Mo}_{72}\text{Fe}_{30}$  on the functional status of such organs of experimental animals as the liver, kidneys, and pancreas, confirmed the absence of appreciable negative effects [345, 346]. In addition, the available experimental data on the effects of  $\text{Mo}_{72}\text{Fe}_{30}$  on liver and blood cells [347] suggest that this nanocluster does not cause the autoimmune reaction of lymphocytes to hepatocytes. POM and products of their destruction showed no prolonged accumulation in the body.

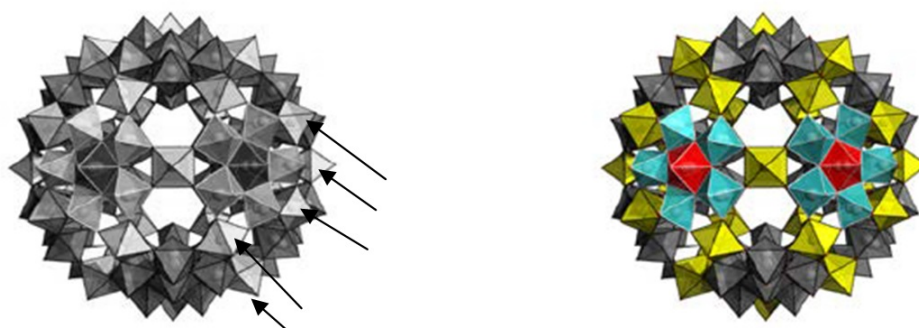


FIG. 5. Schematic representation of the POM  $\text{Mo}_{72}\text{Fe}_{30}$  structure (adapted from [353])

The positions of some oxygen polyhedra belonging to iron ions are shown by arrows (such polyhedra are highlighted yellow in the electronic version of the paper) One of the above-mentioned octahedra is located directly in the center of the structure.

In aqueous solutions  $\text{Mo}_{72}\text{Fe}_{30}$  is known to exhibit the properties of a weak acid, that is, it partially dissociates to form negatively charged polyanions with the maximum charge of 22- [348]. Since the  $\text{Mo}_{72}\text{Fe}_{30}$  nanocluster exists in solution in the ionized form, its movement can be controlled by means of an electric field, and therefore, its introduction into the body by iontophoresis is possible. For instance, *in vitro* and *in vivo* experiments (on rats) have demonstrated that  $\text{Mo}_{72}\text{Fe}_{30}$  is transferred through the skin under the action of an electric field of the corresponding polarity more rapidly than during passive transfer [349–351]. The electrophoretic (iontophoretic) drug administration method has several advantages compared with injection methods of administration, e.g., non-invasive nature of the procedure, i.e., no disruption of the body's natural barriers during the procedure; a possibility to have a predominantly local impact, and to achieve a prolonged action due to the creation of a drug depot in tissues, etc. A weakness of the method is the significantly limited rate of drug administration compared with the injection methods. The results of studies on the possibility of using  $\text{Mo}_{72}\text{Fe}_{30}$  for transporting bioactive substances are given below. It should be noted that the organic part of the molecules in the considered POM does not contain toxic components, while iron and molybdenum are essential microelements that are necessary for the body as components of the vitamin-mineral complexes involved in the blood production, enzymatic reactions and other important biological processes [352].

## 5.2. Transport characteristics of polyoxometalates: modeling and experimental study

The first data on the transport properties of POM  $\text{Mo}_{72}\text{Fe}_{30}$  and  $\text{Mo}_{132}$  were obtained with regard to their pure aqueous solutions, in particular, in the case of capillary electrophoresis. The diffusion coefficient for  $\text{Mo}_{132}$  and  $\text{Mo}_{72}\text{Fe}_{30}$  ions in water was  $1.8 \cdot 10^{-7} \text{ cm}^2/\text{s}$  (at a concentration of  $4 \cdot 10^{-4} \text{ mol/l}$ ) and  $7.3 \cdot 10^{-7} \text{ cm}^2/\text{s}$  ( $10^{-5} \text{ mol/l}$ ), respectively [342, 354]. The magnitude of the electrical mobility of these ions was similar and amounted to  $6.4 \cdot 10^{-8} \text{ m}^2/\text{V} \cdot \text{s}$ . The reference [340] offers data on the specific and ionic conductivities of the considered POM solutions; the values of ionic conductivity at infinite dilution for  $\text{Mo}_{72}\text{Fe}_{30}$  and  $\text{Mo}_{132}$  were 6 and  $14 \text{ S} \cdot \text{m}^2 \text{ mol}^{-1}$ , respectively. The number of POM polyanion transfers in aqueous solutions is estimated at 10–20%. The obtained

data showed ion mobility to be sufficient for transport purposes. This made it possible to proceed to the next stage of research, i.e., the study of the POM transcutaneous electrical transport.

POM anions transcutaneous transport was modeled *in vitro* using native skin samples and also studied *in vivo* [339, 349]. The obtained data made it possible to evaluate the diffusion coefficient for  $\text{Mo}_{72}\text{Fe}_{30}$  through the studied membrane; the average value of which was  $1.8 \pm 0.2 \cdot 10^{-11} \text{ cm}^2/\text{s}$ , and the calculated electrical mobility was found to be  $5.5 \cdot 10^{-10} \text{ m}^2/(\text{V} \cdot \text{s})$ . Under the action of an electric field, the diffusion flux of Keplerate ions through the dermal membrane increased, at least by an order of magnitude, and was quite acceptable for practical use. In contrast to the above-described experiments, which showed the absence of long-term accumulation of POM in organs and tissues after intravenous, intramuscular, or oral administration, transcutaneous transport experiments resulted in temporary drug accumulation in the skin, which was confirmed by the analysis of skin thin sections obtained after POM electrophoresis and sample freezing in liquid nitrogen [355]. The analysis (Fig. 6) was performed by the X-ray fluorescence method. The content of iron, reflecting the concentration of POM after the electric transport of  $\text{Mo}_{72}\text{Fe}_{30}$ , was significantly higher than in the intact sample. The POM content in the skin has its maximum, which confirms the possibility of accumulation [351], localized in the region preceding the zone of the maximally dense capillary network (Fig. 6), through which the enhanced POM outflow into the circulatory system is possible. The difference in absolute values of POM concentration in two parallel experiments may be due to the individual characteristics of the biological objects, i.e., of the native membranes taken for the experiments. The relatively low POM concentration in the skin's upper layers is determined by the fact that the epidermis that contains little water, does not accumulate, as a rule, the injected substances that travel through its pores.

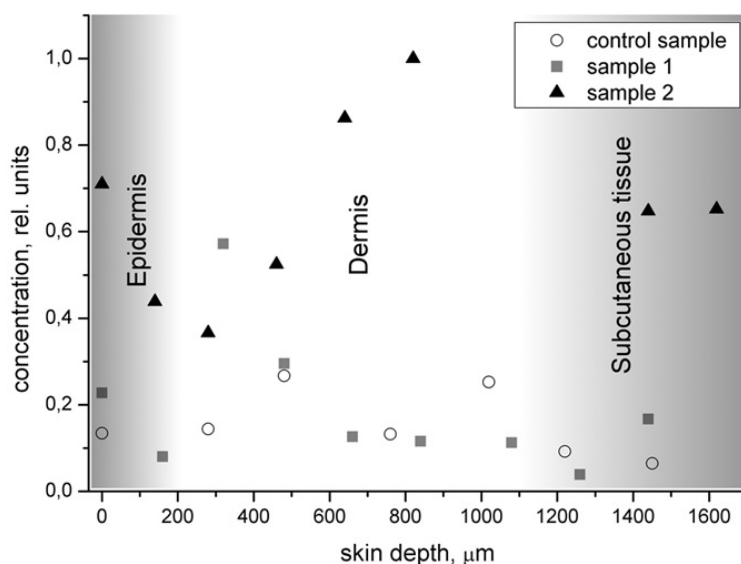


FIG. 6. The distribution of iron, a POM component, within skin depth [355]

After confirming the principal possibility to transport Keplerates electrophoretically through the isolated skin, their diffusion was investigated in an *in vivo* experiment [349]. Of interest are the results indicating an increase in the ability of POM to penetrate the skin during iontophoresis when they are components of some ointments used to increase skin permeability. For instance, the content of POM components in the blood plasma increased about three-fold 1 hour after the procedure that used a silicone-based ointment (gel), while the silicon-titanium-containing glycerogel did not yield such an effect.

Experiments were conducted to select the parameters of iontophoretic procedures, and the current-voltage characteristic of the electrode system [355] (Fig. 7) was obtained, when lead or lead-tin alloy electrodes were separated directly by the native skin membrane. Upon reaching the applied voltage of 4 V, the current reached its maximum and then dropped due to the anodic passivation of the electrode material. That is why 4 V was chosen as the optimal operating voltage. The study of polarization phenomena on the skin membrane has shown that they are capable of reducing the effective value of the electric field acting on the transported ions. The potential difference was measured in the original cell on different sides of the membrane using additional electrodes placed in close proximity to the skin, with a voltage of 4 V applied to the working electrodes (Fig. 8). The cathode part of the cell was filled with the

Mo<sub>72</sub>Fe<sub>30</sub> solution (0.5 g/l, or 2.68<sup>-5</sup> M). In presence of pure water on the anode side of the membrane, polarization of the initial concentration occurred and counteracted the applied field, however it gradually decreased with the penetration of a part of ions across the membrane. This case models electric transport into such media of the body where the dissolved ions concentration is low. When the anode space of the cell contained cattle blood serum, then such polarization did not occur initially due to the presence of ions with different signs in it, like in the electrolyte, but increased as the electrophoresis proceeded, because POM anions are much less mobile than, e.g., metal cations found in the serum. The local maximum on this curve may be due to the accumulation and release from the membrane of a component of a complex system that contains biological materials. The obtained data can be used when modeling processes and calculating the parameters of electrotransport in native membranes.

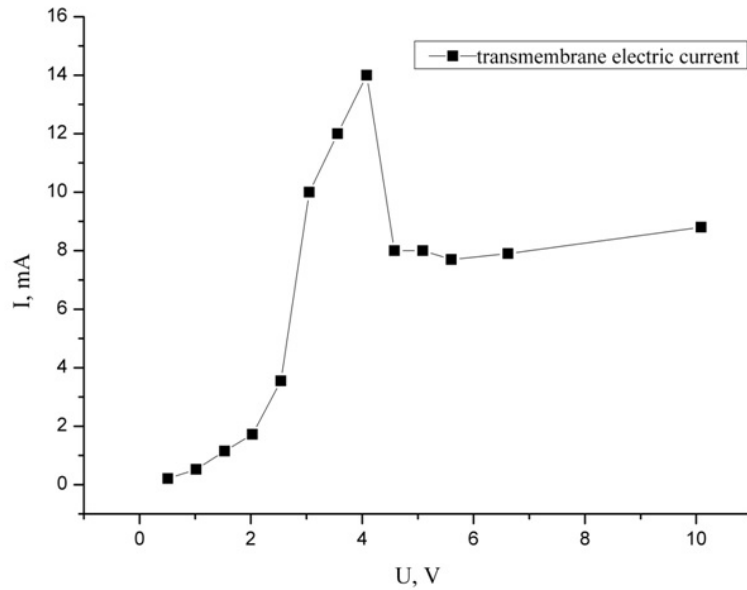


FIG. 7. Volt-ampere characteristic of the electrodes/skin membrane system [355]

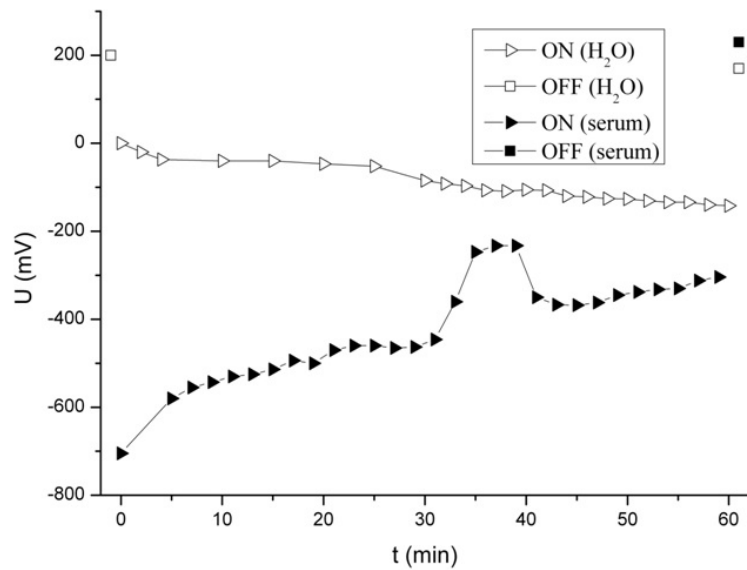


FIG. 8. Skin membrane polarization with water or blood serum in the anode space, with the field on and off [355]

The correctness of parameter choice for the iontophoretic effect was verified in [349] using the level of glucose in the blood of animals as a non-specific indicator of a stressful situation. The level of glucose did not increase

during iontophoresis in comparison with this indicator in intact animals (Table 3), which means that they did not experience strong discomfort. The experiment did not detect significant changes in the indicators characterizing the functional state of the heart, liver, kidneys and pancreas, which indicates the absence of a pronounced toxic effect from this method of POM administration. The  $\text{Mo}_{72}\text{Fe}_{30}$  concentration in the iontophoretic solution was 1 mg/ml. The molybdenum and iron content determined in plasma and skin are presented in Table 4. The introduction of POM by iontophoresis contributed to an increase in the molybdenum content in the blood by almost 8 times, and by 4.2 times in the skin, thus indicating effectiveness of the technique and the possibility of POM transport into the body *in vivo*.

TABLE 3. Animal blood plasma biochemical indicators 1 hour after a single iontophoretic introduction of the iron-molybdenum POM

Indicator	Group of animals	
	Intact	After iontophoresis
Glucose, mmol/l	6.9±0.1	6.7±1.0
AST, U/l	13.2±0.7	13.5±1.2
ALT, U/l	9.1±0.5	11.3±1.2
AST/ALT	1.46±0.10	1.22±0.18
Alkaline phosphatase, U/l	50.4±3.0	51.2±7.1
Alpha-amylase, mg/s-l	29.7±2.9	33.9±6.5
Total protein, g/l	72.0±2.7	71.4±1.5
Creatinine, $\mu\text{mol/l}$	65.8±6.2	57.3±1.2

AST – aspartate aminotransferase;

ALT - alanine aminotransferase

TABLE 4. Mo and Fe content in the skin and blood plasma before and after iontophoretic introduction of the iron-molybdenum POM

Group	Mo, $\mu\text{g/l}$		Fe, $\mu\text{g/l}$	
	Skin	Plasma	Skin	Plasma
1 – intact	2.3±1.0	11.6±2.9	30.0±0.1	73.3±0.1
2 – electrophoresis	9.7±1.*	89.3±0.3*	208.0±0.7*	53.5±0.3*

\* – differences from the intact group are significant with the error probability  $P < 0.05$

The *in vivo* experiments have shown the possibility of iontophoretic transfer of ionic  $\text{Mo}_{72}\text{Fe}_{30}$  associates with lanthanum [350], when the positively recharged complexes moved to the cathode instead of anode. The observed simultaneous increase in concentration in the skin of all three elements (iron, molybdenum, lanthanum) during the transport from the anode to cathode is possible only if the associate is transferred as a whole. The absence of a significant increase in the molybdenum and iron concentration in the muscle tissues immediately after iontophoresis, as well as the oppositely directed change in the content of these elements in the deep muscles one hour after the procedure, along with an increased content of lanthanum there, suggest that the transferred ion species dissociates after passing through the skin barrier and its components get carried away by the bloodstream. In this case, the POM-transferred drug should be released in the area adjacent to the electrophoresis area. It is important to note that the lanthanum/molybdenum mass ratio determined in the obtained keplerate-lanthanum associate, is about 0.8. The value of this indicator in the skin of animals immediately after iontophoresis, taking into account the content of elements in the skin of intact animals, is about 0.79, which almost coincides with the original value.

The  $\text{Mo}_7\text{Fe}_{30}$  transfer through the skin was theoretically modeled in [351]. The basic initial data for modeling the POM transfer process were taken from the results of experiments from [349] performed in the absence of a difference in potentials and with the application of an electric field, which show an increase in the POM concentration during the observation time (45 minutes). According to the data obtained without the electric field application, the coefficient of the POM diffusion through the studied membrane was estimated by the formula:

$$D = \frac{\Delta m}{S \cdot \Delta t} \cdot \frac{\Delta x}{\Delta c},$$

where  $\Delta x$  is the membrane thickness,  $\Delta c$  is the difference in Keplerates (POM) concentrations in the upper and lower solutions, and  $\Delta t$  is time period. The time-averaged value of the coefficient of POM diffusion through the skin membrane ( $1.77 \pm 0.20$ )  $10^{-11}$   $\text{m}^2/\text{s}$  was obtained and further used in numerical calculations using the proposed model. Experiments involving the electric field action also made it possible to estimate the POM electric mobility.

A model of the POM transfer through the skin membrane as a porous medium was considered. The model of a porous medium employed the expressions for the diffusion (D index) and external electric flows (E index), which take into account their mutual influence:

$$J_D = -D \frac{dc}{dx} - \mu c(x) \frac{\partial \varphi}{\partial x}, \quad J_E = -\alpha \frac{\partial c(x)}{\partial x} - \gamma \frac{\partial \varphi}{\partial x}, \quad (6)$$

where  $c(x)$  is the diffusing particles concentration ( $[c]=\text{mol}/\text{m}^3$ ),  $D$  is the free diffusion coefficient ( $[D]=\text{mol}/\text{m}^3$ ),  $\alpha$  is the unknown coefficient that further requires determination ( $[\alpha]=\text{A}\cdot\text{m}^2/\text{mol}$ ),  $\gamma$  is the medium electrical conductivity coefficient ( $[\gamma]=1/\text{m}\cdot\text{Ohm}$ ),  $\mu = q_i D/RT_0$  (the Nernst-Einstein relation), a quantity characterizing particle mobility in an electric field ( $[\mu]=\text{A}\cdot\text{m}^2/\text{J}$ ),  $R$  is the universal gas constant ( $[R]=\text{J}/\text{K}\cdot\text{mol}$ ), and  $T_0$  is the absolute temperature. When deriving the equation and performing calculations, the dependence of the electrical conductivity ( $\gamma$ ) on the POM concentration ( $c$ ) was taken into account. The experimental value of  $\mu$  was  $1.50 \cdot 10^{-8}$   $\text{m}^2/(\text{V}\cdot\text{s})$ . It was established that under the action of an electric field, the diffusion flux of POM ions through the skin membrane increased at least by an order of magnitude, as is already indicated above. According to the Onsager's principle of cross-coefficients symmetry,  $\alpha = \mu RT_0$ . Using the thermodynamic approach [356, 357], a differential equation was obtained for the POM concentration in the membrane:

$$\frac{\partial c}{\partial t} = D \frac{\partial^2 c}{\partial x^2} + \mu \frac{\partial c}{\partial x} \frac{\partial \varphi}{\partial x} + \frac{c}{RT_0} \left( \frac{\partial \varphi}{\partial x} \right)^2 \left( \frac{\partial \gamma}{\partial c} \right). \quad (7)$$

The derived equation shows that there is a weak spatial heterogeneity of the concentration gradient in relation to the total POM concentration in the membrane. This one-dimensional diffusion equation was used in numerical calculations, taking into account the initial and boundary conditions, as well as the dependence of the specific electrical conductivity of the membrane on the concentration. This equation describes the POM diffusion, taking into account the influence of the electric field  $\varphi$ . To solve the equation (7) numerically, the following basic assumptions were used. The direct POM accumulation can occur only in the epidermis, since the dermis and papillary layer are permeated by a large number of blood vessels that contribute to the spreading throughout the body of the particles, which have passed through the upper layers of the skin. Therefore, the POM concentration at the lower boundary of the skin is  $c(l) = 0$ . Due to the relative smallness of the diffusion coefficient, it can be assumed that the concentration of the POM solution on the outer surface of the skin is constant (i.e.,  $c(0)=\text{const}$ ). The numerical calculation of equation (7) was performed using the implicit difference schemes method widely used in various fields of science [358–362].

Thus, the transcutaneous POM transfer into the body was mathematically modeled. The experiments on the POM iontophoretic transport into animals [350] have shown that the content of molybdenum after iontophoresis in the muscle tissue layers adjacent to the skin is significantly lower than in the skin. A Keplerate accumulation is formed in the skin, while the POM that reached its inner boundary are intensively transported away via the bloodstream. A mathematical model of the dependence of the POM concentration distribution within the skin layer on the time and membrane thickness was used to perform numerical calculations for the conditions when a voltage of 4 V was applied, and the distance between electrodes was 2 cm at  $T_0=300$  K. The experimentally estimated values of the diffusion coefficient ( $D=1.77 \cdot 10^{-11}$   $\text{m}^2/\text{s}$ ) and of mobility ( $\mu=1.50 \cdot 10^{-8}$   $\text{m}^2/\text{V}\cdot\text{s}$ ) were used in this case. In equation (7), the term with the derivative ( $\partial \gamma / \partial c$ ), i.e., the dependence of the specific electrical conductivity on the concentration, remained unknown; therefore, it was set empirically as a power function  $\gamma = ac^b$ . The values calculated for the constants  $a$  and  $b$  were found to be  $1 \cdot 10^{-14}$  for  $a$ , and  $-2.2$  for  $b$ . These parameters were determined taking into account the experimental value of the coefficient of POM diffusion through the skin membrane. Based on the calculations using equation (7), POM concentration profiles in the skin after switching the electric field on were built (Fig. 9a). A theoretical prediction showed that POM accumulation can occur near the upper boundary of the skin layer.

An increase in the POM concentration in the membrane (Fig. 9a) over time and its drop with the advance deeper into the skin may be due to a strong POM outflow from the inner boundary (the anode space). In this case, a sharp

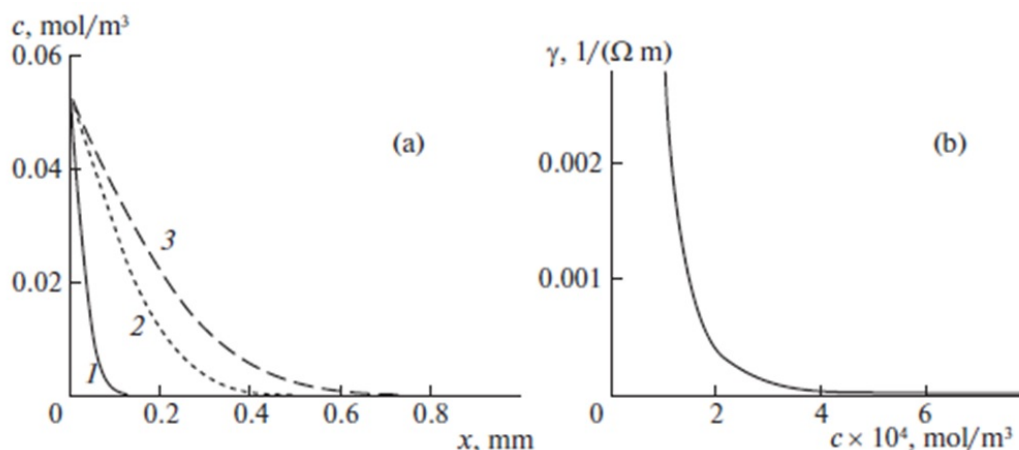


FIG. 9. a) POM concentration as a function of variable  $x$  (skin thickness), which varies within the limits  $[0; l]$  ( $l$  is the skin layer thickness,  $l = 1$  mm): curve 1 – 50 s; 2 – 150 s; 3 – 1800 s; b) Dependence of the POM specific electrical conductivity on the concentration ( $c$ ) in the membrane [351]

increase in the POM concentration in the upper layer of the membrane already at the initial moments of time, accompanied by a decrease in electrical conductivity to the minimum values (Fig. 9b), leads to the situation when further on the penetration of POM into the membrane proceeds due to chemical diffusion, and this fact indicates the formation of a POM depot in the membrane.

The concentration profiles helped to determine the coefficient of POM diffusion in the skin. By using the inclination angle tangent ( $\tan \alpha$ ) for the dependence of  $\ln(C)$  on  $x^2$ , the diffusion coefficient  $D$  was determined according to the formula  $D = 1/(4t \cdot \tan \alpha)$ , where  $t$  is the current time, to which the spatial concentration profile taken for evaluation corresponds. The diffusion coefficient  $D$  value of  $1.5 \cdot 10^{-11}$  m<sup>2</sup>/s obtained by numerical calculations is close to the experimental  $D = 1.77 \cdot 10^{-11}$  m<sup>2</sup>/s, which proves the adequacy of the proposed mathematical model of POM transport in a membrane. The calculated data correlated well with the experimental concentration profiles (Fig. 6) of POM distribution within the skin thickness, which also confirmed the conclusions made. Thus, the possibility of intensifying the process of iontophoretic transcutaneous POM transfer is shown by an increase in the transferred flux by an order of magnitude compared with self-diffusion. In principle, this confirms the possibility of creating an effective system for the delivery by POM of the associated bioactive substances. The created model contains the empirical dependence of the coefficient of POM specific electrical conductivity in the membrane on the concentration, which allows the evaluation of the membrane electrical conductivity.

The use of the technique developed in [363] demonstrates the ability of POM to increase the permeability of cell membranes for drugs, e.g., antifolate cytostatic agents. It is important for potential use in oncology and requires further research [364,365]. To study the influence of Mo<sub>72</sub>Fe<sub>30</sub> on the transport of cytostatic into the cells, *Drosophila melanogaster* flies were used at the pupa and larva early and late embryogenesis stages, and aminopterin was used as a model drug, the increased effect of which in the presence of POM indicates the potential reduction of the therapeutic doses to be used.

### 5.3. POM-based transcutaneous transport of associates

Proceeding from the results of studies on the association of POM with bioactive substances and the possibility of organic substances retention in the internal cavity and external sphere of POM [366], experiments were conducted and demonstrated that it is promising to use the electrophoretic (iontophoretic) transcutaneous transport of the resulting associates (conjugates). The possibility of efficient transport of the bioactive substances with POM has been experimentally confirmed [367]. The *in vitro* experiments showed the electric field-stimulated transfer of Mo<sub>72</sub>Fe<sub>30</sub> associated with thiamine chloride as a model substance. Also, the transcutaneous transfer of the POM-associated insulin was demonstrated; moreover, insulin retained biological activity [367], as its concentration in the trans-membrane space was measured by enzyme immunoassay.

The described experiments yielded an estimate of the effective coefficients of the conjugates diffusion concerning thiamine and POM, which were  $6.79 \cdot 10^{-12}$  and  $1.04 \cdot 10^{-11}$  m<sup>2</sup>/s, respectively. For pure POM, the values of  $D$  in these conditions ranged from  $1.02 \cdot 10^{-11}$  to  $2.14 \cdot 10^{-11}$  m<sup>2</sup>/s (the spread of  $D$  values may be due to the individual characteristics of skin samples obtained from different animals). However, in general, the coefficient of Mo<sub>72</sub>Fe<sub>30</sub>

diffusion in the presence of thiamine chloride does not differ much from  $D$  of pure POM. To calculate the value of  $D$ , some approximations were assumed for a single-layer homogeneous membrane. The electric field inside the membrane was considered uniform. The potential difference applied to the electrodes and the distance between the contacts allowed estimation of the field intensity. The diffusing particle concentration in the initial solution was considered constant. The concentration in the trans-membrane solution was assumed to be zero. In such an approximation, the process of electrodiffusion of the charged particles (in particular, of POM particles) obeys the Nernst–Planck equation [351]. The Nernst–Planck equation was solved numerically.

The results of *in vitro* iontophoretic experiments that were performed at room temperature and involved  $\text{Mo}_7\text{Fe}_{30}$  associates with polyvinylpyrrolidone in a 160:1 molar ratio between the polymer monomolecular units number and POM showed a possibility of their transport through the skin. Estimates of the increase in the concentration of associate components (molybdenum and iron) in the anode space over time (the maximum duration of each experiment was 45 min) made possible the determination of the effective diffusion coefficient  $D$  for POM. The estimated diffusion coefficient value was  $7.34 \cdot 10^{-13} \text{ m}^2/\text{s}$  in the experiments. The reduced mobility of associates in the skin as compared to pure POM is due not only to the increase in the size of formations (aggregates). It may be assumed that it was mainly caused by the fairly active interaction of the polymeric shell with the protein components contained in, e.g., cell membranes, and, apparently, with the phospholipid part of these membranes with the outward-facing polar moieties. Fairly strong interaction between polyvinylpyrrolidone and proteins was shown in particular in [368], and also there were indications of the interaction of other water-soluble polymers with molecules in the media of the body [369]. On the other hand, the formation of POM  $\text{Mo}_7\text{Fe}_{30}$  associates with polyvinylpyrrolidone is thermodynamically beneficial [370], as is noted above. These two factors seem to contribute to the slowing down of the POM associate movement in the skin and creation of a depot. In this relation it should be noted that a significant role in the transport and conjugation properties of both nanoscale particles in general and POM in the body's media is played by their ability to form associates with proteins [371–377]. Proteins form a peculiar crown on the nanoscale particles, which largely determine the behavior of the latter in the body, their interaction with albumins, globulins and other proteins in the blood serum, in particular, POM stabilization [372].

## 6. Conclusion

An analysis of the information available in the literature taking into account the historical aspect of the development of fundamental and applied research in the field of targeted drug delivery, permits one to draw the following conclusions. The development of modern means of targeted delivery follows the way of creating hybrid nanocompositions, including those that contain organic and inorganic components. The hybrid systems can combine the functions of diagnosis and treatment of the affected organs and tissues. They include components that serve to identify biological targets, as well as to actively influence the affected areas due to the local release of drugs, or to photo- and magnetodynamic effects. Significant progress has been achieved in the use of such means of targeted delivery, including liposomal methods. Attention is paid to exploring the possibility of expanding the practical application of the carbon material-based therapeutic agents, such as buckyballs (fullerenes), graphene, carbon nanotubes, nanodiamonds, etc. An important aspect of the research and practical implementation is the study of the properties of metal, oxide and other inorganic nanosized particles, including those with magnetic, luminescent properties, which can have their own bioactivity, as well as be used as part of diagnostics and photo- and magnetodynamic therapy methods. Technologies for obtaining nanoscale particles with specified characteristics, adapted for the formation of nanocompositions, are being actively developed. The use of magnetic particles makes possible their delivery and localization under the action of the corresponding fields, or magnetic hyperthermia. The systems of targeted delivery with the electrically charged particles can be used for efficient transport, including transcutaneous, under the action of an electric field. The use of nanocomposites in biomedicine is associated with the development of shells consisting, in particular, of polymeric components (dendrimers, block copolymers, natural biocompatible polymers, proteins, lipids, etc.), as well as with the inclusion of targeted delivery vectors, including intracellular (proteins, antibodies, nucleic acids, etc.). Much attention is paid to the possibility of developing harmless biocompatible composite means of targeted delivery.

For the effective use of the above-mentioned means of transcutaneous drug transport, model representations have been developed for predicting the delivery processes. Models for the means of transport for targeted delivery take into account special properties of nanostructured objects and real skin as a transfer medium to a varying extent, which, in one way or another, complicates the setting of boundary conditions and calculations using such models, but increases reliability of calculations. The models of the means of targeted delivery transportation are continuously improving.

Nanocluster polyoxometalates, in particular those based on molybdenum compounds, possess properties that make it possible to consider them among other means of targeted delivery. For instance, some polyoxometalates have their own bioactivity, for example, their anticancer activity has been detected. On the other hand, there exist water-soluble polyoxometalates that are practically non-toxic to the body of warm-blooded animals and can form multiply

charged anions that are able to associate with protein molecules, polymers and drugs. The model and experimental studies have shown the possibility of effective transdermal iontophoretic transport of drugs as part of conjugates with polyoxometalates. Such polyoxometalates include the iron-molybdenum compound  $\text{Mo}_{72}\text{Fe}_{30}$  with the keplerate type structure, which has, among other things, an internal cavity and pores that link it to the environment. On the one hand, this compound and its components do not accumulate in the body for a long time; while on the other hand, Keplerates are capable of accumulating in the skin, which can be used for the prolonged drug action. In addition, this polyoxometalate increases the cell membranes permeability for cytostatics (experiments were performed on insect larvae), which, in principle, allows a reduction in the therapeutic dose of such drugs. It is of interest to further study nanocluster polyoxomolybdates with keplerate-type structure as a basis for new promising systems for targeted delivery of bioactive substances and actual therapeutic agents.

## Acknowledgements

The paper was prepared in the framework of implementation of the state assignment from the Ministry of Education and Science of the Russian Federation (Projects Nos. 4.6653.2017/8.9 and AAAA-A18-118020590107-0), and of the Program for Increasing Competitiveness of UrFU (Agreement No. 02.A03.21.0006).

## References

- [1] Holgado M.A., Martin-Banderas L., Alvarez-Fuentes J., Fernandez-Arevalo M., Arias J.L. Drug Targeting to Cancer by Nanoparticles Surface Functionalized with Special Biomolecules. *Curr. Med. Chem.*, 2012, **19**(19), P. 3188–3195.
- [2] Parashar A.K., Kakde D., Chadhar V., Devaliya R., Shrivastav V., Jai U.K. A review on Solid Lipid Nanoparticles (SLN) for controlled and targeted delivery of medicinal agents. *Curr. Res. Pharm. Sci.*, 2011, **1**(2), P. 367–47.
- [3] Ventola C.L. Progress in Nanomedicine: Approved and Investigational Nanodrugs. *Pharm. and Therapeutics*, 2017, **42**(12), P. 742–755.
- [4] Farokhzad O.C., Langer R. Impact of Nanotechnology on Drug Delivery. *ACS Nano*, 2009, **3**(1), P. 16–20.
- [5] Chen Y., Bose A., Bothun G.D. Controlled Release from Bilayer-Decorated Magnetoliposomes via Electromagnetic Heating. *ACS Nano*, 2010, **4**(6), P. 3215–3221.
- [6] Ganta S., Devalapally H., Shahiwala A., Amiji M. A review of stimuli-responsive nanocarriers for drug and gene delivery. *J. Control Release*, 2008, **126**(3), P. 187–204.
- [7] Torchilin V.P. *Nanoparticulates as drug carriers*. Imperial College Press, London, 2006, 754 p.
- [8] Pal S.L., Jana U., Manna P.K., Mohanta G.P., Manavalan R. Nanoparticle: An overview of preparation and characterization. *J. Appl. Pharm. Sci.*, 2011, **1**(6), P. 228–234.
- [9] Niu Z. Targeted transport therapeutic nanoparticles into adipose tissue. *J. Pharm. Drug Deliv. Res.*, 2018, **7**, P. 76.
- [10] Alyautdin R., Khalin I., Nafeeza M.I., Haron M.H., Kuznetsov D. Nanoscale drug delivery systems and the blood–brain barrier. *Intern. J. Nanomed.*, 2014, **9**, P. 795–811.
- [11] Lu C.T., Jin R.-R., Yi-Na Jiang Y.N., Lin Q., Yu W.-Z., Mao K.-L., Tian F.-R., Zhao Y.-P., Zhao Y.-Z. Gelatin nanoparticle-mediated intranasal delivery of substance P protects against 6-hydroxydopamine-induced apoptosis: an *in vitro* and *in vivo* study. *Drug Design, Development and Therapy*, 2015, **9**, P. 1955–1962.
- [12] Sahoo S.K., Labhasetwar V. Enhanced antiproliferative activity of transferrin-conjugated paclitaxel-loaded nanoparticles is mediated via sustained intracellular drug retention. *Mol. Pharm.*, 2005, **2**, P. 373–383.
- [13] Prabh V., Uzzaman S., Grace V.M.B., Guruvayoorappan C. Nanoparticles in Drug Delivery and Cancer Therapy: The Giant Rats Tail. *J. Cancer Therapy*, 2011, **2**, P. 325–334.
- [14] Gu F., Langer R., Omid C., Farokhzad O.C. Formulation/Preparation of Functionalized Nanoparticles for *In Vivo* Targeted Drug Delivery. *Micro and Nano Technologies in Bioanalysis, Methods in Molecular Biology (Humana Press, a part of Springer Science + Business Media, LLC 2009)*, 2009, **544**(Ch.37), P. 589–598.
- [15] Jain K.K. The Role of Nanobiotechnology in Drug Discovery. *Drug Discover Today*, 2005, **10**(21), P. 1435–1442.
- [16] Mishra B., Patel B.B., Tiwari S. Colloidal Nanocarriers: A Review on Formulation Technology, Types and Applications toward Targeted Drug Delivery. *Nanomed.*, 2010, **6**(1), P. 9–24.
- [17] Majuru S., Oyewumi O. Nanotechnology in Drug Development and Life Cycle Management. *Nanotechnology in Drug Delivery*, 2009, **10**(4), P. 597–619.
- [18] Pridgen E.M., Alexis F., Kuo T.T., Levy-Nissenbaum E., Karnik R., Blumberg R.S., Langer R., Farokhzad O.C. Trans epithelial Transport of Fc-Targeted Nanoparticles by the Neonatal Fc Receptor for Oral Delivery. *Sci. Transl. Med.*, 2013, **5**(213), P. 213–237.
- [19] Yu M.K., Park J., Jon S. Targeting Strategies for Multifunctional Nanoparticles in Cancer Imaging and Therapy. *Theranostics*, 2012, **2**(1), P. 3–44.
- [20] Allen T.M., Cullis P.R. Drug delivery systems: entering the mainstream. *Science*, 2004, **303**, P. 1818–1822.
- [21] Brannon-Peppas L., Blanchette J.O. Nanoparticle and target systems for cancer therapy. *Adv. drug delivery rev.*, 2004, **56**, P. 1649–1659.
- [22] Perr D., Karp J.M., Hong S., Farokhzad O.C., Magalit R., Langer R. Nanocarriers as an emerging platform for cancer therapy. *Nature nanotechnology*, 2007, **2**(12), P. 751–760.
- [23] Lao J., Madani J., Puértolas T., Álvarez M., Hernández H., Pazo-Cid R.C., Artañ A., Antonio A. Liposomal Doxorubicin in the Treatment of Breast Cancer Patients: A Review. *J. Drug Delivery*, 2013, **3**, P. 1–12.
- [24] Bagherifam S., Skjeldal F.M., Griffiths G., Mælandsmo G.M., Olav Engebråten O., Nyström B., Hasirci V., Hasirci N. pH-Responsive Nano Carriers for Doxorubicin Delivery. *Pharm. Res.*, 2015, **32**, P. 1249–1263.
- [25] Gardikis K., Tsimplouli C., Dimas K., Micha-Screttas M., Demetzos C. New chimeric advanced Drug Delivery nano Systems (chi-aDDnSs) as doxorubicin carriers. *Int. J. Pharm.*, 2010, **402**(1-2), P. 231–237.

- [26] Hira S.K., Mishra A.K., Ray B., Manna P.P. Targeted Delivery of Doxorubicin-Loaded Poly( $\epsilon$ -caprolactone)-*b*-Poly (N-vinylpyrrolidone) Micelles Enhances Antitumor Effect in Lymphoma. *PLoS ONE*, 2014, **9**(4), P. 1–17.
- [27] Takahama H., Minamino T., Asanuma H. et al. Prolonged targeting of ischemic/reperfused myocardium by liposomal adenosine augments cardioprotection in rats. *J. Amer. College Cardiol.*, 2009, **53**(8), P. 709–717.
- [28] Navarro G., Pan J., Torchilin V.P. Micelle-like Nanoparticles as Carriers for DNA and siRNA. *Mol. Pharm.*, 2015, **12**, P. 301–313.
- [29] Zhang C., Zhu W., Liu Y., Yuan Z., Yang S., Chen W., Li J., Zhou X., Liu C., Zhang X. Novel polymer micelle mediated co-delivery of doxorubicin and P-glycoprotein siRNA for reversal of multidrug resistance and synergistic tumor therapy, 2016. ([www.nature.com/scientificreports/](http://www.nature.com/scientificreports/)). P. 1–12.
- [30] Zuckerman J.E., Gritli I., Tolcher A., Heidel J.D., Lim D., Morgan R., Chmielowski B., Ribas A., Davis M.E., Yen Y. Correlating animal and human phase Ia/Ib clinical data with CALAA-01, a targeted, polymer-based nanoparticle containing siRNA. *Proc. Nat. Acad. Sci.*, 2014, **111**, P. 11449–11454.
- [31] Baskar G., George G.B., Chamundeeswari M. Synthesis and Characterization of Asparaginase Bound Silver Nanocomposite Against Ovarian Cancer Cell Line A2780 and Lung Cancer Cell Line A549. *J. Inorg. and Organomet. Polymers and Mater.*, 2017, **27**(1), P. 87–94.
- [32] Rosales-Martínez P., Cornejo-Mazón M., Arroyo-Maya I.J., Hernández-Sánchez H. Chitosan Micro- and Nanoparticles for Vitamin Encapsulation. *Nanotech. Appl. Food Industr.*, 2018, **19**, P. 429–442.
- [33] Hwang J., Rodgers K., Oliver J.C., Schlupe Th.  $\alpha$ -Methylprednisolone conjugated cyclodextrin polymer-based nanoparticles for rheumatoid arthritis therapy. *Inter. J. Nanomed.*, 2008, **3**, P. 359–371.
- [34] *Nanotechnology in Drug Delivery*. Ed. de Villiers M.M., Aramwit P., Kwon G.S.: Springer-Verlag, New York, 2009, 662 p.
- [35] *Fundamentals and Applications of Controlled Release Drug Delivery*. Ed. Siepmann J., Siegel R.A., Rathbone M.J. Springer US, 2012, 594 p.
- [36] Demetzos C. *Pharmaceutical Nanotechnology*. ADIS, 2016, 203 p.
- [37] *Nanotechnology Applied To Pharmaceutical Technology*. Ed. Rai M., dos Santos C.A. Springer International Publishing, 2017, 386 p.
- [38] Hoffman A.S. The origins and evolution of “controlled” drug delivery systems. *J. Controlled Release*, 2008, **132**(3), P. 153–163.
- [39] Nanjunda Reddy B.H., Venkata Lakshmi V., Vishnu Mahesh K.R., Mylarappa M., Raghavendra N., Venkatesh T. Preparation of chitosan/different organomodified clay polymer nanocomposites: studies on morphological, swelling, thermal stability and antibacterial properties. *Nanosystems: Physics, Chemistry, Mathematics*, 2016, **7**(4), P. 667–674.
- [40] Iwai K., Maeda H., Konno T. Use of oily contrast medium for selective drug targeting to tumor: enhanced therapeutic effect and X-ray image. *Cancer research*, 1984, **44**(5), P. 2115–2121.
- [41] Kryuk T.V., Mikhal'chuk V.M., Petrenko L.V., Nelepova O.A., Nikolaevskii A.N. Antioxidative Stabilization of Polyethylene Glycol in Aqueous Solutions with Herb Phenols. *Russ. J. Appl. Chem.*, 2004, **77**(1), P. 131–135.
- [42] Ostrovskii V.A. Interphase Transfer Catalysis of Organics Reactions. *Soros Education J.*, 2000, **6**(11), P. 30–34.
- [43] Lasic D.D., Barenholz Y. *Handbook of nonmedical applications of liposomes: Theory and basic sciences*. 1, CRC Press, Boca Raton, FL, USA, 1996, 368 p.
- [44] Goble T.N. Sur la lécithine et la cérébrine. *J. de Pharmacie et de Chimie*, 1874, **20**, P. 346–354.
- [45] Strecker A. Ueber das Lecithin. *Annalen der Chemie und Pharmacie*, 1868, **148**(1), P. 77–90.
- [46] Bangham A., Horne R. Negative staining of phospholipids and their structural modification by surface-active agents as observed in the electron microscope. *J. Molec. Biol.*, 1964, **8**(5), P. 660–668.
- [47] Deshmukh R.R., Gawale S.V., Bhagwat M.K., Ahire P.A., Derle N.D. A review on liposomes. *World J. Pharm. Pharm. Sci.*, 2016, **5**(3), P. 506–517.
- [48] Bangham A., Standish M., Watkins J. Diffusion of univalent ions across the lamellae of swollen phospholipids. *J. Molec. Biol.*, 1965, **13**(1), P. 238–252.
- [49] Bozzuto G., Molinari A. Liposomes as nanomedical devices. *Int. J. Nanomed.*, 2015, **10**(1), P. 975–999.
- [50] Biju S.S., Talegaonkar S., Mishra P.R., Khar R.K., Vesicular systems: An overview. *Ind. J. Pharm. Sci.*, 2006, **68**(2), P. 141–153.
- [51] Garg T., K. Goyal A. Liposomes: Targeted and Controlled Delivery System. *Drug Delivery Lett.*, 2014, **4**(1), P. 62–71.
- [52] Szoka F., Papahadjopoulos D. Procedure for preparation of liposomes with large internal aqueous space and high capture by reverse-phase evaporation. *Proc. Nat. Acad. Sci.*, 1978, **75**(9), P. 4194–4198.
- [53] Akbarzadeh A., Rezaei-Sadabady R., Davaran S., Joo S.W., Zarghami N., Hanifehpour Y., Samiei M., Kouhi M., Nejati-Koshki K. Liposome: Classification, Preparation, and Applications. *Nanoscale Res. Lett.*, 2013, **8**(1), P. 102–110.
- [54] Batzli S., Korn E.D. Single bilayer liposomes prepared without sonication. *Biochimica et Biophysica Acta (BBA)-Biomembranes*, 1973, **298**(4), P. 1015–1019.
- [55] Olson F., Hunt C.A., Szoka F.C., Vail W.J., Papahadjopoulos D. Preparation of liposomes of defined size distribution by extrusion through polycarbonate membranes. *Biochimica et Biophysica Acta (BBA)-Biomembranes*, 1979, **557**(1), P. 9–23.
- [56] Toutou E., Junginger H., Weiner N., Nagai T., Mezei M. Liposomes as Carriers for Topical and Transdermal Delivery. *J. Pharm. Sci.*, 1994, **83**(9), P. 1189–1203.
- [57] Toutou E., Levi-Schaffer F., Dayan N., Alhague F., Ricciari F. Modulation of Caffeine Skin Delivery by Carrier Design: Liposomes versus Permeation Enhancers. *Int. J. Pharm.*, 1994, **103**(2), P. 131–136.
- [58] Laouini A., Jaafar-Maalej C., Limayem-Blouza I., Sfar S., Charcosset C., Fessi H. Preparation, Characterization and Applications of Liposomes: State of the Art. *J. Colloid Sci. and Biotechn.*, 2012, **1**(2), P. 147–168.
- [59] Torchilin V.P. Recent advances with liposomes as pharmaceutical carriers. *Nat. Rev. Drug Discov.*, 2005, **4**, P. 145–160.
- [60] Takahama H., Minamino T., Asanuma H. Fujita M., Asai T., Wakeno M., Sasaki H., Kikuchi H., Hashimoto K., Oku N., Asakura M., Kim J., Takashima S., Komamura K., Sugimachi M., Mochizuki N., Kitakaze M. Prolonged targeting of ischemic/reperfused myocardium by liposomal adenosine augments cardioprotection in rats. *J. Amer. College of Cardiology*, 2009, **53**(8), P. 709–717.
- [61] Gregoriadis G., Swain C.P., Wills E.J., Tavill A.S. Drug-carrier potential of liposomes in cancer chemotherapy. *Lancet*, 1974, **1**, P. 1313–1316.
- [62] Tam Y.C., Chen S., Cullis P.R. Advances in Lipid Nanoparticles for siRNA Delivery. *Pharmaceutic*, 2013, **5**, P. 498–507.
- [63] Anwekar H., Patel S., Singhai A.K. Liposomes as drug carriers. *Int. J. Pharm. Life Sci. (IJPLS)*, 2011, **2**(7), P. 945–951.
- [64] Akbarzadeh A., Rezaei-Sadabady R., Nejati K. Liposome: classification, preparation, and applications. *Nanoscale Research Letters*, 2013, **8**(1), P. 102–111.

- [65] Johnston M.J., Semple S.C., Klimuk S.K., Ansell S., Maurer N., Cullis P.R. Characterization of the drug retention and pharmacokinetic properties of liposomal nanoparticles containing dihydrospingomyelin. *Biochim. Biophys. Acta*, 2007, **1768**, P. 1121–1127.
- [66] Raney S.G., Wilson K.D., Sekirov L., Chikh G., de Jong S.D., Cullis P.R., Tam Y.K. The effect of circulation lifetime and drug-to-lipid ratio of intravenously administered lipid nanoparticles on the biodistribution and immunostimulatory activity of encapsulated CpG-ODN. *J. Drug Target*, 2008, **16**(7), P. 564–77.
- [67] Fenske D.B., Chonn A., Cullis. Liposomal Nanomedicines: An Emerging Field. *Toxicologic Pathology*, 2008, **36**, P. 21–29.
- [68] Fenske D.B., Cullis P.R. Liposomal Nanomedicines. *Expert Opin. Drug. Deliv.*, 2008, **5**(1), P. 25–44.
- [69] Barsukov L.I. Liposomes. *Soros Education J.*, 1998, **10**, P. 2–9.
- [70] Smyslov R.Yu., Ezdakova K.V., Kopitsa G.P., Khripunov A.K., Bugrov A.N., Tkachenko A.A., Angelov B., Pipich V., Szekely N.K., Baranchikov A.E., Latysheva E., Chetverikov Yu.O., Haramus V. Morphological structure of *Gluconacetobacter xylinus* cellulose and cellulose-based organic-inorganic composite materials. *J. Phys.: Conf. Ser.*, 2017, **848**(1), P. 012017.
- [71] Almjasheva O.V., Garabadzhiu A.V., Kozina Yu.V., Litvinchuk L.F., Dobritsa V.P. Biological effect of zirconium dioxide-based nanoparticles. *Nanosystems: Physics, Chemistry, Mathematics*, 2017, **8**(3), P. 391–396.
- [72] Bugrov A.N., Zavialova A.Yu., Smyslov R.Yu., Anan'eva T.D., Vlasova E.N., Mokeev M.V., Kryukov A.E., Kopitsa G.P., Pipich V. Luminescence of  $\text{Eu}^{3+}$  ions in hybrid polymer-inorganic composites based on poly(methyl methacrylate) and zirconia nanoparticles. *Luminescence*, 2018, **33**(5), P. 837–849.
- [73] Popov A.L., Shcherbakov A.B., Zholobak N.M., Baranchikov A.Ye., Ivanov V.K. Cerium dioxide nanoparticles as third-generation enzymes (nanozymes). *Nanosystems: Physics, Chemistry, Mathematics*, 2017, **8**(6), P. 760–781.
- [74] Bugrov A.N., Rodionov I.A., Zvereva I.A., Smyslov R.Yu., Almjasheva O.V. Photocatalytic activity and luminescent properties of Y, Eu, Tb, Sm and Er-doped  $\text{ZrO}_2$  nanoparticles obtained by hydrothermal method. *Int. J. Nanotechnology*, 2016, **13**(1/2/3), P. 147–157.
- [75] Shydlovska O., Kharchenko E., Zholobak N., Shcherbakov A., Marynin A., Ivanova O., Baranchikov A., Ivanov V. Cerium oxide nanoparticles increase the cytotoxicity of TNF alpha *in vitro*. *Nanosystems: Physics, Chemistry, Mathematics*, 2018, **9**(4), P. 537–543.
- [76] Almjasheva O.V., Smirnov A.V., Fedorov B.A., Tomkovich M.V., Gusarov V.V. Structural features of  $\text{ZrO}_2\text{-Y}_2\text{O}_3$  and  $\text{ZrO}_2\text{-Gd}_2\text{O}_3$  nanoparticles formed under hydrothermal conditions. *Russ. J. Gen. Chem.*, 2014, **84**(5), P. 804–809.
- [77] Popov A.L., Savintseva I.V., Mysina E.A., Shcherbakov A.B., Popova N.R., Ivanova O.S., Kolmanovich D.D., Ivanov V.K. Cytotoxicity analysis of gadolinium doped cerium oxide nanoparticles on human mesenchymal stem cells. *Nanosystems: Physics, Chemistry, Mathematics*, 2018, **9**(3), P. 430–438.
- [78] Jayakumar G., Irudayaraj A., Dhayal Raj A., Anusuya M. Investigation on the preparation and properties of nanostructured cerium oxide. *Nanosystems: Physics, Chemistry, Mathematics*, 2016, **7**(4), P. 728–731.
- [79] Vardanyan Z., Gevorkyan V., Ananyan M., Vardapetyan H., Trchounian A. Effects of various heavy metal nanoparticles on *Enterococcus hirae* and *Escherichia coli* growth and proton-coupled membrane transport. *J. Nanobiotechnol.*, 2015, **13**(69), P. 2–9.
- [80] Bugrov A.N., Smyslov R.Yu., Zavialova A.Yu., Kirilenko D.A., Pankin D.V. Phase composition and photoluminescence correlations in nanocrystalline  $\text{ZrO}_2\text{:Eu}^{3+}$  phosphors synthesized under hydrothermal conditions. *Nanosystems: Physics, Chemistry, Mathematics*, 2018, **9**(3), P. 378–388.
- [81] Popov A.L., Ermakov A.M., Shekunova T.O., Shcherbakov A.B., Ermakova O.N., Ivanova O.S., Popova N.R., Baranchikov A.Ye., Ivanov V.K. PVP-stabilized tungsten oxide nanoparticles inhibit proliferation of NCTC L929 mouse fibroblasts via induction of intracellular oxidative stress. *Nanosystems: Physics, Chemistry, Mathematics*, 2019, **10**(1), P. 92–101.
- [82] Sharker S.Md., Kim S.M., Lee J.E., Choi K.H., Shin G., Lee S., Lee D.K., Jeong J., Park S.Y. Functionalized biocompatible  $\text{WO}_3$  nanoparticles for triggered and targeted *in vitro* and *in vivo* photothermal therapy. *J. Control. Release*, 2015, **217**, P. 211–220.
- [83] Zhou Z., Kong B., Yu C., Shi X., Wang M., Liu W., Sun Y., Zhang Y., Yang H., Yang S. Tungsten Oxide Nanorods: An Efficient Nanoplatform for Tumor CT Imaging and Photothermal Therapy. *Sci. Rep.*, 2014, **4**, P. 3653–3663.
- [84] Xing Y., Li L., Ai X., Fu L. Polyaniline-coated upconverting nanoparticles with upconverting luminescent and photothermal conversion properties for photothermal cancer therapy. *Intern. J. Nanomed.*, 2016, **11**, P. 4327–4338.
- [85] Popov A.L., Savintseva I.V., Mysina E.A., Shcherbakov A.B., Popova N.R., Ivanova O.S., Kolmanovich D.D., Ivanov V.K. Cytotoxicity analysis of gadolinium doped cerium oxide nanoparticles on human mesenchymal stem cells. *Nanosystems: Physics, Chemistry, Mathematics*, 2018, **9**(3), P. 430–438.
- [86] Slowing I.I. Mesoporous silica nanoparticles as controlled release drug delivery and gene transfection carriers. *Adv. Drug Deliv. Rev.*, 2008, **60**(11), P. 1278–1288.
- [87] Vasilevskaya A. K., Almjasheva O.V., Gusarov V.V. Formation of nanocrystals in the  $\text{ZrO}_2\text{-H}_2\text{O}$  system. *Russ. J. Gen. Chem.*, 2015, **85**(12), P. 1937–1942.
- [88] Popkov V.I., Tugova E.A., Bachina A.K., Almyasheva O.V. The formation of nanocrystalline orthoferrites of rare-earth elements  $\text{XFeO}_3$  (X = Y, La, Gd) via heat treatment of coprecipitated hydroxides. *Russ. J. Gen. Chem.*, 2017, **87**(11), P. 1771–1780.
- [89] Popkov V.I., Almjasheva O.V., Semenova A.S., Kellerman D.G., Nevedomskiy V.N., Gusarov V.V. Magnetic properties of  $\text{YFeO}_3$  nanocrystals obtained by different soft-chemical methods. *J. Mater. Sci: Mater Electron.*, 2017, **28**(10), P. 7163–7170.
- [90] Berezhnaya M.V., Al' myasheva O.V., Mittova V.O., Nguen A.T., Mittova I.Ya. Sol-Gel Synthesis and Properties of  $\text{Y}_{1-x}\text{Ba}_x\text{FeO}_3$  Nanocrystals. *Russ. J. Gen. Chem.*, 2018, **88**(4), P. 626–631.
- [91] Komlev A.A., Panchuk V.V., Semenov V.G., Almjasheva O.V., Gusarov V.V. Effect of the sequence of chemical transformations on the spatial segregation of components and formation of periclase-spinel nanopowders in the  $\text{MgO-Fe}_2\text{O}_3\text{-H}_2\text{O}$  System. *Russ. J. Appl. Chem.*, 2016, **89**(12), P. 1932–1938.
- [92] Kuznetsova V.A., Almjasheva O.V., Gusarov V.V. Influence of microwave and ultrasonic treatment on the formation of  $\text{CoFe}_2\text{O}_4$  under hydrothermal conditions. *Glass Phys. Chem.*, 2009, **35**(2), P. 205–209.
- [93] Proskurina O.V., Tomkovich M.V., Bachina A.K., Sokolov V.V., Danilovich D.P., Panchuk V.V., Semenov V.G., Gusarov V.V. Formation of Nanocrystalline  $\text{BiFeO}_3$  under Hydrothermal Conditions. *Russ. J. Gen. Chem.*, 2017, **87**(11), P. 2507–2515.
- [94] Almjasheva O.V., Gusarov V.V. Prenucleation formations in control over synthesis of  $\text{CoFe}_2\text{O}_4$  nanocrystalline powders. *Russ. J. Appl. Chem.*, 2016, **89**(6), P. 689–695.
- [95] Sharikov F.Yu., Almjasheva O.V., Gusarov V.V. Thermal analysis of formation of  $\text{ZrO}_2$  nanoparticles under hydrothermal conditions. *Russ. J. Inorg. Chem.*, **51**(10), P. 1538–1542.

- [96] Almjasheva O.V., Gusarov V.V. Prenucleation formations in control over synthesis of  $\text{CoFe}_2\text{O}_4$  nanocrystalline powders. *Russ. J. Appl. Chem.*, 2016, **89**(6), P. 851–856.
- [97] Almjasheva O.V., Krasilin A.A., Gusarov V.V. Formation mechanism of core-shell nanocrystals obtained via dehydration of coprecipitated hydroxides at hydrothermal conditions. *Nanosystems: Phys. Chem. Math.*, 2018, **9**(4), P. 568–572.
- [98] Abiev R.Sh., Al'myasheva O.V., Gusarov V.V., Izotova S.G. Method of producing nanopowder of cobalt ferrite and microreactor to this end. RF Patent 2625981, Bull. **20**, 20.07.2017.
- [99] Abiev R.S., Almyasheva O.V., Izotova S.G., Gusarov V.V. Synthesis of cobalt ferrite nanoparticles by means of confined impinging-jets reactors. *J. Chem. Tech. App.*, 2017, **1**(1), P. 7–13.
- [100] Proskurina O.V., Nogovitsin I.V., Il'ina T.S., Danilovich D.P., Abiev R.Sh., Gusarov V.V. Formation of  $\text{BiFeO}_3$  Nanoparticles Using Impinging Jets. *Microreactor. Russ. J. Gen. Chem.*, 2018, **88**(10), P. 2139–2143.
- [101] Bugrov A.N., Vlasova E.N., Mokeev M.V., Popova E.N., Ivan'kova E.M., Al'myasheva O.V., Svetlichnyi V.M. Distribution of zirconia nanoparticles in the matrix of poly(4,4'-oxydiphenylenepyromellitimide). *Polym. Sci. Ser. B.*, 2012, **54**(9-10), P. 486–495.
- [102] Almjasheva O.V., Gusarov V.V. Effect of  $\text{ZrO}_2$  nanocrystals on the stabilization of the amorphous state of alumina and silica in the  $\text{ZrO}_2$ - $\text{Al}_2\text{O}_3$  and  $\text{ZrO}_2$ - $\text{SiO}_2$  systems. *Glass Phys. Chem.*, 2006, **32** (2), P. 162–166.
- [103] Kotov Y.A. Electric explosion of wires as a method for preparation of nanopowders. *J. Nanoparticle Research*, 2003, **5**(5-6), P. 539–550.
- [104] Kotov Y.A., Azarkevich E.I., Beketov I.V., Demina T.M., Murzakaev A.M., Samatov O.M. Producing A1 and A1203 nanopowders by electrical explosion of wire. *Key Engineering Materials*, 1997, **132–136**, P. 173–176.
- [105] Kotov Y.A., Samatov O.M. Production of nanometer-sized AlN powders by the exploding wire method. *Nanostruct. Mater.*, 1999, **12**, P. 119–122.
- [106] Sherman P. Generation of submicron metal particles. *Colloid and Interface Sci.*, 1975, **51**(1), P. 87–93.
- [107] Karioris F., Fish B. An Exploding Wire Aerosol Generator. *J. Colloid Science*, 1962, **17**, P. 155–161.
- [108] Bennett F.D. High-temperature cores in exploding wires. *Phys. Fluids*, 1965, **8**(6), P. 1106–1108.
- [109] Chace W.G. Exploding Wires. *Physics Today*, 1964, **17**(87), P. 19.
- [110] Kaori K., Hirashi I., Vasio M. The formation and characteristics of Powders by wire explosion. 2-nd report. *Nippon Tungsten Rev.*, 1972, **5**, P. 20.
- [111] Gusev A.I., Rempel A.A. *Nanocrystalline Materials*. Cambridge, International Science Publishing Cambridge, 2004, 351 p.
- [112] Alymov M.I., Maltina E.I., Stepanov Y.N. Model of Initial Stage of Ultrafine Metal Powder Sintering. *Nanostructured Mater.*, 1994, **4**(6), P. 737–742.
- [113] Bennett F.D., Kahl G.D., Wedemeyer E.H. Resistance Changes caused by Vaporization Waves Exploding Wires. *Exploding Wires*, 1964, **3**, Plenum Press, New York, 1964, P. 65–84.
- [114] Ivanov G., Lerner M., Tepper F. Intermetallic Alloy Formation from Nanophase Metal Powders Produced by Electro-Exploding Wires. *Advances in Powder Metallurgy & Particulate Materials*, 1996, **40**, P. 15/55–15/63.
- [115] Jonson R., Siegel B. Chemical Reactor Utilising Successive Multiple Electrical Explosions of Metal Wires. *Rev. Sci. Instr.*, 1970, **42**(6), P. 854–859.
- [116] Miller J.C. A brief history of laser ablation. Laser ablation: mechanisms and applications – II. *AIP Publishing*, 1993, **2889**(1), P. 619–622.
- [117] Kirichenko N.A., Sukhov I.A., Shafeev G.A., Shcherbina M.E. Evolution of the distribution function of Au nanoparticles in a liquid under the action of laser radiation. *Quantum Electronics*, 2012, **42**(2), P. 175–180.
- [118] Sukhov I.A., Shafeev G., Voronov V.V., Sygletou M., Stratakis E., Fotakis C. Generation of nanoparticles of bronze and brass by laser ablation in liquid. *Appl. Surface Sci.*, 2014, **302**, P. 79–82.
- [119] Zhil'nikova M.I., Barmina E.V., Shafeev G.A. Laser-Assisted Formation of Elongated Au Nanoparticles and Subsequent Dynamics of Their Morphology under Pulsed Irradiation in Water. *Physics of Wave Phenomena*, 2018, **26**(2), P. 85–92.
- [120] Hiramatsu H., Osterloh F.E. A simple large-scale synthesis of nearly monodisperse gold and silver nanoparticles with adjustable sizes and with exchangeable surfactants. *Chem. Mater.*, 2004, **16**(13), P. 2509–2511.
- [121] Simakin A.V., Voronov V.V., Shafeev G.A., Brayner R. Nanodisks of Au and Ag produced by laser ablation in liquid environment. *Chem. Phys. Lett.*, 2001, **348**(3), P. 182–186.
- [122] Kuzmin P.G., Shafeev G.A., Viau G., Warot-Fonrose B., Barberoglou M., Stratakis E., Fotakis C. Porous nanoparticles of Al and Ti generated by laser ablation in liquids. *Appl. Surf. Sci.*, 2012, **258**(23), P. 9283–9287.
- [123] Amendola V., Riello P., Meneghetti M., 2011. Magnetic Nanoparticles of Iron Carbide, Iron Oxide, Iron@Iron Oxide, and Metal Iron Synthesized by Laser Ablation in Organic Solvents. *J. Phys. Chem. C*, 2010, **115**(12), P. 5140–5146.
- [124] Tsuji T., Iryo K., Watanabe N., Tsuji M. Preparation of silver nanoparticles by laser ablation in solution: influence of laser wavelength on particle size. *Appl. Surf. Sci.*, 2002, **202**(1–2), P. 80–85.
- [125] Dolgaev I., Simakin A.V., Voronov V.V., Shafeev G.A., Bozon-Verduraz F. Nanoparticles produced by laser ablation of solids in liquid environment. *Appl. Surf. Sci.*, 2002, **186**(1), P. 546–551.
- [126] Kamat P.V., Flumiani M., Hartland G.V. Picosecond dynamics of silver nanoclusters. Photoejection of electrons and fragmentation. *J. Phys. Chem. B.*, 1998, **102**(17), P. 3123–3128.
- [127] Hamad A., Li L., Liu Z. A comparison of the characteristics of nanosecond, picosecond and femtosecond lasers generated Ag,  $\text{TiO}_2$  and Au nanoparticles in deionised water. *Appl. Phys. A*, 2015, **120**(4), P. 1247–1260.
- [128] Kurland H.-D., Stotzel Ch., Grabow J., Zink I., Müller E., Staupendahl G., Müller F.A. Preparation of Spherical Titania Nanoparticles by  $\text{CO}_2$  Laser Evaporation and Process-Integrated Particle Coating. *J. Amer. Ceram. Soc.*, 2010, **93**(5), P. 1282–1289.
- [129] Popp U., Herbig R., Michel G., Müller E., Oestreich Ch. Properties of nanocrystalline ceramic powders prepared by laser evaporation and recondensation. *J. Eur. Ceram. Soc.*, 1998, **18**, P. 1153–116.
- [130] Osipov V.V., Kotov Yu.A., Ivanov M.G., Samatov O.M., Lisenkov V.V., Platonov V.V., Murzakayev A.M., Medvedev A.I., Azarkevich E.I. Laser synthesis of nanopowders. *Laser Phys.*, 2006, **16**(1), P. 116–125.
- [131] Kurland H.D., Grabow J., Staupendahl G., Andre M.E., Dutz S., Bellemann M.E. Magnetic iron oxide nanopowders produced by  $\text{CO}_2$  laser evaporation. *J. Magnet., Magn. Mater.*, 2007, **311**, P. 73–77.
- [132] Sato T., Diono W., Sasaki M., Goto M. Silver nanoparticles generated by pulsed laser ablation in supercritical  $\text{CO}_2$  medium. *High Pressure Res.*, 2012, **32**(1), P. 1–7.

- [133] Varma A., Mukasyan A.S., Deshpande K.T., Pranda P., Erri P.R. Combustion Synthesis of Nanoscale Oxide Powders: Mechanism, Characterization and Properties. *MRS Proc.*, 2003, **800**, P. AA4.1–AA4.12.
- [134] Mokkelbost T., Kaus I., Grande T., Einarsrud M.A. Combustion Synthesis and Characterization of Nanocrystalline CeO<sub>2</sub> Based Powders. *Chem. Mater.*, 2004, **16**(25), P. 5489–5494.
- [135] Wang X., Qin M., Fang F., Jia B., Wu H., Qu X., Volinsky A.A. Effect of glycine on onestep solution combustion synthesis of magnetite nanoparticles. *J. Alloys Compd.*, 2017, **719**, P. 288–295.
- [136] Mukasyan A.S., Epstein P., Dinka P. Solution combustion synthesis of nanomaterials. *Proc. Combust. Inst.*, 2007, **31**(2), P. 1789–1795.
- [137] Rogachev A.S., Mukasyan A.S. *Combustion for Material Synthesis*. Boca Raton, CRC Press, 2014, 424 p.
- [138] Varma A., Mukasyan A.S., Rogachev A.S., Manukyan K.V. Solution Combustion Synthesis of Nanoscale Materials. *Chem. Rev.*, 2016, **116**(23), P. 14493–14586.
- [139] Ostroushko A.A. Russkikh O.V. Oxide Material Synthesis by Combustion of Organic-Inorganic Compositions. *Nanosystems: Physics, Chemistry, Mathematics*, 2017, **8**(4), P. 476–502.
- [140] Kuchma E., Zolotukhin P., Belanova A., Soldatov M., Lastovina T., Kubrin S., Nikolsky A., Mirmikova L., Soldatov A. Low Toxic Maghemite Nanoparticles for Theranostic Applications. *International Journal of Nanomedicine*, 2017, **12**, P. 6365–6371.
- [141] Lojk J., Bregar V.B., Strojkan K., Hudoklin S., Verani P., Pavlin M., Kreft M.E. Increased Endocytosis of Magnetic Nanoparticles into Cancerous Urothelial Cells versus Normal Urothelial Cells. *Histochemistry and Cell Biology*, 2018, **149**(1), P. 45–59.
- [142] Firouzi M., Poursalehi R., Delavari H., Saba F., Oghabian M.A. Chitosan coated tungsten trioxide nanoparticles as a contrast agent for X-ray computed tomography. *Int. J. Biol. Macromol.*, 2017, **98**, P. 479–485.
- [143] Gelperina S., Maksimenko O., Khalansky A., Vanchugova L., Shipulo E., Abbasova K., Berdiev R., Wohlfart S., Chepurnova N., Kreuter J. Drug delivery to the brain using surfactant-coated poly (lactide-co-glycolide) nanoparticles: influence of the formulation parameters. *Eur. J. Pharm. Biopharm.*, 2010, **74**, P. 157–163.
- [144] Popova N.R., Popov A.L., Shcherbakov A.B., Ivanov V.K. Layer-by-layer capsules as smart delivery systems of CeO<sub>2</sub> nanoparticle-based theranostic agents. *Nanosystems: Physics, Chemistry, Mathematics*, 2017, **8**(2), P. 282–289.
- [145] Venkatesan H., Radhakrishnan S., Parthibavarman M., Kumar R.D., Sekar C. Synthesis of polyethylene glycol (PEG) assisted tungsten oxide (WO<sub>3</sub>) nanoparticles for L-dopa bio-sensing applications. *Talanta*, 2011, **85**(4), P. 2166–2174.
- [146] Porcel E., Liehn S., Remita H., Usami N., Kobayashi K., Furusawa Y., Sech C.L., Lacombe S. Platinum Nanoparticles: A Promising Material for Future Cancer Therapy? *Nanotechnology*, 2010, **21**(8), P. 85–103.
- [147] Mornet S., Vasseur S., Grasset F., Duguet E. Magnetic Nanoparticle Design for Medical Diagnosis and Therapy. *Journal of Materials Chemistry*, 2004, **14**(14), P. 2161–2175.
- [148] Garanina A.S., Kireev I.I., Alieva I.B., Majouga A.G., Davydov V.A., Murugesan S., Khabashesku V.N., Agafonov V.N., Uzbekov R.E. New superparamagnetic fluorescent Fe@C-C<sub>5</sub>ON<sub>2</sub>H<sub>10</sub>-Alexa Fluor 647 nanoparticles for biological applications. *Nanosystems: Physics, Chemistry, Mathematics*, 2018, **9**(1), P. 120–122.
- [149] Morones J.R., Elechiguerra J.L., Camacho A., Holt K., Kouri J.B., Ramirez J.T., Yacaman M.J. The Bactericidal Effect of Silver Nanoparticles. *Nanotechnology*, 2005, **16**(10), P. 2346–2353.
- [150] Alieva I., Kireev I., Rakhmanina A., Garanina A., Strelkova O., Zhironkina O., Cherepaninets V., Davydov V., Khabashesku V., Agafonov V., Uzbekov R. Magnetinduced behavior of iron carbide (Fe<sub>7</sub>C<sub>3</sub>@C) nanoparticles in the cytoplasm of living cells. *Nanosystems: Physics, Chemistry, Mathematics*, 2016, **7**(1), P. 158–160.
- [151] Koulikova M., Kochubey V.I. Synthesis and Optical Properties of Iron Oxide Nanoparticles for Photodynamic Therapy. *Reports of Samara Scientific Center of Russian Academy of Sciences (RAS)*, 2012, **14**(4), P. 206–209.
- [152] Selvamuthumari J., Meenakshi S., Ganesan M., Nagaraj S., Pandian K. Antibacterial and catalytic properties of silver nanoparticles loaded zeolite: green method for synthesis of silver nanoparticles using lemon juice as reducing agent. *Nanosystems: Physics, Chemistry, Mathematics*, 2016, **7**(4), P. 768–773.
- [153] Dykman L.A., Khlebtsov N.G. Gold Nanoparticles in Biology and Medicine: Recent Advances and Prospects. *Acta Naturae*, 2011, **3**(2), P. 34–55.
- [154] Preethika R.K., Ramya R., Ganesan M., Nagaraj S., Pandian K. Synthesis and characterization of neomycin functionalized chitosan stabilized silver nanoparticles and study its antimicrobial activity. *Nanosystems: Physics, Chemistry, Mathematics*, 2016, **7**(4), P. 759–764.
- [155] Akbarzadeh A., Mohammad Samiei M., Soodabeh Davaran S. Magnetic nanoparticles: preparation, physical properties, and applications in biomedicine. *Nanoscale Res. Lett.*, 2012, **7**, P. 144–157.
- [156] Tartaj P., Morales M.D.D., Veintemillas-Verdaguer S., Gonzalez-Carreno T., Serna C.J. The preparation of magnetic nanoparticles for applications in biomedicine. *J. Phys. D: Appl. Phys.*, 2003, **36**, P. R182–R197.
- [157] Ghadiri M., Vasheghani-Farahani E., Atyabi F., Kobarfard F., Mohamadyar-Toupkanlou F., Hosseinkhani H. Transferrin-conjugated magnetic dextran-spermine nanoparticles for targeted drug transport across blood-brain barrier. *J. Biomed. Mater. Res. A*, 2017, **105A**(10), P. 2851–2864.
- [158] MacBain S.C., Yiu H.H., Dobson J. Magnetic nanoparticles for gene and drug delivery *Int. J. Nanomed.*, 2008, **3**(2), P. 169–180.
- [159] Akbarzadeh A., Asgari D., Zarghami N., Mohammad R., Davaran S. Preparation and in vitro evaluation of doxorubicin-loaded Fe<sub>3</sub>O<sub>4</sub> magnetic nanoparticles modified with biocompatible co-polymers. *Int. J. Nanomed.*, 2012, **7**, P. 511–526.
- [160] Akbarzadeh A., Zarghami N., Mikaeili H., Asgari D., Goganian A.M., Khiabani H.K., Samiei M., Davaran S. Synthesis, characterization, and in vitro evaluation of novel polymer-coated magnetic nanoparticles for controlled delivery of doxorubicin. *Nanotechnol. Sci. Appl.*, 2012, **5**, P. 13–25.
- [161] Reddy L.H., Arias J.L., Nicolas J., Couvreur P. Magnetic nanoparticles: design and characterization, toxicity and biocompatibility, pharmaceutical and biomedical applications. *Chem. Rev.*, 2012, **112**, P. 5818–5878.
- [162] Kayal S., Ramanujan R.V. Anti-cancer drug loaded iron – gold core – shell nanoparticles (Fe@Au) for magnetic drug targeting. *J. Nanosci. Nanotechnol.*, 2010, **10**, P. 5527–5539.
- [163] Sharker S.M., Kim S.M., Lee J.E., Choi K.H., Shin G., Lee S., Lee K.G., Jeong J., Lee H., Park S.Y. Functionalized biocompatible WO<sub>3</sub> nanoparticles for triggered and targeted in vitro and in vivo photothermal therapy. *J. Control. Release*, 2015, **217**, P. 211–220.
- [164] Popov A., Zholobak N., Balko O.I., Balko O.B., Shcherbakov A.B., Popova N.R., Ivanova-Polezhaeva O.S., Baranchikov A.E., Ivanov V.K. Photo-induced toxicity of tungsten oxide photochromic nanoparticles. *J. Photochem. Photobiol. B*, 2018, **178**, P. 395–403.

- [165] Qiu J., Xiao Q., Zheng X., Zhang L., Xing H., Ni D., Liu Y., Zhang S., Ren Q., Hua Y., Zhao K., Bu W. Single  $W_{18}O_{49}$  nanowires: A multifunctional nanoplatform for computed tomography imaging and photothermal/photodynamic/radiation synergistic cancer therapy. *Nano Research*, 2015, **8**(11), P. 3580–3590.
- [166] Li G., Chen Y., Zhang L., Zhang M., Li S., Li L., Wang T., Wang C. Nano-Micro Lett. Facile Approach to Synthesize Gold Nanorod@Polyacrylic Acid/Calcium Phosphate Yolk–Shell Nanoparticles for Dual-Mode Imaging and pH/NIR-Responsive Drug Delivery. *Nano-Micro Lett.*, 2018, **10**(7), P. 1–11.
- [167] Espinosa A., Corato R.D., Kolosnjaj-Tabi J., Flaud P., Pellegrino T., Wilhelm C. Duality of Iron Oxide Nanoparticles in Cancer Therapy: Amplification of Heating Efficiency by Magnetic Hyperthermia and Photothermal Bimodal Treatment. *ACS Nano*, 2016, **10**(2), P. 2436–2446.
- [168] Antonii F. *Panacea aurea-auro potabile*. Hamburg, Ex Bibliopolio Frobeniano, 1618, 238 p.
- [169] Guterres S.S., Poletto F., Colom'e L., Raffin R., Pohlmann A. Polymeric Nanocapsules for Drug Delivery: An Overview. *Colloids in Drug Delivery*, 2010, Taylor & Francis/CRC Press, **3**, P. 71–98.
- [170] Yiyun C., Zhenhua X., Minglu M., Tonguen X. Dendrimers as Drug Carriers: Applications in Different Routes of Drug. *J. Pharma. Sci.*, 2008, **97**(1), P. 123–143.
- [171] Inagamov S.Y., Sattarov S.S., Shadmanov K.K., Karimov A.K. Interpolymer complexes on the basis of sodium carboxymethyl cellulose – carriers nanoparticles of medicinal preparations. Mat. Conf. (Munich, Germany, 31 Oct. – 5 Nov. 2018). Education and science without borders, Fundamental and applied research in nanotechnology, 2018, **6**, (<http://www.science-sd.com/478-25428> and <http://www.science-sd.com/pdf/2018/6/25428.pdf>).
- [172] Lu C.T., Jin R.R., Jiang Y.N., Lin Q., Yu W.Z., Mao K.L., Tian F.R., Zhao Y.P., Zhao Y.Z. Gelatin nanoparticle-mediated intranasal delivery of substance P protects against 6-hydroxydopamine-induced apoptosis: an in vitro and in vivo study. *Drug Design, Development and Therapy*, 2015, **9**, P. 1955–1962.
- [173] Svenson S. Dendrimers as versatile platform in drug delivery applications. *Eur. J. Pharm. Biopharm.*, 2009, **71**, P. 445–462.
- [174] Chan J.M., Valencia P.M., Zhang L., Langer R., Farokhzad O.C. Polymeric Nanoparticles for Drug Delivery. *Cancer Nanotechnology*, 2010, **624**, P. 163–175.
- [175] Sambanis A. Encapsulated cell systems: the future of insulin delivery? *Therapeutic delivery*, 2012, **3**, P. 1029–1032.
- [176] Zhang Y., Chan H.F., Leong K.W. Advanced materials and processing for drug delivery: the past and the future. *Adv. Drug Delivery Rev.*, 2013, **65**, P. 104–120.
- [177] Hernández R.M., Orive G., Murua A., Pedraz J.L. Microcapsules and microcarriers for in situ cell delivery. *Adv. Drug Delivery Rev.*, 2010, **62**, P. 711–730.
- [178] De Geest B.G., De Koker S., Sukhorukov G.B., Kreft O., Parak W.J., Skirtach A.G., Demeester J., De Smedt S.C., Hennink W.E. Polyelectrolyte microcapsules for biomedical applications. *Soft Matter*, 2009, **5**, P. 282–291.
- [179] Jämsä S., Mahlberg R., Holopainen U., Ropponen J., Savolainen A., Ritschkoff A.-C. Slow release of a biocidal agent from polymeric microcapsules for preventing biodeterioration. *Progress in Organic Coatings*, 2013, **76**, P. 269–276.
- [180] Kaur I.P., Singh H. Nanostructured drug delivery for better management of tuberculosis. *J. Controlled Release*, 2014, **184**, P. 36–50.
- [181] Hamley I.W., Castelletto V., Fundin J., Crothers M., Attwoodand D., Talmon Y. Close-packing of Diblock Copolymer Micelles. *Colloid Polym. Sci.*, 2004, **282**, P. 514–517.
- [182] Hamley I.W. Nanoshells and Nanotubes from Block Copolymers. *Soft Matter*, 2005, **1**, P. 36–43.
- [183] Taboada P., Velasquez G., Barbosa S., Castelletto V., Nixon S.K., Yang Z., Heatley F., Hamley I.W., Mosquera V., Ashford M., Attwoodand D., Booth C. Block copolymers of ethylene oxide and phenyl glycidyl ether: Micellization, gelation and drug solubilization. *Langmuir*, 2005, **21**, P. 5263–5271.
- [184] Manjappa A.S., Chaudhari K.R., Venkataraju M.P., Dantuluri P., Nanda B., Sidda C., Sawant K.K., Murthy R.S.R. Antibody derivatization. *J. Controlled Release*, 2011, **150**(1), P. 2–22.
- [185] Kedar U., Phutane P., Shidhaye S., Kadam V. Advances in polymeric micelles for drug delivery and tumor targeting. *Nanomed.*, 2010, **6**, P. 714–729.
- [186] Wagh A., Law B. Methods for Conjugating Antibodies to Nanocarriers. In: Ducry L. (eds.) *Antibody-Drug Conjugates. Methods in Molecular Biology (Methods and Protocols)*, 2013, **1045**, P. 249–266.
- [187] Cui J., Fan D., Hao J. Magnetic  $Mo_72Fe_{30}$ -embedded hybrid nanocapsules. *Journal of colloid and interface science*, 2009, **330**(2), P. 488–492.
- [188] Kroto H.W., Heath J.R., O'Brien S.C., Curl, R.F.  $C_{60}$ : Buckminsterfullerene. *Nature*, 1985, **318**, P. 162–163.
- [189] Kratschmer W., Lamb L.D., Fostiropoulos K., Huffman D.R. Solid  $C_{60}$ : a new form of carbon. *Nature*, 1990, **347**(6291), P. 354–358.
- [190] Ala'a K. Isolation, separation and characterisation of the fullerenes  $C_{60}$  and  $C_{70}$ : the third form of carbon. *J. Chemical Soc., Chem. Commun.*, 1990, **20**, P. 1423–1425.
- [191] Gerasimov V.I., Matuzenko M.Y., Proskurina O.V. Purity Analysis of Trade Produced  $C_{60}$  Fullerene. *Mat. Phys. and Mechanics*, 2012, **18**(3), P. 181–185.
- [192] Gerasimov V.I., Trofimov A., Proskurina O. Isomers of Fullerene  $C_{60}$ . *Mat. Phys. and Mechanics*, 2014, **20**(1), P. 25–32.
- [193] Mendes R.G., Bachmatiuk A., Buchner B., Cuniberti G., Rummeli M.H. Carbon nanostructures as multi-functional drug delivery platforms. *J. Mater. Chem. B*, 2013, **1**(4), P. 401–428.
- [194] Mikheev I.V., Bolotnik T.A., Volkov D.S., Korobov M.V., Proskurmin M.A. Approaches to the determination of  $C_{60}$  and  $C_{70}$  fullerene and their mixtures in aqueous and organic solutions. *Nanosystems: Physics, Chemistry, Mathematics*, 2016, **7**(1), P. 104–110.
- [195] Mazur A.S., Karpunin A.E., Proskurina O.V., Gerasimov V.I., Pleshakov I.V., Matveev V.V., Kuz'min Yu.I. Nuclear Magnetic Resonance Spectra of Polyhydroxylated Fullerene  $C_{60}(OH)_n$ . *Phys. Solid State*, 2018, **60**(7), P. 1468–1470.
- [196] Mikheev I.V., Pirogova M.O., Bolotnik T.A., Volkov D.S., Korobov M.V., Proskurmin M.A. Optimization of the solvent exchange process for highyield synthesis of aqueous fullerene dispersions. *Nanosystems: Physics, Chemistry, Mathematics*, 2018, **9**(1), P. 41–45.
- [197] Karpunin A.E., Gerasimov V.I., Mazur A.S., Pleshakov I.V., Fofanov Y.A., Proskurina O.V. NMR Investigation of Composite Material, Formed by Fullerene in Polymer Matrix of Polyvinyl Alcohol. *IEEE International Conference on Electrical Engineering and Photonics (EEEPolytech)*, 2018, P. 168–171.
- [198] Andrievsky G.V., Klochkov V.K., Bordyuh A., Dovbeshko G.I. Comparative Analysis of Two Aqueous-Colloidal Solution of  $C_{60}$  Fullerene with Help of FT-IR Reflectance and UV-VIS Spectroscopy. *Chem. Phys. Lett.*, 2002, **364**, P. 8–17.

- [199] Andrievsky G.V., Bruskov V.I., Tykhomyrov A.A., Gudkov S.V. Peculiarities of the antioxidant and radioprotective effects of hydrated C<sub>60</sub> fullerene nanostructures in vitro and in vivo. *Free Radical Biology & Medicine*, 2009, **47**, P. 786–793.
- [200] Semenov K.N., Charykov N.A., Postnov V.N., Sharoyko V.V., Murin I.V. Phase equilibria in fullerene-containing systems as a basis for development of manufacture and application processes for nanocarbon materials. *Russ. Chem. Rev.*, 2016, **85**(1), P. 38–59.
- [201] Jargalan N., Tropin T.V., Avdeev M.V., Aksenov V.L. Investigation and modeling of evolution of C<sub>60</sub>/NMP solution UVVis spectra. *Nanosystems: Physics, Chemistry Mathematics*, 2016, **7**(1), P. 99–103.
- [202] Mchedlov-Petrosyan N.O., Kamneva N.N., Al-Shuuchi Y.T.M., Marynin A.I., Shekhovtsov S.V., “The peculiar behavior of fullerene C<sub>60</sub> in mixtures of good’ and polar solvents: Colloidal particles in the toluene–methanol mixtures and some other systems”, *Colloid Surf. A-Physicochem. Eng. Asp.*, 2016, **509**, P. 631–637.
- [203] Charykov N.A., Semenov K.N., Keskinov V.V., Garamova P.V., Tyurin D.P., Semenyuk I.V., Petrenko V.V., Kurilenko A.V., Matuzenko M.Yu., Kulenova N.A., Zolotarev A.A., Letenko D.G. Cryometry data and excess thermodynamic functions in the binary system: water soluble bisadduct of light fullerene C<sub>70</sub> with lysine. Asymmetrical thermodynamic model of virtual Gibbs energy decomposition – VDAS. *Nanosystems: Physics, Chemistry, Mathematics*, 2017, **8**(3), P. 397–405.
- [204] Semenov K.N., Charykov N.A., Iurev G.O., Ivanova N.M., Keskinov V.A., Letenko D.G., Postnov V.N., Sharoyko V.V., Kulenova N.A., Prikhodko I.V., Murin I.V. Physico-chemical properties of the C<sub>60</sub> - l-lysine water solutions, *J. Mol. Liq.*, 2017, **225**, P. 767–777.
- [205] Semenov K.N., Andrusenko E.V., Charykov N.A., Litasova E.V., Panova G.G., Penkova A.V., Murin I.V., Piotrovskiy L.B. Carboxylated Fullerenes: Physico-Chemical Properties and Potential Applications. *Prog. Solid State Chem.*, 2017, **47-48**, P. 19–36.
- [206] Tyurin D.P., Kolmogorov F.S., Cherepkova I.A., Charykov N.A., Semenov K.N., Keskinov V.A., Safyannikov N.M., Pukhareno Y.V., Letenko D.G., Segeda T.A., Shaimardanov Z. Antioxidant properties of fullereneol-d. *Nanosystems: Physics, Chemistry, Mathematics*, 2018, **9**(6), P. 798–810.
- [207] Safyannikov N.M., Charykov N.A., Garamova P.V., Semenov K.N., Keskinov V.A., Kurilenko A.V., Cherepkova I.A., Tyurin D.P., Klepikov V.V., Matuzenko M.Y., Kulenova N.A., Zolotarev A.A. Cryometry data in the binary systems bisadduct of C<sub>60</sub> and indispensable aminoacids – lysine, threonine, oxyproline. *Nanosystems: Physics, Chemistry Mathematics*, 2018, **9** (1), P. 46–48.
- [208] Dubinina I.A., Kuzmina E.M., Dudnik A.I., Vnukova N.G., Churilov G.N., Samoylova N.A. Study of antioxidant activity of fullereneols by inhibition of adrenaline autoxidation. *Nanosystems: Physics, Chemistry, Mathematics*, 2016, **7**(1), P. 153–157.
- [209] Shultz M.D., Duchamp J.C., Wilson J.D., Shu C.Y., Ge J., Zhang J., Gibson H.W., Fillmore H.L. Encapsulation of a radiolabeled cluster inside a fullerene cage, <sup>177</sup>Lu<sub>x</sub>Lu<sub>(3-x)</sub>N@C<sub>80</sub>: an interleukin-13-conjugated radiolabeled metallofullerene platform. *J. Amer. Chem. Soc.*, 2010, **132**(14), P. 4980–4981.
- [210] Bolskar R.D. Gadofullerene MRI contrast agents. *Nanomedicine (Lond.)*, 2008, **3**(2), P. 201–213.
- [211] Zhen M., Zheng J., Ye L., Li S., Jin C., Li K., Qiu D., Han H., Shu C., Yang Y., Wang C. Maximizing the relaxivity of Gd-complex by synergistic effect of HSA and carboxylfullerene. *ACS Appl. Mater. Interfaces*, 2012, **4**(7), P. 3724–3729.
- [212] Lebedev V.T., Kulvelis Yu.V., Runov V.V., Szhogina A.A., Suyasova M.V. Biocompatible water-soluble endometallofullerenes: peculiarities of self-assembly in aqueous solutions and ordering under an applied magnetic field. *Nanosystems: Physics, Chemistry, Mathematics*, 2016, **7**(1), P. 22–29.
- [213] Elistratova J., Akhmadeev B., Gubaidullin A., Korenev V., Sokolov M., Nizameev I., Stepanov A., Ismaev I., Kadirov M., Voloshina A., Mustafina A. Nanoscale hydrophilic colloids with high relaxivity and low cytotoxicity based on Gd(III) complexes with Keplerate polyanions. *New J. Chem.*, 2017, **41**, P. 5271–5275.
- [214] Kondrin M.V., Brazhkin V.V. Is graphane the most stable carbon monohydride? *Nanosystems: Physics, Chemistry, Mathematics*, 2016, **7**(1), P. 44–50.
- [215] Mo K., Jiang T., Sun W., Gu Z. ATP-responsive DNA-graphene hybrid nanoaggregates for anticancer drug delivery. *Biomater.*, 2015, **50**, P. 67–74.
- [216] Thabitha P., Shareena D., McShan D., Dasmahapatra A.K., Tchounwou P.B. A Review on Graphene-Based Nanomaterials in Biomedical Applications and Risks in Environment and Health. *Nano-Micro Lett.*, 2018, **10**(53); P. 1–34.
- [217] Amirov R.H., Iskhakov M.E., Shavelkina M.B. Synthesis of high purity multilayer graphene using plasma jet. *Nanosystems: Physics, Chemistry, Mathematics*, 2016, **7**(1), P. 60–64.
- [218] Ren L., Zhang Y., Cui C., Bi Y., Ge X. Functionalized graphene oxide for anti-VEGF siRNA delivery: preparation, characterization and evaluation in vitro and in vivo. *RSC Adv.*, 2017, **7**, P. 20553–20566.
- [219] Seliverstova E.V., Ibrayev N.Kh., Dzhanabekova R.K. Study of graphene oxide solid films prepared by Langmuir–Blodgett technology. *Nanosystems: Physics, Chemistry, Mathematics*, 2016, **7**(1), P. 65–70.
- [220] Kondrin M.V., Brazhkin V.V. Is graphane the most stable carbon monohydride? *Nanosystems: Physics, Chemistry, Mathematics*, 2016, **7**(1), P. 44–50.
- [221] Iijima S., Ichihashi T. Single-Shell Carbon Nanotubes of 1-nm Diameter. *Nature*, 1993, **363**, P. 603–605.
- [222] Tessonnier J.-P., Rosenthal D., Yansen T.W., Hess C., Schuster M.E., Matthey J., Blume R., Girsdies F., Pfnder N., Timpe O., Su D. Analysis of the structure and chemical properties of some commercial carbon nanostructures. *Carbon*, 2009, **47**, P. 1779–1798.
- [223] Trostenson E.T., Ren Z., Chou T.W. Advances in the science and technology of carbon nanotubes and their composites: a review. *Composites Sci. and Technology*, 2001, **61**, P. 1899–1912.
- [224] Eletskii A.V. Carbon nanotubes. *Advances in Physical Sciences*, 1997, **167**(9), P. 945–972.
- [225] Oncel C., Yurum Y. Carbon Nanotube Syntesis via Catalytic CVD Method: A Review on the Effect of Reaction Parameters. *Fullerenes, Nanotubes and Carbon Nanostructures*, 2006, **14**, P. 17–37.
- [226] Resasco D.E., Alvarez W.E., Pompeo F., Balzano L., Herrera J.E., Kitiyanan B., Borgna A. A scalable process for production of single-walled carbon nanotubes (SWNTs) by catalytic disproportionation of CO on a solid catalyst. *J. Nanoparticle Res.*, 2002, **4**, P. 131–136.
- [227] Kitiyanan B., Alvarez W.E., Harwell J.H., Resasco D.E. Controlled production of single-wall carbon naotubes by catalutic decomposition of CO on bimetallic Co-Mo catalysts. *Chem. Phys. Lett.*, 2000, **317**, P. 497–503.
- [228] Xu, F., Zhao, H., Tse, S.D. Carbon nanotube synthesis on catalytic metal alloys in methane/air counter flow diffusion flames. *Proc. Combust. Inst.*, 2007, **31**, P. 1839–1847.
- [229] Nasibulin A.G., Moiala A., Jiang H., Kauppinen E.I. Carbon nanotube synthesis from alcohols by a novel aerosol method. *J. Nanoparticle Res.*, 2006, **8**, P. 465–475.

- [230] Sadeghian Z. Large-scale production of multi-walled carbon nanotubes by low-cost spray pyrolysis of hexane. *New Carbon Mater.*, 2009, **24**(1), P. 33–38.
- [231] Liu X., Ly J., Han S., Zhang D., Requich A., Thompson E., Zhou C. Synthesis and Electronic Properties of Individual Single-Walled Carbon Nanotube/Polyppyrrrole Composite Nanocables. *Adv. Mater.*, 2005, **17**, P. 2727–2732.
- [232] Nasibulin A.G., Moisala A., Brown D.P., Jiang H., Kauppinen E.I. A novel aerosol method for single walled carbon nanotube synthesis. *Chem. Phys. Lett.*, 2005, **402**, P. 227–232.
- [233] Nyamori V.O., Nxumalo E.N., Coville N.J. The effect of arylterrocene ring substituents on the synthesis of multi-walled carbon nanotubes. *J. Organomet. Chem.*, 2009, **343**, P. 290–298.
- [234] Bronikowski M.J., Willis P.W., Colbert D.T., Smith K.A., Smolley R.E. Gas-phase production of carbon single-walled nanotube from carbon monoxide via the HiPCO process: A parametric study. *J. Vac. Sci. Technol. A*, 2001, **19**(4), P. 1800–1805.
- [235] Ebbesen T.W., Ajayan P.M., Hiura H., Tanigaki K. Purification of nanotubes. *Nature*, 1994, **367**, P. 519.
- [236] Hou P.X., Liu C., Cheng H.M. Purification of carbon nanotubes. *Carbon*, 2008, **46**, P. 2003–2025.
- [237] Jakubek L.M., Marangoudakis S., Raingo J., Liu X., Lipscombe D., Hurt R.H. The inhibition of neuronal calcium ion channels by trace levels of yttrium released from carbon nanotubes. *Biomater.*, 2009, **30**, P. 6351–6357.
- [238] Bianco A., Kostarelos K., Partidos C.D., Prato M. Biomedical applications of functionalized carbon nanotubes. *Chem. Commun. (Cambridge, UK)*, 2005, **5**, P. 571–577.
- [239] Singh R., Pantarotto D., McCarthy D. Binding and condensation of plasmid DNA onto functionalized carbon nano-tubes: toward the construction of nanotube-based gene delivery vectors. *J. Am. Chem. Soc.*, 2005, **127**, P. 4388–4396.
- [240] Mahmood M., Karmakar A., Fejleh A., Mocan T., Iancu C., Mocan L., Iancu D.T., Xu Y., Dervishi E., Li Z., Biris A.R., Agarwal R., Ali N., Galanzha E.I., Biris A.S., Zharov V.P. Synergistic enhancement of cancer therapy using a combination of carbon nanotubes and antitumor drug. *Nanomed. (London)*, 2009, **4**, P. 883–893.
- [241] Liu Z., Fan A.C., Rakhra K., Sherlock S., Goodwin A., Chen X., Yang Q., Felsner D.W., Dai H. Supramolecular stacking of doxorubicin on carbon nanotubes for *in vivo* cancer therapy. *Angew. Chem. Int. Ed. Engl.*, 2009, **41**(48), P. 7668–7672.
- [242] Pastorin G., Wu W., Wiecek S., Briand J.P., Kostarelos K., Prato M., Bianco A. Double functionalization of carbon nanotubes for multimodal drug delivery. *Chem. Commun.*, 2006, **11**, P. 1182–1184.
- [243] Kateb B., Yamamoto V., Alizadeh D., Zhang L., Manohara H.M., Bronikowski M.J., Badie B. Multi-walled carbon nanotube (MWCNT) synthesis, preparation, labeling, and functionalization. *Immunotherapy of Cancer, Methods in Molecular Biology*, 2010, **651**, P. 307–317.
- [244] Garcia B.O., Kharisova O.V., Rasika Dias H.V., Servando Aguirre T.F., Salinas Hernandez J. Nanocomposites with antibacterial properties using CNTs with magnetic nanoparticles. *Nanosystems: Physics, Chemistry, Mathematics*, 2016, **7**(1), P. 161–168.
- [245] Dastjerdi R., Montazer M. A review on the application of inorganic nanostructured materials in the modification of textiles: Focus on antimicrobial properties. *Coll. Surf. B: Biointerfaces*, 2010, **79**, P. 5–18.
- [246] Bocharov G.S., Egin M.S., Eletsii A.V., Kuznetsov V.L. Filling carbon nanotubes with argon. *Nanosystems: Physics, Chemistry, Mathematics*, 2018, **9**(1), P. 85–88.
- [247] Jakubek L.M., Marangoudakis S., Raingo J., Liu X., Lipscombe D., Hurt R.H. The inhibition of neuronal calcium ion channels by trace levels of yttrium released from carbon nanotubes. *Biomater.*, 2009, **30**, P. 6351–6357.
- [248] Foldvari M., Bagonluri M. Carbon nanotubes as functional excipients for nanomedicines: II. Drug delivery and biocompatibility issues. *Nanomed.*, 2008, **4**(3), P. 183–200.
- [249] Cai D., Mataraza J.M., Qin Z.H., Huang Z., Huang J., Chiles T.C., Carnahan D., Kempa K., Ren Z. Highly efficient molecular delivery into mammalian cells using carbon nanotube spearing. *Nat. Methods*, 2005, **2**, P. 449–454.
- [250] Turcheniuk K., Mochalin V.N. Biomedical Applications of Nanodiamond (Review). *Nanotechnology*, 2017, **28**, P. 252001–252027.
- [251] Rosenholm J.M., Vlasov I.I., Burikov S.A., Dolenko T.A., Shenderova O.A. Nanodiamond Based Composite Structures for Biomedical Imaging and Drug Delivery (Review). *J. Nanosci. Nanotechnol.*, 2015, **15**, P. 959–971.
- [252] Kulvelis Y.V., Shvidchenko A.V., Aleksenskii A.E., Yudina E.B., Lebedev V.T., Shestakov M.S., Dideikin A.T., Khozyaeva L.O., Kuklin A.I., Gy T., Rulev M.I., Vul A.Y. Stabilization of detonation nanodiamonds hydrosol in physiological media with poly (vinylpyrrolidone). *Diamond and Related Mater.*, 2018, **87**, P. 78–89.
- [253] Girard H., Pager V., Simic V., Arnault J.C. Peptide nucleic acid nanodiamonds: Covalent and stable conjugates for DNA targeting. *RSC Adv.*, 2014, **4**, P. 3566–3572.
- [254] Mochalin V.N., Shenderova O., Ho D., Gogotsi Y. The Properties and Applications of Nanodiamonds. *Nature Nanotechnology*, 2011, **7**(1), P. 11–23.
- [255] Bokarev A.N., Plastun I.L. Possibility of drug delivery due to hydrogen bonds formation in nanodiamonds and doxorubicin: molecular modeling. *Nanosystems: Physics, Chemistry, Mathematics*, 2018, **9**(3), P. 370–377.
- [256] Giammarco J., Mochalin V.N., Haeckel J., Gogotsi Y. The adsorption of tetracycline and vancomycin onto nanodiamond with controlled release. *J. Colloid Interface Sci.*, 2016, **468**, P. 253–261.
- [257] Vervald E.N., Laptinskiy K.A., Vlasov I.I., Shenderova O.A., Dolenko T.A. DNA nanodiamond interactions influence on fluorescence of nanodiamonds. *Nanosystems: Physics, Chemistry, Mathematics*, 2018, **9**(1), P. 64–66.
- [258] Schimke M., Steinmüller-Nethl D., Kern J., Krüger A., Lepperdinger G. Biofunctionalization of nano-scaled diamond particles for use in bone healing and tissue engineering. *Experimental Gerontology*, 2015, **68**, P. 100.
- [259] Chen M., Pierstorff E.D., Li Sh-Y., Lam R., Huang H., Osawa E., Ho D. Nanodiamond-mediated delivery of water-insoluble therapeutics. *ASC Nano*, 2009, **7**(3), P. 2012–2022.
- [260] Solomatin A.S., Yakovlev R.Yu., Efremenkova O.V., Sumarukova I.G., Kulakova I.I., Lisichkin G.V. Antibacterial activity of Amikacin immobilized detonation nanodiamond. *Nanosystems: Physics, Chemistry, Mathematics*, 2017, **8**(4), P. 531–534.
- [261] Danilenko V.V. On the History of the Discovery of Nanodiamond Synthesis. *Physics of the Solid State*, 2004, **46**(4), P. 595–599.
- [262] Vul A.Y., Dideikin A.T., Alexenskii A.E., Baidakova M.V. Detonation nanodiamonds: Synthesis, Properties and Applications. Chapter 2. In: Nanodiamond. Ed. Williams O.A. Published by the Royal Society of Chemistry, Cambridge, 2014, P. 27–48.
- [263] Bondar' V.S., Puzyr' A.P. Nanodiamonds for Biological Investigations. *Physics of the Solid State*, 2004, **46**(4), P. 716–719.

- [264] Tomchuk O., Volkov D., Bulavin L., Rogachev A., Proskurnin M., Korobov M., Avdeev M. Structural characteristics of aqueous dispersions of detonation nanodiamond and their aggregate fractions as revealed by small-angle neutron scattering *J. Phys. Chem. C*, 2015, **119**(1), P. 794–802.
- [265] Kulakova I.I. Surface Chemistry of Nanodiamonds. *Phys. Solid State*, 2004, **46**(4), P. 636–643.
- [266] Dideikin A.T., Aleksenskii A.E., Baidakova M.V., Brunkov P.N., Brzhezinskaya M., Davydov V.Y., Levitskii V.S., Kidalov S.V., Kukushkina Y.A., Kirilenko D.A., Shnitov V.V., Shvidchenko A.V., Senkovskiy B.V., Shestakov M.S., Vul A.Y. Rehybridization of carbon on facets of detonation diamond nanocrystals and forming hydrosols of individual particles. *Carbon*, 2017, **122**, P. 737–745.
- [267] Greiner N.R., Phillips D.S., Johnson J.D., Volk F. Diamonds in detonation soot. *Nature*, 1988, **333**, P. 440–442.
- [268] Xu K., Xue Q. A New Method for Deaggregation of Nanodiamond from Explosive Detonation: Graphitization–Oxidation Method. *Phys. Solid State*, 2004, **46**(4), P. 649–650.
- [269] Vervald A.M., Burikov S.A., Vlasov I.I., Shenderova O.A., Dolenko T.A. Interactions of nanodiamonds and surfactants in aqueous suspensions. *Nanosystems: Physics, Chemistry, Mathematics*, 2018, **9**(1), P. 49–51.
- [270] Zhang Q., Mochalin V.N., Neitzel I., Knoke I.Y., Han J., Klug C.A., Zhou J.G., Lelkes P.I., Gogotsi Y. Fluorescent PLLA-nanodiamond composites for bone tissue engineering. *Biomater.*, 2011, **32**(1), P. 87–94.
- [271] Bobrysheva I.V., Kashchenko S.A. *Histology, Cytology, Embryology: Textbook*, Knowledge, Lugansk: 2011, 529 p.
- [272] Vasudeva N., Mishra S. *Inderbir Singh's Textbook of Human Histology with Colour Atlas and Practical Guide*. Jaypee Brothers Medical Publishers (P) Ltd, New Delhi, 2014, 439 p.
- [273] Bykov V.L. *Special Histology of Human: Textbook*. St. Petersburg: SOTIS, 1999, 301 p.
- [274] Krause W.J. *Krause's Essential Human Histology*. Univ. Missouri Columbia, 2005, 315 p.  
(<https://mospace.umsystem.edu/xmlui/bitstream/handle/10355/11238/KrausesEssentialHuman.pdf?sequence=1&isAllowed=y>).
- [275] Membrino M.A. *Transdermal Delivery of Therapeutic Compounds by Iontophoresis*. University of Florida, 2002, 283 p.
- [276] Scheuplein R.J. Mechanism of Percutaneous Absorption: II. Transient Diffusion and the Relative Importance of Various Routes of Skin Penetration. *J. Investigative Dermatol.*, 1967, **48**(1), P. 79–88.
- [277] *Methods in Molecular Biology. Permeability Barrier: Methods and Protocols*. Ed. Turksen K., Totowa, NJ: Humana Press, 2011, 439 p.
- [278] Zesch A., Schaefer H. Penetrationskinetik von radiomarkiertem Hydrocortison aus verschiedenartigen Salbengrundlagen in die menschliche Haut II. In vivo. *Archives Dermatol. Res.*, 1975, **252**(4), P. 245–256.
- [279] Schaefer H., Zesch A., Stüttgen G. *Skin Permeability*. Berlin, Heidelberg: Springer Berlin Heidelberg, 1982, 896 p.
- [280] Kuznetsova E.G., Ryzhikova V.A., Salomatina L.A., Sevastianov V.I. Transdermal Drug Delivery and Methods to Enhance It. *Russ. J. Transplant. Artificial Organs*, 2016, **18**(2), P. 152–162.
- [281] Asbrill C.S., El-Kattan A.F., Marchiniak B. Enhancement of transdermal drug delivery: chemical and physical approaches. *Crit. Rev. Ther. Drug Carrier Syst.*, 2000, **17**(6), P. 612–658.
- [282] Paudel K.S., Milewski M., Swadley C.L. Challenges and opportunities in dermal/transdermal delivery. *Ther. Deliv.*, 2010, **1**(1), P. 109–131.
- [283] Hupfeld S., Gravem H. Transdermal therapeutic systems for drug administration. *Tidsskr. Nor. Laegeforen.*, 2009, **129**(6), P. 532–533.
- [284] Sugino M., Todo H., Sugibayashi K. Skin permeation and transdermal delivery systems of drugs: history to overcome barrier function in the stratum corneum. *Yakugaku Zasshi*, 2009, **129**(12), P. 1453–1458.
- [285] Heather Benson A.E. Transdermal Drug Delivery: Penetration Enhancement Techniques. *Current Drug Deliv.*, 2005, **2**, P. 23–33.
- [286] Moskvin S.V., Minenkov A.A. The mechanism of transcutaneous drug transfer assisted by laserophoresis. *Klin. Dermatol. Venerol.*, 2010, **5**, P. 78–83.
- [287] Polat B.E., Figueroa P.L., Blankschtein D., Langer R. Transport Pathways and Enhancement Mechanisms within Localized and Non-Localized Transport Regions in Skin Treated with Low-Frequency Sonophoresis and Sodium Lauryl Sulfate. *J. Pharm. Sci.*, 2011, **100**(20), P. 512–529.
- [288] Naegel A., Heisig M., Wittum G. Detailed Modeling of Skin Penetration An Overview. *Advanced Drug Delivery Reviews*, 2013, **65**(2), P. 191–207.
- [289] Guy R.H., Hadgraft J., Maibach H.I. A Pharmacokinetic Model for Percutaneous Absorption. *International Journal of Pharmaceutics*, 1982, **11**(2), P. 119–129.
- [290] Frasch H.F., Barbero A.M. Application of Numerical Methods for Diffusion-Based Modeling of Skin Permeation. *Advanced Drug Delivery Reviews*, 2013, **65**(20), P. 208–220.
- [291] Mitragotri S., Anissimov Y.G., Bunge A.L., Frasch H.F., Guy R.H., Hadgraft J., Kasting G.B., Lane M.E., Roberts M.S. Mathematical Models of Skin Permeability: An Overview. *International Journal of Pharmaceutics*, 2011, **418**(1), P. 115–129.
- [292] Anissimov Y.G., Roberts M.S. Diffusion Modeling of Percutaneous Absorption Kinetics. 1. Effects of Flow Rate, Receptor Sampling Rate, and Viable Epidermal Resistance for a Constant Donor Concentration. *Journal of Pharmaceutical Sciences*, 1999, **88**(11), P. 1201–1209.
- [293] Lindstrom T.F., Ayres J.W. Diffusion Model for Drug Release from Suspensions II: Release to a Perfect Sink. *Journal of pharmaceutical sciences*, 1977, **66**(5), P. 662–668.
- [294] Todo H., Oshizaka T., Kadhum W., Sugibayashi K. Mathematical Model to Predict Skin Concentration after Topical Application of Drugs. *Pharmaceutics*, 2013, **5**(4), P. 634–651.
- [295] Guy R.H., Hadgraft J., Maibach H.I. A Pharmacokinetic Model for Percutaneous Absorption. *International Journal of Pharmaceutics*, 1982, **11**(2), P. 119–129.
- [296] Guy R.H., Hadgraft J. Transdermal Drug Delivery: A Simplified Pharmacokinetic Approach. *Int. J. Pharm.*, 1985, **24**(2–3), P. 267–274.
- [297] Riegelman S. Pharmacokinetics; Pharmacokinetic Factors Affecting Epidermal Penetration and Percutaneous Absorption. *Clinical Pharmacology & Therapeutics*, 1974, **16**(5, part 2), P. 873–883.
- [298] Tojo K. Mathematical Modeling of Transdermal Drug Delivery. *Journal of Chemical Engineering of Japan*, 1987, **20**(3), P. 300–308.
- [299] Vieth W.R., Howell J.M., Hsieh J.H. Dual Sorption Theory. *Journal of Membrane Science*, 1976, **1**, P. 177–220.
- [300] Chandrasekaran S., Michaels A., Campbell P., Shaw J. Scopolamine Permeation through Human Skin in Vitro. *AIChE Journal*, 1976, **22**(5), P. 828–832.
- [301] Chandrasekaran S.K., Bayne W., Shaw J.E. Pharmacokinetics of Drug Permeation through Human Skin. *Journal of pharmaceutical sciences*, 1978, **67**(10), P. 1370–1374.

- [302] Shen J., Kromidas L., Schultz T., Bhatia S. An in silico skin absorption model for fragrance materials. *Food and Chemical Toxicology*, 2014, **74**, P. 164–176.
- [303] Flynn G. Physicochemical Determinants of Skin Absorption. In *Principles of route-to-route extrapolation for risk assessment* / Ed. Gerrity T.R., Henry C.J. New York: Elsevier, 1990, P. 93–127.
- [304] Barratt M. Quantitative Structure-Activity Relationships for Skin Permeability. *Toxicology in Vitro*, 1995, **9**(1), P. 27–37.
- [305] Godin B., Touitou E. Transdermal Skin Delivery: Predictions for Humans from in Vivo, Ex Vivo and Animal Models. *Advanced Drug Delivery Reviews*, 2007, **59**(11), P. 1152–1161.
- [306] Potts R.O., Guy R.H. Predicting Skin Permeability. *Pharmaceutical Research*, 1992, **9**(5), P. 663–669.
- [307] Geinoz S., Guy R.H., Testa B., Carrupt P.-A. Quantitative Structure-Permeation Relationships (QSPeRs) to Predict Skin Permeation: A Critical Evaluation. *Pharmaceutical Research*, 2004, **21**(1), P. 83–92.
- [308] Enbäck J., Laakkonen P. Tumour-homing peptides: tools for targeting, imaging and destruction. *Biochemical Society Transactions*, 2007, **35**(4), P. 780–783.
- [309] Un F., Zhou B., Yen Y. The Utility of Tumor-specifically Internalizing Peptides for Targeted siRNA Delivery into Human Solid Tumors. *Anticancer Research*, 2012, **32**, P. 4685–4690.
- [310] Rihova B. Targeting of Drugs to Cell Surface Receptors. *Critical Reviews in Biotechnology*, 1997, **17**(2), P. 149–169.
- [311] Ivonin A.G., Pimenov E.V., Oborin V.A., Devrshov D.A., Kopylov S.N. Directed Transport of Drugs: Current State and Prospects. *Proceedings of the Komi Science Centre of the Ural Division of the Russian Academy of Sciences*, 2012, **1**(9), P. 46–55.
- [312] Guillemard V., Uri Saragovi N. Prodrug chemotherapeutics bypass p-glycoprotein resistance and kill tumors in vivo with high efficacy and target-dependent selectivity. *Oncogene*, 2004, **23**(20), P. 3613–3621.
- [313] Baselga J. A review of EGFR targeted therapy. *Clin. Adv. Hemato.l Oncol.*, 2003, **1**(4), P. 218–219.
- [314] Sharman W.M., van Lier J.E., Allen C.M. Targeted photodynamic therapy via receptor mediated delivery systems. *Adv. Drug Deliv. Rev.*, 2004, **56**(1), P. 53–76.
- [315] Manoharan M. Oligonucleotide conjugates as potential antisense drugs with improved uptake, biodistribution, targeted delivery, and mechanism of action. *Antisense Nucieic Acid Drug Dev.*, 2002, **12**(2), P. 103–128.
- [316] Stern M., Herrmann R. Overview of monoclonal antibodies in cancer therapy: present and promise. *Crit. Rev. Oncol. Hematol.*, 2005, **54**(1), P. 11–29.
- [317] Casi G., Neri D. Antibody-drug conjugates: basic concepts, examples and future perspectives. *J. Cont. Release*, 2012, **161**(2), P. 422–428.
- [318] Wei, C., Su, D., Wang, J., Jian W., Zhang D. LC–MS Challenges in Characterizing and Quantifying Monoclonal Antibodies (mAb) and Antibody-Drug Conjugates (ADC) in Biological Samples. *Curr. Pharmacol. Rep.*, 2018, **4**(1), P. 45–63.
- [319] Bareford L.M., Swaan P.W. Endocytic mechanisms for targeted drug delivery. *Adv. Drug. Deliv. Rev.*, 2007, **59**(8), P. 748–758.
- [320] Marsh M., McMahon H.T. The structural era of endocytosis. *Science*, 1999, **285**(5425), P. 215–220.
- [321] Mousavi S.A., Malerod L., Berg T., Kjekken R. Clathrin-dependent endocytosis. *Biochem. J.*, 2004, **377**(1), P. 1–16.
- [322] Rodemer C., Haucke V. Clathrin/AP-2-dependent endocytosis: a novel playground for the pharmacological toolbox? *Handb. Exp. Pharmacol.*, 2008, **186**, P. 105–122.
- [323] Krippendorff B.F., Kuester K., Kloft C., Huisinga W. Nonlinear pharmacokinetics of therapeutic proteins resulting from receptor mediated endocytosis. *J. Pharmacokinet. Pharmacodyn.*, 2009, **36**(3), P. 239–260.
- [324] Khalil I.A., Kogure K., Akita H., Harashima H. Uptake pathways and subsequent intracellular trafficking in nonviral gene delivery. *Pharmacol. Rev.*, 2006, **58**(1), P. 32–45.
- [325] Rawat A., Vaidya B., Khatri K., Goyal A.K., Gupta P.N., Mahor S., Paliwal R., Rai S., Vyas S.P. Targeted intracellular delivery of therapeutics: an overview. *Die Pharmazie*, 2007, **62**(9), P. 643–658.
- [326] Bildstein L., Dubernet C., Couvreur P. Prodrug-based intracellular delivery of anticancer agents. *Adv. Drug. Deliv. Rev.*, 2011, **63**(1-2), P. 3–23.
- [327] Yu S., Li A., Liu Q., Li T., Yuan X., Han X., Wu K. Chimeric antigen receptor T cells: a novel therapy for solid tumors. *J. Hematol. Oncol.*, 2017, **10**(1), P. 1–13.
- [328] Rosenkranz A.A., Ulasov A.V., Slastnikova T.A., Khramtsov Y.V., Sobolev A.S. Use of Intracellular Transport Processes for Targeted Drug Delivery into a Specified Cellular Compartment. *Biochem. (Moscow)*, 2014, **79**(9), P. 928–946.
- [329] Pauling L. *The Nature of the Chemical Bond*, 3-d edition. Itaca, New York, Cornell University Press, London, Oxford University Press, 1960, 643 p.
- [330] Yamase T. Polyoxometalates for Molecular Devices: Antitumor Activity and Luminescence. *Molecular Eng.*, 1993, **3**(1–3), P. 241–262.
- [331] Yamase T., Fujita H., Fukushima K. Medical Chemistry of Polyoxometalates. Part 1. Potent Antitumor Activity of Polyoxomolybdates on Animal Transplantable Tumors and Human Cancer Xenograft. *Inorg. Chim. Acta*, 1988, **151**(1), P. 15–18.
- [332] Yang H.-K., Cheng Y.-X., Su M.-M., Xiao Y., Hu M.-B., Wang W., Wang Q. Polyoxometalate–biomolecule Conjugates: A New Approach to Create Hybrid Drugs for Cancer Therapeutics. *Bioorganic & Med. Chem. Lett.*, 2013, **23**(5), P. 1462–1466.
- [333] Bijelic A., Aureliano M., Rompel A. Polyoxometalates as Potential Next-Generation Metallodrugs in the Combat Against Cancer. *Angew. Chem. Int. Ed.*, 2019, **58**, P. 2980–2999.
- [334] Datta L.P., Mukherjee R., Subharanjan Biswas S., Das T.K. Peptide-Based Polymer-Polyoxometalate Supramolecular Structure with a Differed Antimicrobial Mechanism. *Langmuir*, 2017, **33**, P. 14195–14208.
- [335] Müller A., Krickemeyer E., Bögge H., Schmidtmann M., Peters F. Organizational Forms of Matter: An Inorganic Super Fullerene and Keplerate Based on Molybdenum Oxide. *Angew. Chem. Int. Ed.*, 1998, **37**(24), P. 3359–3363.
- [336] Müller A., Gouzerh P. From Linking of Metal-Oxide Building Blocks in a Dynamic Library to Giant Clusters with Unique Properties and towards Adaptive Chemistry. *Chem. Soc. Rev.*, 2012, **41**(22), P. 7431–7463.
- [337] Awada M., Floquet S., Marrot J., Haouas M., Morcillo S.P., Bour Ch., Gandon V., Coeffard V., Greck Ch., Cadot E. Synthesis and Characterizations of Keplerate Nanocapsules Incorporating L- and D-Tartrate Ligands. *J. Clust. Sci.*, 2017, **28**(2), P. 799–812.
- [338] Ostroushko A.A., Adamova L.V., Eremina E.V., Grzhegorzhevskii K.V. Interaction between nanocluster polyoxometallates and low-molecular-weight organic compounds. *Russ. J. Phys. Chem. A*, 2015, **89**(8), P. 1439–1444.
- [339] Tonkushina M.O., Gagarin I.D., Grzhegorzhevskii K.V., Ostroushko A.A. Electrophoretic Transfer of Nanocluster Polyoxometalate Mo<sub>72</sub>Fe<sub>30</sub> Associates through the Skin Membrane. *Bull. Ural Med. Acad. Sci.*, 2014, **3**(49), P. 59–61.

- [340] Ostroushko A.A., Grzhegorzhevskii K.V. Electric Conductivity of Nanocluster Polyoxomolybdates in the Solid State and Solutions. *Russ. J. Phys. Chem. A*, 2014, **88**(6), P. 1008–1011.
- [341] Müller A., Shah S. Q. N., Bögge H., Schmidtman M., Sarkar S., Kögerler P., Hauptfleisch B., Trautwein A.X., Schönemann V. Archimedean Synthesis and Magic Numbers: “Sizing” Giant Molybdenum-Oxide-Based Molecular Spheres of the Keplerate Type. *Angew. Chem. Int. Ed.*, 1999, **38**(21), P. 3238–3241.
- [342] Ostroushko A.A., Tonkushina M.O., Korotaev V.Yu., Prokof'eva A.V., Kutyashev I.B., Vazhenin V.A., Danilova I.G., Men'shikov S.Yu. Stability of the  $\text{Mo}_72\text{Fe}_{30}$  Polyoxometalate Buckyball in Solution. *Russ. J. Inorg. Chem.*, 2012, **57**(9), P. 1210–1213.
- [343] Ostroushko A.A., Tonkushina M.O. Destruction of Molybdenum Nanocluster Polyoxometallates in Aqueous Solutions. *Russ. J. Phys. Chem. A*, 2015, **89**(3), P. 443–446.
- [344] Ostroushko A.A., Danilova I.G., Gette I.F., Medvedeva S.Yu., Tonkushina M.O., Prokofieva A.V., Morozova M.V. Study of Safety of Molybdenum and Iron-Molybdenum Nanocluster Polyoxometalates Intended for Targeted Delivery of Drugs. *J. Biomat. Nanobiotechnol.*, 2011, **2**(5), P. 557–560.
- [345] Ostroushko A.A., Gette I.F., Medvedeva S.Y., Danilova I.G., Mukhlynina E.A., Tonkushina M.O., Morozova M.V. Study of Acute and Subacute Action of Iron-Molybdenum Nanocluster Polyoxometalates. *Nanotechnologies in Russia*, 2013, **8**(9–10), P. 672–677.
- [346] Gette I.F., Medvedeva S.Yu., Ostroushko A.A. Condition of the Immune System Organs and Blood Leucocytes in Rats after the Exposition of Iron-Molybdenum Polyoxometalates. *Russian J. of Immunol.*, 2017, **11**(2), P. 280–282
- [347] Danilova I.G., Gette I.F., Medvedeva S.Y., Mukhlynina E.A., Tonkushina M.O., Ostroushko A.A. Changing the Content of Histone Proteins and Heat-Shock Proteins in the Blood and Liver of Rats after the Single and Repeated Administration of Nanocluster Iron-Molybdenum Polyoxometalates. *Nanotechnologies in Russia*, 2015, **10**(9–10), P. 820–826.
- [348] Liu T., Imber B., Diemann E., Liu G., Cokleski K., Li H., Chen Z., Müller A. Deprotonations and Charges of Well-Defined  $\text{Mo}_72\text{Fe}_{30}$  Nanoacids Simply Stepwise Tuned by pH Allow Control/Variation of Related Self-Assembly Processes. *J. Am. Chem. Soc.*, 2006, **128**(49), P. 15914–15920.
- [349] Ostroushko A.A., Gette I.F., Danilova I.G., Mukhlynina E.A., Tonkushina M.O., Grzhegorzhevskii K.V. Studies on the Possibility of Introducing Iron–Molybdenum Buckyballs into an Organism by Electrophoresis. *Nanotechnologies in Russia*, 2014, **9**(9–10), P. 586–591.
- [350] Ostroushko A.A., Danilova I.G., Gette I.F., Tonkushina M.O., Behavior of Associates of Keplerate-Type Porous Spherical  $\text{Mo}_72\text{Fe}_{30}$  Clusters with Metal Cations in Electric Field-Driven Ion Transport. *Russ. J. Inorg. Chem.*, 2015, **60**(4), P. 500–504.
- [351] Ostroushko A.A., Grzhegorzhevskii K.V., Bystrai G.P., Okhotnikov S.A. Modeling the Processes of Electrophoretic Transfer for Spherical Nanoclusters of Iron–Molybdenum Polyoxometalates. *Russ. J. Phys. Chem. A*, 2015, **89**(9), P. 1638–1641.
- [352] Michelis F.V., Delitheos A., Tiligada E. Molybdate modulates mitogen and cyclosporin responses of human peripheral blood lymphocytes. *J. Trace Elements in Med. and Biol.*, 2011, **25**, P. 138–142.
- [353] Müller A., Sarkar S., Shah S.Q.N., Bögge H., Schmidtman M., Sarkar S., Kögerler P., Hauptfleisch B., Trautwein V.X., Schönemann V. Archimedean Synthesis and Magic Numbers: “Sizing” Giant Molybdenum-Oxide-Based Molecular Spheres of the Keplerate Type. *Angew. Chem. Int. Ed. Engl.*, 1999, **38**(21), P. 3238–3241.
- [354] Ostroushko A.A., Tonkushina M.O., Martynova N.A. Mass and charge transfer in systems containing nanocluster molybdenum polyoxometallates with a fullerene structure. *Russ. J. Phys. Chem. A*, 2010, **84**(6), P. 1022–1027.
- [355] Gagarin I.D., Kulesh N.A., Tonkushina M.O., Vlasov D.A., Ostroushko A.A. Physico-chemical aspects of electrotransport of keplerate-type nanocluster polyoxoanions in native membranes. *Physical and chemical aspects of the study of clusters, nanostructures and nanomaterials*, 2017, **9**, P. 147–152.
- [356] Bystrai G.P. *Thermodynamics of irreversible processes in open systems. (Termodinamika neobratimyykh processov w otkrytykh sistemakh)*, Moscow - Izhevsk: Research Center of Regular and Random Dynamics, 2011. 264 pp. (in Russian)
- [357] Prigogine I. *Introduction to Thermodynamics of Irreversible Processes*, 3-rd Ed., Interscience Publishers, a division of John Wiley & Sons New York, London, Sydney, 1967, 146 p.
- [358] Kahaner D., Moler C., Nash S. *Numerical Methods and Software*, Prentice Hall, 1989, 495 p.
- [359] Kamont Z., Czernous W. Implicit Difference Methods for Hamilton-Jacobi Functional Differential Equations. *Numerical Anal. Appl.*, 2009, **2**(1), P. 46–57.
- [360] Ardelyan I.V. On the use of iterative methods when realizing implicit difference schemes of two-dimensional magnetohydrodynamics. *USSR Comp. Mathem. Mathem. Phys.*, 1983, **23**(6), P. 84–90.
- [361] Czernous W. Implicit Difference Methods for Hamilton-Jacobi Functional Differential Equations. *Numerical Anal. Appl.*, 2009, **2**(1), P. 46–57.
- [362] Gu X.M., Huang T.Z., Ji C.C., Carpentieri B., Alikhanov A.A. Fast Iterative Method with a Second-Order Implicit Difference Scheme for Time-Space Fractional Convection–Diffusion Equation. *J. Sci. Comp.*, 2017, **72**(3), P. 957–985.
- [363] Shikhova S.V. The Genotoxic Effect of Aminopterin and Methotrexate on Fertility of Several Lines Wild Type of *Drosophila Melanogaster*. *Proceedings of Voronezh State University. Series Chem., Biol., Pharm.*, 2017, **4**, P. 93–98.
- [364] Ostroushko A.A., Gagarin I.D., Grzhegorzhevskii K., Gette I.F., Vlasov D.A., Ermoshin F.A., Antosyuk O.N., Shikhova S.V., Danilova I.G. New Aspects of Studying of Physico-chemical Propertis of Nanocluster Polyoxomolybdates as Perspective Materials for Biomedicine. Conferences Cluster 2018. X International Conference “Kinetics and mechanism of crystallization”. July 1-6, 2018, Suzdal, Russia. P. 29–30.
- [365] Shikhova S.V., Grzhegorzhevskii K.V., Gagarin I.D. Assessment of address delivery efficiency of aminopterin by means of iron-molybdenum nanocluster polyoxometalal with use of the biotest. Transactions of the XVth All-Russian scientific and practical Conference with international participation “Biodiagnostics of a Condition of Natural and Natural-Technogenic Systems”. Kirov. 4-6 Dec. 2017. Kirov: Vyatka State University, 2017, P. 198–202.
- [366] Ostroushko A.A., Safronov A.P., Tonkushina M.O., Korotaev V.Yu., Barkov A.Yu. Interaction between  $\text{Mo}_{132}$  Nanocluster Polyoxometalate and Solvents. *Russ. J. Phys. Chem. A*, 2014, **88**(12), P. 2179–2182.
- [367] Ostroushko A.A., Gagarin I.D., Tonkushina M.O., Grzhegorzhevskii K.V., Danilova I.G., Gette I.F., Kim G.A. Iontophoretic Transport of Associates Based on Porous Keplerate-Type Cluster Polyoxometalate  $\text{Mo}_72\text{Fe}_{30}$  and Containing Biologically Active Substances. *Russ. J. Phys. Chem. A*, 2017, **91**(9), P. 1811–1815.
- [368] Timin A.S., Solomonov A.V., Musabirov I.I. Sergeev S.N., Ivanov S.P., Rummyantsev E.V., Goncharenko A. Immobilization of bovine serum albumin onto porous poly (vinylpyrrolidone)-modified silicas. *Ind. Eng. Chem. Res.*, 2014, **53**(35), P. 13699–13710.

- [369] Kadajji V.G., Betageri G.V. Water Soluble Polymers for Pharmaceutical Applications. *Polymers*, 2011, **3**, P. 1972–2009.
- [370] Ostroushko A.A., Safronov A.P., Tonkushina M.O. Thermochemical Study of Interaction between Nanocluster Polyoxomolybdates and Polymers in Film Compositions. *Russ. J. Phys. Chem. A*, 2014, **88**(2), P. 295–300.
- [371] Bijelic A., Rompel A. The use of polyoxometalates in protein crystallography – An attempt to widen a well-known bottleneck. *Coord. Chem. Rev.*, 2015, **299**, P. 22–38.
- [372] Gagarin I., Tonkushina M., Ostroushko A. Stabilization of keplerate-type spheric porous nanocluster polyoxometalate Mo<sub>72</sub>Fe<sub>30</sub>. 2018 Ural Symposium on Biomedical Engineering, Radioelectronics and Information Technology (USBREIT), 2018, P. 41–44.
- [373] Cedervall T., Lynch I., Lindman S., Berggard T., Thulin E., Nilsson H., Dawson K.A., Linse S. Understanding the nanoparticle–protein corona using methods to quantify exchange rates and affinities of proteins for nanoparticles. *Proc. Natl Acad. Sci. USA*, 2007, **104**, P. 2050–2055.
- [374] Lundqvist M., Stigler J., Elia G., Lynch I., Cedervall T., Dawson K.A. Nanoparticle size and surface properties determine the protein corona with possible implications for biological impacts *Proc. Natl Acad. Sci. USA*, 2008, **105**, P. 14265–14270.
- [375] Casals E., Pfaller T., Duschl A., Oostingh G.J., Puntès V. Quantitative study of protein coronas on gold nanoparticles with different surface modifications. *ACS Nano*, 2010, **4**, P. 3623–3632.
- [376] Docter D., Westmeier D., Markiewicz M., Stolte S., Knauer S.K., Stauber R.H. The nanoparticle biomolecule corona: lessons learned – challenge accepted? *Chem. Soc. Rev.*, 2015, **44** P. 6094–6121.
- [377] Walkey C.D., Olsen J.B., Song F., Liu R., Guo H., Olsen D.W., Cohen Y., Emili A., Chan W.C. Protein corona fingerprinting predicts the cellular interaction of gold and silver nanoparticles. *ACS Nano*, 2014, **8** P. 2439–2455.

## Experimental studies of barium titanate nanofibers prepared by electrospinning

M. V. Someswararao<sup>1</sup>, R. S. Dubey<sup>2\*</sup>

<sup>1</sup>Department of Physics, SRKR Engineering College, Bhimavaram, (A.P.), India

<sup>2</sup>Department of Nanotechnology, Swarnandhra College of Engineering and Technology,  
Seetharamapuram, Narsapur (A.P.), India

\*rag\_pcw@yahoo.co.in

DOI 10.17586/2220-8054-2019-10-3-350-354

This paper reports the fabrication and characterization of BaTiO<sub>3</sub> nanofibers prepared by the electrospinning method. The X-ray diffraction (XRD) pattern revealed the formation of tetragonal phase corresponding to the Bragg angle  $2\theta = 31^\circ$  and  $45^\circ$ . The formation of metal oxide is confirmed by the FTIR measurement. SEM study evidenced the smooth and randomly grown nanofibers with their average sizes 472 and 515 nm with respect to the samples BT1 and BT2 prepared at 8 and 12 kV dc voltages. TG/DTA analysis was performed to study the heating behavior of the composite BaTiO<sub>3</sub>/PVP mat and 49 % weight loss was observed at 725 °C.

**Keywords:** electrospinning, barium titanate, scanning electron microscopy, X-ray diffraction.

*Received:* 4 February 2019

*Revised:* 22 April 2019

### 1. Introduction

Barium titanate (BaTiO<sub>3</sub>) has excellent ferroelectric and piezoelectric properties. This material has been utilized in several industrial applications like capacitors, actuators, non-volatile RAM etc. [1–4]. In the absence of an external field, BaTiO<sub>3</sub> possess ferroelectric polarization. Over BaTiO<sub>3</sub> particles, nanofibers are reported to be promising one due to their large dielectric permittivity. Electrospinning technique has been reported to be as the simplest method for the fabrication of composite nanofibers of BaTiO<sub>3</sub>. It consists of mainly three parts such as power source, collector and the syringe pump. Upon applied dc voltage, the loaded solution flows under the region of strong electrostatic field which experiences a repulsive force and as a result fine jet formed [5].

Several literature have been reported on the fabrication and characterization of BaTiO<sub>3</sub> nanofibers by the electrospinning method [6–8]. Study of BaTiO<sub>3</sub> nanofibers was reported after the calcination of as-prepared fiber mat at different temperatures followed by drying at 80 °C under vacuum condition [9]. The investigation by electron scanning microscopy (SEM) showed the fibers diameters from 160 – 300 nm. The X-ray diffraction (XRD) study endorsed the presence of tetragonal perovskite structure while Fourier transform infrared spectroscopy (FTIR) confirmed the various bonds corresponding to the BaTiO<sub>3</sub> nanofibers. The O–H stretching peaks at 3430 and 1425 cm<sup>-1</sup> was found to be weak with respect to the increased calcination temperature while Ti–O peak at 570 cm<sup>-1</sup> became strong. Remarkably, BaTiO<sub>3</sub> nanofibers calcined in nitrogen environment could convert the tetragonal phase to cubic perovskite structure which has been attributed to the elimination of carbonate content. Electrospun fiber mats of PVDF/BaTiO<sub>3</sub> nanocomposites were studied [10]. By SEM analysis the prepared fibers were noticed to be well grown in random directions with diameter from 200 – 400 nm. The XRD study revealed the presence of both  $\alpha$  and  $\beta$  phases in PVDF whereas enhanced  $\beta$  phase was noticed in PVDF/BaTiO<sub>3</sub> sample. Further, the thermal emissivity was studied for both the samples and found to be reduced for the PVDF/BaTiO<sub>3</sub> sample. An approach of controlled morphology of barium titanate nanofibers has been reported [11]. The prepared nanofibers were investigated and observed to be polycrystalline in nature. The morphology was found to be ribbon-like form with their diameter and grain size 200 and 30 nm respectively. BaTiO<sub>3</sub> fibrils were obtained with the increased precursor with their diameter below 50 nm while the morphology was the same as ribbon-like. Further, fibers calcined at temperature 700 °C were observed to be in tetragonal phase as identified by XRD analysis. BaTiO<sub>3</sub> nanofibers calcined at temperature at 750 °C showed the fibers diameter from 80 – 190 nm [12]. This investigation was claimed to the stand-alone formation of ferroelectric nanofibers.

Here, we present the fabrication and characterization of BaTiO<sub>3</sub> nanofibers prepared at two distinct dc voltages (8 and 12 kV). In Section 2, the experimental approach is presented and the obtained results are discussed in Section 3. Finally, the work is summarized in Section 4.

## 2. Experimental approach

The chemicals, titanium-IV butoxide (TBOT), polyvinylpyrrolidone (PVP with m.wt. 1300000), barium acetate, ethyl alcohol and glacial acetic acid were procured and used without additional purification. To prepare the barium titanate ( $\text{BaTiO}_3$ ) solution, the following sol-gel process was carried out. For the preparation of solution 'S1', 2 g barium acetate was added in 5 ml acetic acid and kept for stirring for few minutes. Later, 3 ml titanium (IV) butoxide was drop-wise added to the above solution and stirred for 1 hr. In a similar way, 0.5 g polyvinylpyrrolidone was added in 5 ml ethanol and stirred for 30 min to get the solution 'S2'. Finally, both the solutions (S1 and S2) were mixed under constant stirring for few hrs. After observing the homogeneous and viscous solution, the prepared solution was loaded in syringe for the electrospinning process. The electrospinning process is summarized in Fig. 1. The drum collector was used to collect the electrospun mat while the DC voltage was applied in between the drum collector and the metal tip at room temperature while maintain humidity 40 %.

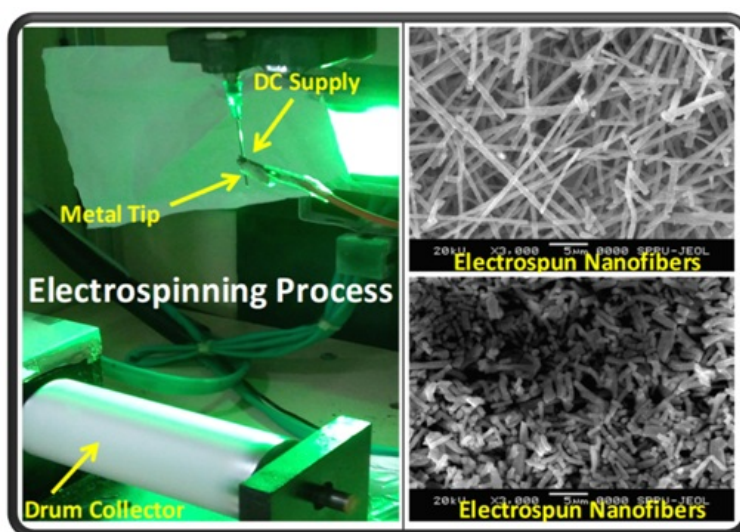


FIG. 1. Preparation of nanofibers by electrospinning method

For the preparation of nanofibers, two distinct dc voltages 8 and 12 kV were evaluated while the solution flow rate and distance jet-collector drum were maintained to 1 ml/h and 10 cm respectively. After electrospinning process, the collected samples were calcined at 600 °C for 1 hr.

The samples prepared at 8 and 12 kV voltages were named as BT1 and BT2 respectively and characterized to examine the phase and crystallinity by X-ray Diffraction (XRD-Bruker AXS D8 Advance, Germany), the qualitative and quantitative analysis by Fourier-transform infrared spectroscopy (FTIR-Shimadzu, Japan), thermal response by thermogravimetric differential thermal analysis (TG-DTA, DTG-60H, Shimadzu), the surface morphology by scanning electron microscope (SEM, JSM-6360, USA) and the elemental composition investigation by EDX attached to SEM.

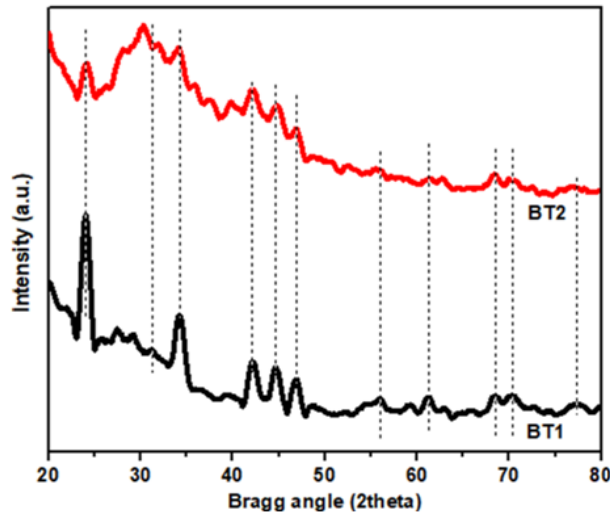
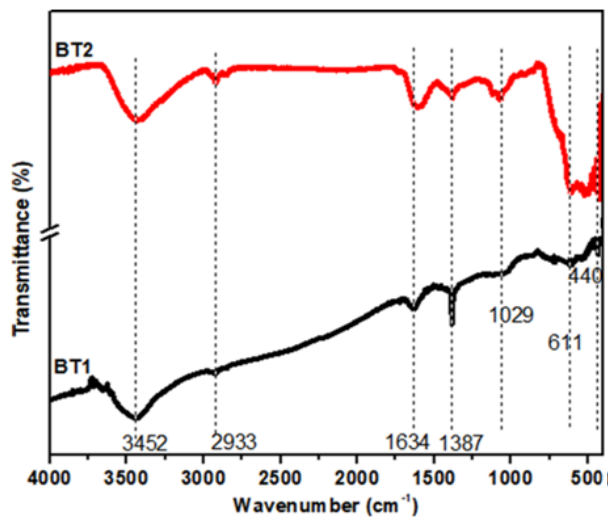
## 3. Results and discussion

X-ray diffraction (XRD) patterns of samples BT1 and BT2 were recorded in the range  $2\theta = 20 - 80^\circ$ , which is plotted in Fig. 2. As the calcination temperature was maintained at 600 °C for 1 h therefore, the diffraction peaks at  $2\theta = 24.1^\circ, 27^\circ, 42^\circ, 47^\circ$  and  $56^\circ$  reveal the presence of orthorhombic phase of  $\text{BaCO}_3$  in both the samples and matched with the JCPDS#45-1471) [9, 11]. In addition, peaks at  $2\theta = 31^\circ$  and  $45^\circ$  are found to be associated with the tetragonal phase which are assigned to the planes (101) and (002) according to JCPDS#05-0626.

To know the chemical bonds, FTIR measurements were carried out for both the samples and results are plotted in Fig. 3. The peaks at wavenumbers  $3434$  and  $2933 \text{ cm}^{-1}$  are assigned to the O-H and C-H stretching vibrations respectively [11].

A vibration peak corresponding to C-H stretching can be observed from  $2923 - 2853 \text{ cm}^{-1}$  [13]. Other vibration peaks related to C=O and C-C can also be observed at  $1634$  and  $1387 \text{ cm}^{-1}$  respectively. For the BT1 sample, a small peak nearly at  $570 \text{ cm}^{-1}$  is associated with the stretching vibration of Ti-O, however, the peak position was shifted to a slightly higher value for the case of sample BT2 prepared at increased dc voltage [13].

To investigate the morphology of  $\text{BaTiO}_3$ , both samples BT1 and BT2 were characterized using scanning electron microscopy (SEM). Both the images shown in Fig. 4(a and b) depicts the uniform and homogeneous growth of  $\text{BaTiO}_3$

FIG. 2. XRD patterns of electrospun BaTiO<sub>3</sub> nanofibersFIG. 3. FTIR spectra of electrospun BaTiO<sub>3</sub> nanofibers

nanofibers. As compared to BT1 sample prepared at 8 kV, BT2 endorses the smooth and well aligned growth of the nanofibers. The average diameters of the BT1 and BT2 were found to be 515 and 472 nm respectively. The decreased diameter of the BT2 sample is attributed to the increased applied voltage which could enhance the rapid evaporation of the solvent [14].

The thermal behavior of as-prepared PVP-BaTiO<sub>3</sub> mat was studied by thermogravimetric & differential thermal analysis (TG/DTA) measurements which is plotted in Fig. 5. Referring to TG curve, the trend of the curve below 200 °C indicates the elimination of the water and solvent contents. Another trend of weight loss between 250 °C and 400 °C can be observed which is regarded the decomposition of the used polymer and acetate molecules [13]. Further, the weight loss in between 600 – 700 °C is noticed which is associated with the decomposition of organic groups. At temperature 725 °C, the weight loss was ended with maximum of 49 % of the total weight. In a similar way, DTA analysis reveals an endothermic peak at 300 °C related to the evaporation of the unwanted contents like water/solvent.

The exothermic peaks at 359 °C and 468 °C is attributed to the decomposition of barium acetate while peak corresponding to the decomposition of the main chain of PVP is also observed at 624 °C. Furthermore, at 725 °C the presence of the organic groups was eliminated.

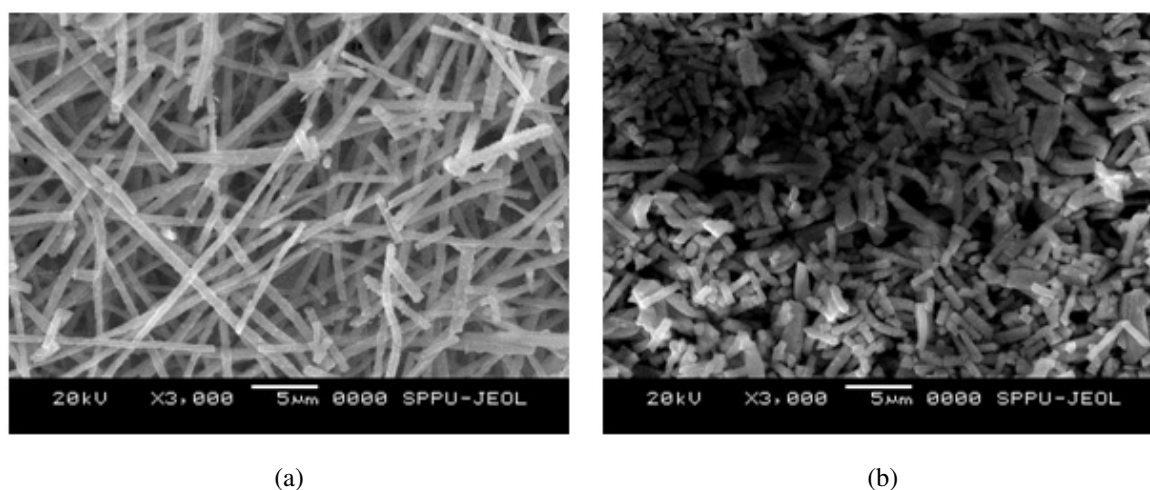


FIG. 4. SEM image of BT1 and BT2 samples prepared at 8 and 12 kV dc voltages respectively

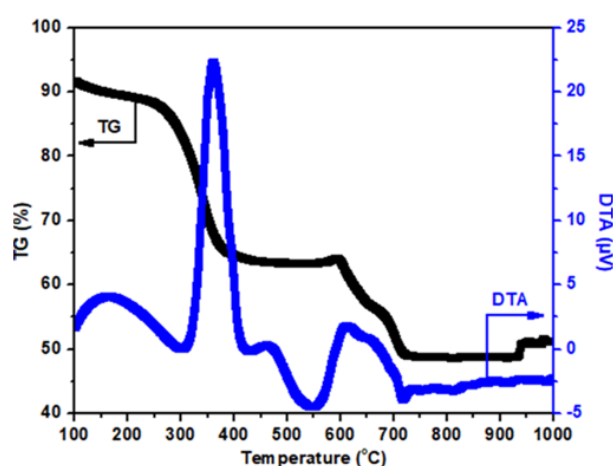


FIG. 5. TG/DTA curves of electrospun BaTiO<sub>3</sub> nanofibers

#### 4. Conclusion

We have presented the preparation and characterization of electrospun BaTiO<sub>3</sub> nanofibers at two distinct voltages, 8 and 12 kV. The XRD pattern endorses the formation of the tetragonal phase in both the samples BT1 and BT2. FTIR investigation showed the various vibration peaks including Ti–O bond in between 570 – 600 cm<sup>-1</sup>. SEM measurement evidenced the decreased diameter of the BaTiO<sub>3</sub> nanofibers with the increased dc voltage. The TG/DTA investigation revealed the various temperature regions associated with the decomposition of BaTiO<sub>3</sub>-PVP mat and finally, the weight loss was vanished with 49 % loss of the total weight at temperature 725 °C.

#### Acknowledgements

Authors are thankful to Prof. M. A. More (University of Pune) for the provided accessibility of the characterization facilities.

## References

- [1] Ávila H.A., Reboredo M.M., Castro M., Parra R. Nanofibers obtained by electrospinning of BaTiO<sub>3</sub> particles dispersed in polyvinyl alcohol and ethylcellulose. *Materials Research*, 2013, **16** (4), P. 839–843.
- [2] Zhuang Y., Li F., et al. Fabrication and Piezoelectric Property of BaTiO<sub>3</sub> Nanofibers. *J. Am. Ceram. Soc.*, 2014, **1**, P. 1–6.
- [3] Suaste-Gomez E., Rodriguez-Montoya C., et al. Preparation of Nanoporous Fibers of BaTiO<sub>3</sub> via Electrospinning of BaTiO<sub>3</sub>/PVC and Thermal Treatment Effects. *Ferroelectrics*, 2015, **482**, P. 1–10.
- [4] Yan Wei, Yu Song, et al. Dielectric and Ferroelectric Properties of BaTiO<sub>3</sub> Nanobers Prepared via Electrospinning. *J. Mater. Sci. Technol.*, 2014, **30** (8), P. 743–747.
- [5] *Electrospun Nanofibers*, First Edition, ed. Mehdi Afshari, Woodhead Publishing, United Kingdom, 2016, 648 p.
- [6] Deuk Yong Lee, Myung-Hyun Lee, et al. Effect of Calcination Temperature and Atmosphere on Crystal Structure of BaTiO<sub>3</sub>. *Nanofibers, Met. Mater. Int.*, 2010, **16** (3), P. 453–457.
- [7] Avinash Baji, Mojtaba Abtahi. Fabrication of barium titanate-bismuth ferrite using electrospinning. *Advances in Nano Research*, 2013, **1** (1), P. 183–192.
- [8] Lijie Wang, Yaun He, et al. Dc Humidity sensing properties of BaTiO<sub>3</sub> nanofiber sensors with different electrode materials. *Sensor and Actuator B*, 2011, **115**, P. 460–464.
- [9] Xiong Z.X., Pan J., et al. Preparation and properties of BaTiO<sub>3</sub> ceramic fibers for ferroelectric applications. *Ferroelectrics*, 2014, **466**, P. 29–35.
- [10] Chetan Vishnu Chanmal, Jyoti Prakash Jog. Electrospun PVDF/BaTiO nanocomposites: polymorphism and thermal emissivity studies. *Int. J. Plast. Technol.*, 2011, **15** (1), P. S1-S9.
- [11] McCann T., Chen J.L.L., et al. Electrospinning of polycrystalline barium titanate nanobers with controllable morphology and alignment. *Chemical Physics Letters*, 2006, **424**, P. 162–166.
- [12] Yuh J., Nino J.C., Sigmund W.M. Synthesis of barium titanate (BaTiO<sub>3</sub>) nanofibers via electrospinning. *Materials Letters*, 2005, **59**, P. 3645–3647.
- [13] Sahoo B., Panda P.K. Preparation and characterization of barium titanate nanofibers by electrospinning. *Ceramics Int.*, 2012, **8** (6), P. 5189–5193.
- [14] Someswararao M.V., Dubey R.S., Subbarao P.S.V., Singh S. Electrospinning process parameters dependent investigation of TiO<sub>2</sub> nanofibers. *Results in Physics*, 2018, **11**, P. 223–231.

## Morphological and optical properties of dielectric multilayer structures prepared with distinct precursor concentrations

Venkatesh Yepuri<sup>1,2</sup>, R. S. Dubey<sup>1\*</sup>, Brijesh Kumar<sup>2</sup>

<sup>1</sup>Department of Nanotechnology, Swarnandhra College of Engineering and Technology, Seetharampuram, Narsapur (A.P.), India

<sup>2</sup>Amity Institute of Nano Science and Technology, Amity University, Gurgaon, (Haryana), India  
rag\_pcw@yahoo.co.in

DOI 10.17586/2220-8054-2019-10-3-355-360

For optical filters, TiO<sub>2</sub> and SiO<sub>2</sub> films are better choices due to their large refractive index contrast. In spite of the various available techniques, the sol-gel spin coating method is one of the easiest and inexpensive technique. Here, we report the experimental studies of (TiO<sub>2</sub>/SiO<sub>2</sub>)<sub>2.5</sub> bilayer-based structures prepared with two distinct precursor concentrations. FTIR analysis showed the characteristic vibration peaks of the Ti-O-Ti and Si-O-Si bonds. XRD measurements of both the samples based on the low and high-precursor concentrations, revealed the dominant peaks of TiO<sub>2</sub>-anatase phase. FESEM study endorsed the increased thicknesses of the individual layers due to enhanced precursor concentrations. Both samples evidenced for the reflection/stop bands with 100% reflectivity. Furthermore, multilayer structure of (TiO<sub>2</sub>/SiO<sub>2</sub>)<sub>2.5</sub> bilayers showed the corresponding shift of the reflection band from the visible-infrared wavelength region in accordance with the low-high precursor concentration. This shifting of the reflection band is attributed to the increased thicknesses of the films which is due to the enhanced grains size as confirmed by the AFM studies.

**Keywords:** reflectors, multilayers structures, cross-section SEM morphology, precursor concentration.

*Received: 4 February 2019*

*Revised: 18 April 2019*

### 1. Introduction

Dielectric multilayer structures are the choice of passive components in optoelectronic and photonic devices. These passive components are promising for the manipulation of light in an efficient manner. Multilayer structures, composed of two distinct materials, have been investigated as the stop band filters in the design and fabrication of solar cells, waveguide, micro cavities etc. [1–6]. Such multilayer structures can be prepared by either of the techniques, such as chemical vapor deposition, electrodeposition, sputtering and sol-gel spin coating process [7–9]. Among aforementioned techniques, the sol-gel spin coating process is inexpensive and has advantages to tune the film properties by manipulating the synthesis parameters. For these dielectric mirrors or reflectors, titanium dioxide (TiO<sub>2</sub>) and silicon dioxide (SiO<sub>2</sub>) are the best chosen materials due to their high and low refractive indices respectively and therefore, such multilayers structures offer high refractive index contrast which is the primary need to possess the reflection band in the specified wavelength range [10]. The properties of films can be modulated by sol reactivity, viscosity, water alkoxide ratio, solution pH, catalyst etc. [11–13]. Further, spin coating parameters such as spin speed and time including calcination temperature plays a vital role for the film deposition.

Sang Hun Nam et al. studied the growth mechanism of hydrophilic TiO<sub>2</sub> thin films by changing the precursor temperatures. The preferred calcination temperature was 500°C whereas the process temperatures were maintained to 75° and 60°C for the deposition. The film prepared at precursor temperature 60°C showed transmittance about 77% in the wavelength from 400–700 nm with the low contact angle due to super-hydrophilic nature of TiO<sub>2</sub> surface. However, films deposited at precursor temperature below 50°C or greater than 75°C were not satisfactory [14]. S. Sali et al. synthesized the nanocrystalline TiO<sub>2</sub> thin films on planar and textured quartz and silicon substrates by spray pulverization method. The aim of this study was to explore the anti-reflective properties prepared at different temperatures using XRD, FTIR, Raman and UV-Vis. The film deposited on the textured substrate showed the better properties with its 80% transmittance, 15–9 nm grains size, 3.28–3.38 eV band gap, and 2.19–2.39 refractive index. The coatings thicknesses and refractive indices could be controlled to exhibit optimal optical properties for the solar cells [15]. H. Sedrati et al. presented the structural and optical properties of SiO<sub>2</sub>/TiO<sub>2</sub> alternating layers by sol-gel dip-coating process. The prepared multilayers were characterized for XRD, FTIR, SEM and UV-Vis spectroscopy. SEM analysis revealed the deposition of homogeneous layers of SiO<sub>2</sub> and TiO<sub>2</sub>. By FTIR measurement, the vibration of Si-O-Ti bond was confirmed, however, the transmittance of the multilayer was found to be decreased from 4.58% to 0.55%, as shown by UV-Vis spectroscopy study [16]. H. H. Nguyen et al. studied the effect of precursor concentration on TiO<sub>2</sub> thin film nanostructure using plasma chemical vapor deposition (PCVD) system. They reported the granular

morphology in the prepared sample with the low concentration of titanium tetra-isopropoxide (TTIP) and the columnar morphology with the increased TTIP concentration. SEM analysis showed the granular and columnar shapes with the particles size 20, 60 and 100 nm [17].

In this paper, we report the morphological and optical properties of the dielectric mirrors consisting of two and half  $\text{TiO}_2/\text{SiO}_2$  bilayers using a simple and inexpensive chemical method. This study explores the effect of precursor concentrations upon the deposited multilayer structures. Section second describes the experimental approach and the results are discussed in section third. Finally, the work is summarized in section four.

## 2. Experimental

The as-procured chemicals, titanium isopropoxide (TTIP), tetraethyl orthosilicate (TEOS), ethanol ( $\text{C}_2\text{H}_5\text{OH}$ ), deionized water (DI) and hydrochloric acid (HCl) were used without any purification. Various sol-gel processes were carried out as described here. For the preparation of low-precursor based solutions of  $\text{TiO}_2$  and  $\text{SiO}_2$ ,  $\text{C}_2\text{H}_5\text{OH}:\text{DI}:\text{TTIP}:\text{HCl}$  and  $\text{C}_2\text{H}_5\text{OH}:\text{DI}:\text{TEOS}:\text{HCl}$  in the molar ratios of 20:1:1:0.02 and 20:1:1:0.02 respectively were used. In a similar way, for the preparation of high-precursor based solutions of  $\text{TiO}_2$  and  $\text{SiO}_2$  the volume of TTIP and TEOS was increased to 1.5 ml. All the solutions were aged for 24 hr and later spin coated on the glass substrates in the sequence  $\text{TiO}_2/\text{SiO}_2$  films. Before the spin coating process, the glass substrates were sonicated in ethanol and rinsed with deionized water. The spin speed was maintained to 3000 RPM for 30 sec. After spin coating, each films were thermally treated over the period of 30 min to remove the volatile solvents. Finally,  $\text{TiO}_2$  films were calcined for 60 min at temperature  $500^\circ\text{C}$  while  $300^\circ\text{C}$  was maintained for the  $\text{SiO}_2$  films.

The prepared bilayers were characterized for phase identification using X-ray diffraction (Bruker D8 Advance), chemical bond analyses by Fourier transform infrared (FTIR) spectroscopy (Bruker Vertex 70) surface topography by atomic force microscopy (AFM: Nanoscope -NSE in contact mode), surface morphology by field-emission scanning electron microscopy (FESEM: ZIESS) and reflectance study by ultraviolet-visible (UV-vis) spectrophotometer with a specular reflectance attachment (UV1800 Shimadzu).

## 3. Results and discussion

The multilayer structures of  $(\text{TiO}_2/\text{SiO}_2)_{2.5}$  bilayer prepared with low and high-precursor concentrations were studied for the investigation of phase identification. Fig. 1 depicts the XRD pattern of  $(\text{TiO}_2/\text{SiO}_2)_{2.5}$  bilayer prepared with low and high precursor concentrations. The diffraction peaks were found corresponding to the pure anatase phase; however, a rutile peak was also observed for the sample prepared with high-precursor concentrations. The diffraction peaks were assigned to planes (101), (112), (200), (211) and (204) located at  $2\theta = 25^\circ, 38^\circ, 48^\circ, 55^\circ$  and  $62^\circ$  respectively for both the cases. However, an additional peak located at  $2\theta = 27^\circ$  was also found corresponding to the presence of rutile phase. The XRD patterns of both the samples are well matched with JCPDS#21-1272 and JCPDS#21-1276 which corresponds to the anatase and rutile phases of  $\text{TiO}_2$ . One can also notice the broadening of anatase  $\text{TiO}_2$  peak corresponding to the plane (101) in both the samples which is assumed to be associated with the amorphous nature of  $\text{SiO}_2$  layer beneath the top  $\text{TiO}_2$  layer [15].

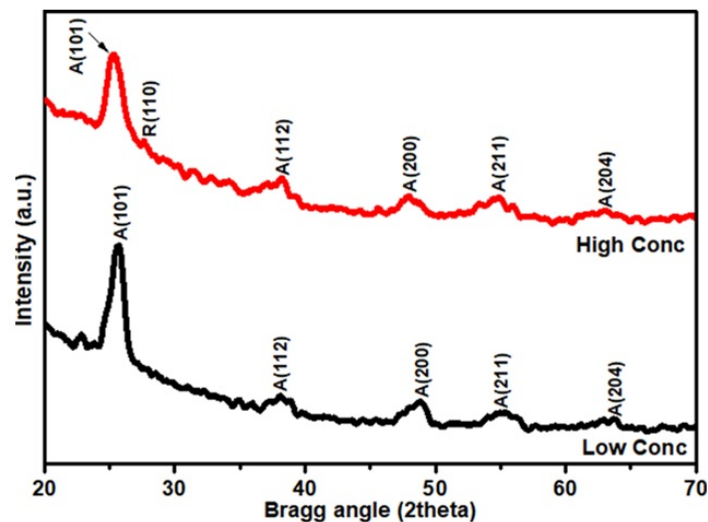


FIG. 1. XRD patterns of  $(\text{TiO}_2/\text{SiO}_2)_{2.5}$  bilayer prepared with low and high-precursor concentrations

Figure 2 depicts the FTIR spectra of  $(\text{TiO}_2/\text{SiO}_2)_{2.5}$  bilayers prepared with the low and high- precursor concentrations of TTIP and TEOS respectively. The region from  $600\text{--}900\text{ cm}^{-1}$  corresponds to the stretching vibrations of the Ti–O–Ti and Ti–O bonds.

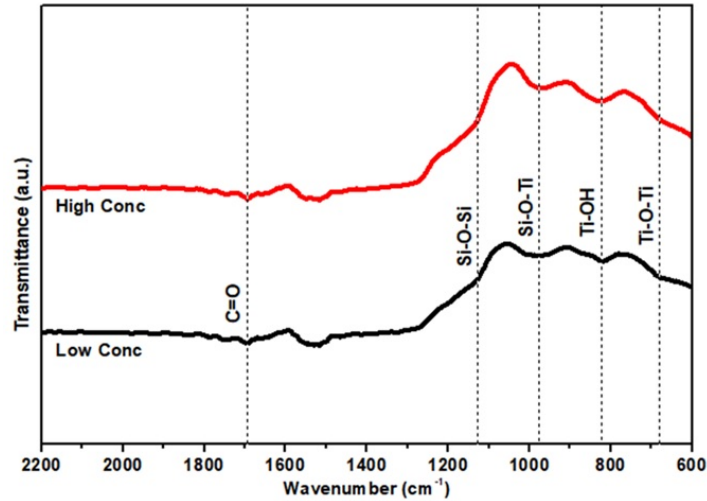


FIG. 2. FTIR spectra of  $(\text{TiO}_2/\text{SiO}_2)_{2.5}$  bilayer prepared with low and high-precursor concentrations

We can observe a peak located at around  $968\text{ cm}^{-1}$  which represents the vibration of Si–O–Ti bond. The peak corresponding to the stretching vibration mode of Si–O–Si is found located at  $1128\text{ cm}^{-1}$ . However, the peak originated at  $1742\text{ cm}^{-1}$  is associated with the carbonyl bond C=O which could be attributed to the non-hydrolytic sol-gel reaction of used acid and TTIP precursor. These vibration peaks coincide with the reported works [15, 16]. The trend of the FTIR curves is almost identical the samples which were prepared with low and high- precursor concentrations.

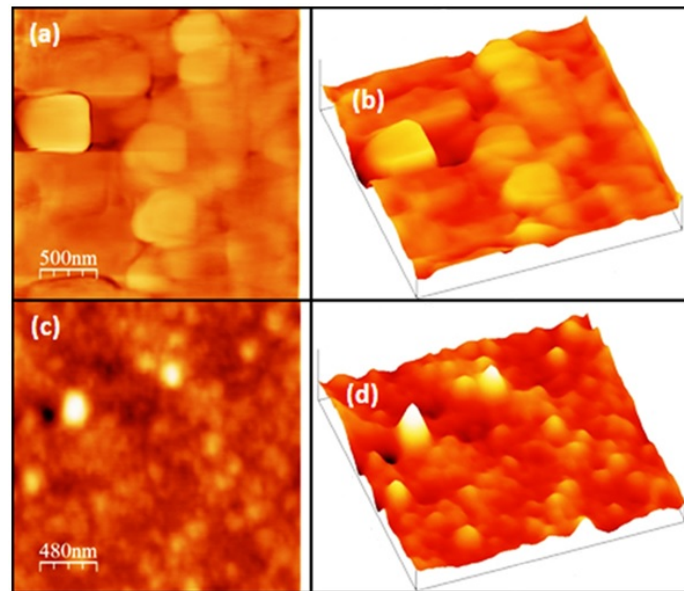


FIG. 3. AFM images of  $(\text{TiO}_2/\text{SiO}_2)_{2.5}$  bilayer prepared with the high (a,b) and low-precursor (c,d) concentrations

To study the surface topography, we have performed the atomic force microscopy analysis of both the samples. Fig. 3 shows the AFM images of  $(\text{TiO}_2/\text{SiO}_2)_{2.5}$  bilayers prepared with the low and high-precursor concentrations. Referring to Fig. 3(a and b), one can see the bigger grain size with their average size  $362\text{ nm}$  corresponds to the sample prepared with high-TTIP concentration. But for the case of low-precursor concentration based sample, a decreased average grains size  $104\text{ nm}$  can be noticed as depicted in Fig. 3(c and d). Similar, enhanced grains size

with the increased precursor concentrations has been reported [16–18]. The high precursor concentration led to bigger crystallite size as a results increased grain size was observed. In addition, plate shape grains were also noticed which could be associated with the defects.

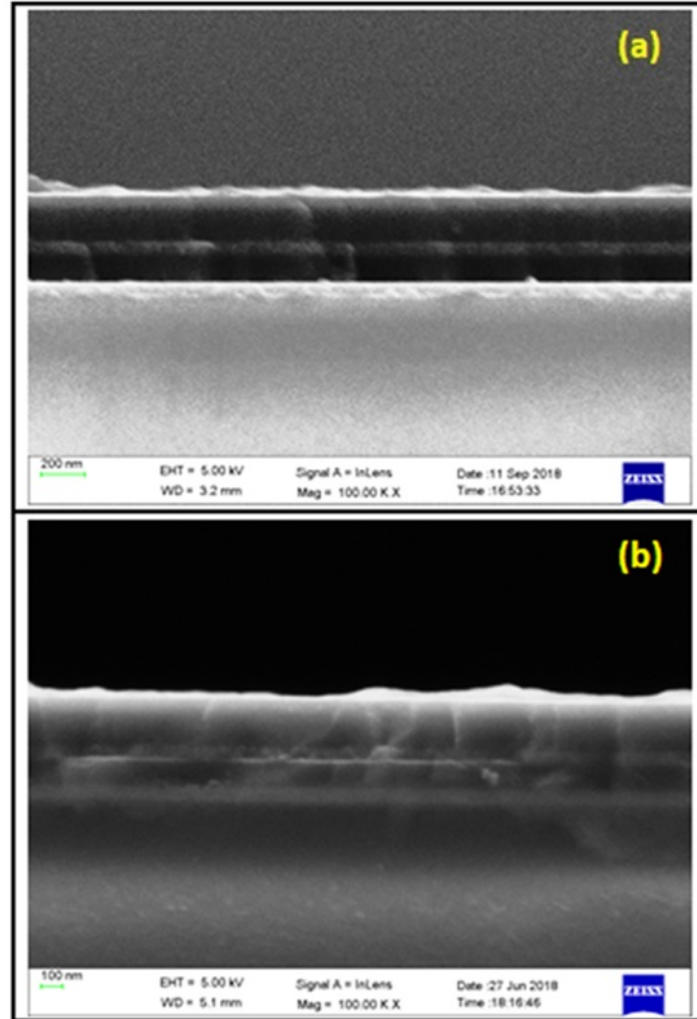


FIG. 4. Cross-section FESEM images of  $(\text{TiO}_2/\text{SiO}_2)_{2.5}$  bilayer prepared with low (a) and high (b) precursor concentrations

One-dimensional periodic structure of  $\text{TiO}_2/\text{SiO}_2$  films can be observed in Fig. 4. As depicted in Fig. 4(a), the low-precursor based sample shows the distinguished layers of  $\text{TiO}_2$  (brighter) and  $\text{SiO}_2$  (darker) films as compared to Fig. 4(b) which shows the disturbed interfaces of the top two films of  $\text{TiO}_2$  and  $\text{SiO}_2$ . In addition, the enhanced precursor concentrations disclose the disturbed surface morphology as observable in Fig. 4(b). For the case of low-precursor concentrations, the thicknesses of the  $\text{TiO}_2$  and  $\text{SiO}_2$  films (from bottom) were 51, 95, 68, 118 and 58 nm whereas 60, 103, 70, 130 and 67 nm respectively for the high-precursor concentrations based sample.

The prepared Bragg mirrors were studied for the reflectance from the range of ultra-violet to infrared wavelength as shown in Fig. 5. We can clearly observe the appearance of reflection windows (stop bands) from wavelength 552–958 nm and 545–1100 nm for the multilayer structures prepared with the low and high-precursor concentrations respectively. Both samples exhibit as much as 100% reflectance. As compared to previously reported works, visible reflectors consisting of 7 bilayers of  $\text{TiO}_2/\text{SiO}_2$  were prepared by Anaya et al., Dubey et al. and Zhou et al. along with the 10 bilayer based structure reported by Dhruv et al, our samples show the better results only with 2.5 bilayers [19–22]. In addition, previously reported results were limited to their reflectance in visible wavelength region whereas our 2.5 bilayers based samples show the reflectance in the infrared region. In this way, our preparation of such multilayer reflectors reduces the efforts, time and the fabrication cost Remarkably, the reflection band for the case of the sample prepared at high-precursor concentrations shifted towards the further infrared wavelength. This shifting of

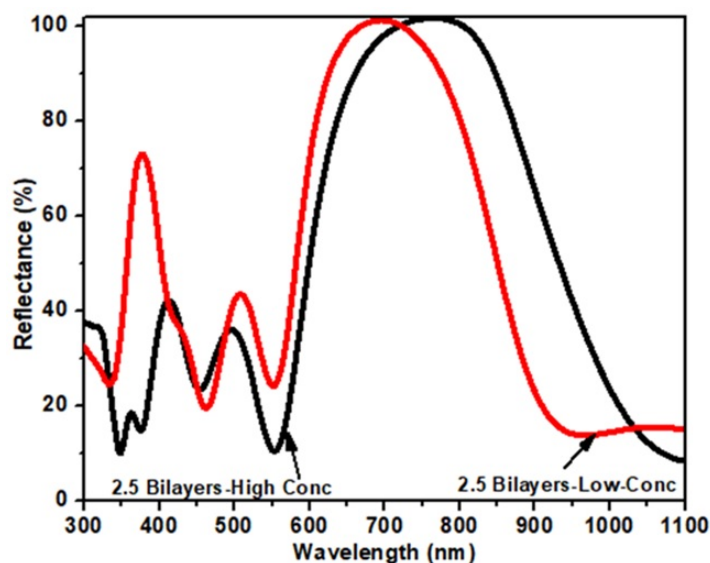


FIG. 5. Reflectance spectra of  $(\text{TiO}_2/\text{SiO}_2)_{2.5}$  bilayer prepared with low and high-precursor concentrations

the reflection band is attributed to the increased grains size as observed in Fig. 3, due to which the thickness of the individual films were also increased as seen in Fig. 4. The center wavelengths of the Bragg mirrors prepared with low and high-precursor concentrations were found to be at 720 and 764 nm respectively.

#### 4. Conclusion

Multilayer structures of  $(\text{TiO}_2/\text{SiO}_2)_{2.5}$  bilayers fabricated by the sol-gel spin coating method have been studied. XRD measurement endorsed the dominant peaks of the anatase phase of  $\text{TiO}_2$ . However, the broadening of predominant peak of the plane (101) was also noticed which could be associated with the amorphous nature of the  $\text{SiO}_2$  film fabricated beneath the top  $\text{TiO}_2$  film. FTIR investigation showed the corresponding vibration stretching peaks for the Ti–O–Ti, Si–O–Si and Ti–O–Si bonds. By AFM measurement, the estimated average grains size of the 5 layer- $\text{TiO}_2/\text{SiO}_2$  films were 104 and 362 nm for the samples prepared with low and high-precursor concentrations respectively. FESEM study endorsed the fabrication of five-alternate films of  $\text{TiO}_2$  and  $\text{SiO}_2$ . The thicknesses of the individual films were observed to be increased as compared to films prepared with the low-precursor concentrations. This increment is attributed to the increased grains size as evidenced by the AFM measurement. The reflectance of both the samples is found to be satisfactory in terms of the Bragg mirrors from the visible-infrared wavelength region. The center wavelengths of the Bragg mirrors were 720 and 764 nm corresponding to the samples prepared with low and high-precursor concentrations respectively. With the increased precursor concentrations, the reflection band is observed to be shifted towards the near-infrared region. This shifting of reflection band is attributed to the increased grain size which is due to the high-precursor concentrations. Finally, the Bragg mirrors of  $(\text{TiO}_2/\text{SiO}_2)_{2.5}$  bilayers fabricated by the simple process demonstrated the broad reflectance band in the visible-infrared wavelength range.

#### Acknowledgements

We acknowledge the financial support provided by the UGC-DAE CSR, Indore (India).

#### References

- [1] Tikhonravov A.V. Some theoretical aspects of thin-film optics and their applications. *Applied Optics*, 1993, **32**, P. 5417–5426.
- [2] Schock H.W. Thin film photovoltaics. *Applied Surface Science*, 1996, **92**, P. 606–616.
- [3] Dubey R.S., Ganesan V. Visible and near-Infrared wavelength selective dielectric reflectors for light management Applications. *Superlattices and Microstructures*, 2018, **122**, P. 228–234.
- [4] Joannopoulos J.D., et al. *Photonic crystals:molding the flow of light*. Princeton University Press, Princeton, 2-nd edn, 2008.
- [5] Chen K.M., Sparks A.W., Luan H.C., Lim D.R., Wada K., Kimerling L.C.  $\text{SiO}_2/\text{TiO}_2$  omnidirectional reflector and microcavity resonator via the sol-gel method. *Appl. Phys. Lett.*, 1999, **75**, P. 3805–3808.
- [6] Johnson D.C., Ballard I., Barnham K.W.J., Bishnell D.B., Connolly J.P., Lynch M.C., Tibbits T.N.D., Ekins-Daukes N.J., Mazzer M., Airey R., Hill G., Roberts J.S. Advances in Bragg stack quantum well solar cells. *Sol. Energy Mater. Sol. Cells*, 2005, **87**, P. 169–179.
- [7] Vossen J.L., Kern W. *Thin Film Processes II*. 1-st ed., Academic Press, San Diego, CA, 1991.

- [8] K.-Il Jang, Hong E., Kim J.H. Effect of an electrodeposited TiO<sub>2</sub> blocking layer on efficiency improvement of dye-sensitized solar cell. *Korean J. Chem. Eng.*, 2012, **29**, P. 356–361.
- [9] Chopra S., Sharma S., Goel T.C., Mendiratta R.G. Electrical and optical properties of sol-gel derived La modified PbTiO<sub>3</sub> thin films. *Appl. Surf. Sci.*, 2004, **236**, P. 321–327.
- [10] Gracia F., Yubero F., Holgado J.P., Espinós J.P., González-Elipé A.R., Girardeau T. SiO<sub>2</sub>/TiO<sub>2</sub> thin films with variable refractive index prepared by ion beam induced and plasma enhanced chemical vapor deposition. *Thin Solid Films*, 2006, **500**, P. 19–26.
- [11] Yang L.-L., Lai Y.-S., Chen J.S., Tsai P.H., Chen C.L., Chang C.J. Compositional tailored sol-gel SiO<sub>2</sub>-TiO<sub>2</sub> thin films: Crystallization, chemical bonding configuration and optical properties. *J. Mater. Res.*, 2005, **20**, P. 3141–3149.
- [12] Gauthier, Bourgeois S., Sibillot P., Maglione M., Sacilotti M. Growth and characterization of AP-MOCVD iron doped titanium dioxide thin films. *Thin Solid Films*, 1999, **340**, P. 175–182.
- [13] Sarah P., Saad M., Sutan H.B., Shariffudin S.S. TiO<sub>2</sub> thin film via sol-gel method: Investigation on molarity effect. *IOP Conf. Ser. Mater. Sci. Eng.*, 2015, **99**, P. 12006.
- [14] Sang-Hun Nam, Sang-Jin Cho and Jin-Hyo Boo. Growth behavior of titanium dioxide thin films at different precursor temperatures. *Nanoscale Res. Lett.*, 2012, **7**(89), P. 1-6.
- [15] Sedrati A.H., Bensaha R., Brahim M., Dehdouh H., Bensouyad H., Abbas F., Toubal B. Correlation between structural and optical properties of SiO<sub>2</sub>/TiO<sub>2</sub> multibilayers processed by sol-gel technique and applied to Bragg reflectors. *Materials Science An Indian Journal*, 2013, **9**(3), P. 113–118.
- [16] Sali S., Kermadi S., Zougar L., Benzaoui B., Saoula N., Mahdid K., Aitameur F., Boumaour M. Nanocrystalline properties of TiO<sub>2</sub> thin film deposited by ultrasonic spray pulverization as an anti-reflection coating for solar cells applications. *J. Elect. Eng.*, 2017, **68**, P. 24–30.
- [17] Nguyen H.H., Kim D.-J., Park D.-W., Kim K.-S. Effect of initial precursor concentration on TiO<sub>2</sub> thin film nanostructures prepared by PCVD system. *Journal of Energy Chemistry*, 2013, **22**, P. 375–381.
- [18] Lalchand A Patil, Dinesh N Suryawanshi, Idris G Pathan, Dhanashri G Patil. Effect of variation of precursor concentration on structural, microstructural, optical and gas sensing properties of nanocrystalline TiO<sub>2</sub> thin films prepared by spray pyrolysis techniques. *Bull. Mater. Sci.*, 2013, **36**(7), P. 1153–1160.
- [19] Miguel Anaya, Andrea Rubino, Mauricio E. Calvo and Hernan Miguez. Solution processed high refractive index contrast distributed Bragg reflectors. *J. Mater. Chem. C*, 2016, **4**, P. 453–4537.
- [20] Dubey R.S., Ganesan V. Fabrication and characterization of TiO<sub>2</sub>/SiO<sub>2</sub> based Bragg reflectors for light trapping applications Results in Physics, 2017, **7**, P. 2271–2276.
- [21] Shengjun Zhou, Haohao Xu, Mengling Liu 1,2, Xingtong Liu, Jie Zhao, Ning Li and Sheng Liu, Effect of Dielectric Distributed Bragg Reflector on Electrical and Optical Properties of GaN-Based Flip-Chip Light-Emitting Diodes. *Micromachines*, 2018, **9**, P. 650.
- [22] Dhruv Pratap Singh, Seung Hee Lee, Il Yong Choi, and Jong Kyu Kim. Spatially graded TiO<sub>2</sub>-SiO<sub>2</sub> Bragg reflector with rainbow-colored photonic band gap. *Optics Express*, 2015, **23**(13), P. 17568–17575.

## Structure and photoluminescent properties of $\text{TiO}_2\text{:Eu}^{3+}$ nanoparticles synthesized under hydro and solvothermal conditions from different precursors

A. Yu. Zavalova<sup>1,2</sup>, A. N. Bugrov<sup>1,3</sup>, R. Yu. Smyslov<sup>3,4</sup>, D. A. Kirilenko<sup>5,6</sup>,  
T. V. Khamova<sup>7</sup>, G. P. Kopitsa<sup>7,8</sup>, C. Licitra<sup>9</sup>, D. Rouchon<sup>9</sup>

<sup>1</sup>Saint Petersburg Electrotechnical University “LETI”, ul. Professora Popova 5, 197376 Saint Petersburg, Russia

<sup>2</sup>Saint-Petersburg State Institute of Technology (Technical University), Moskovsky prospect 26,  
Saint Petersburg, 190013, Russia

<sup>3</sup>Institute of macromolecular compounds RAS, Bolshoy pr. 31, 199004 Saint Petersburg, Russia

<sup>4</sup>Peter the Great Saint Petersburg Polytechnic University, Polytechnicheskaya 29, 195251 Saint Petersburg, Russia

<sup>5</sup>Ioffe Institute RAS, Politekhnicheskaya ul. 26, 194021 Saint Petersburg, Russia

<sup>6</sup>ITMO University, 197101, Kronverskii avenue 49, Saint Petersburg, Russia

<sup>7</sup>Grebenshchikov Institute of Silicate Chemistry RAS, Makarova nab. 2., letter B, 199034 Saint Petersburg, Russia

<sup>8</sup>Petersburg Nuclear Physics Institute, NRC KI, Orlova roscha mcr. 1, 188300, Gatchina, Leningrad region, Russia

<sup>9</sup>University Grenoble Alpes, CEA, LETI, F-38000 Grenoble, France

zavalova.a.y@gmail.com, alexander.n.bugrov@gmail.com, urs1968@gmail.com, demid.kirilenko@mail.ioffe.ru,  
tamarakhamova@gmail.com, kopitsa\_gp@npni.nrcki.ru, christophe.licitra@cea.fr, denis.rouchon@cea.fr

**PACS 78.67. n; 78.67.Bf**

**DOI 10.17586/2220-8054-2019-10-3-361-373**

Crystalline phosphors of  $\text{Eu}^{3+}$ -doped titania ( $\text{TiO}_2\text{:Eu}^{3+}$ ) were prepared by hydro and solvothermal synthesis with luminescent ion concentration of 2 mol.%. The structure and shape of the synthesized nanoparticles were characterized using X-ray powder diffraction, transmission electron microscopy, and Raman spectroscopy. Changes in the emission, excitation spectra, and the intensity decay of the photoluminescence for  $\text{TiO}_2\text{:Eu}^{3+}$  nanoparticles were analyzed their phase composition. The photoluminescence of synthesized  $\text{TiO}_2\text{:Eu}^{3+}$  crystalline phosphors depends on whether the said nanophosphors are formed from organometallic or inorganic precursors under hydro- and solvothermal conditions. Indeed, photoluminescence excitation at wavelengths ranging from 350–550 nm leads to splitting of electron dipole transitions into Stark components according to the symmetry of the  $\text{Eu}^{3+}$  surroundings. Also, both nanoparticles with the anatase structure and phosphors predominantly containing rutile showed very short photoluminescence lifetimes.

**Keywords:** hydrothermal synthesis, titania, europium, solid solution, anatase, rutile, nanophosphors, photoluminescence, fluorescence lifetime.

*Received: 18 June 2019*

### 1. Introduction

The phosphors with lanthanide ions as photoluminescence centers are promising materials that have been used in artificial lighting sources [1], cathode ray tubes [2], emission displays [3], solid-state lasers [4], fluorescent probes [5] and biomedical devices [6, 7]. The luminescent properties of such emitting materials depend on the efficiency of energy transfer from the absorption center (ligand) to the emission center (lanthanide ion) and on the concentration of quenchers (OH groups) surrounding photoactive ions [8]. Europium (III) ions are most often used as photoactive centers due to their intensive well-distinguishable luminescence at a wavelength of 630 nm, long luminescence lifetime and sensitivity to the symmetry of the local environment [9, 10]. Luminescence of  $\text{Eu}^{3+}$  ions can be effectively sensitized by the energy transfer from the excited host matrix to the photo active center as a result of allowing the  $4f-4f$  absorption transitions by electric dipole mechanism, these transitions forbidden between the states with the same parity according to the Laporte’s rule in the “pure” state (without influence of a ligand-field under non-centrosymmetric interactions) [11, 12].

As a rule, structures of both organic and inorganic origin with high transparency in the wavelength range of interest and low phonon energy act as the host material [13]. Organic ligands, including polymeric ones, can bind  $\text{Eu}^{3+}$  and efficiently luminesce [14, 15]. However, it was noted in the literature that organic compounds, such as terpyridine complexes, complexes of picric acid and n-methyl caprolactam, serving as antenna sensitizers for  $\text{Eu}^{3+}$  ions, have a significant drawback, namely low photostability [16]. Oxides, sulfides, phosphates, and fluoride nanocrystals doped with  $\text{Eu}^{3+}$  are a promising alternative to organic phosphors. Compared with the latter, inorganic nanoparticles doped with  $\text{Eu}^{3+}$  exhibit unique luminescent properties, such as large anti-Stokes shifts, long fluorescence lifetimes, narrow emission bands, high resistance to photobleaching [17–20].

Recently, oxide matrices have become the most popular due to their high optical and semiconductor properties [21]. The broad band gap, high refractive index, and transparency in the ultraviolet and visible ranges of oxide nanoparticles provide a high luminescence quantum yield for  $\text{Ln}^{3+}$  ions embedded in their structure [22]. Among metal oxide crystal structures, titania should be distinguished, which fully complies with all the above characteristics [23]. The band gap of  $\text{TiO}_2$  depends on the structure, and for anatase, rutile, and brookite modifications, it is 3.25, 3.0, and 1.9 eV, respectively [24]. Anatase and rutile can be obtained in pure form and differ in the lengths of the Ti – O and Ti – Ti bonds, which determines the direction of crystal growth along the axis corresponding to the longest bond length (001 plane in anatase and 110 in rutile). Therefore, rutile  $\text{TiO}_2$  modification is most often obtained in an acidic medium or in the presence of surfactants that block the crystallization process of the 001 plane [25]. Introduction to the titania structure of  $\text{Eu}^{3+}$  ions, with sizes exceeding  $\text{Ti}^{4+}$  by 38%, leads to a distortion of its crystal lattice and a change in phase formation processes in the  $\text{TiO}_2 - \text{H}_2\text{O}$  system [26].

Many different methods have been developed for the synthesis of  $\text{TiO}_2:\text{Eu}^{3+}$  nanoparticles in various polymorphic modifications, since their photophysical properties strongly depend on the structure, crystal size, morphology, and surface area [27–29]. Among the most widely used methods for producing  $\text{TiO}_2:\text{Eu}^{3+}$  nanoparticles are high-temperature hydrolysis [30], sol-gel [31], hydrothermal [32], and microemulsion synthesis [33]. From our point of view, a very perspective methods for obtaining  $\text{TiO}_2:\text{Eu}^{3+}$  nanophosphors are hydro and solvothermal methods of synthesis, since they allow to obtain particles of a given size, phase composition and morphology due to the possibility of flexible variation of synthesis parameters (temperature, isothermal holding time, composition of the reaction medium). Thus, the optical properties of  $\text{Eu}^{3+}$  included in the  $\text{TiO}_2$  matrix can be adapted by controlling the size and structural characteristics of the nanoparticles during the synthesis process, which is very attractive when making photoactive functional materials.

In the present study, we analyzed the effect of the europium introduction into the crystal structure of titania on the phase composition of  $\text{TiO}_2:\text{Eu}^{3+}$  nanoparticles formed in hydro and solvothermal conditions, on their size, morphology and surface properties. Using europium (III) ions as a luminescent probe, we established the selectivity of the substitution of  $\text{Ti}^{4+}$  ions by them in the titania structure with respect to the anatase phase. We considered changes in the photophysical properties (intensity and lifetime of luminescence, excitation spectra) of  $\text{TiO}_2$  nanoparticles doped with 2 mol.%  $\text{Eu}^{3+}$  depending on the conditions of their synthesis (precursor nature, the composition of the reaction medium and isothermal holding time).

Thus, this work aimed to synthesize  $\text{TiO}_2:\text{Eu}^{3+}$  phosphors from precursors of different nature under hydro and solvothermal conditions and to identify correlations between the chemical history and the structural characteristics of the nanoparticles being formed, as well as their photophysical properties. Complementary analytical methods (XRD, TEM and microdiffraction) were used for this, the data of which were compared with the excitation and emission spectra of the obtained nanocrystals.

## 2. Experimental methods

### 2.1. Preparation of $\text{TiO}_2$ -based nanoparticles with anatase structure

Titania-based nanoparticles with the anatase structure were synthesized under hydro- and solvothermal conditions. Solvothermal synthesis of undoped  $\text{TiO}_2$  nanoparticles was carried out by dissolving titanium (IV) n-butoxide ( $\text{Ti}(\text{OBu}^t)_4$ ; Aldrich; CAS: 5593-70-4; purum,  $\geq 97.0\%$ ) in toluene, followed by treatment the resulting solution in isobaric-isothermal conditions at 250 °C and 7 MPa for 72 hours (Sample 1).

Anatase-type  $\text{TiO}_2:\text{Eu}^{3+}$  nanoparticles were obtained in several stages. At the first, europium acetylacetonate hydrate ( $\text{Eu}(\text{C}_5\text{H}_7\text{O}_2)_3 \cdot x\text{H}_2\text{O}$ ; Aldrich; CAS: 181266-82-0; 99.9% trace metals basis) was dissolved in toluene with rapid mixing under magnetic stirrer within three hours. In the next step, titanium (IV) n-butoxide was added to the  $\text{Eu}(\text{C}_5\text{H}_7\text{O}_2)_3$  solution. The resulting mixture was stirred for 24 hours. Then the solution containing europium and titanium ions was transferred to a stainless-steel autoclave with an inner Teflon vessel and heated under the same conditions as in the case of undoped nanoparticles (Sample 2).

The obtained  $\text{TiO}_2$  and  $\text{TiO}_2:\text{Eu}^{3+}$  powders were then washed repeatedly with ethanol and dried at 100 °C. At the last stage, the powders were annealed for 2 hours at 500 °C to remove organic products.

Pure  $\text{TiO}_2$  anatase nanocrystals were formed for 4 hours in the dehydration process of  $\text{Ti}(\text{OH})_4$  under hydrothermal conditions at 250 °C and 7 MPa (Sample 3). The titanium hydroxide itself was pre-precipitated from its chloride ( $\text{TiCl}_4$ ; Aldrich; CAS: 7550-45-0, 99.9%) using 25% ammonium hydroxide solution.

The hydrothermal synthesis of  $\text{TiO}_2$  nanoparticles doped with 2 mol.%  $\text{Eu}^{3+}$  consisted of the sequence actions given below. Europium chloride hexahydrate ( $\text{EuCl}_3 \cdot 6\text{H}_2\text{O}$ ; Aldrich; CAS: 13759-92-7; 99.9% trace metals basis) was dissolved in distilled water acidified with 0.25 M HCl solution.  $\text{TiCl}_4$  was dissolved in cold acidified water using a cooling bath with ice. The concentration of the titanium chloride solution was 0.5 M. The obtained solutions were

mixed and stirred for 30 minutes by glass stirrer. The precipitation was carried out by adding drop by drop of the 25%  $\text{NH}_4\text{OH}$  solution dropwise to the resulting mixture. The precipitate was washed with distilled water until a negative reaction for chlorine ions and dried in an oven at 100 °C. Then the obtained white powder was placed in an autoclave and isothermally maintained at 250 °C for 4 hours (Sample 4).

## 2.2. Preparation of $\text{TiO}_2$ -based nanoparticles with rutile structure

Undoped  $\text{TiO}_2$  nanoparticles with rutile structure were prepared by hydrothermal treatment of titanium (IV) n-butoxide in 1 M hydrochloric acid solution at 250 °C, 7 MPa for 8 hours. (Sample 5).

In the case of the synthesis of  $\text{TiO}_2:\text{Eu}^{3+}$  nanophosphors, europium acetylacetonate hydrate was initially dissolved in 1 M HCl with magnetic stirring until a clear solution was obtained. Then,  $\text{Ti}(\text{O}i\text{Bu})_4$  was added to the resulting solution and stirred for 24 hours. At the next stage, the clear solution was transferred to an autoclave and heated under the above conditions (Sample 6).

Finally, the powders of both undoped titania nanoparticles and with trivalent europium inclusions formed under hydrothermal conditions were dried at 120 °C.

## 2.3. General Characterization

For the pure and  $\text{Eu}^{3+}$ -doped titania nanoparticles, the crystalline phases were characterized by the X-ray diffraction using Rigacu SmartLab diffractometer with the source  $\text{CuK}_\alpha$  tube. The average size of the coherent scattering regions of  $\text{TiO}_2$ -based nanopowders was estimated from the broadening of X-ray maxima using the Scherrer formula. The X-ray fluorescence spectrometer SPECTROSCAN MAX-G was used to determine the quantitative composition of the samples. Microstructure, morphology and size of  $\text{TiO}_2:\text{Eu}^{3+}$  nanoparticles were investigated using the transmission electron microscope Jeol JEM-2100F at accelerating voltage 200 kV and point-to-point resolution 0.19 nm. The specific surface area ( $S_{\text{BET}}$ ) and the size distribution of pores for  $\text{TiO}_2$  and  $\text{TiO}_2:\text{Eu}^{3+}$  powders were measured by the low-temperature nitrogen adsorption method on a QuantaChrome Nova 1200 analyzer. Based on the data obtained, the specific surface areas  $S_{\text{BET}}$  for the samples were calculated using the Brunauer–Emmett–Teller model (BET) and the seven-points-method within the relative pressure range  $P/P_0=0.07-0.25$  (where  $P_0$  is the saturation pressure). The calculation of the pore size distribution was carried out based on nitrogen desorption-isotherm according to the Barrett-Joyner-Halenda method (BJH). Raman spectra were recorded in the backscattering geometry using a Jobin Yvon T64000 triple monochromator equipped with a liquid  $\text{N}_2$ -cooled charge coupled device detector. The light was focused onto the sample surface using a 100X (0.9 numerical aperture) short working distance objective. The resulting spot diameters were around 0.8  $\mu\text{m}$ . The excitation wavelength  $\lambda$  was 488 nm from an  $\text{Ar}^+$  laser with a typical laser power of  $\sim 1$  mW. Photoluminescence lifetimes and excitation spectra were measured using the luminescence spectrophotometer LS-100 (PTI®, Canada). The photoluminescence emission spectra were recorded using a Horiba LabRAM HR Evolution system equipped with a He-Cd excitation laser emitting at 325 nm with a maximum power of 1 mW at the sample and equipped with a 100 grooves/mm grating and a Peltier-cooled charge coupled device detector. The light was focused onto the sample surface thanks to a 15X (0.32 numerical aperture) objective.

## 3. Results and discussion

### 3.1. Elemental analysis

The elemental analysis data of  $\text{TiO}_2:\text{Eu}^{3+}$  nanoparticles obtained by the methods of hydro and solvothermal synthesis are presented in Table 1. The average europium content in the samples was 2 mol.%, except the  $\text{TiO}_2:\text{Eu}^{3+}$  nanopowder obtained under hydrothermal conditions in 1M HCl (Sample 6). The losses in the last sample can be explained by the selectivity of the substitution of  $\text{Ti}^{4+}$  by europium (III) ions in the titania structure with respect to the anatase phase, which will be discussed later.

TABLE 1. The elemental composition of  $\text{TiO}_2:\text{Eu}^{3+}$  samples, obtained by X-ray fluorescence spectroscopy

Component	mol. %		
	Sample 2	Sample 4	Sample 6
Europium	2.1±0.1	1.9±0.1	0.8±0.1
Titanium	97.9±3	98.1±3	99.2±2.8

### 3.2. X-ray powder diffraction

Figure 1 shows the X-ray diffraction (XRD) patterns of undoped  $\text{TiO}_2$  (Samples 1, 3, 5) and  $\text{TiO}_2:\text{Eu}^{3+}$  (Samples 2, 4, 6) nanoparticles obtained by hydro and solvothermal synthesis. Some reflexes correspond only to the structure of the anatase on XRD patterns of Samples 1–4 (Fig. 1, patterns 1–4). The peaks of nanoparticles containing europium (III) ions have a characteristic shift and broadening associated with the formation of solid solutions. The shift of the X-ray maxima toward small angles by  $0.65^\circ$  is observed for Samples 1 and 2 obtained in toluene (Fig. 1, compare curve 1 with curve 2). The diffraction peaks of  $\text{TiO}_2:\text{Eu}^{3+}$  nanoparticles synthesized from chlorides by the hydrothermal method have an offset of  $0.13^\circ$  toward larger angles compared with pure titania formed under the same conditions (Fig. 1, compare curves 3 and 4).

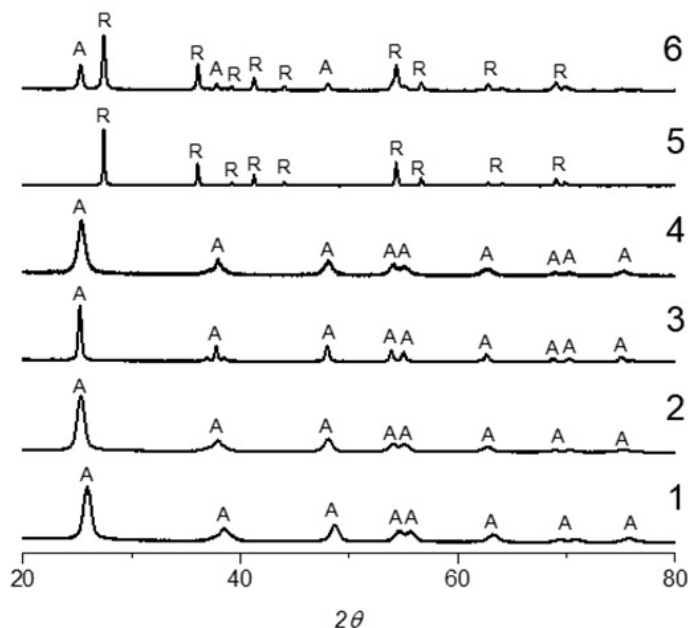


FIG. 1. XRD patterns of  $\text{TiO}_2$  (1,3,5) and  $\text{TiO}_2:\text{Eu}^{3+}$  (2,4,6) nanoparticles obtained by the solvothermal synthesis in toluene (1,2) or under hydrothermal treatment in distilled water (3,4) and in hydrochloric acid solution (5,6)

The peaks in the XRD pattern of pure  $\text{TiO}_2$  nanoparticles obtained in an acidic medium (Sample 5) correspond only to the rutile structure (Fig. 1, pattern 5). XRD analysis of  $\text{Eu}^{3+}$ -doped  $\text{TiO}_2$  nanoparticles synthesized in the same conditions showed that, along with the main peaks corresponding to the rutile modification, reflexes confirm the presence of crystallites with the anatase structure (Fig. 1, pattern 6). The ratio of anatase and rutile modifications in Sample 6 is 1 to 4.

Calculated by the Debye–Scherrer equation, the average crystallite sizes were  $12 \pm 2$  nm and  $30 \pm 3$  nm for Sample 1 and 3, respectively. This fact suggests that the use of titanium alkoxide as a precursor and carrying out the nucleation processes in a non-polar solvent at elevated temperature and pressure contribute to the formation of smaller crystallites even after 72 hours of isothermal holding compared to  $\text{TiO}_2$  nanoparticles obtained from inorganic salt in hydrothermal conditions for a significantly shorter period. The introduction of europium (III) ions into the titania crystal lattice during the solvothermal synthesis of nanoparticles from organometallic compounds did not affect the size of the crystallites formed. In contrast, for Samples 3 and 4, the replacement of  $\text{Ti}^{4+}$  with  $\text{Eu}^{3+}$  ions in the titania structure during crystallization of nanoparticles under hydrothermal conditions leads to a decrease in the average size of coherent scattering regions from 30 to 12 nm. In the case of Sample 6 prepared in HCl solution, the size of the coherent scatter regions for anatase modification was  $23 \pm 3$  nm.

The size and shape of the obtained  $\text{TiO}_2$ -based nanoparticles were determined by the method of transmission electron microscopy (TEM) (Fig. 2).  $\text{TiO}_2$  and  $\text{TiO}_2:\text{Eu}^{3+}$  nanoparticles obtained by solvothermal treatment of organometallic compounds had a predominantly quasispherical shape, and their average diameter was 12 nm (Fig. 2, images 1a, 2a). In the case of hydrothermal treatment of titanium hydroxide precipitated from  $\text{TiCl}_4$ , mainly rhombic particles *ca.* 30 nm in size were formed (Fig. 2, image 3a). Sample 4 obtained under similar conditions was  $\text{TiO}_2:\text{Eu}^{3+}$  nanoparticles of both quasispherical and rhombic shapes with an average size of about 12 nm (Fig. 2, image 4a). In

addition, microphotograph of  $\text{TiO}_2\text{:Eu}^{3+}$  phosphors also show an insignificant number of nanoparticles in their morphology similar to the rutile phase, but this was not confirmed either by XRD or electron microdiffraction. Titania with rutile structure crystallizes in the form of rods with an average axial ratio of 3 as a result of  $\text{Ti}(\text{OBU}^t)_4$  hydrothermal treatment in 1M HCl (Fig. 2, images 5a, 5b). Besides rutile rod-like structures with an average length of  $70 \pm 10$  nm and a diameter of  $20 \pm 5$  nm, Sample 6 contains anatase  $\text{TiO}_2\text{:Eu}^{3+}$  particles with an average size of  $25 \pm 3$  nm.

Electron microdiffraction patterns show the presence of main anatase reflexes for  $\text{TiO}_2$  and  $\text{TiO}_2\text{:Eu}^{3+}$  nanoparticles in Samples 1–4 (Fig. 2, patterns 1b–4b). Concentric rings, corresponding exclusively to the rutile structure, are observed in the electron microdiffraction pattern for  $\text{TiO}_2$  nanoparticles, obtained by hydrothermal treatment of titanium and europium organic precursors in hydrochloric acid solution (Fig. 2, pattern 5b). In the microdiffraction pattern for Sample 6, reflections of the rutile and anatase phases appear (Fig. 2, pattern 6b). It should be noted that the TEM and electron microdiffraction data confirm the structural and dimensional characteristics of the  $\text{TiO}_2$ -based nanoparticles determined as a result of X-ray phase analysis.

The specific surface area and porosity of the obtained nanopowders were investigated by the method of low-temperature nitrogen adsorption. According to the analysis of titania nanopowders by the Brunauer-Emmett-Teller method, Samples 1, 3, and 5 are characterized by specific surface area ( $S_{BET}$ ) values of 54.0, 47.6, and 33.4  $\text{m}^2/\text{g}$ , respectively (Table 2). Fig. 3 shows the isotherms of adsorption and desorption for undoped  $\text{TiO}_2$  nanoparticles prepared under different synthesis conditions. By appearance, all the presented isotherms belong to type IV according to the IUPAC classification. This behavior is typical for mesoporous materials, in the pores of which capillary condensation of the adsorbent can occur. In turn, it leads to the appearance of hysteresis between the adsorption and desorption isotherms (Fig. 3). At the same time, both the type of hysteresis and its value explicitly depend on the synthesis conditions of titania nanoparticles. Thus, for Samples 1 and 2 with the anatase structure synthesized from  $\text{Ti}(\text{OBU}^t)_4$  and  $\text{TiCl}_4$ , the course of the capillary-condensation hysteresis loop according to IUPAC classification can be attributed to type H1. This fact indicates the presence of cylindrical mesopores open on both sides in titania nanopowders. Sample 5, represented exclusively by the rutile modification of  $\text{TiO}_2$ , has an H3 type hysteresis, which is associated with the presence of slit-shaped pores, typical for the materials consisting of lamellar particles. Moreover, the hysteresis loop of the last sample is closed in the region of low nitrogen partial pressures (less than 0.3), which indicates a significant content of micropores in the powder.

The pore size distribution calculated for the desorption branch using the BJH algorithm for undoped  $\text{TiO}_2$  nanopowders also significantly depends on the method of their synthesis (Fig. 4). For example, Samples 1 and 3 with the anatase structure obtained from both inorganic and organic precursors are characterized by a bimodal distribution of pores in size. At the same time, while in Sample 1, large pores dominate with a maximum  $D_{pore-2}$  of ca. 17 nm. In Sample 5, on the contrary, small pores dominate with a maximum  $D_{pore-1}$  of ca. 2 nm, the second maximum being significantly blurred. Moreover, only the sample obtained by hydrothermal treatment of titanium hydroxide precipitated from a solution of its chloride demonstrates practically log-normal behavior of pore distribution in the range from 10 to 35 nm with a maximum at ca. 24 nm.

The doping of titania with europium (III) ions leads to significant changes in the texture characteristics of  $\text{TiO}_2$  nanopowders. Estimates of the specific surface area of  $\text{TiO}_2\text{:Eu}^{3+}$  samples (Table 2) indicate a significant increase in  $S_{BET}$  from 1.2 times in the case of Sample 5 to 2.3 times for Sample 3 compared to their undoped counterparts. The introduction of  $\text{Eu}^{3+}$  into the titania crystal lattice also influences both the appearance of the adsorption/desorption isotherms for  $\text{TiO}_2\text{:Eu}^{3+}$  nanopowders (Fig. 5) and the corresponding pore size distribution (Fig. 6). The loop of capillary-condensation hysteresis for Sample 2 is significantly reduced, and in the case of Sample 6 it almost collapses, which does not allow us to estimate the shape of pores for this sample (Fig. 5). Only for Sample 4 it is noticeably increased. Analysis of the pore size distribution for  $\text{TiO}_2\text{:Eu}^{3+}$  nanoparticles (Fig. 6) shows that the bimodal distribution is observed only in the case of Sample 6, with the maximum  $D_{pore-1}$  of ca. 4 nm shifted towards larger sizes, and the maximum  $D_{pore-2}$  of ca. 13 nm on the contrary. For Sample 4, the log-normal pore size distribution is maintained (Fig. 6), but with a significant contraction and shift of the maximum to a smaller  $D_{pore}$  size of ca. 10 nm.

### 3.3. Raman spectroscopy

The Raman spectra for  $\text{TiO}_2\text{:Eu}^{3+}$  nanoparticles are shown in Fig. 7. It is reported [34,35] that  $\text{TiO}_2$  with anatase structure has six modes: three  $E_g$  at 143, 195, and 639  $\text{cm}^{-1}$ , two  $B_{1g}$  at 396 and 518  $\text{cm}^{-1}$ , the latter representing a double peak relating both to  $B_{1g}$  and to  $A_{1g}$ . For all  $\text{TiO}_2\text{:Eu}^{3+}$  nanoparticles obtained in different conditions, all six modes of the anatase structure are present in the Raman spectra, which is consistent with the XRD analysis data. The  $E_g$  mode has the highest intensity at 143  $\text{cm}^{-1}$  in the  $\text{TiO}_2\text{:Eu}^{3+}$  nanopowders obtained in 1M HCl solution by hydrothermal treatment (Fig. 7, curve 3). The 143  $\text{cm}^{-1}$   $E_g$  modes in Samples 2 and 4 differ little in intensity, but in the first case, it is slightly lower (Fig. 7, compare curve 1 with curve 2). The decrease in intensity seems to be related to

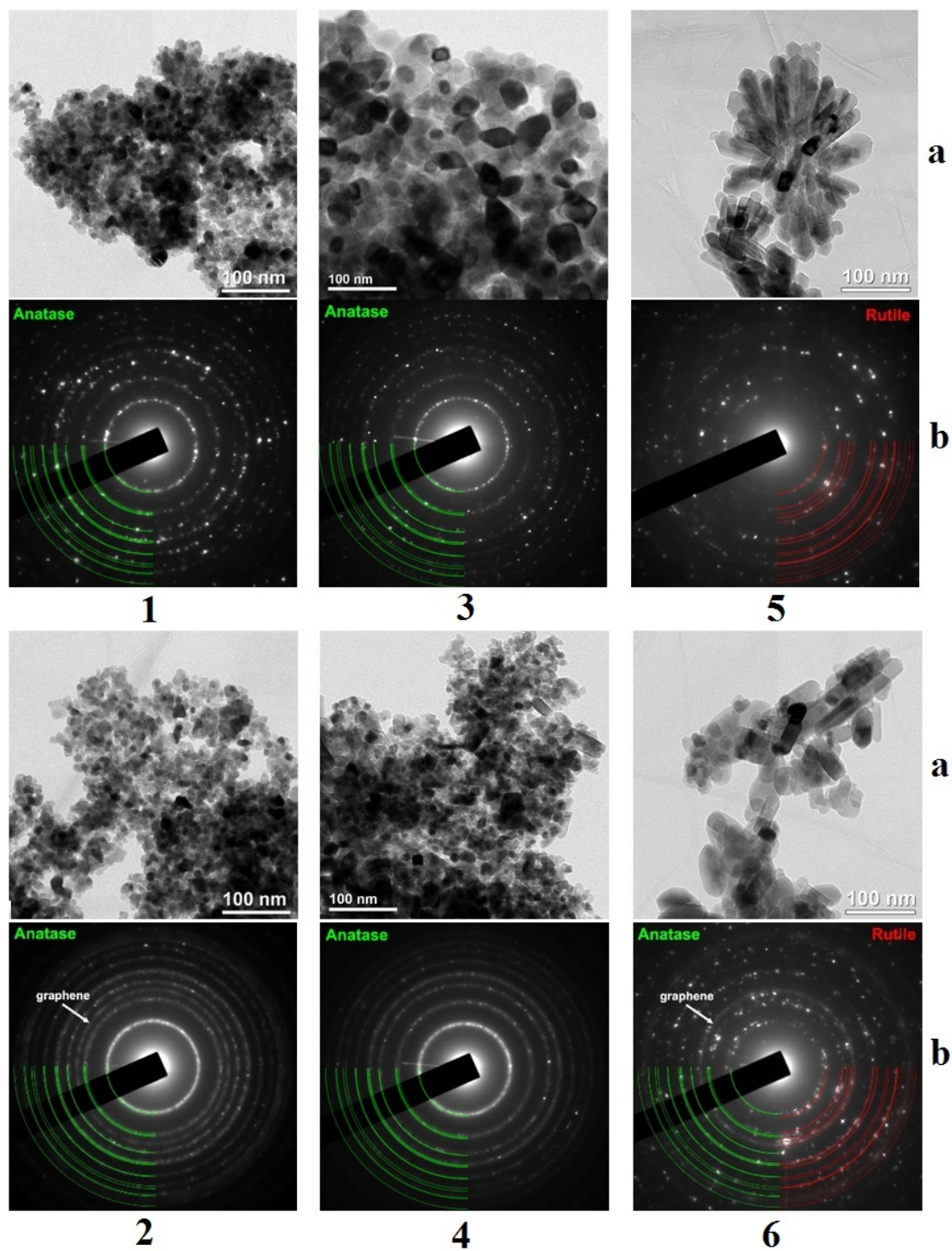


FIG. 2. TEM microphotographs (a) and electron microdiffraction (b) of  $\text{TiO}_2$  (1,3,5) and  $\text{TiO}_2:\text{Eu}^{3+}$  (2,4,6) nanoparticles obtained by the solvothermal synthesis in toluene (1,2) or hydrothermal treatment in distilled water (3,4) and in hydrochloric acid solution (5,6)

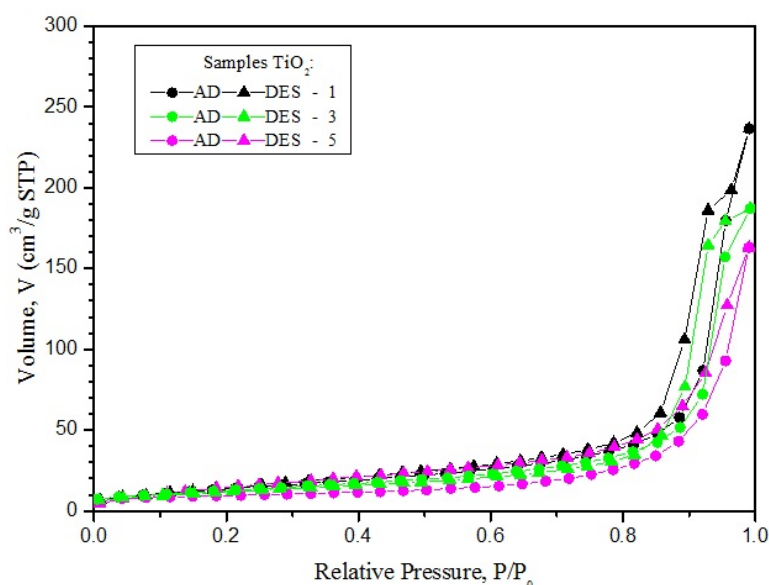


FIG. 3. Nitrogen adsorption/desorption isotherms of  $\text{TiO}_2$  nanopowders obtained by the solvothermal synthesis in toluene (1) or hydrothermal treatment in distilled water (3) and in hydrochloric acid solution (5)

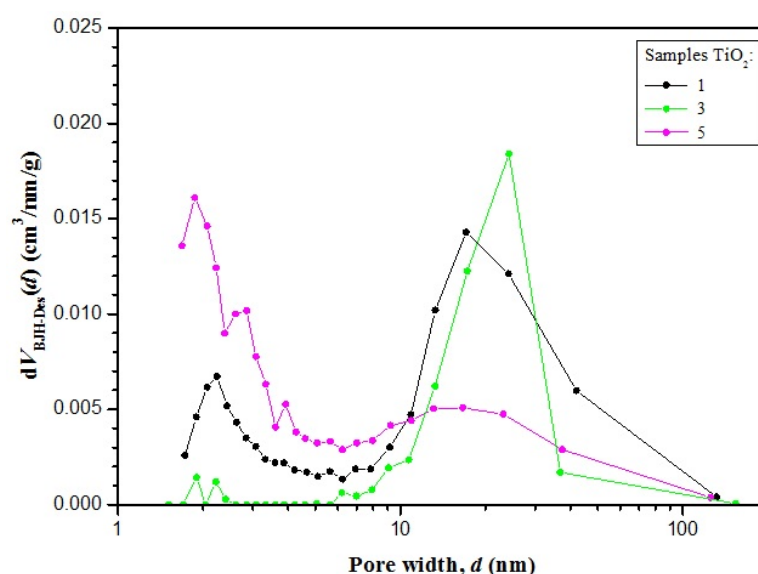


FIG. 4. Pore size distributions of  $\text{TiO}_2$  nanopowders obtained by the solvothermal synthesis in toluene (1) or hydrothermal treatment in distilled water (3) and in hydrochloric acid solution (5)

the amount of  $\text{Eu}^{3+}$  dopant in the anatase-type  $\text{TiO}_2$  nanocrystals. Drastically decreasing the intensity of the  $E_g$  mode can also indicate an increase in the number of defects in the structure and a violation of the translational symmetry of the crystals. In addition to the vibrational modes of the anatase structure, two more are observed related to Ti – O bond vibrations of the rutile modification for Sample 6 (Fig. 7, curve 3). Thus, the presence of  $E_g$  and  $A_{1g}$  modes at 440 and  $611.8\text{ cm}^{-1}$  in the Raman spectra indicates the existence of a rutile phase [36] in a sample synthesized from titanium alkoxide in the 1M solution of HCl, which also agrees with the XRD data.

### 3.4. Luminescence properties

The photoluminescence (PL) excitation spectra of  $\text{TiO}_2:\text{Eu}^{3+}$  nanoparticles synthesized from different precursors under hydro and solvothermal conditions are presented in Fig. 8. The PL excitation spectrum of Sample 2 shows three narrow peaks being typical for europium (III) ions in the range of 230–270 nm due to electron transferring from the

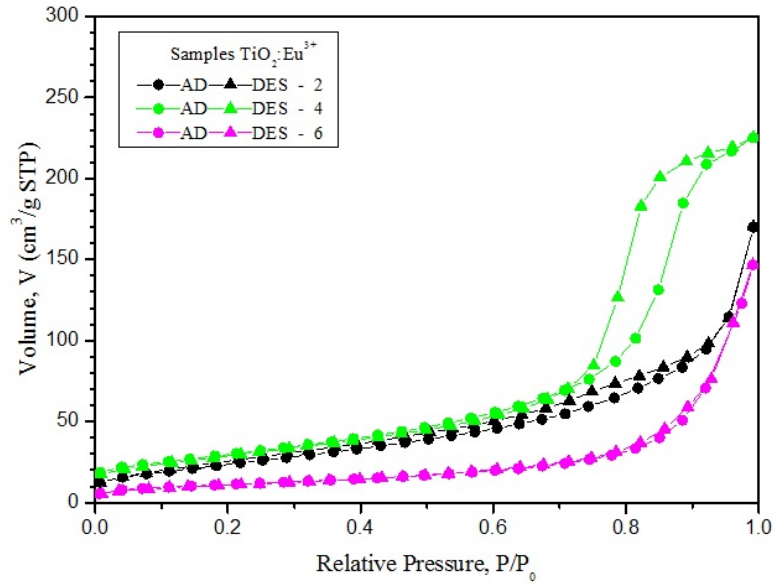


FIG. 5. Nitrogen adsorption/desorption isotherms of  $\text{TiO}_2:\text{Eu}^{3+}$  nanopowders obtained by the solvothermal synthesis in toluene (2) or hydrothermal treatment in distilled water (4) and in hydrochloric acid solution (6)

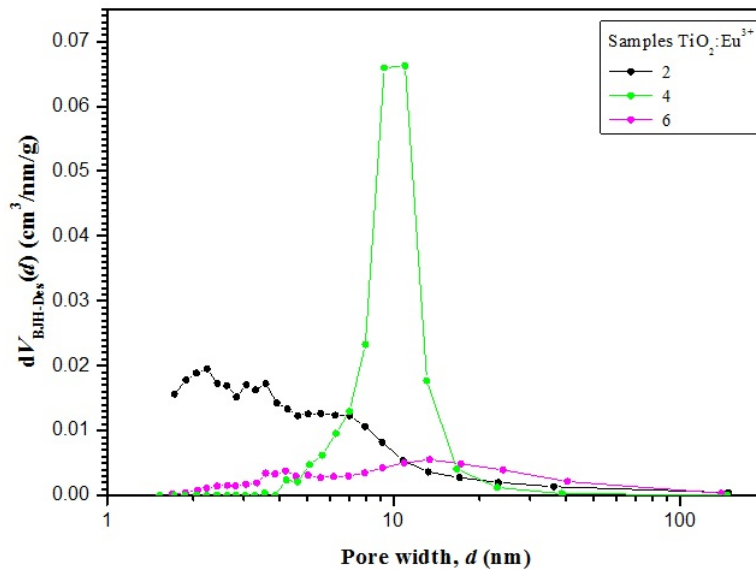


FIG. 6. Pore size distributions of  $\text{TiO}_2:\text{Eu}^{3+}$  nanopowders obtained by the solvothermal synthesis in toluene (2) or hydrothermal treatment in distilled water (4) and in hydrochloric acid solution (6)

2p orbital of  $\text{O}^{2-}$  to the 4f orbital of  $\text{Eu}^{3+}$  [22, 37] with excitation maxima at 231, 248, 261 nm (Fig. 8, spectrum 2). Moreover, the quasilinear PL excitation band is observed in the region of 380–540 nm, which corresponds to the intraconfiguration optical f–f electron absorption transitions. These said transitions manifest itself at 383, 395, 463 and 532 nm, with an absolute maximum of PL excitation at 395 nm [38]. PL excitation peaks are not delineated in the region of 230–270 nm for  $\text{TiO}_2:\text{Eu}^{3+}$  nanophosphors synthesized from chlorides and organometallic compounds of the corresponding metals under hydrothermal conditions (Fig. 8, spectra 4 and 6). The excitation spectrum is shifted to a longer wavelength region with four narrow peaks centered at 400, 420, 468 and 536 nm in the case of nanoparticles obtained by hydrothermal treatment of  $\text{Ti}(\text{O}i\text{Bu})_4$  and  $\text{Eu}(\text{C}_5\text{H}_7\text{O}_2)_3 \cdot x\text{H}_2\text{O}$  in hydrochloric acid solution. The absolute excitation maximum for Sample 6 is located at 468 nm, as seen in the graph. In contrast, four above-mentioned narrow excitation peaks are shifted for Sample 4 to short wavelengths.

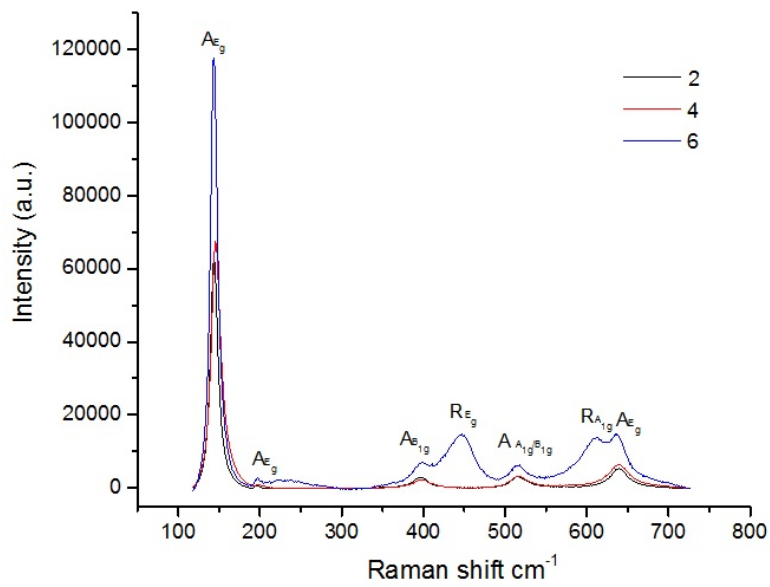


FIG. 7. Raman spectra of  $\text{TiO}_2:\text{Eu}^{3+}$  nanoparticles obtained by the solvothermal synthesis in toluene (2) or hydrothermal treatment in distilled water (4) and in hydrochloric acid solution (6)

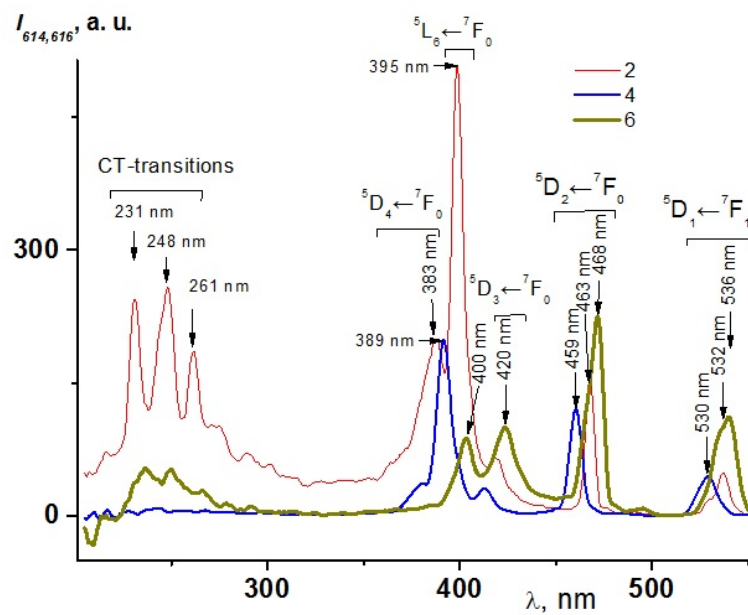


FIG. 8. Excitation spectra of  $\text{TiO}_2:\text{Eu}^{3+}$  nanoparticles obtained by the solvothermal synthesis in toluene (2) or hydrothermal treatment in distilled water (4) and in hydrochloric acid solution (6). The photoluminescence observation is at 614 (2, 4) and 616 nm (6)

TABLE 2. Textural parameters of TiO<sub>2</sub> and TiO<sub>2</sub>:Eu<sup>3+</sup> nanopowders obtained by the low-temperature nitrogen adsorption method

Name	$S_{BET}, m^2/g$	$D_{pore-1}, nm$	$D_{pore-2}, nm$	$V_{pore}, cm^3/g$
Sample 1	$54.0 \pm 3.0$	2.3	17.1	0.38
Sample 2	$93.2 \pm 5.9$	2.2	–	0.27
Sample 3	$47.6 \pm 2.0$	–	24.2	0.30
Sample 4	$109.5 \pm 4.4$	–	10.0	0.36
Sample 5	$33.4 \pm 0.5$	1.9	16.6	0.26
Sample 6	$40.4 \pm 0.8$	4.2	13.3	0.23

Figure 9 shows the photoluminescence spectra of Samples 2, 4, and 6. The quasi linear emission band of Eu<sup>3+</sup> according to optical transitions  $^5D_0 \rightarrow ^7F_j$  is observed for all three samples. Spectrum 2 shows an emission band of anatase-type TiO<sub>2</sub>:Eu<sup>3+</sup> nanoparticles obtained under solvothermal conditions at excitation wavelength of 352 nm. According to the Stark splitting for  $^5D_0 \rightarrow ^7F_0$ ,  $^5D_0 \rightarrow ^7F_1$ ,  $^5D_0 \rightarrow ^7F_2$ ,  $^5D_0 \rightarrow ^7F_3$  and  $^5D_0 \rightarrow ^7F_4$ , maxima are observed at 578, 590, 613, 654 and 716 nm, respectively. The transition  $^5D_0 \rightarrow ^7F_1$  is splitting into 2 Stark sublevels: a maximum at 590 nm and a shoulder at 596 nm. The latter indicates an axial symmetry. At that, for these TiO<sub>2</sub>:Eu<sup>3+</sup> nanoparticles, in the transition  $^5D_0 \rightarrow ^7F_2$  ones observe 4 Stark sublevels: maxima at 606, 613, 625 nm, and a shoulder at 633 nm. This combination of 2+4 indicates a tetragonal crystal system for anatase and rutile, but not brookite.

The presence of three sublevels in the  $^5D_0 \rightarrow ^7F_1$  term as a maximum at 590 nm and two shoulders on the left and right at 585 and 595 nm (spectrum 4, Fig. 9) indicates the position of europium (III) ions in the centers with low symmetry for Sample 4. This result shows that Eu<sup>3+</sup> ions are probably located in the interstices of the anatase TiO<sub>2</sub> lattice. A similar situation is observed for nanoparticles obtained under hydrothermal conditions from Ti(OBu<sup>t</sup>)<sub>4</sub> and Eu(C<sub>5</sub>H<sub>7</sub>O<sub>2</sub>)<sub>3</sub> · xH<sub>2</sub>O (spectrum 6, Fig. 9). The vast difference in the intensity of the  $^5D_0 \rightarrow ^7F_1$  and  $^5D_0 \rightarrow ^7F_2$  terms upon excitation by any wavelength also indicates the low symmetry index calculated as the ratio of  $^5D_0 \rightarrow ^7F_1 / ^5D_0 \rightarrow ^7F_2$ , which corresponds to the low-symmetry emission sites as interstitials in Sample 4 and 6.

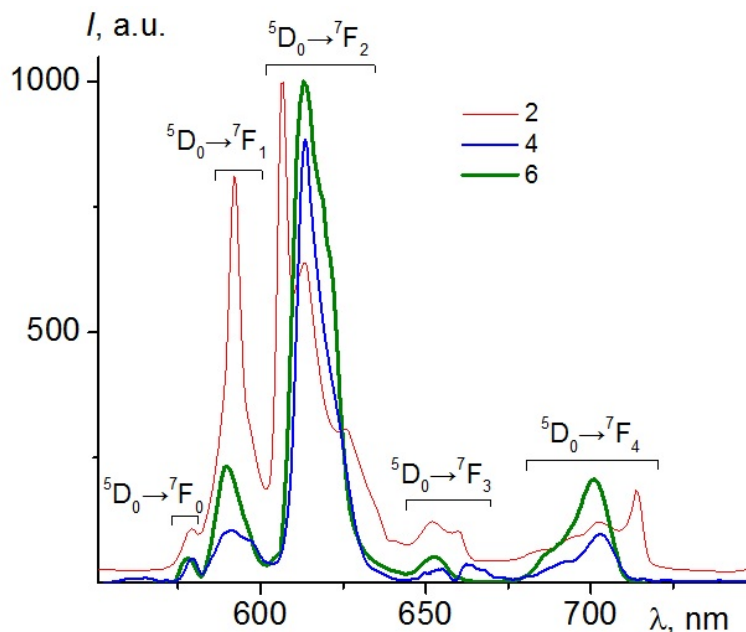


FIG. 9. Emission spectra of TiO<sub>2</sub>:Eu<sup>3+</sup> nanoparticles obtained by the solvothermal synthesis in toluene (2) or hydrothermal treatment in distilled water (4) and in hydrochloric acid solution (6). Excitation is at 352 nm (2, 4) and 399 nm (6)

TABLE 3. The luminescence lifetime<sup>1)</sup> in the two-exponential approximation for the photoluminescence intensity decay of TiO<sub>2</sub>:Eu<sup>3+</sup> nanoparticles

Name	Ru- tile	Ana- tase	A <sub>1</sub>	$\tau_{PL1}$ , ms	A <sub>2</sub>	$\tau_{PL2}$ , ms	$\chi^2$	DWP <sup>2)</sup>	Z <sup>3)</sup>	$\langle\tau_w\rangle^4$ , ms	$\langle\tau\rangle$ , ms
Sample 2	1	99	0.83	0.082(2)	0.17	2.95(4)	3.157	–	–	2.607	0.570
Sample 4	1	99	0.96(1)	0.00113(2)	0.043(1)	0.135(2)	4.614	0.807	– 7.437	0.114	0.007
Sample 6	80	20	0.334(6) <sup>5)</sup>	0.98(2)	0.666(6)	3.04(1)	1.523	0.577	– 5.802	2.753	2.352

<sup>1)</sup>Excitation at 472 nm. Observation at 614 nm. Good statistics are provided with  $\chi^2$  in the range of 0.9–1.2.

<sup>2)</sup>Darbin–Watson parameter: DWP > 1.75.

<sup>3)</sup>Run Z-test: Z > –1.96.

<sup>4)</sup>The weighted average duration of the luminescence in the two-exponential approximation:  $\langle\tau_w\rangle = \frac{\sum_{i=1}^2 A_i \tau_{PLi}^2}{\sum_{i=1}^2 A_i \tau_{PLi}}$ .

<sup>5)</sup>The designation of the error in the last character.

The photoluminescence lifetime for TiO<sub>2</sub>:Eu<sup>3+</sup> nanoparticles with different chemical prehistory is presented in Table 3. Nanophosphors with longer PL lifetimes were crystallized from organometallic compounds under hydro and solvothermal conditions in comparison with their analogs formed from inorganic precursors. Indeed, the root mean square (RMS) lifetimes of Samples 2 and 4 are in the range of 2.61–2.75 ms in the dependence of the phase content (see Table 3, Rows 1 and 2). At the same time, the RMS lifetime of Sample 4 is 0.114 ms, which is in the magnitude of one order less than the other ones. This fact is probably related to the low symmetry of the Eu<sup>3+</sup> environment in the crystal lattice of anatase TiO<sub>2</sub> nanoparticles formed from europium and titanium chlorides.

#### 4. Conclusions

Nanoparticles of TiO<sub>2</sub> and TiO<sub>2</sub> doped with 2 mol.% Eu<sup>3+</sup> were synthesized from precursors of different nature under hydro and solvothermal conditions. Dehydration under hydrothermal conditions of titanium hydroxide precipitated from TiCl<sub>4</sub> leads to the formation of quasispherical and rhombic anatase crystals of larger size compared to the solvothermal treatment of organometallic compounds, where faceted nanoparticles are not observed. The introduction of Eu<sup>3+</sup> ions into the TiO<sub>2</sub> structure in the thermal process of organic precursors at elevated pressure in toluene or hydrochloric acid solution, as well as titanium and europium hydroxides in distilled water, improves surface properties of the resulting nanopowders. Moreover, a reduction in the size of nanocrystals due to the substitution of Ti<sup>4+</sup> by trivalent europium is achieved only in the case of a sample obtained from chlorides. The hydrothermal treatment of Ti(OBu<sup>t</sup>)<sub>4</sub> in the presence of Eu<sup>3+</sup> ions in a strongly acidic medium contributes to the formation of not only rutile-type TiO<sub>2</sub> nanoparticles but also Ti<sub>1-x</sub>Eu<sub>x</sub>O<sub>2-0.5x</sub> solid solutions with anatase structure.

The most significant result of the work is associated with the analysis of the excitation and emission spectra of Eu<sup>3+</sup>-doped TiO<sub>2</sub> nanoparticles obtained by the hydro and solvothermal synthesis. It turned out that the absorption capacity of europium (III) ions in titania nanoparticles depends on their phase composition. For TiO<sub>2</sub>:Eu<sup>3+</sup> phosphors, which are a mixture of crystallites with anatase and rutile structures in a 1:4 ratio, a more pronounced contribution to the absorption spectra in the visible region (390–540 nm) at the long-wave edges of optical transitions is observed compared to the excitation spectra of single-phase nanoparticles. The synthesis of nanoparticles under hydrothermal conditions, regardless of the precursor nature and the acidity of the reaction medium, leads to the loss of the possibility of sufficient luminescence excitation in the UV region up to 300 nm. In the case of nanoparticles formed at elevated pressure and temperature in a non-polar organic solvent, the Stark sublevel peaks in the electric dipole transition of the optical term <sup>5</sup>D<sub>0</sub>→<sup>7</sup>F<sub>2</sub> are more clearly visible in comparison with other phosphors synthesized in this study. Namely, there are two peaks for <sup>5</sup>D<sub>0</sub>→<sup>7</sup>F<sub>1</sub> and four peaks for <sup>5</sup>D<sub>0</sub>→<sup>7</sup>F<sub>2</sub> because of tetragonal symmetry. It was shown using luminescent spectroscopy that during the hydrothermal synthesis of TiO<sub>2</sub>:Eu<sup>3+</sup> nanoparticles from organometallic

compounds in 1 HCl solution, there is a disproportionation of europium (III) ions between the resulting rutile and anatase phases, with the majority of photoactive centers being incorporated into the anatase structure.

For further research, it is also necessary to try to obtain a brookite phase that differs from rutile and anatase by other values of the band gap, which will affect the photophysical properties of  $\text{TiO}_2:\text{Eu}^{3+}$  nanoparticles. There are also some fundamental problems associated with the symmetry effect of the crystal field on the luminescence of europium (III) ions and other lanthanides ( $\text{Tb}^{3+}$ ,  $\text{Sm}^{3+}$ ,  $\text{Tm}^{3+}$ ). In this regard, the synthesis and study of the properties of  $\text{TiO}_2$  matrices with different phase composition and concentration of lanthanide ions will allow to adapt the photoluminescent characteristics of such phosphors and expand the possibilities of their optical and medical applications.

## Acknowledgements

Alexander N. Bugrov appreciates the Russian Foundation for Basic Research (grant No 16-33-60227) for the financial support. The experimental work was facilitated by the Engineering Center equipment of the St. Petersburg State Technological Institute (Technical University). TEM studies were performed using equipment of the Federal Joint Research Center “Material science and characterization in advanced technology” supported by the Ministry of Education and Science of the Russian Federation (id RFMEFI62117X0018). The authors express appreciation to Kopitsa G. P. from Petersburg Nuclear Physics Institute for the study of nanoparticles by the method of low-temperature nitrogen adsorption. Ruslan Yu. Smyslov is thankful for his funding received from the EU-H2020 research and innovation program under grant agreement No 654360 having benefitted from the access provided by CEA/LETI in Grenoble within the framework of the NFFA-Europe Transnational Access Activity.

## References

- [1] Hingwe V.S., Bajaj N.S., Omanwar S.K.  $\text{Eu}^{3+}$  doped N-UV emitting  $\text{LiSrPO}_4$  phosphor for W-LED application. *Optik – International Journal for Light and Electron Optics*, 2017, **130**, P. 149–153.
- [2] Ozawa L., Itoh M. Cathode ray tube phosphors. *Chemical Reviews*, 2003, **103**(10), P. 3835–3856.
- [3] Lovisa L.X., Andrs J., Gracia L., Li M.S., Paskocimas C.A., Bomio M.R.D., Arajo V.D., Longo E., Motta F.V. Photoluminescent properties of  $\text{ZrO}_2:\text{Tm}^{3+}$ ,  $\text{Tb}^{3+}$ ,  $\text{Eu}^{3+}$  Powders—A combined experimental and theoretical study. *Journal of Alloys and Compounds*, 2017, **695**, P. 3094–3103.
- [4] Nguyễn T.-L., Castaing M., Gacoin T., Boilot J.-P., Balembois F. Single  $\text{YVO}_4:\text{Eu}$  nanoparticle emission spectra using direct  $\text{Eu}^{3+}$  ion excitation with a sum-frequency 465-nm solid-state laser. *Optics Express*, 2014, **22**(17), P. 20542–20550.
- [5] Bugrov A.N., Zavalova A.Yu., Smyslov R.Yu., Anan'eva T.D., Vlasova E.N., Mokeev M.V., Kryukov A.E., Kopitsa G.P., Pipich V. Luminescence of  $\text{Eu}^{3+}$  ions in hybrid polymer-inorganic composites based on poly(methyl methacrylate) and zirconia nanoparticles. *Luminescence*, 2018, **33**(5), P. 837–849.
- [6] Julia'n-Lo'pez P.E.B., Planelles-Arago J., Cordoncillo E., Vianab B., Sanchez C. Photonic and nanobiophotonic properties of luminescent lanthanide-doped hybrid organic-inorganic materials. *Journal of Materials Chemistry*, 2008, **18**, P. 23–40.
- [7] Almjasheva O.V., Garabadzhiu A.V., Kozina Yu.V., Litvinchuk L.F., Dobritsa V.P. Biological effect of zirconium dioxide-based nanoparticles. *Nanosystems: physics, chemistry and mathematics*, 2017, **8**(3), P. 391–396.
- [8] Di W., Wang X., Chen B., Lu S., Zhao X. Effect of  $\text{OH}^-$  on the luminescent efficiency and lifetime of  $\text{Tb}^{3+}$ -doped yttrium orthophosphate synthesized by solution precipitation. *Journal of Physical Chemistry B*, 2005, **109**, P. 13154–13158.
- [9] Tiseanu C., Cojocaru B., Parvulescu V.I., Sanchez-Dominguez M., Primus P.A., Boutonnet M. Order and disorder effects in nano- $\text{ZrO}_2$  investigated by micro-Raman and spectrally and temporarily resolved photoluminescence. *Physical Chemistry Chemical Physics*, 2012, **14**, P. 12970–12981.
- [10] Bugrov A.N., Smyslov R.Yu., Zavalova A.Yu., Kirilenko D.A., Pankin D.V. Phase composition and photoluminescence correlations in nanocrystalline  $\text{ZrO}_2:\text{Eu}^{3+}$  phosphors synthesized under hydrothermal conditions. *Nanosystems: physics, chemistry and mathematics*, 2018, **9**(3), P. 378–388.
- [11] Bünzli J.C.G., Eliseeva S.V. Basics of lanthanide photophysics. In: Hänninen P., Härmä H. (eds) *Lanthanide Luminescence. Springer Series on Fluorescence (Methods and Applications)*, 2010, **7**, P. 1–45.
- [12] Maciel G.S., Rakov N. Photon conversion in lanthanide -doped powder phosphors: concepts and applications. *RSC Advances*, 2015, **5**, P. 17283–17295.
- [13] Som T., Karmakar B. Optical properties of  $\text{Eu}^{3+}$ -doped antimony-oxide-based low phonon disordered matrices. *Journal of Physics: Condensed Matter*, 2010, **22**(035603), P. 11.
- [14] Bünzli J.C.G. On the design of highly luminescent lanthanide complexes. *Coordination Chemistry Reviews*, 2015, **293–294**, P. 19–47.
- [15] Yakimanskii A.V., Goikhman M.Ya., Podeshvo I.V., Anan'eva T.D., Nekrasova T.N., Smyslov R.Yu. Luminescence of  $\text{Ln}^{3+}$ . Lanthanide complexes in polymer matrices. *Polymer Science, Ser. A*, 2012, **54**(12), P. 921–941.
- [16] Bekiari V., Lianos P. Multicolor emission from terpyridine-lanthanide ion complexes encapsulated in nanocomposite silica/poly(ethyleneglycol) sol-gel matrices. *Journal of Luminescence*, 2003, **101**, P. 135–140.
- [17] Kolesnikov I.E., Povolotskiy A.V., Mamonovaa D.V., Lähderant E., Manshina A.A., Mikhailov M.D. Photoluminescence properties of  $\text{Eu}^{3+}$  ions in yttrium oxide nanoparticles: defect vs. normal sites. *RSC Advances*, 2016, **8**, P. 9.
- [18] Liu Y., Zhou S., Tu D., Chen Z., Huang M., Zhu H., Ma E., Chen X. Amine-functionalized lanthanide-doped zirconia nanoparticles: Optical spectroscopy, time-resolved fluorescence resonance energy transfer biodetection, and targeted imaging. *Journal of the American Chemical Society*, 2012, **134**, P. 15083–15090.

- [19] Bugrov A.N., Smyslov R.Yu., Zavalova A.Yu., Kopitsa G.P. The influence of chemical prehistory on the structure, photoluminescent properties, surface and biological characteristics of  $\text{Zr}_{0.98}\text{Eu}_{0.02}\text{O}_{1.99}$  nanophosphors. *Nanosystems: Physics, Chemistry, Mathematics*, 2019, **10**(2), P. 164–175.
- [20] Zhu X., Su Q., Feng W., Li F. Anti-Stokes shift luminescent materials for bio-applications. *The Royal Society of Chemistry*, 2016, P. 15.
- [21] Luo W., Liu Y., Chen X. Lanthanide-doped semiconductor nanocrystals: electronic structures and optical properties. *Science China Materials*, 2015, **58**(10), P. 819–850.
- [22] Meetei S.D., Singh S.D. Effects of crystal size, structure and quenching on the photoluminescence emission intensity, lifetime and quantum yield of  $\text{ZrO}_2:\text{Eu}^{3+}$  nanocrystals. *Journal of Luminescence*, 2014, **147**, P. 328–335.
- [23] Zhang J., Zhou P., Liub J., Yu J. New understanding of the difference of photocatalytic activity among anatase, rutile and brookite  $\text{TiO}_2$ . *Physical Chemistry Chemical Physics*, 2014, **16**, P. 20382.
- [24] Ovenstone J., Titler P.J., Withnall R., Silver J. A Study of the Effects of Europium Doping and Calcination on the Luminescence of Titania Phosphor Materials. *Journal of Physical Chemistry B*, 2001, **105**, P. 7170–7177.
- [25] Almjashveva O.V. Formation and structural transformations of nanoparticles in the  $\text{TiO}_2\text{--H}_2\text{O}$  system. *Nanosystems: Physics, Chemistry, Mathematics*, 2016, **7**(6), P. 1031–1049.
- [26] Chen W., Zhou A., Yang X., Liu Y. Synthesis, structure and luminescence properties of  $\text{TiO}_2:\text{Eu}^{3+}$  for white light-emitting diode. *Journal of Alloys and Compounds*, 2013, **581**, P. 330–334.
- [27] Li H., Sheng Y., Zhao H., Song Y., Gao F., Huo Q., Zou H. Facile synthesis and luminescent properties of  $\text{TiO}_2:\text{Eu}^{3+}$  nanorods and spindle-shaped nanoparticles from titanate nanotubes precursors. *Materials Research Bulletin*, 2012, **47**, P. 4322–4328.
- [28] Li H., Sheng Y., Zhang H., Xue J., Zheng K., Huo Q., Zou H. Synthesis and luminescent properties of  $\text{TiO}_2:\text{Eu}^{3+}$  nanotubes. *Powder Technology*, 2011, **212**(2), P. 372–377.
- [29] Duong N.T., Tuan D.A., Son N.M., Tung V.T. Photoluminescent properties of  $\text{Eu}^{3+}$  doped  $\text{TiO}_2$  nanoparticles synthesized using an acid sulfuric method. *Wulfenia*, 2018, **25**(8), P. 136–146.
- [30] Tong T., Zhang J., Tian B., Chen F., He D., Anpo M. Preparation of Ce- $\text{TiO}_2$  catalysts by controlled hydrolysis of titanium alkoxide based on esterification reaction and study on its photocatalytic activity. *Journal of Colloid and Interface. Science*, 2007, **315**(1), P. 382–388.
- [31] Xie Y., Yuan C., Li X. Photosensitized and photocatalyzed degradation of azo dye using  $\text{Ln}^{n+}\text{-TiO}_2$  sol in aqueous solution under visible light irradiation. *Materials Science and Engineering B*, 2005, **117**, P. 325–333.
- [32] Liu H., Yu L., Chen W., Li Y. The progress of  $\text{TiO}_2$  nanocrystals doped with rare earth ions. *Journal of Nanomaterials*, 2012, P. 9.
- [33] Zakaria S.A., Kassim A., Lim H.N., Anwar N.S., Huang N.M. Synthesis of titanium dioxide microstructures via sucrose ester microemulsion-mediated hydrothermal method. *Sains Malaysiana*, 2010, **39**(6), P. 975–979.
- [34] Ohsaka T., Izumi F., Fujiki Y. Raman spectrum of anatase,  $\text{TiO}_2$ . *Journal of Raman spectroscopy*, 1978, **7**(6), P. 321–324.
- [35] Choi H.C., Jung Y.M., Kim S.B. Size effects in the Raman spectra of  $\text{TiO}_2$  nanoparticles. *Vibrational Spectroscopy*, 2005, **37**, P. 33–38.
- [36] Cheng H., Ma J, Zhao Z. et al. Hydrothermal preparation of uniform nanosize rutile and anatase particles *Chemistry of Materials*, 1995, **7**, P. 663–671.
- [37] Ebendor-Heidepriem H., Ehrh D. Formation and UV absorption of cerium, europium and terbium ions in different valencies in glasses. *Optical Materials*, 2000, **15**, P. 7–25.
- [38] Görrler-Walrand C., Binnemans K. Spectral intensities of f–f transitions. In: Gschneidner K.A.Jr., Eyring L. *Handbook on the physics and chemistry of rare earths*. Elsevier BV, Amsterdam, Ch. 167, 1998, **25**.

## Influence of carbon or nitrogen dopants on the electronic structure, optical properties and photocatalytic activity of partially reduced titanium dioxide

V. P. Zhukov<sup>1</sup>, M. G. Kostenko<sup>1</sup>, A. A. Rempel<sup>2</sup>, I. R. Shein<sup>1</sup>

<sup>1</sup>Institute of Solid State Chemistry, Ural Branch of the Russian Academy of Sciences, Russia

<sup>2</sup>Institute of Metallurgy, Ural Branch of the Russian Academy of Sciences, Russia

Zhukov@ihim.uran.ru

PACS 71.20.Nr, 61.72.Ji, 71.55.i

DOI 10.17586/2220-8054-2019-10-3-374-382

For titanium dioxide with anatase structure doped with carbon or nitrogen, the first-principle method of projector augmented waves (PAW) is used to calculate electronic band structure, to evaluate vacancy formation energy for the oxygen sublattice, and to analyze optical absorption. It is demonstrated that the presence of carbon dopants results in the stabilization of oxygen vacancies and leads to increased absorption in the visible spectrum, which can facilitate the photocatalytic activity. The presence of nitrogen dopant also facilitates vacancy stabilization but no increase in the interband absorption is expected in the visible spectrum, i.e., the presence of nitrogen dopant cannot be considered as a factor contributing to increased photocatalytic activity. It follows from the calculated data that the maximum photocatalytic activity should be expected for the partially-reduced anatase doped with carbon because of the absorption in the visible spectrum that combines with long time of electron-hole recombination.

**Keywords:** titanium dioxide, vacancies, doping, electronic structure, optical absorption, photocatalysis.

*Received: 12 February 2019*

*Revised: 22 April 2019*

### 1. Introduction

Titanium dioxide with anatase structure is stable, inexpensive, and exhibits photocatalytic activity in the UV range, which makes it a promising material for application in the development of photocatalysts capable of operating efficiently under solar radiation [1–7]. To this end, the material has to be modified to enhance its optical absorption in the visible spectrum comprising a majority of the radiation energy, i.e., it is required to increase the number of photocatalytically active electron-hole pairs. At the same time, electrons and holes are required to retain high mobility, while their recombination rate should be low.

Doping with  $2p$ -,  $3p$ -,  $6p$ - and  $3d$ - elements is regarded to be an effective method for enhancing absorption in the visible spectrum and partial reduction of titanium dioxide. The reduction results in vacancies formed in the oxygen sublattice, which is also considered to be of utility for enhancing photocatalytic activity. In particular, a process of photocatalytic decomposition of organic molecules on partially-reduced anatase under visible light irradiation is reported in [8–12]. State-of-the-art theoretical methods developed for calculating electronic structure and properties can be instrumental in designing efficient photocatalysts. Such methods are useful for obtaining information about the states of oxygen vacancies and other defects present in the band gap. They can be applied to explore defect-related characteristics of optical absorption, to study mobility of current carriers and to determine electron-hole recombination rates. A significant amount of research has been reported in the literature, along with calculations of electronic band structure, calculations of defect formation energy [13–19], crystalline geometry modifications near dopants [13, 14, 16, 18], and interpretation of optical [14, 20], photoemission [14] and EPR spectra [14]. However, the cited references have some drawbacks that hinder realization of the state-of-the-art capabilities developed for modeling the electronic structure and characteristics of solids. Thus, the cited sources [13–17, 19, 21] fail to include calculations of optical properties and to consider correlations between the band structure and the optical properties. Also disputable is the method applied in [15–17, 19, 21] for calculating the formation energy of vacancies with the charge  $q = +1$  or  $+2$ . When calculating the formation energy of charged vacancies using this approach, the fault is that the presence of charge is modeled by introducing only a uniform charge distribution. However, in real objects, dopant atoms of carbon, nitrogen and other elements may be electron acceptors, which may cause a substantial effect on the chemical bonding around vacancies.

The goal of the present research is to provide the results of a new theoretical study exploring the issues related to the effect of vacancies on the photocatalytic activity of anatase. The study comprises calculations of band structure, reviews the energy aspects of vacancy formation, and provides assessment of optical absorption coefficients at various energies. In addition, an effort is made to model the electronic structure of charged vacancies by introducing impurity centers of nitrogen atoms, which transform vacancies into a charged state of  $q = +1$ , or carbon atoms, which result in

a charged state of  $q = +2$ . The study allowed a number of conclusions to be made about the prospects for enhancing the photocatalytic performance of partially reduced anatase.

## 2. Method for calculating electronic structure and vacancy formation energy

A supercell method was applied to model the defect structure comprising structural vacancies and impurity atoms in titanium dioxide [22]. The extended cell was produced by twofold translations of tetragonal elementary cell of anatase (Fig. 1) in every crystallographic direction; and it contained 32 sites in the titanium sublattice and 64 sites in the oxygen sublattice. The supercell of the specified dimension allowed a minimum concentration of vacancies at 1.56 % to be produced in the oxygen sublattice by removing one atom from the initially complete cell [23]. The calculations were carried out using a pseudo-potential projector augmented waves method (PAW) within the basis of plane waves realized in the VASP software package [24]. Software-provided PAW pseudo-potentials were used; and for the exchange-correlation potential the GGA approximation was applied. The calculations were carried out for the lattice composed of 27 vectors in the irreducible part of the Brillouin zone and with the maximum energy of plane waves at 350 eV. In all calculations, the accuracy of self-consistent total energy was no worse than  $10^{-6}$  eV.

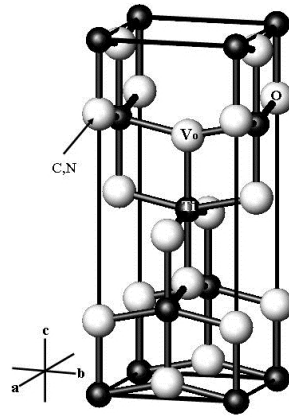


FIG. 1. A tetragonal structure of anatase. Titanium atoms are designated with the black balls, and oxygen atoms are designated with the light balls. Also shown are the oxygen vacancy sites VO and the sites of substituting carbon or nitrogen atoms

In all cases considered below, the lattice parameters and the atomic coordinates were optimized in accordance with the forces acting on the atoms (the optimization method is described in [24]). The total energy minimum was considered to have been achieved if the total energy variation around the minimum did not exceed 0.001 eV. Thus optimized, the parameters of crystal structure turned out to be rather close to the parameters of undoped anatase. For instance, the calculated lattice parameters for carbon-doped anatase amounted to  $a = 3.7946$  Å,  $c/a = 2.5295$ , and for nitrogen-doped anatase the parameters were obtained at the values of  $a = 3.7958$  Å and  $c/a = 2.5208$ , while the corresponding perfect anatase lattice parameters were 3.7845 Å and 2.5140, respectively. For the optimized geometry, the total densities of states (DOS's) obtained by tetrahedron integration [24] were plotted.

Modeling the vacancies having a charge of  $q = +1, +2$  was carried out by introducing one atom of carbon or nitrogen into the supercell. It was demonstrated in [25] that with synthesis under low partial oxygen pressure under thermodynamic equilibrium conditions, the atoms of carbon or nitrogen have a tendency of forming vacancy-dopant pairs. Therefore, in the present study we assumed that the dopants of carbon or nitrogen substitute for the oxygen atoms nearest to vacancy.

Optical absorption coefficients were calculated for all considered variants of the defects in anatase. The calculations were based on the energy-dependent dielectric function that was calculated within the independent particle approximation [24]. The absorption coefficient was calculated from the real and imaginary parts of the dielectric function according to the theory described in [26]. Specifically, within the theory, the absorption coefficient is calculated as follows:

$$K(E) = \frac{\epsilon_2(E)}{2} \frac{1}{\left\{ \frac{\epsilon_1(E)}{2} + \left[ \left( \frac{\epsilon_1(E)}{2} \right)^2 + \left( \frac{\epsilon_2(E)}{2} \right)^2 \right]^{1/2} \right\}^{1/2}},$$

where  $\epsilon_1$  and  $\epsilon_2$  are, respectively, the excitation energy-dependent real and imaginary parts of the dielectric function averaged over directions of the wave vector.

The electron density functional theory, including the PAW method, is known to have a drawback that the bandgap value in semiconductors is underestimated, which can result in erroneous calculations of optical characteristics. To eliminate such errors, we used a so-called LDA+U approach, within which the exchange-correlation potential is improved by introducing one-center Hubbard-type corrections. An option suggested by Dudarev et al in [27] was used, where the exchange-correlation corrections depend on one parameter  $U$ . In all our calculations, we assume the parameter to be  $U = 7.8$  eV, which brings the bandgap of the perfect anatase in a good agreement with experimental data, i.e., 3.2 eV [28].

### 3. Oxygen vacancy formation energy and the effect of doping with carbon or nitrogen

When calculating the vacancy formation energy in anatase, the entropy contribution was neglected and only the first-principle calculations of the total energy were taken into consideration. In this approximation, the free energy of oxygen vacancy formation in the 96-atom anatase cell can be written as follows:

$$E_f(vac) = E_{tot}(Ti_{32}O_{63}) + \mu(O) - E_{tot}(Ti_{32}O_{64}).$$

Here,  $\mu(O)$  is the chemical potential of oxygen atom. Similarly, if a substitutional dopant for oxygen atom  $A_O$ , where  $A$  states for C or N, is added to the cell, then the vacancy formation energy can be calculated as:

$$E_f(vac, A_O) = E_{tot}(Ti_{32}O_{62}A_O) + \mu(O) - E_{tot}(Ti_{32}O_{63}A_O).$$

The method for calculating the chemical potential for oxygen atom was thoroughly described in [25], so here, we only note that this method is based on the calculation of the total energy of oxygen molecule, and includes also the temperature and the partial pressure dependences. Fig. 2 displays the values of chemical potential for three temperatures ranging from room temperature to a temperature of  $T = 900$  K, which is a typical value for annealing during synthesis from precursors. We also assume that the partial oxygen pressure can be varied from 1 to  $10^{-30}$  atm (conditional vacuum).

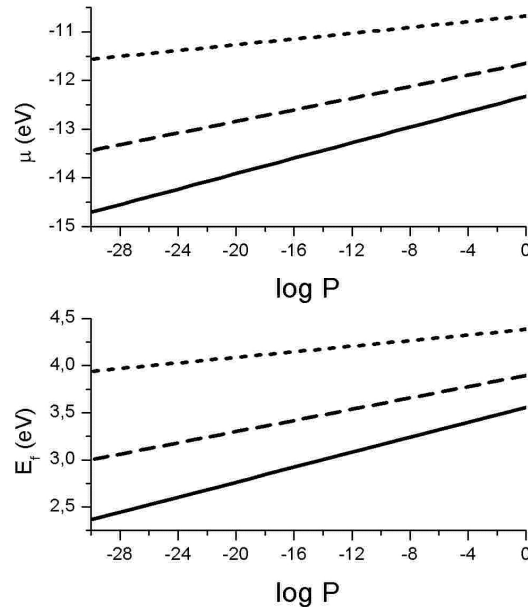


FIG. 2. Calculated values of the chemical potential for oxygen atom (upper panel) and vacancy formation energy (lower panel) in anatase as a function of temperature and partial oxygen pressure  $P$ . Solid lines designate the results for  $T = 900$  ; dashed lines designate the result for 600 , and dotted lines correspond to  $T = 300$

It can be seen that the chemical potential values and, accordingly, the vacancy formation energy values, decrease as temperature increases and partial pressure decreases. However, at all the considered values of  $T$  and  $P$ , the oxygen vacancy formation energy retains a great positive value, i.e., in undoped anatase under thermodynamic equilibrium

synthetic conditions of the formation of vacancies at a high concentration is not feasible. This conclusion agrees with the outcomes reported in [13, 14], even though the values of vacancy formation energy are somewhat different from the ones reported in our study.

The vacancy formation energy values in the presence of carbon or nitrogen dopants as a function of pressure and temperature are shown in Fig. 3.

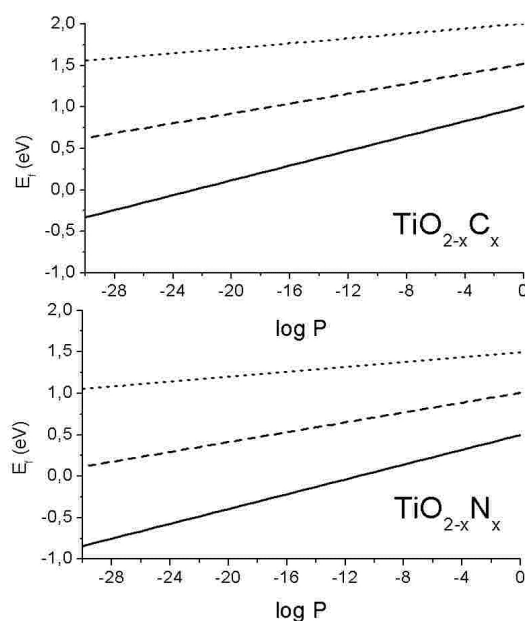


FIG. 3. Calculated values of vacancy formation energy in anatase in the presence of carbon or nitrogen dopants as a function of temperature and partial oxygen pressure  $P$ . The solid lines indicate the results obtained at a temperature of  $T = 900$ ; the dashed line corresponds to  $T = 600$ ; and the dotted line corresponds to  $T = 300$

It can be seen that introduction of carbon or nitrogen atoms into the anatase structure results in a significant decrease in the vacancy formation energy. The energy values become negative at a temperature of 900 and at the partial oxygen pressure  $P = 10^{-24}$  atm for doping with carbon and at the pressure  $P = 10^{-12}$  atm for doping with nitrogen, which is indicative of a possibility to significantly increase the vacancy concentration with the presence of these dopants. This outcome is also in agreement with the conclusions reported in [13, 14]. It can also be seen that the presence of nitrogen results in a more significant decrease in the vacancy formation energy. However, we will show below that increasing the photocatalytic activity of N-doped anatase is unlikely to be achieved by increasing vacancy concentration in anatase.

#### 4. Electronic structure, optical absorption and photocatalytic activity of partially reduced anatase in the presence of carbon or nitrogen dopants

Figure 4 displays densities of states for pristine anatase and for anatase containing 1.56 atom% of oxygen vacancies. Showing a good agreement with experiment, the bandgap width is 3.21 eV for undoped anatase; and it is 3.12 eV for anatase with vacancies. In the presence of vacancies, below the bottom of conduction band at 5.89 eV, there appears a band of vacancy states which contains two electrons and, because of the lack of electron transfer into lower-energy states, is electrically neutral. There is no gap between the vacancy band states and the conduction band states; this agrees with the results reported in [29], according to which the width of bandgap in partially-reduced anatase does not exceed 0.01 eV. Therefore, along with the fundamental absorption, one should expect optical absorption occurring over the entire visible range and near IR due to the excitations from the vacancy states into the conduction band. This is supported quite well with the experimental data reported in [30], which are presented in Fig. 5.

Figure 6 displays the densities of states observed with nitrogen or carbon atoms being introduced into partially reduced anatase; and Fig. 7 shows the corresponding data obtained in the calculations of absorption coefficients. The states of nitrogen atom are localized near the bandgap bottom, and the vacancy states are located near the upper edge of the bandgap. If a nitrogen atom substitutes for an oxygen atom, then it traps one extra electron from the vacancy states, which corresponds to the transition of a vacancy into the state with a charge of  $q = +1$ . It follows from this

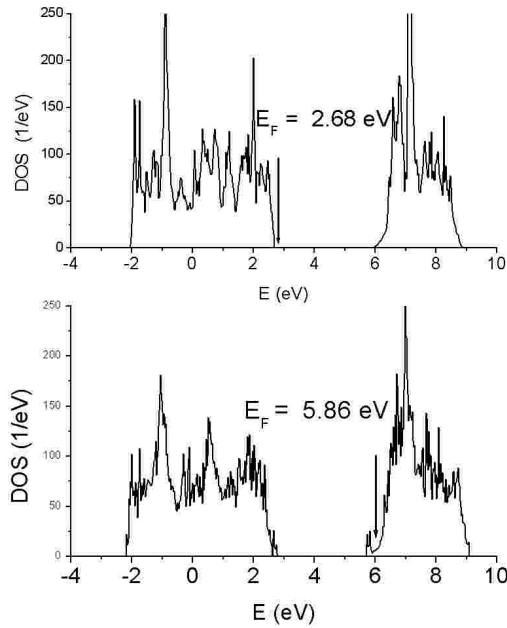


FIG. 4. Density of states in the valence and conduction bands as calculated in the LDA+U approximation for undoped anatase (upper panel) and for anatase containing oxygen vacancies (lower panel). Marked are the Fermi level positions

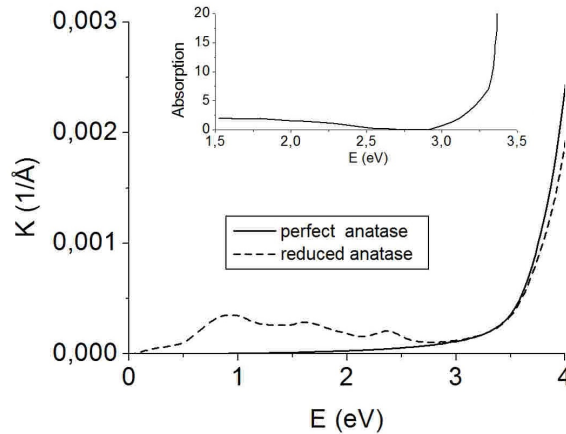


FIG. 5. Calculated absorption coefficients for perfect anatase and that having vacancies in the oxygen sublattice, and the corresponding experimental data reported in [29], in the insert

band structure that, as far as light absorption is concerned, a situation is realized that is similar to the situation for undoped anatase. Really, it can be seen from Fig. 7 that over the entire optical range the absorption profile is rather close to the profile of absorption in the reduced anatase.

However, the situation changes significantly with the presence of carbon atoms. In this case, inside the bandgap there appear two narrow bands of carbon states near 3 and 4 eV, with the Fermi level being positioned at the upper edge of the second band. Two electrons from the vacancy states drop to these states, i.e., a vacancy takes the charge  $q = +2$ . The band near 3 eV is separated from the empty vacancy states with an interval of 2.8 eV, and the band near 4 eV is separated with an interval of 1.9 eV. It can be seen from Fig. 7 that near 2.8 eV, the light absorption is nearly ten times as great as the absorption in reduced undoped anatase. This can lead to increased photocatalytic activity because of the increased number of light quanta absorbed. Comparison with the densities of states demonstrates that the absorption peak at 2.8 eV is partially caused by the transitions from the carbon atomic states near 3 eV into the vacancy states. The second reason for this peak may be the excitations from the carbon band near 4 eV into the states of conduction band that form a peak at 6.8 eV.

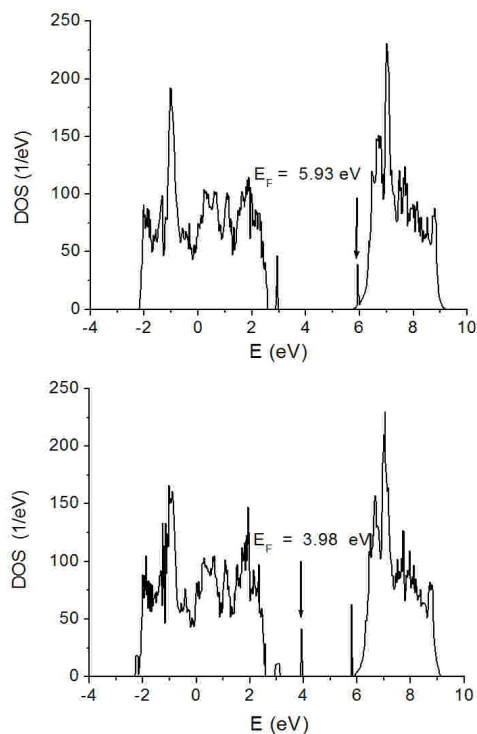


FIG. 6. Density of states in the valence band and in the conduction band, calculated in the LDA+U approximation for anatase containing oxygen vacancies and nitrogen atoms (upper panel) or oxygen vacancies and carbon atoms (lower panel). Marked are the Fermi level positions

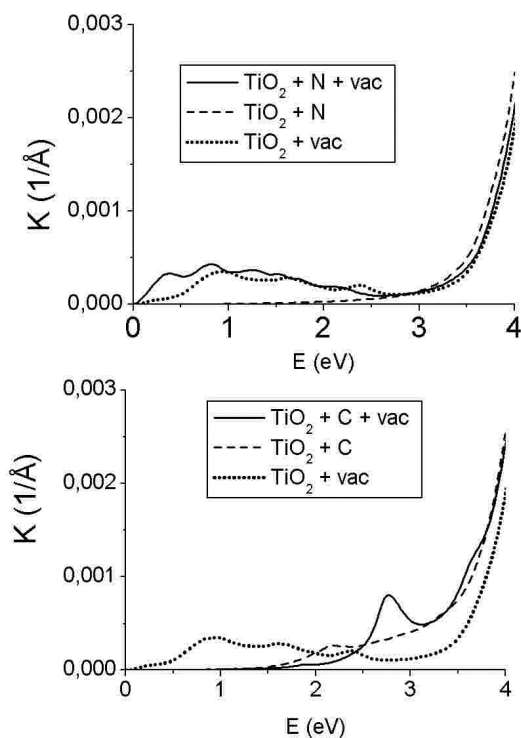


FIG. 7. Calculated values of absorption coefficient of anatase having vacancies in the oxygen sublattice in the presence of nitrogen atoms (upper panel) or carbon atoms (lower panel). Values of absorption coefficients are also given for nitrogen or carbon-doped anatase without oxygen vacancies

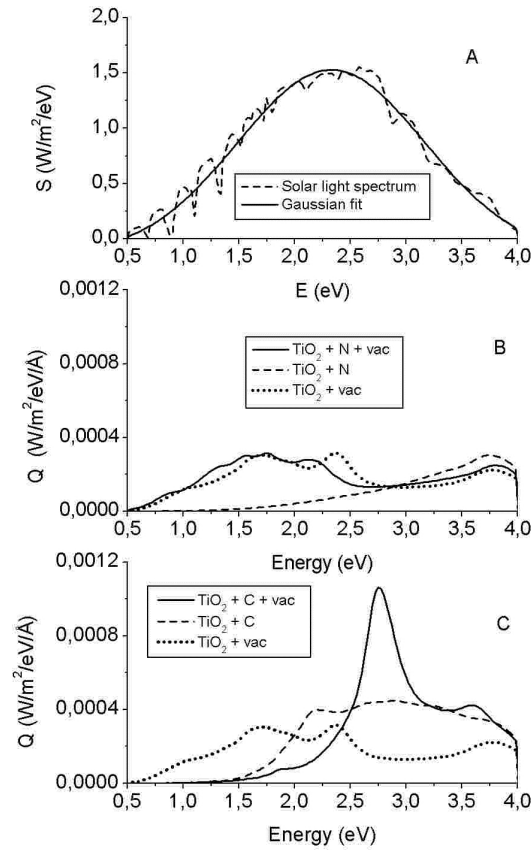


FIG. 8. Panel A: solar radiation spectrum [31] and the corresponding Gaussian approximation; panels B and C display the calculated values of optical efficiency

It is known that upon passing through the atmosphere the solar radiation spectrum looks like a curve approaching the Gaussian distribution with a width of about 2 eV and a maximum located near 2.5 eV. To quantitatively describe the efficiency of solar radiation absorption in the materials under study, we introduce a notion of a catalyst's optical efficiency defined as  $Q(E) = S(E) \times K(E)$ , where  $S(E)$  is the Gaussian approximation to the solar radiation spectrum (see Fig. 8), and also the notion of an integral efficiency defined as  $I_Q = \int Q(E)dE$ , which upon calculation, we confine inside the interval from 0.5 to 4 eV. The results for  $I_Q$  are given in Table 1.

TABLE 1. Integral values of optical efficiency  $I_Q$

Compound	TiO <sub>2</sub>	TiO <sub>2</sub> + vacancy	TiO <sub>2</sub> +N	TiO <sub>2</sub> +N+ vacancy	TiO <sub>2</sub> +C	TiO <sub>2</sub> +C+ vacancy
$I_Q \times 10^4$	2.8	6.3	3.4	6.6	8.3	9.0

Analysis of the data leads to the following conclusions. Perfect anatase, which is seen to absorb only a fraction of UV part of solar radiation, has the lowest optical efficiency, which is nearly one third as much as the optical efficiency of the other materials under study. Since doping with nitrogen causes just a slight red-shift of the fundamental absorption edge, the lack of absorption in the visible spectrum for TiO<sub>2</sub> + N causes only a small increase in the integral quantum efficiency. However, for partially reduced anatase, both in the TiO<sub>2</sub> + vacancy and TiO<sub>2</sub> + N + vacancy cases, the absorption in the visible spectrum results in a doubled increase of  $I_Q$  as compared to the perfect anatase. The maximum integral efficiency is predicted for C-doped anatase, as can be seen from the data for TiO<sub>2</sub> + C and TiO<sub>2</sub> + C + vacancy cases. The reason is that these compounds exhibit increased absorption near the maximum of solar radiation spectrum.

It should be noted, however, that there are certain properties of the band structure, which hinder any significant increase in the photocatalytic activity under doping, regardless of the absorption observed in the visible spectrum and

despite the increased values of optical efficiency. A necessary condition for photocatalytic activity is a sufficiently long time required for the recombination of electron-hole pairs, which should be greater than the time for transferring excited carriers into the reaction medium. It is known that the picoseconds or greater time is required for the recombination of pairs formed via the interband excitations in semiconducting oxides [32, 33]. It is also known that a time of no less than ten ps is required for transferring electrons onto the islands of a sensibilizer (e.g. the time for transferring electrons from  $\text{TiO}_2$  onto platinum islands on the surface), and even a greater time (up to 100 ms) is required, for example, for transferring electrons on oxygen molecules on the surface, see a review reported in [33]. However, one should expect that the recombination time is going to be several orders of magnitude smaller if there is no gap between the vacancy states and the conduction band, as is the cases for  $\text{TiO}_2 + \text{vacancy}$  and  $\text{TiO}_2 + \text{N} + \text{vacancy}$ . It was shown in [34] that, because of the emission of phonons, the excited electrons in the conduction band states of  $\text{TiO}_2$  lose their excitation energy and sink onto the bottom of the band over the time that does not exceed several tens of fs; after this time the electrons recombine with the holes in the vacancy states. These data are also in agreement with the experimental results which reveal that the trapping of conduction band electron onto the states of dopants near the top of the band gap occurs over 100 – 250 fs, while the hole trapping on the states near the bottom of the gap takes 50 – 150 fs [33]. Therefore, one can expect that for these cases, only a small number of electrons are involved in the photocatalytic process. These are the excited electrons which form a high-energy “tail” of the electron distribution in the conduction band [34]; in analogy, a similar distribution of holes inside the valence band can exist [35]. In both cases, as in  $\text{TiO}_2 + \text{vacancy}$  as in  $\text{TiO}_2 + \text{N} + \text{vacancy}$ , the electron-hole pairs can be formed not only because of the excitations inside the conduction band but also because of the excitations into the conduction band from the valence band or from the band of nitrogen states. However, the energy of such excitations is greater than 3 eV, which also prevents any significant increase in the photocatalytic activity as compared to the perfect anatase. It should be noted that, although the nitrogen-doped anatase is a classical subject of photocatalytic studies, there are data available that report about its rather small photocatalytic activity. Thus, in [36–39], the photocatalytic activity of N-doped anatase has been studied in the decomposition reactions of formic acid, ethylene glycol and other compounds, but no positive effect of N-doping has been revealed

Therefore, only in the  $\text{TiO}_2 + \text{C} + \text{vacancy}$  case, that is, for the C-doped partially-reduced anatase, we can expect an increase in the photocatalytic activity caused by the optical absorption accompanied by the long time required for the recombination of excited electron-hole pairs. To our knowledge, there are no systematic data available on the photocatalytic activity of similar compounds; however, the photocatalytic activity of C-doped anatase observed in the visible spectrum has repeatedly been reported in literature (see, for instance, the literature review in [36]). Our calculations provide evidence that the photocatalytic activity of C-doped anatase can be increased through its partial reduction.

## 5. Conclusion

Based on the first-principle calculations of the electronic band structure and oxygen vacancy formation energy for undoped anatase and that containing carbon or nitrogen dopants, we analyzed the influence of vacancies on the photocatalytic activity in visible spectrum. It was demonstrated for undoped anatase that a high vacancy concentration cannot be obtained via synthesis under thermodynamic equilibrium conditions, neither at an elevated temperature nor at a low partial oxygen pressure. In addition, because of the short electron-hole recombination time and because of the high fundamental absorption energy, no significant increase in the photocatalytic activity can be observed for reduced undoped anatase.

We also demonstrate that the vacancy formation energy can be decreased considerably, i.e., the vacancy concentration can be increased, in the presence of carbon or nitrogen atoms substituting the oxygen atoms. This effect is especially pronounced for nitrogen dopants. However, with nitrogen doping, because of the excessive energy of fundamental absorption and short time of electron-hole recombination, one can hardly expect an essential increase in the photocatalytic activity. Our calculations provide evidence that the optical absorption may increase in partially reduced C-doped anatase because of the interband transitions at the energy approaching the solar radiation intensity maximum. This might be a result of tuning the electronic band structure via creation of new states near the middle of the band gap and beneath the bottom of the conduction band.

## Acknowledgements

The calculations were carried out on the URAN cluster of the Institute of Mathematics and Mechanics, Ural Branch of the Russian Academy of Sciences. A deep gratitude is expressed to V.N. Krasilnikov for the fruitful discussions of the research subject.

## References

- [1] Hoffmann M.R., Martin S.T., Choi W., Bahnemann D.W. Environmental applications of the semiconductor photocatalysis. *Chem. Rev.*, 1995, **95** (1), P. 69–96.
- [2] Fujishima A., Rao T.N., Tryk D.A. Titanium dioxide photocatalysis. *J. Photochem. Photobiol. C: Photochem. Rev.*, 2000, **1** (1), P. 1–21.
- [3] Hashimoto K., Irie H., Fujishima A. TiO<sub>2</sub> photocatalysis: a historical overview and future prospects. *Jap. Journ. Appl. Phys.*, 2005, **44** (12), P. 8269–8285.
- [4] Zaleska A. Doped-TiO<sub>2</sub>: a review. *Recent Patents on Engineering*, 2008, **2** (3), P. 157–164.
- [5] Kitano M., Tsujimaru M., Anpo M. Hydrogen producing using highly active titanium oxide-based photocatalysts. *Top. Catal.*, 2008, **49** (1–2), P. 4–17.
- [6] Thakur R.S., Chaudhary R., Singh C.J. Fundamentals and applications of the photocatalytic treatment for the removal of industrial organic pollutants and effects of operational parameters: a review. *Renewable Sustainable Energy*, 2010, **2** (4), P. 042701–04399.
- [7] Gupta S.M., Tripathi M. A review of TiO<sub>2</sub> nanoparticles. *Chinese Sci. Bull.*, 2011, **56** (16), P. 1639–1657.
- [8] Justicia I., Ordejón P., et al. Designed self-doped titanium oxide thin films for efficient visible-light photocatalysis. *Advanced materials*, 2002, **14** (19), P. 1399–1402.
- [9] Martyanov I.N., Uma S., Rodrigues Sh., Klabunde K.J. Structural defects cause TiO<sub>2</sub>-based photocatalysts to be active in visible light. *Chem. Commun.*, 2004, **21**, P. 2476–2477.
- [10] Liu H., Yang W., Ma Y., Yao J. Extended visible light response of binary TiO<sub>2</sub>-Ti<sub>2</sub>O<sub>3</sub> photocatalist prepared by a photo-assisted sol-gel method. *Applied Catalysis A*, 2006, **299** (1), P. 218–223.
- [11] Dong C.X., Xian A.P., Han E.H., Shang J.K. Acid-mediated sol-gel synthesis of visible-light active photocatalysts. *Journ. of Mater. Sci.*, 2006, **41** (18), P. 6168–6170.
- [12] Yang X., Cao Ch., et al. Synthesis of visible-light-active TiO<sub>2</sub>-based photocatalysts by carbon and nitrogen doping. *Journ. of Catalysis*, 2008, **260** (1), P. 128–133.
- [13] Di Valentin C., Pacchioni G., Selloni A. Theory of carbon doping of titanium dioxide. *Chem. Mater.*, 2005, **17** (26), P. 6656–6665.
- [14] Di Valentin C., Finazzi E., et al. N-doped TiO<sub>2</sub>: theory and experiment. *Chem. Phys.*, 2007, **339** (1–3), P. 44–56.
- [15] He J., Sinnott S.B. Ab initio calculations of intrinsic defects in rutile TiO<sub>2</sub>. *Journ. Amer. Ceram. Soc.*, 2005, **88** (3), P. 737–741.
- [16] He J., Behera R.K., et al. Prediction of high-temperature point defect formation in TiO<sub>2</sub> from combined ab initio and thermodynamic calculations. *Acta Materialia*, 2007, **55** (13), P. 4325–4337.
- [17] Xiao Q., Si Zh., et al. Effect of samarium dopant on photocatalytic activity of TiO<sub>2</sub> nanocrystallite for methylen blue degradation. *Journ. of Mater. Sci.*, 2007, **42** (22), P. 9194–9199.
- [18] Islam M.M., Bredow T., Gerson A. Electronic properties of oxygen-deficient and aluminium-doped rutile TiO<sub>2</sub> from first principles. *Phys. Rev. B*, 2007, **76** (4), 045217.
- [19] Osorio-Guillén J., Lany S., Zunger A. Atomic control of conductivity versus ferromagnetism in wide-gap oxides via selective doping: V, Nb, Ta in anatase TiO<sub>2</sub>. *Phys. Rev. Lett.*, 2008, **100** (3), 036601.
- [20] Zainullina V.M., Zhukov V.P., et al. Electronic structure and the optical and photocatalytic properties of anatase doped with vanadium and carbon. *Physics of the Solid State*, 2010, **52** (2), P. 271–280.
- [21] He J., Finnis M.W., Dickey E.C., Sinnott S.B. Charged defects formation energies in TiO<sub>2</sub> using the supercell approximation. *Advances in Science and Technology*, 2006, **45**, P. 1–8.
- [22] Payne M.C., Teter M.P., et al. Iterative minimization techniques for ab initio total-energy calculations: molecular dynamics and conjugate gradients. *Rev. of Modern Physics*, 1992, **64** (4), P. 1045–1098.
- [23] Diebold U. The surface science of titanium dioxide. *Surface Science Reports*, 2003, **48** (5–8), P. 53–229.
- [24] Kresse G., Marsman M., Furthmüller J. Vasp the guide. 2011. URL: <http://cms.mpi.univie.ac.at/vasp/guide/vasp.html>.
- [25] Zhukov V.P., Shein I.R. Ab initio thermodynamic characteristics of the formation of oxygen vacancies, and boron, carbon, and nitrogen impurity centers in anatase. *Physics of the Solid State*, 2018, **60** (1), P. 37–48.
- [26] Ziman J.M. *Principles of the Theory of Solids*. Cambridge University Press, 2013, 452 p.
- [27] Dudarev S.L., Botton G.A., et al. Electron-energy loss spectra and structural stability of nickel oxide: an LSDA+U study. *Phys. Rev. B*, 1998, **57** (3), P. 1505–1509.
- [28] Tang H., Berger H., et al. Photoluminescence in TiO<sub>2</sub> anatase single crystals. *Solid State Commun.*, 1993, **87** (9), P. 847–850.
- [29] Jacimovic J., Vaju C., et al. Pressure dependence of the large-polaron transport in anatase. *EPL*, 2012, **99** (5), 57005.
- [30] Sekiya T., Yagisawa T., et al. Defects in anatase TiO<sub>2</sub> single crystal controlled by heat treatment. *Journ. of the Phys. Soc. of Japan*, 2004, **73** (3), P. 703–710.
- [31] Wu J., Walukiewicz W., et al. Unusual properties of the fundamental band gap of InN. *Appl. Phys. Lett.*, 2002, **80** (21), P. 3967–3969.
- [32] Henderson M.A. A surface science perspective on TiO<sub>2</sub> photocatalysis. *Surface Science Reports*, 2011, **66** (6–7), P. 185–297.
- [33] Schneider J., Matsuoka M., et al. Understanding TiO<sub>2</sub> photocatalysis: mechanisms and materials. *Chemical Review*, 2014, **114** (19), P. 9919–9986.
- [34] Tyuterev V.G., Zhukov V.P., Chulkov E.V., Echenique P.M. Relaxation of highly excited carriers in wide-gap semiconductors. *Journ. of Phys.: Cond. Matter*, 2015, **2**, 02581.
- [35] Zhukov V.P., Tyuterev V.G., Chulkov E.V., Echenique P.M. Hole-phonon relaxation and photocatalytic properties of titanium dioxide and zinc oxide: first-principle approach. *Intern. Journ. of Photoenergy*, 2014, Article Id. 738921.
- [36] Mrowetz M., Balcerski W., Colussi A.J., Hoffmann M.R. Oxidative power of nitrogen-doped TiO<sub>2</sub> photocatalysts under visible illumination. *Journ. of Phys. Chem. B*, 2004, **108** (45), P. 17269–17273.
- [37] Irie H., Watanabe Y., Hashimoto K. Nitrogen-concentration dependence on photocatalytic activity of TiO<sub>2-x</sub>N<sub>x</sub> powders. *Journ. of Phys. Chem. B*, 2003, **107** (23), P. 5483–5486.
- [38] Fu H.B., Zhang L.W., et al. Electron spin resonance spin-trapping of radical intermediates in N-doped TiO<sub>2</sub>-assisted photodegradation of 4-chlorophenol. *Journal of Phys. Chem. B*, 2006, **110** (7), P. 3061–3065.
- [39] Tachikawa T., Fujitsuka M., Majima T. Mechanistic insight into the TiO<sub>2</sub> photocatalytic reactions: design of new photocatalysts. *Journal of Physical Chemistry C*, 2007, **111** (14), P. 5259–5275.



# **NANOSYSTEMS:**

## **PHYSICS, CHEMISTRY, MATHEMATICS**

### **INFORMATION FOR AUTHORS**

The journal publishes research articles and reviews, and also short scientific papers (letters) which are unpublished and have not been accepted for publication in other magazines. Articles should be submitted in English. All articles are reviewed, then if necessary come back to the author to completion.

The journal is indexed in Web of Science Core Collection (Emerging Sources Citation Index), Chemical Abstract Service of the American Chemical Society, Zentralblatt MATH and in Russian Scientific Citation Index.

#### **Author should submit the following materials:**

1. Article file in English, containing article title, the initials and the surname of the authors, Institute (University), postal address, the electronic address, the summary, keywords, MSC or PACS index, article text, the list of references.
2. Files with illustrations, files with tables.
3. The covering letter in English containing the article information (article name, MSC or PACS index, keywords, the summary, the literature) and about all authors (the surname, names, the full name of places of work, the mailing address with the postal code, contact phone number with a city code, the electronic address).
4. The expert judgement on possibility of publication of the article in open press (for authors from Russia).

Authors can submit a paper and the corresponding files to the following addresses: nanojournal.ifmo@gmail.com, popov1955@gmail.com.

#### **Text requirements**

Articles should be prepared with using of text editors MS Word or LaTeX (preferable). It is necessary to submit source file (LaTeX) and a pdf copy. In the name of files the English alphabet is used. The recommended size of short communications (letters) is 4-6 pages, research articles– 6-15 pages, reviews – 30 pages.

##### Recommendations for text in MS Word:

Formulas should be written using Math Type. Figures and tables with captions should be inserted in the text. Additionally, authors present separate files for all figures and Word files of tables.

### Recommendations for text in LaTeX:

Please, use standard LaTeX without macros and additional style files. The list of references should be included in the main LaTeX file. Source LaTeX file of the paper with the corresponding pdf file and files of figures should be submitted.

References in the article text are given in square brackets. The list of references should be prepared in accordance with the following samples:

- [1] Surname N. *Book Title*. Nauka Publishing House, Saint Petersburg, 2000, 281 pp.
- [2] Surname N., Surname N. Paper title. *Journal Name*, 2010, **1** (5), P. 17-23.
- [3] Surname N., Surname N. Lecture title. In: Abstracts/Proceedings of the Conference, Place and Date, 2000, P. 17-23.
- [4] Surname N., Surname N. Paper title, 2000, URL: <http://books.ifmo.ru/ntv>.
- [5] Surname N., Surname N. Patent Name. Patent No. 11111, 2010, Bul. No. 33, 5 pp.
- [6] Surname N., Surname N. Thesis Title. Thesis for full doctor degree in math. and physics, Saint Petersburg, 2000, 105 pp.

### **Requirements to illustrations**

Illustrations should be submitted as separate black-and-white files. Formats of files – jpeg, eps, tiff.



# ***NANOSYSTEMS:***

***PHYSICS, CHEMISTRY, MATHEMATICS***

## **Журнал зарегистрирован**

Федеральной службой по надзору в сфере связи, информационных технологий и массовых коммуникаций

(свидетельство ПИ № ФС 77 - 49048 от 22.03.2012 г.)

ISSN 2220-8054

**Учредитель:** федеральное государственное автономное образовательное учреждение высшего образования

«Санкт-Петербургский национальный исследовательский университет информационных технологий, механики и оптики»

**Издатель:** федеральное государственное автономное образовательное учреждение высшего образования

«Санкт-Петербургский национальный исследовательский университет информационных технологий, механики и оптики»

**Отпечатано** в Учреждении «Университетские телекоммуникации»

Адрес: 197101, Санкт-Петербург, Кронверкский пр., 49

## **Подписка на журнал НФХМ**

На первое полугодие 2020 года подписка осуществляется через

ОАО Агентство «Роспечать»

Подписной индекс 57385 в каталоге «Издания органов научно-технической информации»